KUNGL TEKNISKA HÖGSKOLAN

TRITA-MEK
Technical Report 2002:04
ISSN 0348-467X
ISRN KTH/MEK/TR--02/04--SE

Deployable Tensegrity Structures for Space Applications

Gunnar Tibert

Doctoral Thesis
Stockholm, 2002

Royal Institute of Technology
Department of Mechanics

Deployable Tensegrity Structures for Space Applications

Doctoral Thesis by Gunnar Tibert

ERRATA

11 July 2002

The indices of the cable and strut lengths in Equations (3.2) and (3.3) on pages 35 and 36 should be changed from (i) t to c and (ii) c to s so that they read:

$$l_c^2 = 2R^2(1 - \cos\theta) + H^2, \tag{3.2a}$$

$$l_s^2 = 2R^2\left[1 - \cos\left(\theta + \frac{2\pi i}{v}\right)\right] + H^2, \tag{3.2b}$$

and

$$l_s^2 = 4R^2 \sin\left(\theta + \frac{\pi i}{v}\right)\sin\frac{\pi i}{v} + l_c^2. \tag{3.3}$$

Equation (4.13) on page 83 should read:[1]

$$P_{\text{cr}} = 4\frac{C_M}{l} \tag{4.13}$$

As a result of the error in (4.13), the beginning of the second paragraph on page 84 should read:

...which yields $P_{\text{cr}} = 1315$ N using (4.13). Substituting the buckling load, $\Delta = 3.65$ mm and $M = 13$ Nm into (4.15) yielded $P = 960$ N.

Furthermore, the end of the third sentence on page 85 should read:

...$P_{\text{Eu}} = 5.28$ kN or about $5.5P$.

Finally, the end of line 13 on page 87 should read:

The buckling load of the struts, 960 N,...

---

[1]Thanks are due to Dr. Zhong You for pointing out this error to the author.

Deployable Tensegrity Structures for Space Applications

by

Gunnar Tibert

April 2002
Technical Reports from
Royal Institute of Technology
Department of Mechanics
SE-100 44 Stockholm, Sweden

Akademisk avhandling som med tillstånd av Kungliga Tekniska Högskolan i Stockholm framlägges till offentlig granskning för avläggande av teknologie doktorsexamen måndagen den 15:e april kl 13.00 i Kollegiesalen, Administrationsbyggnaden, Kungliga Tekniska Högskolan, Valhallavägen 79, Stockholm.

Preface

The work presented in this thesis was carried out at the Department of Engineering at the University of Cambridge, the Department of Structural Engineering and the Department of Mechanics at the Royal Institute of Technology between December 1999 and April 2002.

First, I thank Prof. Sergio Pellegrino for giving me the opportunity to work at his excellent Deployable Structures Laboratory (DSL). His guidance, enthusiasm, encouragement and vast knowledge of structures have been invaluable throughout the course of this research.

I thank my supervisor Prof. Anders Eriksson for his constant encouragement and guidance.

A debt of gratitude is owed to Peter Knott, Roger Denston, Alistair Ross and the technicians at the workshop of the Engineering Department in Cambridge and to Olle Läth and Daniel Hissing, at the laboratory of the Department of Structural Engineering in Stockholm, for their technical assistance.

Thanks are due to Prof. Christopher R. Calladine of the University of Cambridge for constructive comments on a draft paper and to Prof. William O. Williams of Carnegie Mellon University in Pittsburgh, USA and Andrea Micheletti of Università di Roma "Tor Vergata" in Rome for valuable discussions on tensegrity.

Many grateful thanks go to Eric Pak for excellent teamwork during the design and construction of the mast models, to Gerard James for interesting discussions and painstaking proof-reading of the manuscript, and to Dr. Anders Ansell and Dr. Karin Forsell for meticulous proof-reading of the manuscript.

I thank Tim Reynolds of the Defence Evaluation and Research Agency in Farnborough, UK for providing the reflector antenna design task and Ian Stern of Harris Corporation in Melbourne, USA for the data on their deployable reflector antennas and for the interesting discussions on deployable tensegrities.

A thank goes to colleagues and former colleagues of the Department of Structural Engineering and Department of Mechanics; in particular, Peter Andrén, Anders Ahlström, Dr. Jean-Marc Battini, Abraham Getachew, Rickard Johnson, Anders Olsson, Dr. Jonatan Paulsson-Tralla, Tom Thöyrä, Roger Ullmann, Anders Salwén, Anders Wiberg and those already mentioned above. I also thank the members of DSL and the Structures Research Group for many helpful discussions and a

great time in Cambridge. Special thanks go to Dr. Marcus Aberle, Lars Ekström, Dr. Annette Fischer, Guido Morgenthal, Dr. Elizbar 'Buba' Kebadze, Sangarapillai Kukathasan, Dr. Jason Lai, Andrew Lennon, Hannes Schmidt, Lin Tze Tan, Alan Watt and Wesley Wong.

Finally, I would like to thank my parents for their encouragement, continuous love and support.

Financial support from the Royal Institute of Technology and The Royal Swedish Academy of Sciences is gratefully acknowledged.

Stockholm, April 2002

Gunnar Tibert

Abstract

This thesis deals with the development of deployable structures, based on the tensegrity concept, for applications in space.

A state-of-the-art review of deployable masts and reflector antennas for space applications is presented. A comparison is made between the various reflector antennas in terms of deployed and stowed sizes, mass and accuracy.

The key step in the design of tensegrity structures is the form-finding analysis. Several methods proposed for this step are scrutinised and classified into two groups, kinematic and static methods, and the advantages and disadvantages of each method are investigated. Two of the statical methods seems to be identical. It is concluded that several form-finding methods are available, but no single method is suitable for general tensegrities. The force method, for the analysis of the kinematic and static properties of large bar frameworks, is presented.

The analysis and design of deployable tensegrity masts, with three struts per stage, is described. A routine for the manufacturing of physical models is proposed and evaluated. Different schemes for deployment are investigated. A way to deploy the struts using self-deployable hinges is introduced and demonstrated by four- and eight-stage mast models. Finally, the tensegrity mast is compared with an existing deployable mast with respect to stiffness. The mast is relatively stiff in the axial direction but very weak in bending.

The requirements for a deployable reflector antenna used on small satellites are formulated. A concept, which uses a triangulated cable network to approximate the reflecting surface, is adopted. The kinematically determinate triangulated cable network is thoroughly analysed. The achievable surface accuracy of the net, both to systematic errors arising from the triangular approximation of the surface and random manufacturing errors, is evaluated. The underlying principles and the statical and kinematical properties of the new concept are presented. A physical model is built to analyse the feasibility of the concept and to test various deployment schemes. The scheme using telescopic struts are identified as the most suitable and a preliminary design an antenna, with a diameter of three metres, for a future space mission is performed. Numerical computations show that the antenna is stiff and extremely light.

Keywords: deployable structures, tensegrity, form-finding, cable net, analysis, design, spacecraft, mast, reflector antenna.

Contents

Preface iii

Abstract v

List of Symbols and Abbreviations xx

1 Introduction 1

1.1 Deployable Structures 1

1.2 Tensegrity 2

1.3 Mechanics of Bar Frameworks 3

1.4 Scope and Aims 5

1.5 Outline of Thesis 6

2 Deployable Space Structures 9

2.1 Introduction 9

2.2 Deployable Masts 10

2.2.1 Thin-Walled Tubular Booms 11

2.2.2 Telescopic Masts 11

2.2.3 Coilable Masts 13

2.2.4 Articulated Trusses 13

2.3 Deployable Reflector Antennas 16

2.3.1 Mesh Antennas 17

2.3.2 Solid Surface Antennas 26

2.3.3 Inflatable Antennas 29

2.3.4 Antenna Comparison 30

3 Analysis Methods for Tensegrity Structures **33**

3.1 Introduction . . . 33

3.2 Kinematic Form-Finding Methods . . . 35

3.2.1 Analytical Solutions . . . 35

3.2.2 Non-Linear Programming . . . 36

3.2.3 Dynamic Relaxation . . . 37

3.3 Static Form-Finding Methods . . . 39

3.3.1 Analytical Solutions . . . 39

3.3.2 Force Density Method . . . 40

3.3.3 Energy Method . . . 41

3.3.4 Reduced Coordinates . . . 44

3.4 Implementation of the Force Density Method . . . 47

3.4.1 A Two-Dimensional Example . . . 47

3.4.2 Tensegrity Prisms . . . 49

3.4.3 Spherical Tensegrities . . . 51

3.5 The Force Method for Analysis of Bar Frameworks . . . 53

3.5.1 Equilibrium and Compatibility Matrices . . . 54

3.5.2 Static and Kinematic Properties . . . 54

3.5.3 Rigid-Body Mechanisms . . . 56

3.5.4 Internal Mechanisms . . . 57

3.5.5 Structural Computations . . . 59

3.5.6 Example: Hanging Triangular Net . . . 60

3.6 Discussion . . . 61

4 Deployable Tensegrity Masts **65**

4.1 Background . . . 65

4.2 Static and Kinematic Properties . . . 65

4.3 Form-Finding . . . 67

4.3.1 Two-Stage Tensegrity Mast . . . 67

4.3.2 Multi-Stage Tensegrity Masts . . . 68

4.4 Manufacturing Technique 70
4.5 Deployment 73
4.5.1 Strut Deployment 74
4.5.2 Demonstrator Masts 75
4.6 Structural Analysis 78
4.6.1 Initial Equilibrium Element Forces 79
4.6.2 Preliminary Design of Struts and Cables 83
4.6.3 Vibration Analysis 86
4.6.4 Static Analysis 89
4.7 Discussion 91

5 Design Prerequisites for a Deployable Reflector Antenna 95

5.1 Small Satellites and Deployable Structures 95
5.1.1 Micro-Satellites Astrid-1 and -2 96
5.1.2 Small Satellite Odin 97
5.1.3 Space Technology Research Vehicles 98
5.1.4 Future STRV Missions 100
5.2 New Reflector Concept for Small Satellites 101
5.2.1 Existing Concepts with Passive Structure 102
5.2.2 Tensegrity Reflector Concept 102
5.3 Geometry of Parabolic Reflector Antennas 104
5.3.1 Axi-Symmetric Reflector 104
5.3.2 Offset Reflector 105
5.3.3 Values for F/D and X_A 109
5.4 Reflector Antenna Theory 110
5.4.1 Antenna Gain 110
5.4.2 Effects of Random Surface Errors 112
5.4.3 Systematic Surface Error of Faceted Paraboloids 113
5.4.4 Allowable Surface Error of Reflector Antennas 115
5.4.5 Ground Resolution 117

5.4.6 Accuracy Goals for the Present Antenna . . . 118
5.5 Selection of Materials . . . 118
5.5.1 Materials for the Antenna Structure . . . 118
5.5.2 Materials for the RF Reflective Surface . . . 119

6 Analysis of Tension Trusses **121**
6.1 Static and Kinematic Properties . . . 122
6.2 Axi-Symmetric Configurations . . . 123
6.2.1 Sag-to-Span Ratio . . . 123
6.2.2 Position of Additional Nodes . . . 126
6.2.3 Tension Tie Force Distribution . . . 126
6.3 Offset Configurations . . . 133
6.3.1 Focal Length and Offset Distance . . . 133
6.3.2 Two Symmetric Offset Configurations . . . 134
6.4 Effects of Manufacturing Errors on the Reflector Accuracy . . . 136
6.4.1 Monte Carlo Technique for the Tension Truss . . . 137
6.4.2 Best-Fit Paraboloid Analysis . . . 137
6.4.3 Extracting the Random Surface Deviations . . . 139
6.4.4 Systematic Facet Surface Deviation . . . 140
6.4.5 Influence of Tension Tie Loading . . . 140
6.4.6 Statistical Considerations . . . 142
6.4.7 Influence of Member Length Imperfections . . . 142
6.4.8 Influence of Tension Tie Load Variation . . . 143
6.4.9 Influence of Ring Structure Distortion . . . 145
6.4.10 Combined Influence of Manufacturing Imperfections . . . 146
6.4.11 Influence of Thermal Strains . . . 147
6.4.12 Achievable Reflector Accuracy . . . 150

7 Tensegrity Reflector Antennas **153**
7.1 Introduction . . . 153

7.2 The AstroMesh Concept . . . 153
7.2.1 Net Generation . . . 153
7.2.2 Deployable Ring Structure . . . 154
7.2.3 Static and Kinematic Properties . . . 154
7.3 New Concept . . . 156
7.3.1 Stiffened Hexagonal Module . . . 157
7.3.2 Hexagonal Tensegrity Module and Tension Trusses . . . 158
7.3.3 Minimum Separation between Front and Rear Nets . . . 160
7.3.4 Three-Ring Axi-Symmetric Reflector . . . 161
7.4 Demonstration Model . . . 164
7.5 Deployment Schemes . . . 166
7.5.1 Hinged Struts . . . 168
7.5.2 Telescopic Struts . . . 169
7.6 Preliminary Design of 3 m Reflectors . . . 170
7.6.1 Design Scheme . . . 170
7.6.2 Axi-Symmetric Reflectors . . . 175
7.6.3 Offset Reflectors . . . 175
7.6.4 Stowage Considerations . . . 179
7.7 Vibration Analysis . . . 181
7.8 Discussion . . . 183

8 Conclusions **187**
8.1 Analysis Methods . . . 187
8.2 Deployable Masts . . . 188
8.3 Deployable Antennas . . . 188
8.4 Further Research . . . 189

Bibliography **191**

A Overlap Values for Tensegrity Masts **207**

B Flat Cable Net for Constructing Tensegrity Masts **213**

C Mesh Generation Procedure for the Tension Truss **217**

List of Symbols and Abbreviations

Roman Symbols

A_a	Aperture area, p. 111
A_b	Projected blockage area, p. 111
a	Side length of equilateral triangle, p. 46
$\mathbf{A}$	$A_{ij} = \partial l_j / \partial g_i$, p. 45
b	Number of pin-jointed elements (bars), p. 4
b_{an}	Number of additional bars for kinematic determinacy, p. 123
c	Number of kinematic constraints, p. 4
$\mathbf{C}$	Compatibility matrix ($b \times 3j - c$), p. 54
$\mathbf{C}_f$	Incidence matrix of constrained coordinates, p. 40
$\mathbf{C}_s$	Incidence matrix, p. 40
$\mathbf{C}_u$	Incidence matrix of free coordinates, p. 40
D	Aperture diameter, p. 30
D_a	Diameter of offset reflector, p. 106
D_p	Diameter of parent paraboloid, p. 105
d	Diameter of stowed antenna, p. 30
$\mathbf{D}$	Matrix of internal mechanisms ($3j - c \times m$), p. 56
$\mathbf{D}_{\mathrm{rb}}$	Matrix of rigid-body mechanisms ($m_{\mathrm{rb}} \times 3j - c$), p. 57
$\overline{\mathbf{D}}$	Force density matrix
$\mathbf{d}$	Vector of nodal displacements ($3j - c$), p. 37
$\dot{\mathbf{d}}$	Vector of nodal velocities ($3j - c$), p. 37
$\ddot{\mathbf{d}}$	Vector of nodal accelerations ($3j - c$), p. 37

$\mathbf{d_e}$	Vector of nodal displacements compatible with $\mathbf{e}$ $(3j-c)$, p. 60
$\mathcal{D}$	Dimension of space, p. 41
e	Element elongation, p. 38
$\mathbf{e}$	Vector of bar elongations (b), p. 54
$\mathbf{e}_0$	Vector of initial bar elongations (b), p. 59
F	Focal length, p. 104
f_1	Lowest natural frequency, p. 30
f_{op}	Operating frequency, p. 32
$\mathbf{f}$	Vector of nodal loads $(3j-c)$, p. 37
G	Gain of reflector antenna, p. 111
g	Generalised coordinate, p. 44
g	Gravity (9.80665 m/s^2), p. 174
$\mathbf{G}_i$	Matrix of geometric loads $(3j-c \times m)$, p. 58
$\mathbf{g}$	Vector of generalised coordinates, p. 44
H	Height, p. 35
H_0	Height of axi-symmetric reflector, p. 104
H_a	Height of offset reflector, p. 106
h	Stage overlap, p. 46
$\mathbf{H}$	Equilibrium matrix $(3j-c \times b)$, p. 54
i	An integer $< v$, p. 35
j	Number of frictionless joints (nodes), p. 3
j_{an}	Number of additional joints for kinematic determinacy, p. 123
$\bar{k}$	Fictitious stiffness, p. 38
$\mathbf{K}$	Stiffness matrix $(3j-c \times 3j-c)$, p. 37
l	Length, p. 5
l_e	Buckling length, p. 173
ℓ	Side length of facet, p. 114
m	Number of internal mechanisms, p. 4

m_{rb}	Number of of rigid-body mechanisms, p. 57
$\mathbf{M}$	Mass matrix ($3j-c \times 3j-c$), p. 37
n	Number of nodes, p. 40
n	Number of mast stages, p. 65
$n_{\max}$	Maximum number of net rings for a given sag-to-span ratio, p. 126
$\mathbf{N}$	Damping matrix ($3j-c \times 3j-c$), p. 37
$\mathbf{n}$	Translation vector (3), p. 43
$\mathcal{N}$	Dimension of nullspace, p. 43
P	External force, p. 5
p	Tension in RF reflective mesh, p. 114
$\mathbf{p}_i$	Nodal coordinates, $(x_i\ y_i\ z_i)^{\mathrm{T}}$, p. 35
q	Force density, p. 39
$\mathbf{Q}$	Diagonal matrix of force densities, p. 40
R	Radius, p. 35
R_a	Radius of offset reflector, p. 105
r	Distance from centre of reflector, p. 112
r_g	Radius of gyration, p. 173
$r_{\mathbf{H}}$	Rank of $\mathbf{H}$, p. 55
$r_{\mathbf{R}}$	Rank of $\mathbf{R}$, p. 57
$\mathbf{R}$	Matrix of kinematic constraints ($c \times 6$), p. 57
$\mathbf{r}$	Rotation vector (3), p. 57
s	Number of self-stress states, p. 4
$\mathbf{S}$	Matrix of states of self-stress ($b \times s$), p. 56
T	Temperature (K), p. 147
t	Axial element force, p. 5
$\mathbf{t}$	Vector of bar axial forces (b), p. 54
$\mathbf{t}_{\mathbf{f}}$	Vector of bar forces in equilibrium with $\mathbf{f}$ (b), p. 59
$\mathbf{U}$	Left singular matrix ($3j-c \times 3j-c$), p. 55

v	Number of vertices of regular polygon (or struts per stage), p. 35
$\mathbf{W}$	Right singular matrix ($b \times b$), p. 55
$X,\ Y,\ Z$	Coordinates in global system (parent paraboloid), p. 105
X_A	Offset distance, p. 106
X_O, Y_O, Z_O	Coordinates of origin (offset reflector), p. 105
$x,\ y,\ z$	Coordinates in global system, p. 104
x', y', z'	Coordinates in local system, p. 105
$\mathbf{x}$	Vector of x-coordinates, p. 40
$\mathbf{x}_f$	Vector of constrained x-coordinates, p. 41
$\mathbf{x}_u$	Vector of free x-coordinates, p. 41

Greek Symbols

α	Azimuth angle, p. 45
α_T	Coefficient of thermal expansion, p. 149
ΔF	Difference between ideal and best-fit focal lengths, p. 138
ΔH	Separation of front and rear nets, p. 158
Δn	Surface deviation in normal direction, p. 112
$\Delta_{\wp}$	Phase error of reflected rays, p. 112
ΔZ_P	Translation of paraboloid apex, p. 138
Δz	Surface deviation in axial direction, p. 112
δ	General displacement, p. 5
δ	Colatitude, p. 45
δ_{rms}	Radiometric rms surface deviation, p. 112
$\delta_{\mathrm{rms},z}$	Axial rms surface deviation, p. 112
ε	Strain, p. 137
η	Overlap ratio of mast stages, p. 65
η_a	Total antenna efficiency factor, p. 111
η_b	Aperture blockage efficiency factor, p. 111
η_r	Random error efficiency factor, p. 112

η_t	Aperture taper efficiency factor, p. 111
θ	Rotation angle, p. 35
θ_0	Angle between z-axis and rim (axi-symmetric reflector), p. 104
θ^*	Rotation angle of interior stages, p. 69
ϑ	Temperature (°C), p. 149
λ	Wavelength of operating frequency f_{op}, p. 111
ν	Relative error, p. 38
ξ	Ellipticity of offset reflector rim, p. 106
ρ	Density
ρ	Sag-to-span ratio, p. 125
ϱ	Areal density, p. 32
σ	Singular value, p. 55
σ_ε	Standard deviation of length imperfections, p. 136
σ_ρ	Standard deviation of ring structure distortion, p. 145
σ_τ	Standard deviation of tension tie loads, p. 143
$\mathbf{\Sigma}$	Matrix of singular values ($3j - c \times b$), p. 55
ϕ_a	Angle between x'-axis and x-axis (offset reflector), p. 105
$\mathbf{\Phi}$	Matrix of bar flexibilities ($b \times b$), p. 59
ω	Element stress (equivalent to q), p. 42
$\mathbf{\Omega}$	Matrix of element stresses ω, p. 42
$\boldsymbol{\omega}$	Vector of element stresses (equivalent to $\mathbf{q}$), p. 42

Abbreviations

ACeS	Asia Cellular Satellite, p. 20
ADAM	Able Deployable Articulated Mast, p. 16
AFRA	Advanced Folding Rib Antenna, p. 20
ARISE	Advanced Radio Interferometry between Space and Earth, p. 30
ASAP	Ariane Structure for Auxiliary Payloads, p. 96
ATS	Applications Technology Satellite, p. 18

BRC	Bi-stable Reeled Composite, p. 11
CFRP	Carbon Fibre Reinforced Plastic, p. 11
CM	Coilable Mast, p. 13
CRTS	Collapsible Rib-Tensioned Surface, p. 101
CSPDA	Cable-Stiffened Pantographic Deployable Antenna, p. 25
CTE	Coefficient of Thermal Expansion, p. 118
CTM	Collapsible Tubular Mast, p. 11
DAISY	Deployable Antenna Integral System, p. 27
DERA	Defence Evaluation and Research Agency, p. 96
DLR	Deutschen Zentrum für Luft- und Raumfahrt, p. 11
DSL	Deployable Structures Laboratory, p. iii
EGS	Energia-GPI-Space, p. 21
ESA	European Space Agency, p. 9
ETS	Engineering Test Satellite, p. 23
FAST	Folding Articulated Square Truss, p. 14
FE	Finite Element, p. 136
FEM	Finite Element Method, p. 58
GEO	Geosynchronous Orbit, p. 96
GPS	Global Positioning System, p. 100
GTO	Geosynchronous Transfer Orbit, p. 99
HALCA	Highly Advanced Laboratory for Communications and Astronomy, p. 23
HCA	Hoop/Column Antenna, p. 20
HRA	Hinged-Rib Antenna, p. 20
HST	Hubble Space Telescope, p. 9
IAE	Inflatable Antenna Experiment, p. 29
IR	Infrared, p. 147
ISAS	Institute of Space and Astronautical Science, p. 23

ISRS	Inflatable Space Rigidised Structure, p. 29
ISS	International Space Station, p. 15
JPL	NASA Jet Propulsion Laboratory, p. 18
LaRC	NASA Langley Research Center, p. 20
LDR	Large Deployable Reflector, p. 102
LEO	Low Earth Orbit, p. 95
MDF	Medium Density Fibreboard
NASA	National Aeronautics and Space Administration, p. 9
NASDA	National Space Development Agency of Japan, p. 23
NGST	Next Generation Space Telescope, p. 1
RF	Radio Frequency, p. 17
rms	root-mean-square, p. 112
RRA	Rigid-Rib Antenna, p. 17
rss	root-sum-of-squares, p. 117
SAR	Synthetic Aperture Radar, p. 100
SBA	Spring-Back Antenna, p. 21
SSC	Swedish Space Corporation, p. 96
SSDA	Solid Surface Deployable Antenna, p. 28
STEM	Storable Tubular Extendible Member, p. 11
STRM	Shuttle Radar Topography Mission, p. 16
STRV	Space Technology Research Vehicle, p. 96
SVD	Singular Value Decomposition, p. 54
TDRS	Tracking and Data Relay Satellite, p. 17
TSR	Tape-Spring Rolling
UV	Ultraviolet, p. 29
WRA	Wrap-Rib Antenna, p. 18

IEEE Frequency Bands

HF	3–30 MHz

VHF	30–300 MHz
UHF	300–1000 MHz
L-band	1–2 GHz
S-band	2–4 GHz
C-band	4–8 GHz
X-band	8–12 GHz
K_u-band	12–18 GHz
K-band	18–27 GHz
K_a-band	27–40 GHz
Millimetre wave band	40–300 GHz

Chapter 1

Introduction

1.1 Deployable Structures

Deployable structures are structures capable of large configuration changes in an autonomous way. Most common is that the configuration changes from a packaged, compact state to a deployed, large state. Usually, these structures are used for easy storage and transportation. When required, they are deployed into their service configuration. A well known example is the umbrella. Deployable structures are sometimes known under other names like expandable, extendible, developable and unfurlable structures.

Deployable structures have many potential applications both on Earth and in space. In civil engineering, temporary or emergency structures have been used for a long time. A more recent application is retractable roofs of large sports stadia. In space, deployable structures have been used since the former Soviet Union launched its first satellite *Sputnik* on October 4, 1957. In the beginning, all spacecraft were small by virtue of the limited capacity of the launch vehicles. As the spacecraft grew bigger so did the launch vehicles, but not at the same rate. In the foreseeable future, the capacity of launch vehicles will remain unchanged while the need to launch very large spacecraft, e.g. the 25 m diameter *Next Generation Space Telescope* (NGST) [82], constantly is growing. Considerable research has been conducted over the last decade on erectable structures, which are assembled in space by astronauts or robots, cf. [82,95]. Erectable structures are versatile and can be compactly stowed, but possess the disadvantage of requiring risky in-space construction. Therefore, deployable structures are the only practical way to construct large, lightweight structures for remote locations in space. Obvious advantages of deployable structures are savings in mass and volume. Another, not easily recognised, benefit is that the structure can better withstand the launch loads in the stowed configuration. In its deployed configuration, the structure is only subjected to the orbital loads, which are considerably lower. An important issue in the design of all deployable space structures is the trade-off between the size of the packaged structure and its precision in the deployed state. Both aspects are usually critical to the mission performance, but are sometimes conflicting requirements.

1.2 Tensegrity

The word *tensegrity*, which is a contraction of *tens*ile int*egrity*, was coined by R. B. Fuller in his patent from 1962 [44]. The meaning of the word is vague and different interpretations are possible. Fuller [44] describes a tensegrity structure as "an assemblage of tension and compression components arranged in a discontinuous compression system..." Referring to the work by Fuller, Pugh [132] defines a tensegrity system as: "A tensegrity system is established when a set of discontinuous compressive components interacts with a set of continuous tensile components to define a stable volume in space." Hanaor [54] describes tensegrity structures as "internally prestressed, free-standing pin-jointed networks, in which the cables or tendons are tensioned against a system of bars or struts". A broader interpretation by Miura and Pellegrino [105] is "that a tensegrity structure is any structure realised from cables and struts, to which *a state of prestress is imposed that imparts tension to all cables*." A narrower interpretation, also by Miura and Pellegrino, adds to the above definition the notion that "as well as imparting tension to all cables, the state of prestress serves the purpose of *stabilising the structure*, thus providing first-order stiffness to its infinitesimal mechanisms."

To explain the mechanical principle of tensegrity structures, Pugh [132] uses a balloon analogy. If the enclosed air is at higher pressure than the surrounding air it pushes outwards against the inwards-pulling balloon skin. If the air pressure inside the balloon is increased, the stresses in the skin become greater and the balloon will be harder to deform. In a tensegrity structure the struts have the role of the air and the cables that of the skin. Increasing the forces in the elements of a tensegrity structure will increase its strength and load bearing capacity.

The origin of tensegrity structures can be pin-pointed to 1921 and a structure called *Study in Balance* made by the Russian constructivist K. Ioganson, Figure 1.1(a). Moholy-Nagy [109] explains "that if the string was pulled the composition would change to another position while maintaining its equilibrium." According to the definitions above, this structure was not a true tensegrity structure, but it bore a close resemblance. Today, it is generally regarded that K. D. Snelson's *X-Piece* structure, Figure 1.1(b), constructed in 1948, represents the birth of the tensegrity concept, cf. [113]. Snelson, who is a sculptor, has since built numerous tensegrity structures, mainly for art exhibitions. While Snelson was the inventor, Fuller [44] was the first to look upon tensegrity structures from an engineering point of view. A more extensive investigation into the origin of tensegrity is given in reference [83].

Even though the concept of tensegrity is more than fifty years old, few applications exist, e.g. Geiger's cable domes [46, 123]. In recent years, the concept has received new attention from mathematicians, engineers and biologists. Ingber [64] argues that tensegrity is the fundamental architecture of life. Tensegrity-like structures in cells have been observed in cell biology experiments. From the deployable structures point of view, tensegrity structures are very interesting since the compressive elements are disjointed. This provides the possibility to fold these members and hence the structure can be compactly stowed.

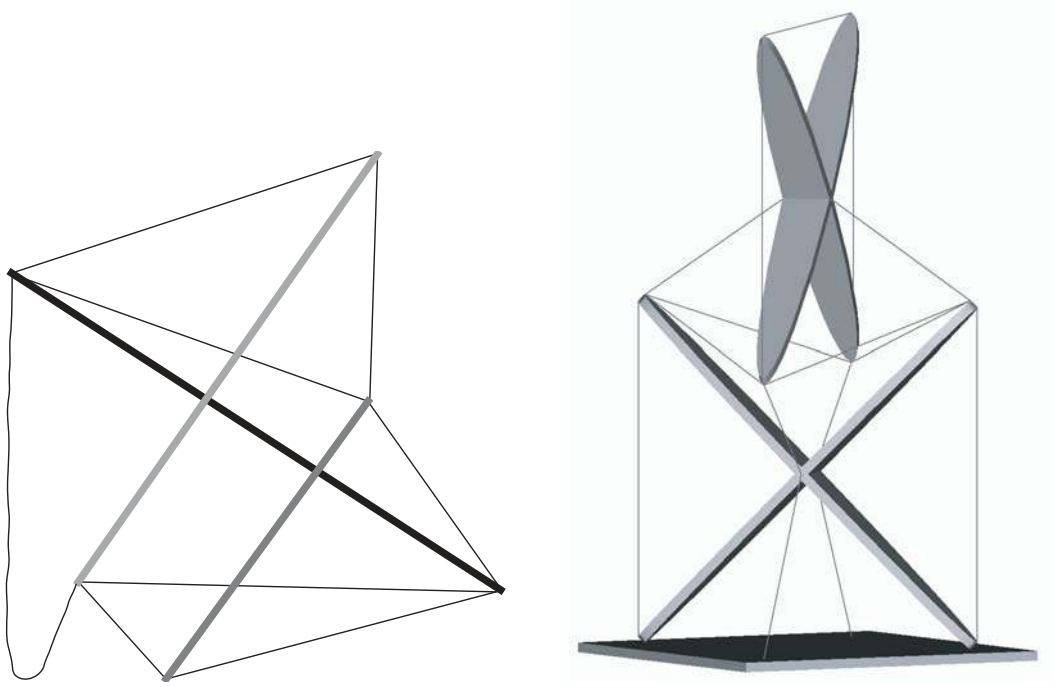

(a) (b)

Figure 1.1: Early tensegrity-like structures: (a) Karl Ioganson's *Study in Balance* and (b) Kenneth Snelson's *X-Piece*.

1.3 Mechanics of Bar Frameworks

When properly prestressed, tensegrity structures can be treated in a similar manner as frameworks with pin-jointed bars. Central to an understanding of the structural mechanics of any framework is the concepts of static and kinematic determinacy.

Möbius [108] was the first to show that a general plane framework consisting of j frictionless joints has to have at least $2j-3$ bars in order to be rigid, while a space framework needs $3j-6$. Möbius is aware of exceptions to this rule and he observes that the determinant of the equilibrium equations of the nodes vanishes in those cases. Möbius also observes that the removal of a bar from a framework with the minimum number of bars, according to the rule, transforms the framework into a finite mechanism. But he further observes that no additional degree of mobility is introduced if the length of the removed bar is either maximum or minimum [121].

About three decades later, Maxwell [90] rediscovers Möbius' rule. Maxwell also anticipates exceptions to the rule by stating [13, 90]: "In those cases where stiffness can be produced with a smaller number of lines, certain conditions must be fulfilled, rendering the case one of a maximum or minimum value of one or more of its lines. The stiffness of the frame is of an inferior order, as a small disturbing force may produce a displacement infinite in comparison with itself." Although it was introduced

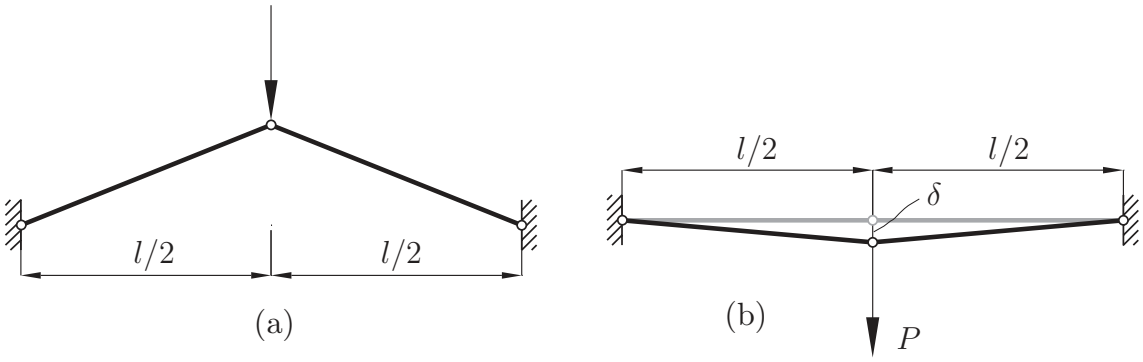

Figure 1.2: A two-bar framework in two configurations.

by Möbius, the rule for the construction of rigid three-dimensional frameworks,

$$3j - b - c = 0, \tag{1.1}$$

where j is the number of joints, b the number of bars and c the number of kinematic constraints ($c \geq 6$ in three dimensions) is now widely known as *Maxwell's rule*.

In 1912, 75 years after Möbius' findings, Kötter [73] presents the first study entirely concerned with the static and kinematic indeterminacy of pin-jointed frameworks. Kötter introduces an analytical way of evaluating whether or not a plane assembly with $b < 2j - 3$ is rigid [121]. The method is rather cumbersome and does not give any general statements.

In 1978, Calladine [13] went back to the paper by Maxwell [90] for an explanation of the mechanics of bar frameworks. Calladine studies a physical model of a tensegrity structure with 12 joints and 24 bars, which should be loose with 6 degrees of freedom, according to Maxwell's rule; yet, it is stiff. The key result from his study is the new version of Maxwell's rule, which includes all possible special cases:

$$3j - b - c = m - s, \tag{1.2}$$

where m is the number of internal mechanisms and s the number of states of self-stress. Equation (1.2), which hereafter will be referred to as the *extended Maxwell's rule*, does not by itself solve m and s of a general bar framework, but it introduces a clear explanation of the fundamental mechanics of bar frameworks. The values of m and s depend not only on the numbers of bars and joints, nor even on the topology of the connections, but on the complete specification of the geometry of the framework [127].

The extended Maxwell's rule can be illustrated by a simple example. Consider the two-dimensional framework in Figure 1.2 with two bars and three joints of which two are fully fixed ($c = 4$). In the first configuration, Figure 1.2(a), the nodes do not lie along the same line and it is easily seen that this framework is rigid. In the second configuration, Figure 1.2(b), all nodes lie along the same line. Both bars can now be prestressed to the same magnitude, $s = 1$, and the assembly has no stiffness against vertical loads, $m = 1$. Resolving the vertical equilibrium at the node yields

$$P \approx 4t_0 \frac{\delta}{l} + 8AE\frac{\delta^3}{l^3}, \tag{1.3}$$

where t_0 is the prestressing force and AE the axial stiffness. Thus, in the absence of prestress, the framework has zero vertical stiffness in the initial configuration. For a small deflection δ the stiffness is proportional to δ^2. However, if the framework is prestressed the stiffness is proportional to the level of prestress. Thus, the mechanism is infinitesimal; as soon as the node is displaced, the elongation of the bars will stiffen the structure. This illustrates what Maxwell means by "stiffness of ... an inferior order". In the case of tensegrity structures, which often have several infinitesimal mechanisms, the prestress stabilises the structure by providing additional stiffness.

1.4 Scope and Aims

Conventional satellite technology has for several decades been focused on a small number of large, complex spacecraft. In many of these, some kind of deployable structure was needed to make them fit into the launch vehicle compartment. In most missions, every attempt is made to circumvent the use of deployables because of their perceived high risk and high cost. Many of the deployable structure concepts available are very complex, but those concepts that have flown are actually very simple and use simple deployment mechanisms. A new era has now begun where the spacecraft production for commercial applications exceeds those of the military. This community requires structural systems that are cheaper, but with the same reliability as their predecessors. Commercial satellites are in many cases quite small, but an important aspect, that is frequently overlooked, is that deployable reflectors are also beneficial for these satellites. Deployables can be used for increased power, aperture or to position sensitive instruments away from the interference caused by the satellite.

Most deployable space structures are aimed for large satellites and, hence, developed for a certain scale. However, the size constraints for a small satellite may be completely different. It is, therefore, not just a matter of scaling down an existing structure. Typically, the volume of the stowed structure must be very small to fit the spacecraft bus. The basis for the present study is the assumption that the stowed volume of deployable structures can be reduced by using the tensegrity concept. Tensegrity structures have, for a long time, been considered suitable for space applications, but no study has considered the entire process from initial idea to working prototype.

The primary aim of this work is to develop deployable tensegrity structures for space applications. To achieve this goal requires the mastering of analysis methods and construction techniques not encountered in normal design work. The first step in the design of a tensegrity structure is to find a prestressed configuration. This step is called form-finding. Several form-finding methods for tensegrity structures have been proposed, but the advantages and limitations of each method have not been clearly described. The aim is therefore to scrutinise and classify the existing form-finding methods for tensegrity structures. The most challenging phase in the development of new deployable structures is certainly the study of the deploy-

ment process. Another aim is therefore to develop simple and reliable deployment mechanisms for tensegrities. This requires studies of suitable hardware and also experiments with physical models. In order to thoroughly evaluate proposed ideas and concepts, two specific deployable space structures, a mast and a reflector antenna, are to be designed.

The present research is concerned with structural aspects, i.e. geometry, strength, stiffness, loading, dynamics, materials, construction, etc., related to the *secondary structures* of a spacecraft, e.g. deployables. No attention is put to the load-carrying *primary structure* of the spacecraft or to other issues normally related to spacecraft design, i.e. orbit type, guidance, propulsion, electric power, communication links, etc. Unless they can be translated into structural terms which directly affect the design of the secondary spacecraft structures considered here.

1.5 Outline of Thesis

In Chapter 2, the current state-of-the-art of deployable structures for space applications is reviewed. The first part of the chapter is concerned with various systems for deployable masts. Deployable reflector antennas from three groups—mesh, solid surface and inflatable antennas—are studied in the second part. The antenna systems are compared with respect to the deployed and stowed size, weight, surface accuracy, natural frequencies, etc.

In Chapter 3, analysis methods for tensegrity structures are presented. Various methods used to find the initial equilibrium configuration of tensegrity structures are described. These methods are classified into two groups, kinematic and static, and the advantages and disadvantages of each method are investigated. Two of the static methods are linked to each other. In the second part of the chapter, an efficient method for structural analysis of large bar frameworks is presented. The method is linear and usually applicable only to assemblies which undergo small displacements. The parts of this chapter concerned with form-finding are reproduced from reference [170] with some minor modifications.

In Chapter 4, the analysis and design of deployable tensegrity masts are described. The chosen mast configuration is that of Snelson [151] with three struts per stage. Two different configurations of the mast are analysed: one with equal strut lengths and one with uniform element forces. A routine for the manufacturing of physical models is proposed and evaluated. Different schemes for deployment are investigated and a way to deploy the struts, using self-deployable hinges, is introduced. The deployment approach is demonstrated by four- and eight-stage mast models. Finally, the tensegrity mast is compared with an existing deployable mast with respect to stiffness.

In Chapter 5, the requirements for a deployable reflector antenna aimed for small satellites are formulated. A concept, which uses a triangulated cable network to approximate the reflecting surface, is proposed. The geometries of axi-symmetric

and offset reflector antennas are given. A good performance of the antenna requires high accuracy of the surface. The effects of different types of errors on the antenna performance are reviewed along with allowable surface accuracies of existing deployable reflector antennas. Another crucial aspect for the performance is the choice of suitable material for the different parts of the antenna. Low weight and high stiffness are important properties.

In Chapter 6, the triangulated cable network is thoroughly analysed. First, a method for making the networks kinematically determinate is described. Then, configuration details for adequate prestress distributions in the nets are determined. Finally, the achievable surface accuracy of the net, both to systematic errors arising from the triangular approximation of the surface and random manufacturing errors, is investigated. This gives a clear indication on how accurate the manufacturing process must be for a satisfactory performance of the antenna.

In Chapter 7, a detailed description of the new antenna concept is given. First, the features of the current state-of-the-art deployable mesh antenna, on which the new concept partly is based, are highlighted. Subsequently, the underlying principles and the static and kinematic properties of the new concept are presented. A physical model is built to analyse the feasibility of the concept and to test various deployment schemes. The scheme using telescopic struts is identified as being the most suitable. A preliminary design of a three metre diameter antenna is performed.

Chapter 8 concludes the study and gives some suggestions for further research.

In Appendix A, overlap values for two- to 50-stage tensegrity masts with equal-length struts are given.

In Appendix B, the various configurations of the two-dimensional cable net used in the construction of tensegrity masts are presented.

In Appendix C, the routine for generating the triangular network for the reflector surface is described.

Chapter 2

Deployable Space Structures

2.1 Introduction

Many space missions have been completed, or are currently being planned, that involve spacecraft which are significantly larger than the volume capacity on available launch vehicles. The cargo compartment of the *National Aeronautics and Space Administration*'s (NASA) Space Shuttle has a diameter of 4.6 m and a length of 18.3 m and the Ariane-5 launcher of Arianespace and the *European Space Agency* (ESA) has a diameter of 4.56 m and is about 11 m in length [77]. As these dimensions are not likely to change very soon, some components of the spacecraft have to be folded to fit into the cargo bay of the launcher and then deployed once the spacecraft is in orbit. Another limiting factor is the maximum allowable spacecraft weight. This depends on the type of launch vehicle and destination of the satellite and are, contrary to the volume constraint, generally negotiable.

Over the past three decades, a significant amount of research has been carried out in the field of deployable space structures. There are some differences between the existing concepts: some structures can be retracted again after they have been deployed, others rely on stored strain energy for deployment and some structures are stiff during deployment. Retraction is not a necessity in space, but may be required in some cases, cf. [125]. Structures not depending on stored energy are deployed by external means, e.g. a motor. Most of the structures do not obtain full stiffness until fully deployed while others can immediately sustain loads.

Despite the amount of research into deployable structures, several high-profile failures have occurred in the last two decades [187]. Failures in space are very expensive and extremely difficult to correct. The most well-known example is the *Hubble Space Telescope* (HST) which, beside its lens problems, experienced unexpected levels of mechanical vibration caused by the thermal loading of its solar arrays. One reason for these failures is an incomplete understanding of the behaviour of the structure. Another reason, probably more rare, is that the concept itself is poor. Miura [101], inventor of several deployable structures, emphasise that "creating a rational structural concept should be the first step in the process of designing a structure and it

precedes the practical design step." The robustness of the concept has to be first proven by analytical and physical models. The actual design procedure that follows involves just a trade-off between packing efficiency, structural stiffness and precision of the deployed structure. The final steps in the construction of a space structure involve extensive ground and, possibly, flight testing, which are extremely costly but unavoidable to ensure mission success.

In the aerospace industry there are three main types of deployable structures:

- Masts,
- Antennas, and
- Solar panels.

Masts are typically used for separating electronic instruments to reduce interference [95] or for supporting other structures such as solar arrays [190]. A vast number of mast concepts exist, cf. [95], whereof only a few will be presented in this chapter. All satellites need to communicate with Earth and therefore need some type of antenna. Amongst the many antenna types available, the parabolic reflector antenna is the most common one mainly due to its high gain, which enables high data rate transmission at low power [158]. Antennas are used not only for communication but also for Earth observation and astronomical studies. The current flexible solar cell technology can produce 223 W/m^2 [136], which means that the solar arrays have to be quite large to produce enough power for the ever increasing number of instruments aboard a satellite. One of the most sophisticated spacecraft is the HST, which requires 4.7 kW for its instruments. Four 2.39×6.06 m^2 solar arrays provide this power [77]. Deployable concepts for solar panels are not within the scope of this thesis and will therefore not be reviewed. For information on solar arrays see [125].

The remaining of this chapter is concerned with the most important concepts available for deployable masts and reflector antennas.

2.2 Deployable Masts

Deployable masts can be divided into the following four groups [95]:

- Thin-walled tubular booms,
- Telescopic masts,
- Coilable masts, and
- Articulated trusses.

A few reviews on deployable masts exist: Mikulas and Thompson [95] present structures developed in the U.S.A., Pellegrino [125] covers concepts that also are retractable, and Jensen and Pellegrino [68] present the most recent and extensive one.

2.2.1 Thin-Walled Tubular Booms

Thin-walled tubular booms are probably the earliest types of deployable and retractable structures. They make use of the elastic deformability of thin-walled shells. Typical materials for thin-walled booms are stainless steel, Copper-Beryllium and *Carbon Fibre Reinforced Plastic* (CFRP) [68, 125].

Storable Tubular Extendable Member

The *Storable Tubular Extendible Member* (STEM) was invented in Canada in the early 1960s [137]. It is an extension of the principle used for coilable self-straightening steel tape measure. While the tape measure only subtends a small angle of the complete cylinder formed by its radius of curvature, the STEM covers more than 360°, Figure 2.1(a). The choice of overlap depends on several factors but is at least 50° [125]. A STEM is quite stiff axially and in bending, but because of the open tubular section it has low torsional stiffness. Increased torsional stiffness can be provided if there is sufficient friction in the overlap region. The STEM is rolled up and flattened onto a drum within a cassette for stowage. It is deployed by rotating the drum whereby the stored elastic energy automatically brings it back into the tubular configuration. The ploy region, where it goes from flat to tubular cross-section, is contained with the stowage cassette. An extension of the STEM is the bi-STEM with two identical strips placed one inside the other, Figure 2.1(b). A bi-STEM has higher bending stiffness and better mechanical damping behaviour. Other advantages of a bi-STEM over a STEM of similar stiffness and length are shorter drums and ploy length, which give a more compact stowage cassette [125]. One version of the bi-STEM has interlocking STEMs, Figure 2.1(c), which increase the torsional stiffness. A recently developed tubular boom is the *Bi-stable Reeled Composite* (BRC) [65], which looks exactly like a STEM but is stable in both the stowed and deployed configuration. This means that the stowage cassette can be made smaller and lighter. In addition, the retraction mechanism can be simplified.

Collapsible Tubular Mast

The *Collapsible Tubular Mast* (CTM) is made from two STEMs bonded at the edges, which create a boom with higher torsional stiffness than the STEM. CTMs are rolled up in a similar way as STEMs. In the deployed configuration, the tube is unstressed and has a lenticular cross-section [125]. A 14 m long CTM to be used for solar sails was recently developed by the *German Aerospace Centre* (DLR). It is made of CFRP and weighs only 0.1 kg/m [33].

2.2.2 Telescopic Masts

Telescopic masts normally consist of a series of concentric, thin-walled cylindrical tubes that are nested inside one another. Limiting factors in terms of length are

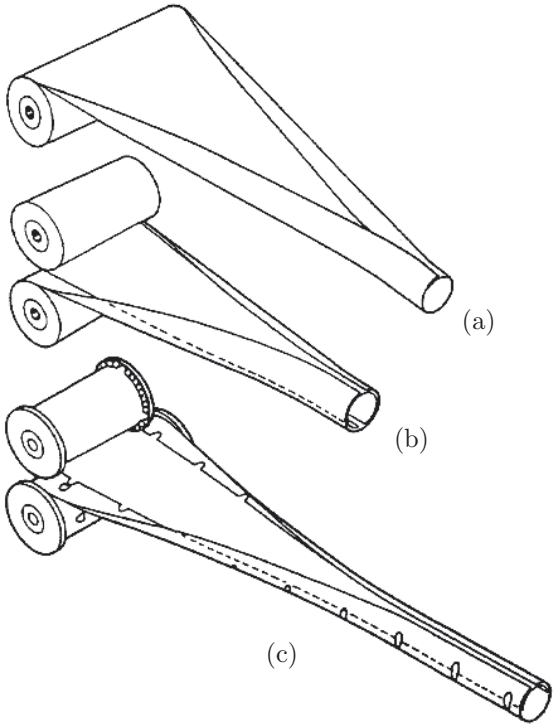

Figure 2.1: Tubular booms: (a) STEM, (b) bi-STEM, and (c) interlocking bi-STEM.

Figure 2.2: Collapsible tubular mast (Courtesy of DLR).

tube thickness and overlap length. Typical thickness of aluminium alloy and CFRP is 0.5 mm. Telescopic masts can be deployed either sequentially using a spindle-and-nut technique, Figure 2.3(a), or synchronously, Figure 2.3(b), by combining the previous technique with cables and pulleys. A 40 m long telescopic mast of CFRP has been developed by the company *Dornier* [77]. The mast consists of 18 segments of about 0.5 m in diameter and has a stowed length of 3 m. A 2.4 m long synchronously deployed telescopic mast consisting of seven tubes has been developed for the Tethered Satellite [125].

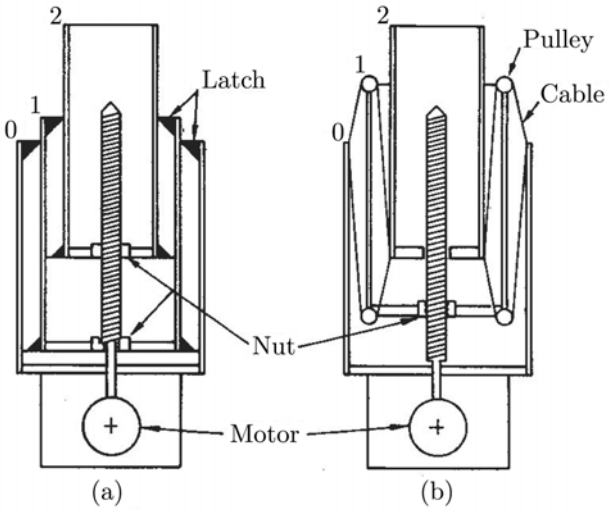

Figure 2.3: Deployment of a telescopic mast: (a) sequential and (b) synchronous (Reproduced from [125]).

2.2.3 Coilable Masts

In 1967, the *Coilable Mast* (CM) was invented by H. R. Mauch of the *Astro Research Corporation* [182]. A coilable mast normally consists of three longitudinal elements braced at regular intervals. The bracing consists of members perpendicular to the longitudinal ones and diagonal members. The mast is stowed by coiling the longerons, Figure 2.4. It can be deployed in two different ways: self or motor driven extension. The first method relies on the stored elastic energy in the coiled longerons and the rate is controlled by a *lanyard*, i.e. an axial cable attached to the tip of the mast, which pays out to control the deployment and reels in to retract the mast. As a result, the tip of the mast rotates during deployment. As the stiffness of the mast is lower during deployment than in the deployed configuration, this method is only suitable for shorter masts, typically less than 3 m [125]. For longer masts, the motor driven method is used whereby the mast is stowed inside a special canister, Figure 2.4. The canister, which is about two mast diameters higher than the retracted mast length, contains a motor driven rotating nut. The transition zone, where a section of the mast goes from stowed to deployed configuration, is contained within the canister so the part leaving the canister has full strength. Another advantage with the canister is that it is the nut rather than the tip of the mast that rotates. A CM is very efficient from a stowage viewpoint; the retracted length is about 2–3% of the deployed length. Masts with diameters up to 0.75 m have been constructed and the practical limit is considered to be about 1 m [95].

2.2.4 Articulated Trusses

Articulated trusses are widely used for space applications and are available in many different configurations. They are capable of higher stiffness, structural efficiency and precision than the previous concepts. One thing that popular truss masts have

Figure 2.4: Deployment of a coilable mast from a canister by a rotating nut (Courtesy of AEC-Able Engineering Company, Inc.).

in common is a constant diameter during deployment. A large number of other ingenious truss concepts have been invented, e.g. the *Variable Geometry Truss* [103] and the *Cable-Stiffened Pantographic Mast* [77, 186], but it is the author's opinion that most of them have fallen into disfavour partly because of their changing diameters.

Folding Articulated Square Truss Mast

The *Folding Articulated Square Truss* (FAST) mast was developed by *AEC-Able Engineering Company*. The mast has revolute hinges along the longerons with axes parallel to the sides of the square bays and two pairs of diagonal bracing cables on each face of the bays [105], Figure 2.5(a). The cables are prestressed by four lateral bows. During folding, half of the bracing cables become slack as the bows bend, Figure 2.5(b) and (c). The strain energy stored in the bows actuates the deployment of one bay of the mast. Hence, each deployed bay has full stiffness. As for CMs, the

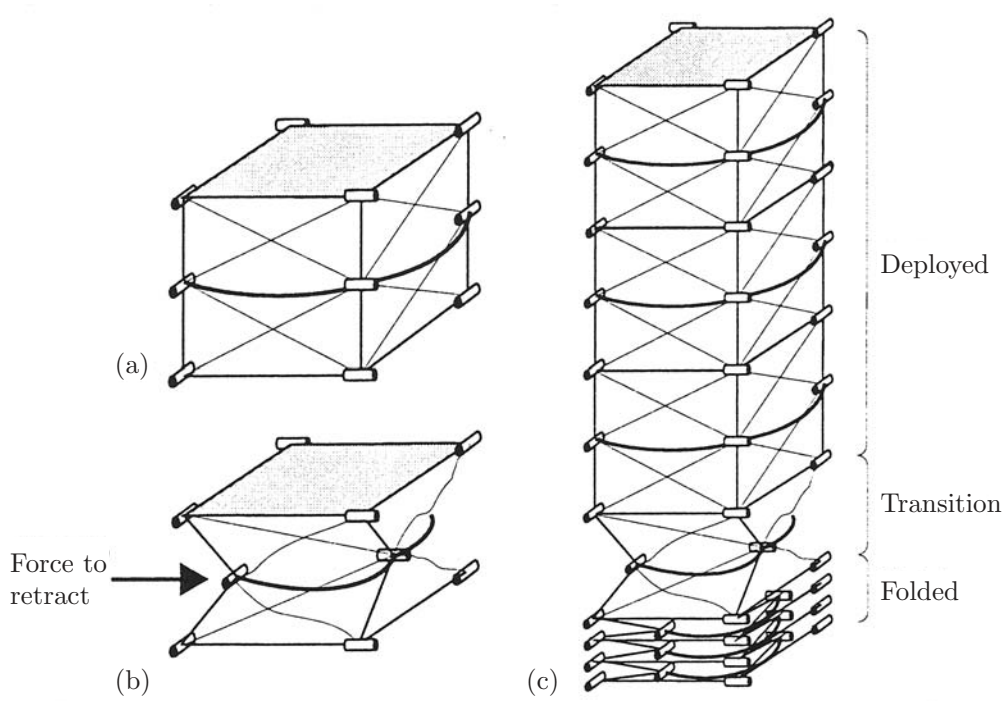

Figure 2.5: Principle of the FAST mast (Courtesy of S. Pellegrino).

Figure 2.6: FAST mast for the ISS (Courtesy of AEC-Able Engineering Company, Inc.).

retracted mast and transition zone are enclosed by a canister. Eight FAST masts, each 1.09 m in diameter and 34.75 m in length, support the solar arrays on the *International Space Station* (ISS), Figure 2.6. The canister length is 2.3 m or about 6.6% of the deployed length [1].

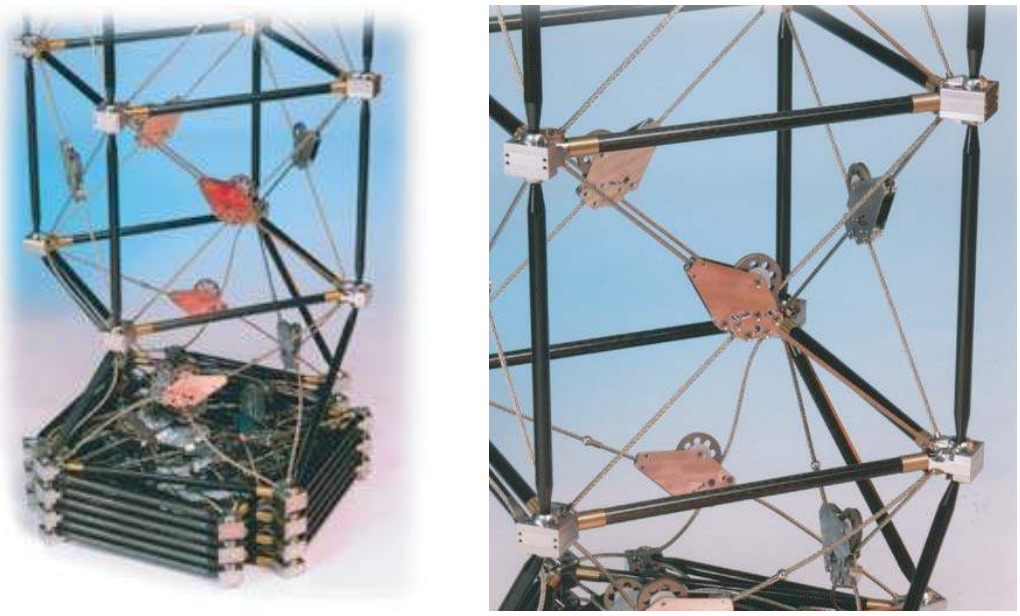

(a) (b)

Figure 2.7: ADAM deployment sequence (Courtesy of AEC-Able Engineering Company, Inc.).

Able Deployable Articulated Mast

AEC-Able Engineering Company recently developed the *Able Deployable Articulated Mast* (ADAM) for applications requiring very long and stiff masts. Compared to the FAST mast, ADAM uses no bows and only one pair of cross bracing cables on each face of a bay, Figure 2.7. Spherical hinges are fitted at the ends of the longitudinal members and the rigid lateral square rotates almost 90° during deployment, Figure 2.7(a). Special latches on the diagonal cables stop the deployment and stiffen each bay, Figure 2.7(b). Like in CMs, a canister/nut technique is used for deployment. A 60 m long ADAM is used in the *Shuttle Radar Topography Mission* (STRM), which maps the Earth. The STRM ADAM, whose prime function is to separate two radar antennas, has a diameter of 1.12 m and consists of 87 bays. Its stowed height is 1.42 m and the length of the canister is 2.92 m or 4.8% of full mast length [1].

2.3 Deployable Reflector Antennas

Several reviews of deployable reflector antennas are available: Freeland [40], Roederer and Rahmat-Samii [138], Rogers *et al.* [139], Mikulas and Thomson [95], Pellegrino [125], and Hachkowski and Peterson [52]. The reviews by Freeland and Mikulas and Thomson cover only concepts developed in USA, while Roederer and Rahmat-Samii also include European ones. Pellegrino focuses on concepts, from

USA, Europe and Japan, which are retractable. The latest one by Hachkowski and Peterson is concerned with the precision of the antennas and includes 50 structures, not only reflectors. In recent years a small number of new, very important concepts have been developed which are not included, or only mentioned briefly, in the previous reviews. A new review, including only the most important structures, is therefore necessary for a more complete background.

Basically, there are three different types of deployable antennas:

- Mesh antennas,
- Solid surface antennas, and
- Inflatable antennas.

In each category, several different concepts have been proposed but only a limited number have proven to be viable and even fewer have actually flown. In the following three sections, the most important concepts from each category will be presented, some of which have flown while others never left the ground. Finally, the antenna concepts will be summarised and compared in terms of packaging efficiency, areal mass, surface accuracy and natural frequency.

2.3.1 Mesh Antennas

The most common type of deployable antennas is the mesh antenna with a reflective surface composed of a knitted lightweight metallic mesh. Although the mesh is discontinuous, it can reflect *radio frequency* (RF) waves up to about 40 GHz [95]. Deployable mesh antennas are available in many configurations which differ in the way the mesh is supported. The most common antenna design is an inverted umbrella with curved ribs emanating from a hub and the mesh suspended between the ribs. Umbrella-type designs are still prevalent but several new concepts, which can achieve higher surface accuracy, are now being developed. In the following, the most important deployable mesh antenna concepts are considered.

Rigid-Rib Antenna

Harris Corporation developed the *Rigid-Rib Antenna* (RRA) for the NASA *Tracking and Data Relay Satellite*[1] (TDRS) and the NASA Galileo mission to Jupiter. The RRA is an umbrella-type antenna with 16 parabolic, tubular CFRP ribs attached to a central hub and an RF reflective mesh between the ribs, Figure 2.8(a). The ribs are hinged only at the hub and they simply fold towards the feed structure, which gives a stowed height about the same as the antenna radius. The antennas constructed for the TDRS and Galileo are almost identical with a diameter of 5 m. In its

[1]The rigid rib antennas by Harris were used on TDRS-A through G and then replaced by the spring-back antenna for TDRS-H through J.

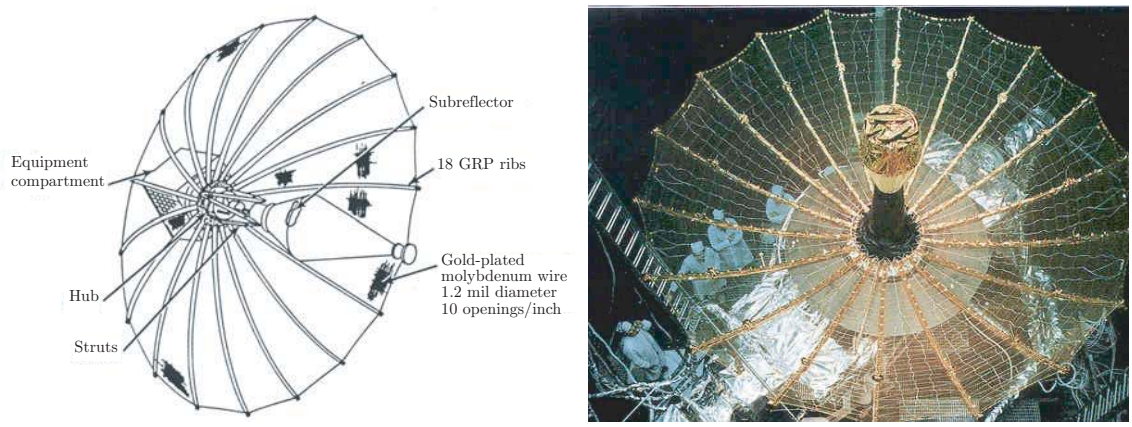

(a) (b)

Figure 2.8: The 5 m diameter rigid rib antenna for the Galileo mission (Courtesy of Harris Corporation).

stowed configuration, the diameter and height is 0.9 and 2.7 m, respectively[2]. The entire antenna structure, including the ribs, reflector surface, feed and deployment mechanisms that fold and unfold the structure, weighs 24 kg. The RRA antenna onboard the Galileo spacecraft, which was launched on October 18, 1989, failed to deploy as commanded on April 11, 1991. The mission objectives could, however, be accomplished using an antenna with lower gain and various enhancements to the communication link. The failure is believed to be caused by very high friction between restraint pins and their receptacles.

Wrap-Rib Antenna

NASA *Jet Propulsion Laboratory* (JPL) and *Lockheed Missiles and Space Company* developed the *Wrap-Rib Antenna* (WRA) in the 1970s. This is an umbrella-type concept with a central hub, parabolic CFRP ribs of lenticular cross-section, and an RF reflective mesh. In the stowed position, the ribs are rotated on vertical hinge pins and then tangentially wrapped around the hub. The ribs are deployed by cutting a restraining cable placed around the hub. Spring-loaded doors are opened and the stored energy in the ribs causes them to un-wrap into their original position. In vacuum, this sequence takes about two seconds. The deployment mechanism is shown in Figure 2.9(b). Note that it is also possible to retract the antenna in orbit by reversing the drive. A 9.1 m diameter WRA was launched in 1974 with the *Applications Technology Satellite* 6 (ATS-6), Figure 2.9(b). The ATS-6 antenna consisted of 48 ribs, which were stowed in a 2.0 m diameter hub with a height of 0.45 m. The whole antenna weighed about 60 kg [87, 138, 146].

[2]From measurement in figure on page 415 of [40].

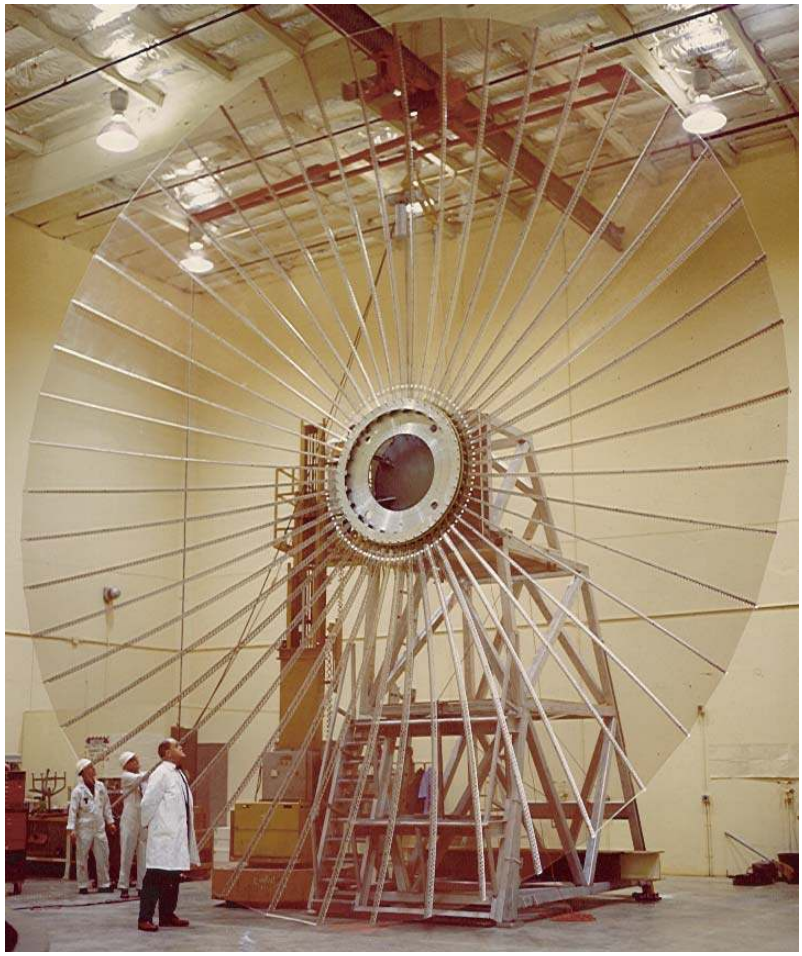

(a) The 9.1 m diameter ATS-6 wrap-rib antenna (Courtesy of Lockheed Missiles and Space Company).

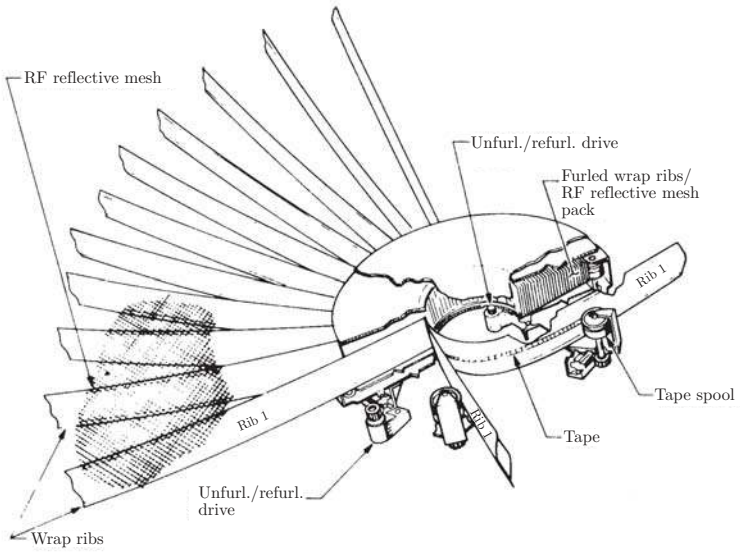

(b) Wrap-rib deployment mechanism.

Figure 2.9: The wrap-rib reflector antenna.

Figure 2.10: The 12 m diameter hinged-rib antenna for the ACeS system (Courtesy of Harris Corporation).

Hinged-Rib Antenna

Harris Corporation developed the *Hinged-Rib Antenna* (HRA) for the Asia Cellular Satellite (ACeS) system. In this concept, the ribs are hinged along their length, which produce a smaller height of the stowed package. In order to provide a smaller package diameter, the ribs are straight and the parabolic mesh surface is shaped by stand-off elements along the ribs, Figure 2.10. Two 12 m diameter HRAs are mounted on the ACeS Garuda-1 satellite, launched February 13, 2000. The stowed diameter and height of each antenna are 0.86 and 4.5 m, respectively. The total weight of the antenna and boom is 127 kg. Harris is currently working on a refined version of the HRA, called *Advanced Folding Rib Antenna* (AFRA), with the same deployed diameter as the ACeS HRA, but with lower mass and smaller stowed diameter and height [154].

Hoop/Column Antenna

NASA *Langley Research Center* (LaRC) and Harris Corporation developed the *Hoop/Column Antenna* (HCA) around 1980, to demonstrate the feasibility of a large space antenna. The concept is a simple tension and compression preloaded structure. A central column and a large-diameter hoop are the compression members, which maintain pre-tension in a cable network. In addition to its structural contributions, the cable network supports and shapes the RF reflective mesh surface [40]. The antenna deploys in three principal steps: the column deploys simultaneously from both top and bottom, Figure 2.11(a) and (b); the hoop deploys by means of motors mounted in eight of the 24 hoop joints, Figure 2.11(c)–(e). Finally, an outward extending preload segment is deployed at the bottom of the column, which pre-tensions all cables and the mesh. A 15 m diameter HCA, with a height of 9.5 m, has been built and tested on ground. In the stowed configuration, the antenna fits inside a cylinder of 2.7 m in height and 0.9 m in diameter. The total weight of the

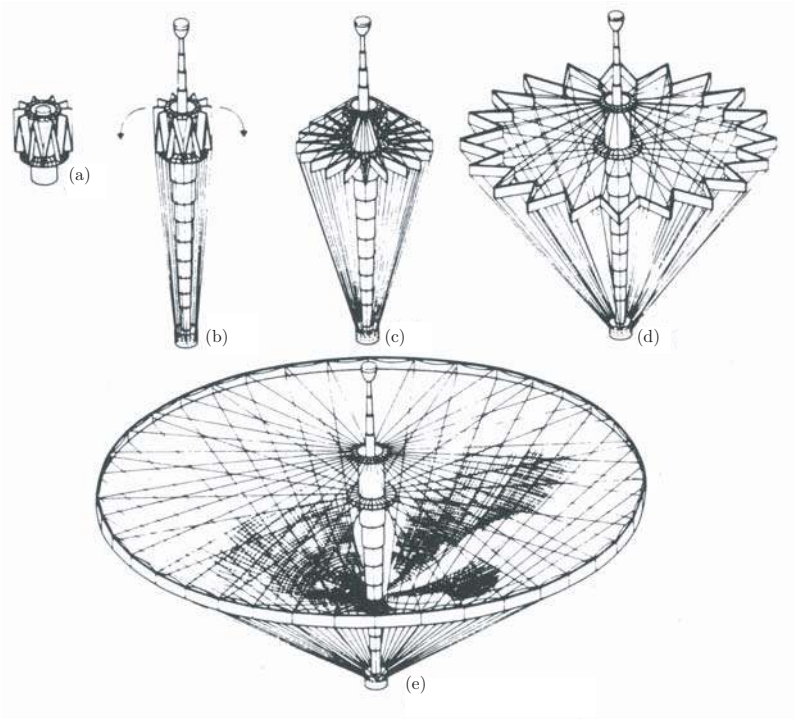

Figure 2.11: Deployment sequence of the hoop/column antenna. Reproduced from [146].

antenna structure alone is 291 kg. The total weight, including the instrumentation and feed, is 410 kg [9].

EGS Antenna

The Russian-Georgian company *Energia-GPI-Space* (EGS) has developed a new concept aimed at deployable reflector antennas in the diameter range 5–25 m. The EGS antenna consists of a circular pantograph ring and radial tensioned membrane ribs connecting to a central hub. An elliptical reflector antenna with dimensions 5.6 m by 6.4 m was tested in space on the Russian orbital station MIR, Figure 2.12. The stowed diameter and height of the antenna are 0.6 and 1.0 m, respectively. The weight of the antenna, including both the mechanical and electrical systems, is 35 kg. A 13.5 m diameter antenna has also been built, but only tested on the ground [4, 91].

Spring-Back Antenna

A totally different antenna concept, without moveable connections, was developed by the *Hughes Space and Communication Company*[3]. The *Spring-Back Antenna* (SBA) consists of a thin graphite mesh dish with an integral lattice of ribs and a stiffening hoop along the rim. The antenna is elastically folded like a taco shell and

[3]Now Boeing Satellite Systems, Inc.

Figure 2.12: A 5.6 m diameter EGS antenna in space. Photo taken from the orbital station MIR on July 28, 1999 (Courtesy of Energia-GPI-Space, Ltd.).

held in that configurations by tie cables along the rim, Figure 2.13. The stowed volume of this antenna is quite large compared to other antennas and the stowed height is about the same as the reflector diameter. In orbit, the reflector deploys by cutting the tie cables, which releases its stored elastic strain energy. The MSAT-1 satellite, launched April 20, 1996, was the first to use the SBA. Each of the two SBAs had a 6.8 m by 5.25 m elliptical shape and weighed 20 kg. In the stowed configuration, the two SBAs are rolled together into a 4.9 m high truncated cone on top of the spacecraft. The top and bottom diameters of the cone are 1.5 and 3.0 m, respectively. In a more recent application, NASA's next generation TDRS, the 5 m diameter RRAs are replaced by 4.6 m diameter SBAs [10, 105].

Tension Truss Antenna

The *Tension Truss* concept was developed by Miura in 1986 [104] to meet demands for high precision large deployable reflectors. In this concept, the reflector is divided into triangular facets instead of gores as in an umbrella-type reflector. The idea of approximating bowl-shaped surfaces by polygons was not new, cf. the geodesic dome, and had been previously applied in space antenna applications. However, the novelty of the tension truss concept was to use flexible members for the sides of the triangles so that the whole assembly could be easily folded. Out-of-plane forces, e.g.

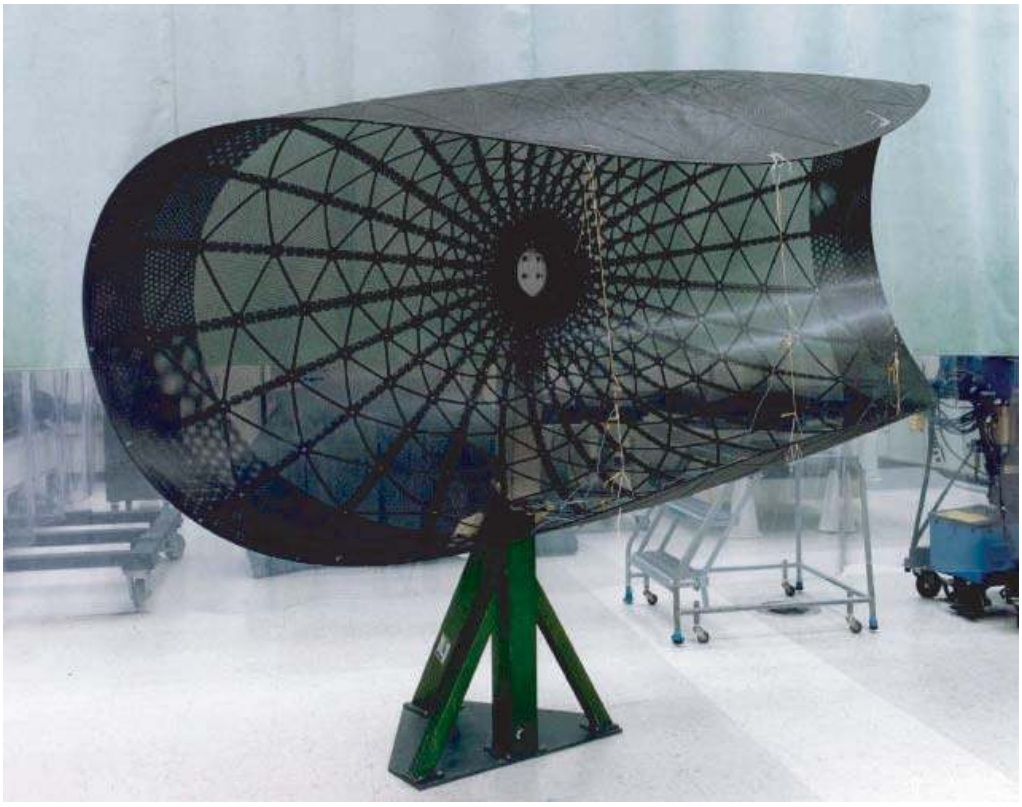

Figure 2.13: Folded spring-back antenna (Courtesy of Hughes Space and Communications Company).

springs, would be used to prestress the triangular network. A main advantage of the tension truss antenna over the umbrella-types is that the surface accuracy can be increased, e.g. by decreasing the size of the triangles, without increasing the number of supports. The triangular prestressed network is the support for the reflective mesh. In Japan, two different types of antennas using the tension truss concept have been developed. The main difference between them is the supporting structure for the triangular network. A reflector with an effective aperture diameter of 8 m was developed by the *Institute of Space and Astronautical Science* (ISAS) and flown on the *Highly Advanced Laboratory for Communications and Astronomy* (HALCA) satellite, Figure 2.14. From the main bus, the tension truss is deployed by six truss masts[4]. Maximum diameter of the antenna is 10 m and the total mass is 246 kg; the mass of the mesh and cables is about 11 kg and that of the six deployable masts is about 100 kg [63]. The *National Space Development Agency of Japan* (NASDA) developed another antenna for their *Engineering Test Satellite* VIII (ETS-VIII). The ETS-VIII antenna is based on a modular approach with 4.8 m diameter hexagonal tension truss modules. A 14-module antenna has an aperture diameter of 13 m, but the total dimension of the antenna is 19.2×16.7 m^2. The stowed size is 1 m in diameter and 4 m in height. The total weight of a 14-module antenna, including supporting booms and deployment mechanics, is about 170 kg [92]. A tension truss

[4]The exact mast type is not known to the author, but according to K. Miura, [102], CMs could not be used because of the high compressive forces.

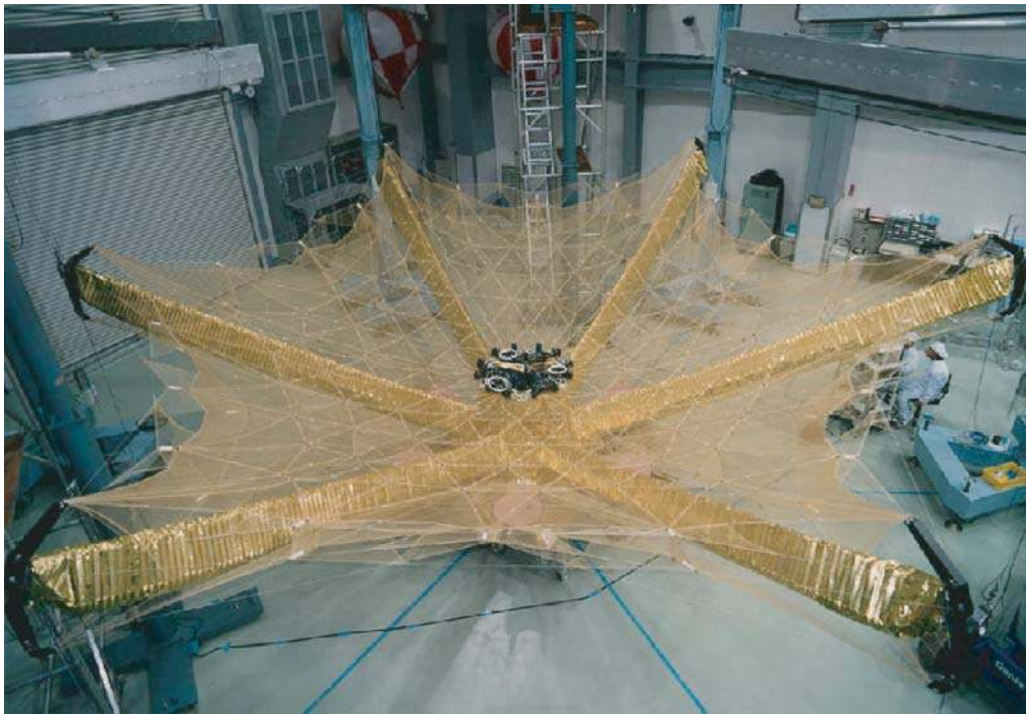

Figure 2.14: Tension truss antenna for HALCA (Courtesy of ISAS).

antenna developed in USA will be described next.

AstroMesh Antenna

In 1990, Astro Aerospace Corporation[5] started developing what is now the current state-of-the-art deployable reflector antenna—the *AstroMesh*. As mentioned in the previous section, the AstroMesh is based on the tension truss concept and its components are shown in Figure 2.15(a). Two identical paraboloidal triangular networks are attached to a deployable ring truss. This assembly is prestressed by tension ties connected to mirroring nodes of the two networks. The RF reflective mesh is attached to the backside of the front net. The antenna is deployed by shortening a cable which continuously runs through the telescopic diagonal members of the ring truss. Deployment synchronisation is achieved through special joints at the truss connections where only three members meet [166], which can be clearly seen in Figure 2.15(c). The latest application of the AstroMesh is onboard the telecommunication satellite *Thuraya*, which was launched on December 5, 2000. This antenna, which is shown in Figures 2.15(b) and (c), has a diameter of 12.25 m and weighs 55 kg. In the stowed configuration, the diameter and height are 1.3 and 3.8 m, respectively [172].

[5]Now TRW Astro Aerospace.

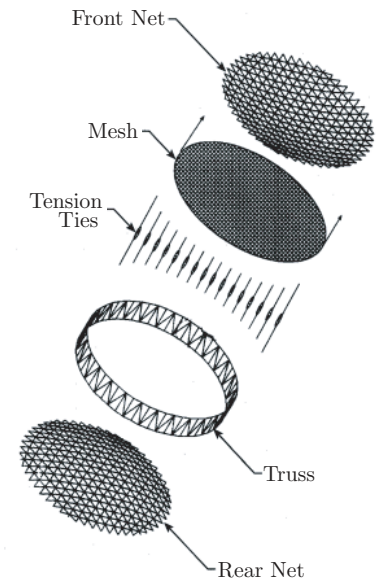

(a)

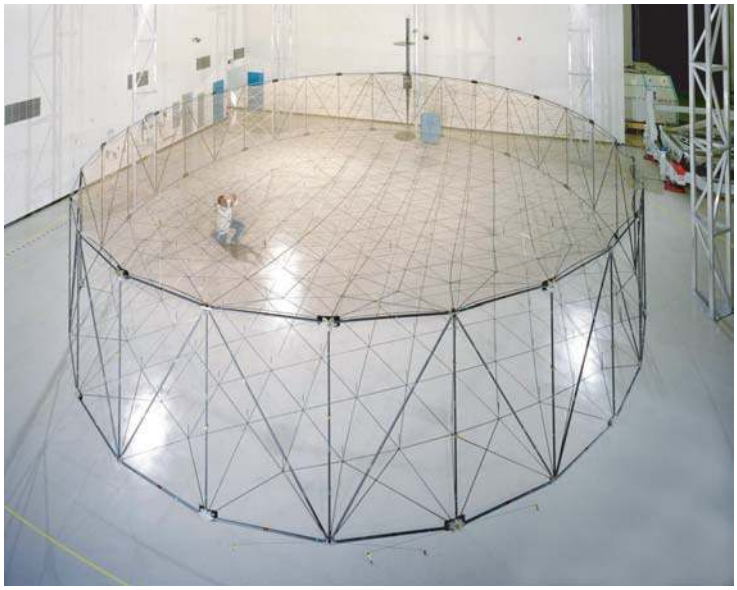

(b)

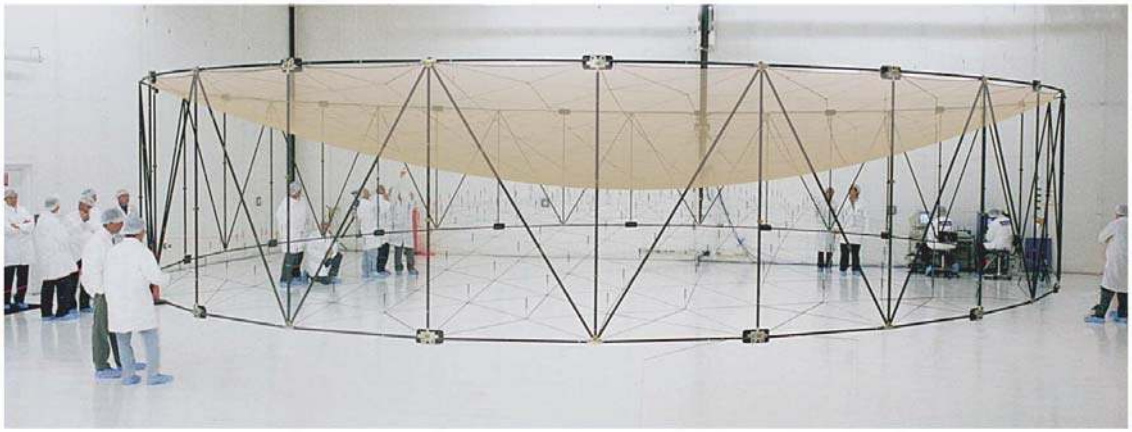

(c)

Figure 2.15: The AstroMesh deployable reflector antenna: (a) concept, (b) and (c) the 12.25 m diameter reflector for Thuraya (Courtesy of M. W. Thomson and TRW Astro Aerospace).

Cable-Stiffened Pantographic Antenna

DSL developed the *Cable-Stiffened Pantographic Deployable Antenna* (CSPDA). The deployable ring structure consists of three different pairs of rods connected by scissor joints. The pairs of rods are connected at their end points to form a circular pantographic structure that can be folded. Crucial to a successful folding is accurate positioning and manufacturing of the scissor and end joints. A 3.5 m diameter model has twelve sides and is composed of 48 pantograph elements, Figure 2.16. A double layer cable network, which supports the RF reflective mesh, is

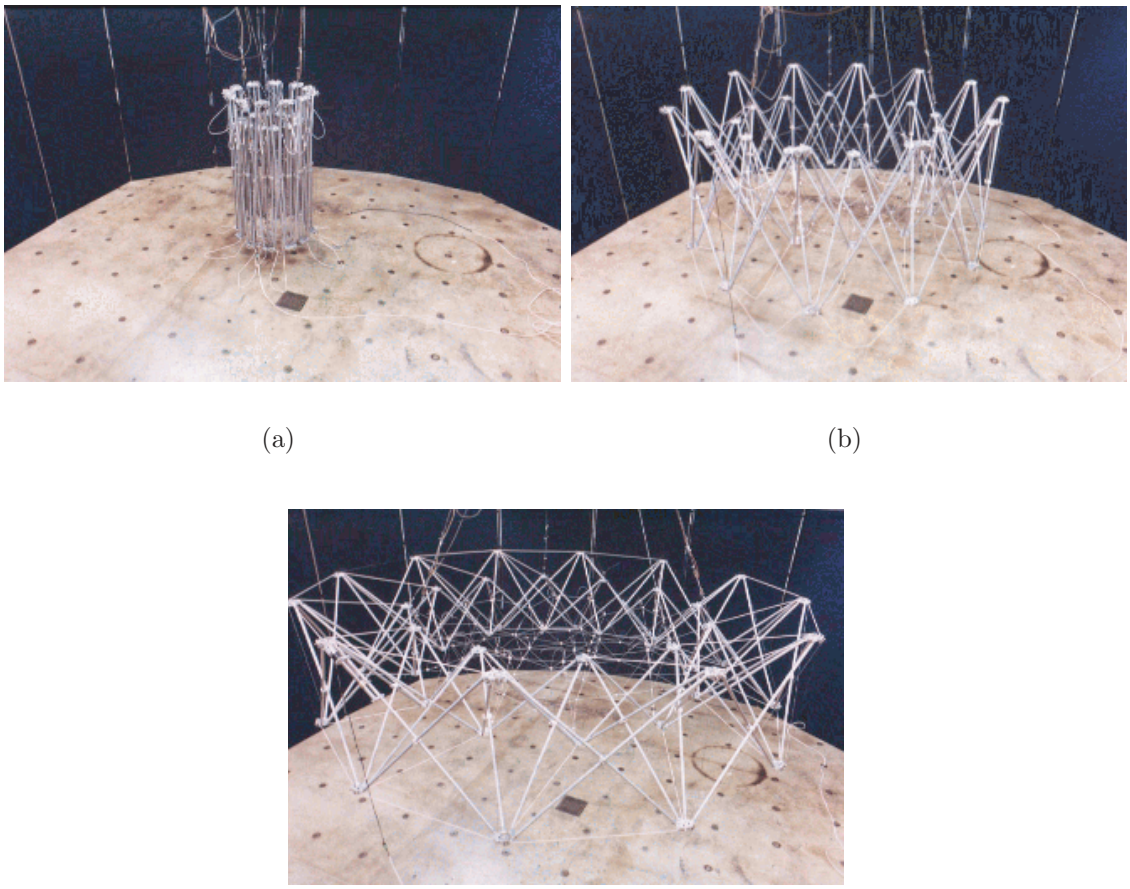

(a) (b)

(c)

Figure 2.16: Deployment sequence of the 3.5 m diameter model of the cable-stiffened pantographic deployable antenna (Courtesy of Z. You and S. Pellegrino).

attached to the ring structure. The layout of the network is chosen such that the total structure is statically determinate, or indeterminate to only a small degree. Like the AstroMesh, an active cable is used to deploy the ring structure. In the stowed configuration, the diameter and height are 0.6 and 1.2 m, respectively [188].

2.3.2 Solid Surface Antennas

Antenna applications operating at frequencies over about 40 GHz require high surface accuracy. Solid material is usually chosen for their reflective surface [95]. Most of the solid surface deployable reflector concepts consist of a central hub with rigid curved panels, often CFRP face sheets over an aluminium honeycomb core, arranged as radial petals. The concepts differ by the manner in which the petals fold [51]. Because of mechanical complexity and launch vehicle size constraints, deployable high precision reflectors are limited to approximately 10 m in diameter [95].

Sunflower

The first concept with rigid panels was the *Sunflower* by TRW, Figure 2.17. It folds using simple revolute joints between the panels, but does not achieve a great reduction in size. A 4.9 m diameter model was built, which has a stowed diameter and height of 2.15 and 1.8 m, respectively [51, 52]. An extended version of the Sunflower, with a diameter of 15 m, stows into a cylinder of 4.4 m in diameter and 6.6 m in height [60]. This version is, however, more complex that the original Sunflower.

DAISY and MEA

The second concept is the *Deployable Antenna Integral System* (DAISY) by ESA and Dornier, Figure 2.18. Here, each panel is connected to the central hub by a revolute joint, which allows the panels to fold by nesting in front of the hub. The position and orientation of the hinges are determined by extensive deployment simulations to achieve good packaging and avoid interference between the panels during deployment. The truss structure on the back of each panel, seen in Figure 2.18, provides additional stiffness for better surface accuracy. An 8 m diameter engineering model has been built, with a stowed diameter and height of 2.9 and 4.1 m, respectively [51, 105].

The third concept, also by Dornier and ESA, is MEA. The folding configuration is similar to the DAISY, with panels nested in front of the hub. Each panel is connected to the hub by a joint that allows rotation about two axes and to neighbouring panels by rods with spherical joints. The panel-to-panel connecting rods compensate for the increased kinematic freedom introduced by the two-axis joints and synchronise the motion of the panels. During folding, each panel folds towards the hub and twists at the same time. A 4.7 m diameter MEA model has a stowed diameter and height of 1.7 and 2.4 m, respectively [51, 186].

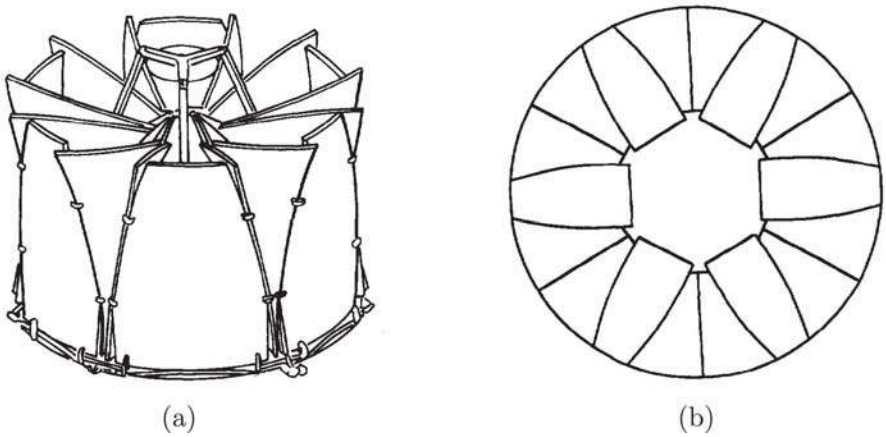

Figure 2.17: Sunflower antenna: (a) folded; (b) deployed, plan view (Courtesy of TRW).

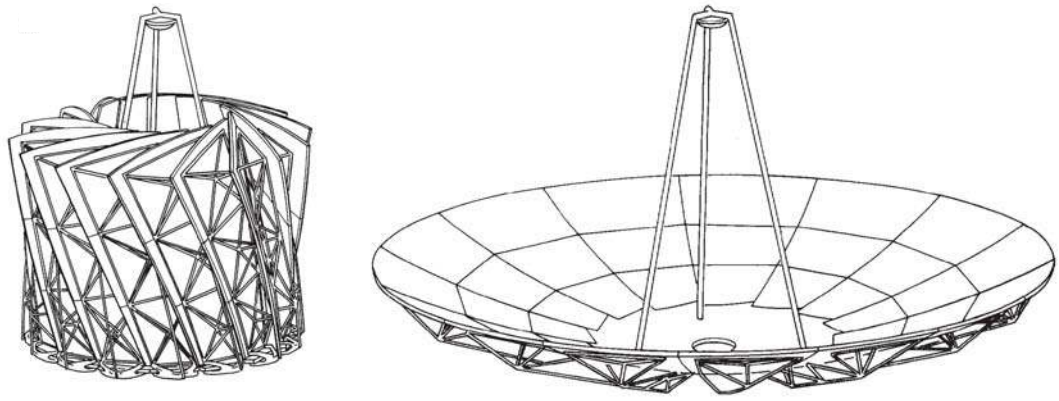

(a) (b)

Figure 2.18: DAISY antenna: (a) folded; (b) deployed (Courtesy of Dornier GmbH).

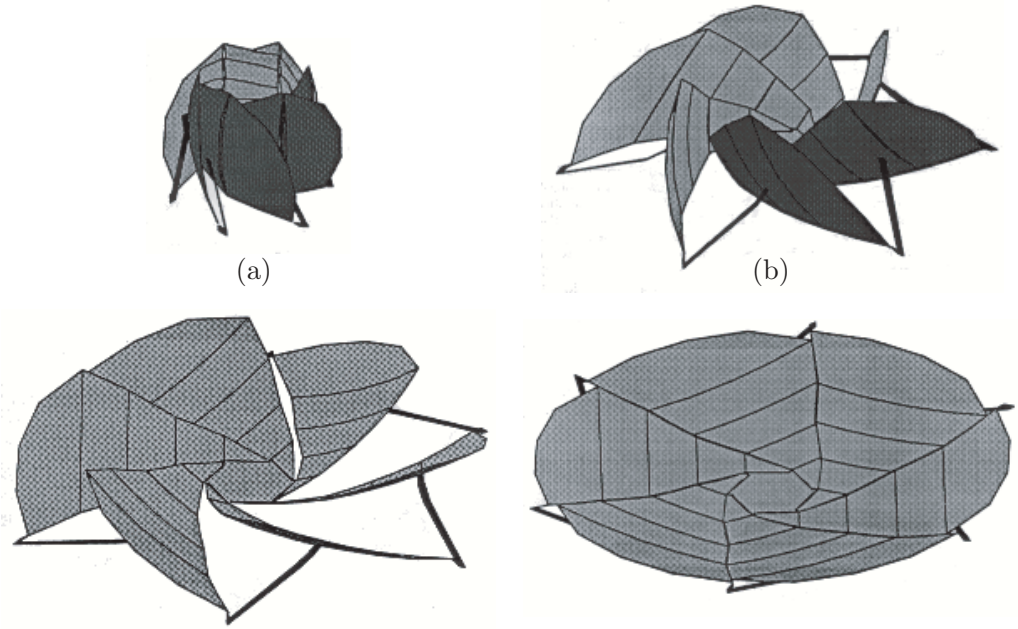

(a) (b)

(c) (d)

Figure 2.19: Deployment sequence of the solid surface deployable antenna: (a)–(d) (Courtesy of S. D. Guest).

Solid Surface Deployable Antenna

The fourth concept, the *Solid Surface Deployable Antenna* (SSDA) by DSL, Figure 2.19, is quite different from the others. In this concept, the surface is split into wings rather than radial petals. Each wing is further subdivided into panels which are connected by revolute joints. This concept is extendable to any number of wings and panels and will package efficiently as the curved panels nest inside one another. A 1.5 m diameter SSDA model with six wings and five panels per wing had a stowed diameter and height of 0.56 and 0.81 m, respectively. Estimates show that increasing the number of panels from five to seven, yield 0.36 and 0.75 m as stowed dimensions [51].

2.3.3 Inflatable Antennas

An inflatable antenna would give the smallest package size and potentially the lowest mass. It is constructed from a thin flexible material which is folded prior to launch and then deployed by inflation. The reflector structure is like a circular paraboloidal cushion with a transparent front side and a reflective rear side. It is stiffened by an inflatable torus along the edge. The structure can be made more rigid by impregnating the membrane material with a resin, which slowly cures at high temperature or by the Sun's *ultraviolet* (UV) rays. The main disadvantage of inflatable antennas is the difficulty of achieving high shape accuracy for the reflective surface [186]. Inflatable structures have a high deployment reliability because of their simplicity and a low number of failure modes. For testing the structures on the ground, a zero gravity environment can be simulated through the use of Helium [40].

Inflatable Space Rigidised Reflector

ESA and the company *Contraves* developed an antenna using *Inflatable Space Rigidised Structure* (ISRS) technology for a joint ESA/NASA programme requiring a large antenna [135]. The antenna structure is made of *Kevlar*[6] membranes, impregnated with an epoxy-type resin. When in orbit, the inflated antenna is positioned so that its faces the Sun. The resin hardens in six hours at a temperature of 110°C, which is easily achieved when the structure is exposed to direct sunlight. After hardening, the inflation gas is expelled [135]. Three engineering models of the antenna, with diameters 3.5, 6 and 12 m, have been built. Figure 2.20 shows the latest model, the 12 m diameter offset reflector. However, no flight test was performed and the programme has now been cancelled [28]. An early design study showed that a 20 m diameter reflector would have a mass of 134 kg [135].

Inflatable Antenna Experiment

To demonstrate the potential of inflatable structure technology for large antennas, JPL initiated the *Inflatable Antenna Experiment* (IAE), Figure 2.21. Together with the company *L'Garde* they developed and manufactured a 14 m diameter inflatable antenna with a low pressure canopy structure, high pressure torus and three high pressure struts, which support the feed. As the antenna would only be used for a short time, no attention was paid to space rigidised material. The canopies were constructed of 6.5 μm *Mylar*[7] film, the front canopy was left transparent while the back was aluminised for reflectivity. The torus and struts were made of 0.3 mm thick Kevlar. A smooth reflective surface could be obtained at a very low pressure of 2.1 Pa. The torus and struts were both pressurised to 6.9 kPa. The total weight of the inflatable structure was 60 kg. The size of the box container, which housed the stowed inflatable structure, was $2.0 \times 1.1 \times 0.46$ m^3. Deployment starts with

[6]Kevlar is a registered trademark of E. I. du Pont de Nemours and Company.
[7]Mylar is a registered trademark of E. I. du Pont de Nemours and Company.

Figure 2.20: The 12 m diameter model of the inflatable space rigidised reflector antenna (Courtesy of A. G. Roederer, ESA).

an ejection of the package from its container. Then, the struts are inflated followed by the torus and finally, the canopy. The IAE was launched on May 29, 1996 and thereby provided the first demonstration of the potential of inflatable precision structures [41, 43]. Currently, JPL and L'Garde are working on a project called *Advanced Radio Interferometry between Space and Earth* (ARISE), which includes the development of a 25 m diameter inflatable antenna pressurised to 2.8 Pa [20].

2.3.4 Antenna Comparison

A comparison between the presented antenna concepts is given in Table 2.1. For mesh antennas, the stowed diameter d varies between 6 and 22% of the deployed diameter D and the stowed height h varies between 5 and 93%. The solid surface antennas have, as expected, worse packaging ratios than their mesh counterparts. The IAE has, as expected, the best packaging ratio with ratios of 6 and 14% in diameter and height. Another crucial parameter is the mass and surface density. Low mass is necessary because of the extremely high launch costs in the order of 10,000 USD/kg [185]. In that respect, it should be noted that the AstroMesh has an areal density significantly lower than other mesh antennas and comparable to those of inflatable antennas. Low mass combined with a high structural stiffness give a high lowest natural frequency of the structure, which is desirable to separate the structural and attitude control system frequencies [55]. The large mesh antennas in Table 2.1 have a fundamental frequency f_1 lower than 1 Hz. Unfortunately, no value

Figure 2.21: The 14 m diameter IAE reflector antenna in space (Courtesy of L'Garde, Inc.).

for the deployed frequency of the 12.25 m diameter AstroMesh reflector is given in references [165, 166]. A 6 m diameter AstroMesh is reported to have a fundamental frequency of 2.0 Hz [166], which can be compared to 17 Hz of the EGS antenna of about the same size. The last parameters, the surface accuracy and operating frequency, will be discussed in Chapter 5 in connection to the development of the tensegrity reflector antenna.

Table 2.1: Comparison of different deployable reflector antenna concepts (sorted by type and aperture size).

Type[a]	Structure	Status[b]	D (m)	d/D	h/D	Mass (kg)	ϱ^c (kg/m^2)	f_1 (Hz)	δ_{rms} (mm)	f_{op} (GHz)	Ref.	Comment
M	HCA	EM	15	0.06	0.18	291	1.65	0.068	1.52	11.6	[9, 17]	Quad-aperture configuration
	TT ETS-VIII	EM	13	0.08	0.31	170	0.81	0.14	2.4	4	[92]	14 modules
	AstroMesh	O	12.25	0.10	0.31	55	0.36	—	—	2	[166, 172]	$D_{\min} = 12.25$ m; $D_{\max} = 16$ m
	HRA ACeS	O	12	0.07	0.38	127	1.12	0.13	—	—	[154]	
	AFRA	—	12	0.07	0.35	120	1.06	0.35	—	—	[154]	Status not known
	WRA	O	9.1	0.22	0.05	60	0.92	—	0.8	8.25	[87, 146]	
	TT HALCA	O	8	—	—	230	4.58	—	0.6	22	[63]	
	EGS	O	5.6	0.11	0.18	35	1.24	17	—	—	[91]	$D_{\min} = 5.6$ m; $D_{\max} = 6.4$ m
	SBA	O	5.25	—	0.93	20	0.71	—	—	2	[10]	$D_{\min} = 5.25$ m; $D_{\max} = 6.8$ m
	RRA TDRS	O	5	0.18	0.54	24	1.22	—	0.56	15	[40, 52]	
	TT ETS-VIII	EM	4.8	0.06	0.73	11	0.73	—	—	—	[98]	One module, 15 m^2
	CSPDA	EM	3.5	0.17	0.34	—	—	—	—	—	[188]	
S	Ext. Sunflower	FS	15	0.29	0.43	—	—	—	—	—	[60]	
	DAISY	EM	8	0.36	0.51	—	6	—	0.008	3000	[51, 134]	
	Sunflower	EM	4.9	0.44	0.37	31	1.64	—	0.051	60	[51, 52]	
	MEA	EM	4.7	0.36	0.51	94	5.42	—	0.2	30	[52, 153]	
	SSDA	EM	1.5	0.37	0.54	—	—	—	—	—	[51]	
I	ARISE	FS	25	—	—	192	0.39	0.3	0.5	86	[20]	Target surface accuracy
	ISRS	EM	20	—	—	134	0.42	3.2	0.98	22	[135]	
	IAE	O	14	0.06	0.14	60	0.39	4	1.00	—	[43]	$d/D = \sqrt{4 \cdot 1.1 \cdot 0.46/\pi}/14 \approx 0.06$

[a] M: mesh, S: solid and I: inflatable.
[b] O: Orbit, EM: Engineering Model, FS: Feasibility Study
[c] Surface area: $\pi D^2/4$ or $\pi D_{\max} D_{\min}/4$ if elliptic.

Chapter 3

Analysis Methods for Tensegrity Structures

3.1 Introduction

A major obstacle in the analysis and design of tensegrity structures is the determination of their equilibrium configuration. This key step in the design procedure is usually known as *form-finding*. For other tension structures, such as membrane and cable nets, efficient form-finding methods have been available for a long time, cf. [5, 147]. For general tensegrity structures, however, the form-finding process has proven to be more complicated.

Early studies, by Fuller [44, 88], Snelson [151] and Emmerich [37] into the form of tensegrity structures, use mainly regular, convex polyhedra as the basis for finding new configurations. This purely geometric research has resulted in a large number of configurations which are classified by Pugh [132] into three pattern types: diamond, circuit and zig-zag. A large number of different tensegrities, with detailed schemes and advice on how to build them, are found in reference [132].

However, physical models of these structures show that the shape of the tensegrity, corresponding to a particular polyhedron, is different from that of the polyhedron. This happens, for example, both for the truncated tetrahedron, Figure 3.1, and the expandable octahedron (icosahedron), Figure 3.2. Hence, the self-stressed shape of a tensegrity is not identical to that of the polyhedron and, therefore, proper form-finding methods are needed to find the equilibrium configuration of even the simplest tensegrity structure [112].

Form-finding methods for tensegrity structures have been investigated by many authors, and recently by Connelly and Terrell [26], Vassart and Motro [177], and Sultan *et al.* [160]. Different approaches are proposed by these authors, but the various methods have not previously been classified or linked. In the first two sections of this chapter the existing methods were classified into two broad families—kinematic and static methods—and advantages and limitations of each method were identified. Closer scrutiny of the seemingly different approaches in references [26, 160, 177]

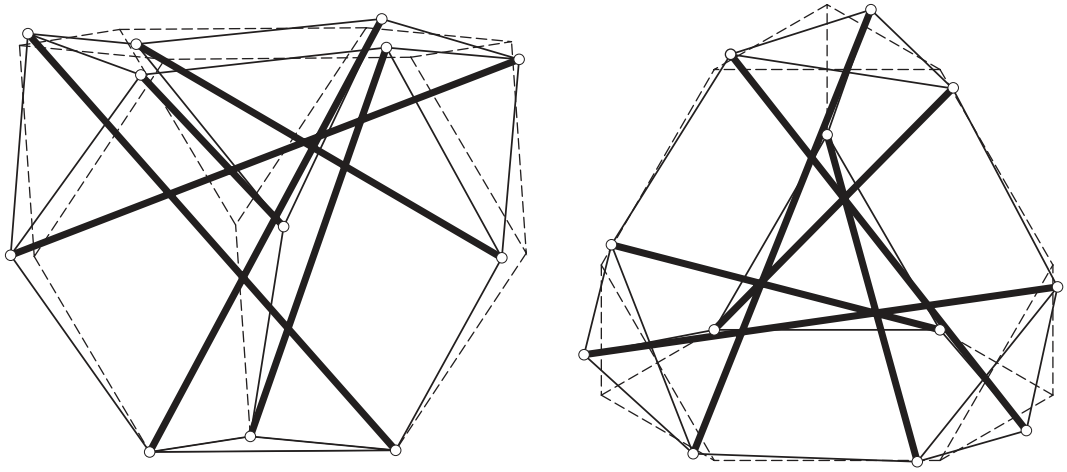

(a) Side view (b) Top view

Figure 3.1: Comparison of truncated tensegrity tetrahedron and the polyhedron from which it originates (drawn with dashed lines). Note the distortion of the hexagonal faces.

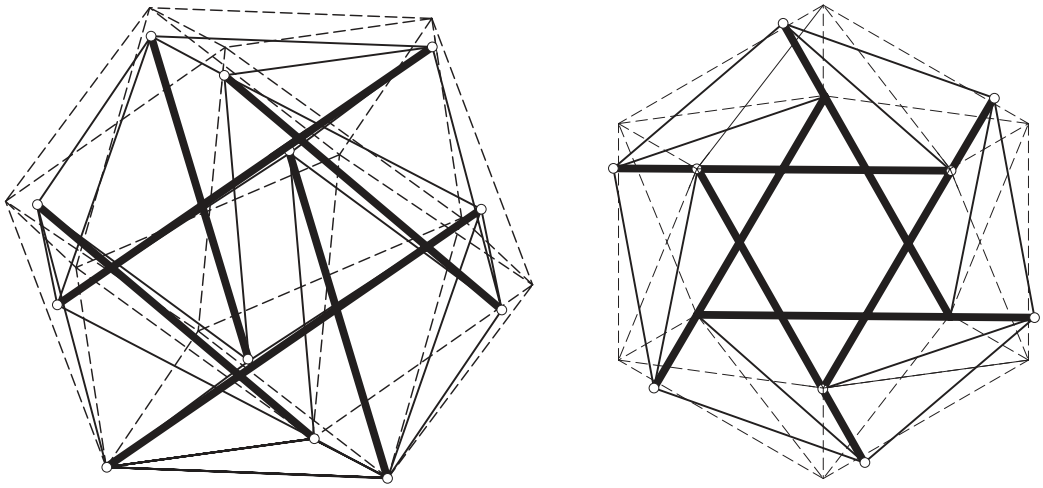

(a) Side view (b) Top view

Figure 3.2: Comparison of expandable octahedron and icosahedron (drawn with dashed lines).

revealed some links: indeed Vassart and Motro's force density method was linked directly to the more abstract energy approach by Connelly.

Once the form-finding step is completed, the static and kinematic properties, i.e. the states of self-stress and internal mechanisms, must be found. A suitable method

for this task is the *Force Method* developed by Pellegrino and Calladine [127]. As this method will be used frequently in the remainder of the thesis, it is described in the last part of this chapter.

3.2 Kinematic Form-Finding Methods

The characteristic of these method is that the lengths of the cables are kept constant while the strut lengths are increased until a *maximum* is reached. Alternatively, the strut lengths may be kept constant while the cable lengths are decreased until they reach a *minimum*. This approach mimics the way in which tensegrity structures are built in practice, without explicitly requiring that the cables be put in a state of pre-tension.

3.2.1 Analytical Solutions

Consider a simple structure consisting of cables arranged along the edges of a regular prism, plus a number of struts connecting the v vertices of the bottom polygon to vertices of the upper polygon. Depending on the value of v and the offset between vertices connected by a strut, there is a special rotation angle θ between the plane, regular top and bottom polygons for which a tensegrity structure is obtained.

A compact description of the geometry of this problem, taking advantage of its symmetry, was introduced by Connelly and Terrell [26], as follows. Figure 3.3 shows the elements connected to one of the nodes of the bottom polygon. In the starting configuration the lateral cable, 1-2, is vertical and the angle between the ends of the strut is $2\pi i/v$, where i is an integer smaller than v, Figure 3.3.

The coordinates of nodes 1–5 are:

$$\mathbf{p}_1 = \begin{pmatrix} R & 0 & 0 \end{pmatrix}^{\mathrm{T}}, \tag{3.1a}$$

$$\mathbf{p}_2 = \begin{pmatrix} R\cos\theta & R\sin\theta & H \end{pmatrix}^{\mathrm{T}}, \tag{3.1b}$$

$$\mathbf{p}_3 = \begin{pmatrix} R\cos\left(\theta + \dfrac{2\pi i}{v}\right) & R\sin\left(\theta + \dfrac{2\pi i}{v}\right) & H \end{pmatrix}^{\mathrm{T}}, \tag{3.1c}$$

$$\mathbf{p}_4 = \begin{pmatrix} R\cos\left(\dfrac{2\pi}{v}\right) & -R\sin\left(\dfrac{2\pi}{v}\right) & 0 \end{pmatrix}^{\mathrm{T}}, \tag{3.1d}$$

$$\mathbf{p}_5 = \begin{pmatrix} R\cos\left(\dfrac{2\pi}{v}\right) & R\sin\left(\dfrac{2\pi}{v}\right) & 0 \end{pmatrix}^{\mathrm{T}}. \tag{3.1e}$$

The kinematic form-finding proceeds as follows, by considering the square of the lengths of the lateral cable, 1-2, and strut, 1-3,

$$l_t^2 = 2R^2(1 - \cos\theta) + H^2, \tag{3.2a}$$

$$l_c^2 = 2R^2\left[1 - \cos\left(\theta + \frac{2\pi i}{v}\right)\right] + H^2, \tag{3.2b}$$

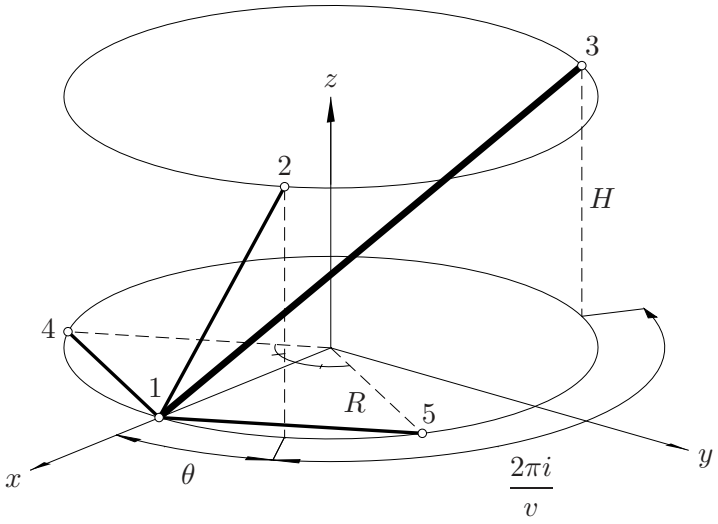

Figure 3.3: Elements meeting at node 1 of structure with v-fold symmetry, radius R and height H.

where the subscripts c and s denote cable and strut, respectively. Equation (3.2b) can be rewritten as:

$$l_c^2 = 4R^2 \sin\left(\theta + \frac{\pi i}{v}\right) \sin\frac{\pi i}{v} + l_t^2. \tag{3.3}$$

For a given cable length l_c the length of the strut l_s is maximised for

$$\theta = \pi\left(\frac{1}{2} - \frac{i}{v}\right). \tag{3.4}$$

The simplicity of the kinematic method for structures with v-fold symmetry is mirrored by the static method, see section 3.3, but for other, non-symmetric, cases the present formulation becomes infeasible due to the large number of variables required to describe a general configuration.

3.2.2 Non-Linear Programming

This general method, proposed by Pellegrino [121], turns the form-finding of any tensegrity structure into a constrained minimisation problem. Starting from a system for which the element connectivity and nodal coordinates are known, one or more struts are elongated, maintaining fixed length ratios, until a configuration is reached in which their lengths are maximised. The general constrained minimisation problem has the form:

$$\begin{aligned} &\text{Minimise} \quad f(x,y,z) \\ &\text{subject to} \quad g_i(x,y,z) = 0 \quad \text{for } i = 1,\ ...,n, \end{aligned} \tag{3.5}$$

where the objective function $f(x,y,z)$ is, for example, the negative length of one of the struts and constraint equations $g_i(x,y,z)$ are the fixed lengths of the cables. Pellegrino [121] applies this method to two tensegrities: the triangular prism and the truncated tetrahedron.

A triangular prism, $v = 3$ and $i = 1$, has nine cables of length $l_c = 1$ and three struts of equal length. One of the base triangles is fixed, hence three of its six nodes are fixed in space. In Cartesian coordinates, the constrained minimisation problem has the form:

$$\begin{aligned} &\text{Minimise} \quad -l_{s1}^2 \\ &\text{subject to} \begin{cases} l_{c1}^2 - 1 = 0 \\ l_{c2}^2 - 1 = 0 \\ \quad \vdots \\ l_{c6}^2 - 1 = 0 \\ l_{s2}^2 - l_{s1}^2 = 0 \\ l_{s3}^2 - l_{s1}^2 = 0 \end{cases} \end{aligned} \tag{3.6}$$

where $c1,\ c2,\ ...,\ c6$ denote the six remaining cables and $s1,\ s2$ and $s3$ the struts. This problem can be solved, for example, using the constrained optimisation function `fmincon` in Matlab [89]. The final length of the struts is 1.468, compared to the theoretical value of $\sqrt{1 + 2/\sqrt{3}} \approx 1.4679$ obtained from (3.3) and (3.4).

Similarly, for the case of the truncated tetrahedron there are six struts and 18 cables, Figure 3.1. The objective function to be minimised, equal to the negative length of one of the struts, has to satisfy 20 constraint equations, 15 on the cable lengths plus 5 on the struts. The final length of the struts is 2.2507. Note that the strut length obtained from a purely geometric analysis of the ideal truncated tetrahedron is $\sqrt{5} \approx 2.2361$; hence the slight warping of the hexagonal faces leads to an increase of the strut length by 0.7%.

An advantage of the non-linear programming approach is that it makes use of general purpose, standard software. However, the number of constraint equations increases with the number of elements so this approach is not feasible for larger systems. Also, although different geometric configurations of structures with the same topology can be found by specifying different relationships between the lengths of the struts, there is no direct way of controlling the corresponding variation in the state of prestress.

3.2.3 Dynamic Relaxation

The method of dynamic relaxation, that had already been successfully used for membrane and cable net structures [6, 31], was put forward by Motro [110] and Belkacem [8] as a general form-finding method for tensegrity structures.

For a structure in a given initial configuration and subject to given general forces the equilibrium configuration can be computed by integrating the following fictitious dynamic equations

$$\mathbf{M}\ddot{\mathbf{d}} + \mathbf{N}\dot{\mathbf{d}} + \mathbf{K}\mathbf{d} = \mathbf{f}, \tag{3.7}$$

where $\mathbf{K}$ is a stiffness matrix, $\mathbf{M}$ a mass matrix, $\mathbf{N}$ a damping matrix, $\mathbf{f}$ the vector of external loads, and $\ddot{\mathbf{d}}$, $\dot{\mathbf{d}}$ and $\mathbf{d}$, are the vectors of acceleration, velocity and

displacement from an initial configuration, respectively. Both **M** and **N** are assumed to be diagonal, for simplicity, and the velocities and displacements are initially set to zero.

There are several ways of carrying out a form-finding analysis, for example by prescribing for each element of the structure a constitutive relationship of the type

$$t = t_0 + \bar{k}e, \tag{3.8}$$

where t is the axial force and e the extension, measured from the initial configuration, of the element; t_0 is the desired prestress and $\bar{k}$ a fictitious, small axial stiffness. In any current configuration of the structure, nodal equations of equilibrium are used to compute out-of-balance forces from which the current acceleration can be obtained through (3.7). The resulting system of uncoupled equilibrium equations can then be integrated using a centred finite difference scheme.

The coefficients of the damping matrix are usually all assigned the same value, chosen such as to maximise the speed of convergence to the equilibrium configuration. Alternatively, a technique called *kinetic damping* can be used, whereby the undamped motion of the structure is traced. When a local peak in the total kinetic energy of the structure is detected, all velocity components are set to zero. The process is then repeated, starting from the current configuration, until the peak kinetic energy becomes sufficiently small [6]. The latter technique usually gives a faster convergence.

Motro [110] applies the dynamic relaxation method to the form-finding of the triangular tensegrity prism. The lengths of the cables were held constant while the struts were gradually elongated, until a state of prestress was set up in the structure. This analysis converged to $l_s/l_c = 1.468$, as above.

Belkacem [8] analyses the triangular and square tensegrity prisms, and also the expandable octahedron. The results for the tensegrity prisms are compared with the theoretical values obtained from (3.3) and those for the expandable octahedron to the results of a static method. The relative error ν in the nodal coordinates is, for node i, computed as

$$\nu_i = \frac{\sqrt{(x_i - \tilde{x}_i)^2 + (y_i - \tilde{y}_i)^2 + (z_i - \tilde{z}_i)^2}}{\sqrt{x_i^2 + y_i^2 + z_i^2}}, \tag{3.9}$$

where $\tilde{}$ denotes the approximate values. This error is computed for each node and the largest error is taken to represent the structure. The relative errors in the nodal coordinates for the three structures are 0.2, 4 and 2%, respectively. For the tensegrity prisms, errors in the rotation angle θ of 1 and 8%, respectively, are obtained. An analysis of the truncated tetrahedron [111] yields a ratio l_s/l_c slightly greater than 2.24, which is close to the value determined by Pellegrino [121].

Motro *et al.* [114] later conclude that the dynamic relaxation method has good convergence properties for structures with only a few nodes but is not effective when the number of nodes increases. Also, the method becomes rather cumbersome if several different ratios between strut lengths and cable lengths are desired, which

restricts its applicability to less regular structural forms. However, the same restriction applies to kinematic methods in general.

3.3 Static Form-Finding Methods

The general characteristic of these methods is that a relationship is set up between equilibrium configurations of a structure with given topology and the forces in its members. This relationship is then analysed by various methods.

3.3.1 Analytical Solutions

Kenner [70] uses node equilibrium and symmetry arguments to find the configuration of the expandable octahedron, Figure 3.2, whose six identical struts are divided into three pairs of struts which are mutually perpendicular. The distance between the struts in each pair is exactly half the strut length. Other, more complex, spherical tensegrities with polyhedral geometries, i.e. the cuboctahedron and the icosidodecahedron, were also analysed using the same approach.

Connelly and Terrell [26] use an equilibrium approach to find the prestress stable form of v-fold symmetric tensegrity prisms. To set up a system of linear equilibrium equations, they use force density[1], i.e. force divided by length, as variable for each element.

Denoting by q_{ij} the force density in element ij—note that $q_{14} = q_{15}$ due to symmetry—the equilibrium of node 1 in the z- and y-direction can be written as

$$q_{12}H + q_{13}H = 0 \tag{3.10}$$

and

$$q_{12}R\sin\theta + q_{13}R\sin\left(\theta + \frac{2\pi i}{v}\right) = 0, \tag{3.11}$$

respectively. Equations (3.10) and (3.11) give

$$q_{12}\left[\sin\theta - \sin\left(\theta + \frac{2\pi i}{v}\right)\right] = 0. \tag{3.12}$$

The only solution of (3.12) for which the cables are in tension is [26]

$$\theta = \pi\left(\frac{1}{2} - \frac{i}{v}\right). \tag{3.13}$$

At the rotation given by (3.13) the resultant force from cable 1-2 and strut 1-3 is radial. The values of θ for tensegrity prisms with v going from 3 to 6 are given in Table 3.1. Note that (3.13) is identical to (3.4), as expected.

Nishimura [117] uses the force method, described in section 3.5 and *Group Theory* to obtain closed-form expressions for the equilibrium geometry of highly symmetric spherical tensegrities. This is discussed further in section 3.4.3.

[1] Also called tension coefficient, cf. [152].

Table 3.1: Values of θ (°) for $v = 3, 4, 5, 6$.

v	i				
	1	2	3	4	5
3	30	−30	—	—	—
4	45	0	−45	—	—
5	54	18	−18	−54	—
6	60	30	0	−30	−60

3.3.2 Force Density Method

The force density method for cable structures, first proposed by Linkwitz and Schek in 1971 [85, 86, 147], uses a simple mathematical trick to transform the non-linear equilibrium equations of the nodes into a set of linear equations. For example, the equilibrium equation in the x-direction for node i is

$$\sum_j \frac{t_{ij}}{l_{ij}}(x_i - x_j) = f_{ix}, \tag{3.14}$$

where node i is connected to j nodes by cables or struts and t_{ij} is the tension in element ij. Although this may appear to be a linear equation in the nodal coordinates, it is actually non-linear because the lengths l_{ij} in the denominator are also functions of the coordinates. These equations can be linearised by introducing for each element the force density

$$q_{ij} = t_{ij}/l_{ij}, \tag{3.15}$$

whose value needs to be known at the start of the form-finding process.

For a general structure with b elements and n nodes the equilibrium equations in the x-direction can be written as

$$\mathbf{C}_s^{\mathrm{T}}\mathbf{Q}\mathbf{C}_s\mathbf{x} = \mathbf{f}_x, \tag{3.16}$$

where $\mathbf{C}_s$ is the incidence matrix, see below, $\mathbf{Q}$ a diagonal matrix containing the force densities, $\mathbf{x}$ a column vector of x-coordinates, and $\mathbf{f}_x$ a column vector of external nodal forces in x-direction. Equations identical in form to (3.16) can be written also in terms of the y- and z-coordinates.

The incidence matrix $\mathbf{C}_s$, of size $b \times n$, describes the connectivity of the structure; if an element connects nodes i and j, then the corresponding row of $\mathbf{C}_s$ has $+1$ in column i and -1 in column j. If the coordinates of some of the nodes are given, e.g. these nodes are attached to a foundation, $\mathbf{C}_s$ can be partitioned as

$$\mathbf{C}_s = [\mathbf{C}_u \;\; \mathbf{C}_f], \tag{3.17}$$

where the restrained nodes have been put at the end of the numbering sequence. Equation (3.16) can now be written as

$$\mathbf{C}_u^{\mathrm{T}}\mathbf{Q}\mathbf{C}_u\mathbf{x}_u = \mathbf{f}_x - \mathbf{C}_u^{\mathrm{T}}\mathbf{Q}\mathbf{C}_f\mathbf{x}_f, \tag{3.18}$$

where $\mathbf{x}_u$ and $\mathbf{x}_f$ are the column vectors of unknown and given x-coordinates, respectively. Equation (3.18), together with analogous equations for the y- and z-directions, can be solved to find the nodal coordinates. Usually, the external loads are zero during form-finding.

In a structure consisting of cables only, e.g. cable net, all tension coefficients are positive, i.e. $q_{ij} > 0$, and hence $\mathbf{C}_u^{\mathrm{T}}\mathbf{Q}\mathbf{C}_u$ is positive definite and, thus, invertible. Therefore, there is always a unique solution to the form-finding problem. The same approach can be extended to the form-finding of membrane structures by converting the stresses in the membrane into forces in a virtual cable net [5, 81].

A similar formulation can be applied to the form-finding of tensegrity structures, but as these structures are self-stressed, there are usually no foundation nodes or external loads. Hence, (3.16) becomes

$$\overline{\mathbf{D}}\mathbf{x} = \mathbf{0}, \tag{3.19}$$

where $\overline{\mathbf{D}} = \mathbf{C}_s^{\mathrm{T}}\mathbf{Q}\mathbf{C}_s$. Analogous equations hold in the y- and z-directions.

The force density matrix $\overline{\mathbf{D}}$ can be written directly [177], without going through $\mathbf{C}_s$ and $\mathbf{Q}$, following the scheme

$$\overline{D}_{ij} = \begin{cases} -q_{ij} & \text{if } i \neq j, \\ \sum_{k \neq i} q_{ik} & \text{if } i = j, \\ 0 & \text{if } i \text{ and } j \text{ are not connected.} \end{cases} \tag{3.20}$$

Note that the $n \times n$ matrix $\overline{\mathbf{D}}$ is always singular, with a nullity, i.e. the dimension of the nullspace, of at least 1 since the row and column sums are zero, by (3.20). Unlike the matrix $\mathbf{C}_u^{\mathrm{T}}\mathbf{Q}\mathbf{C}_u$ for a cable net attached to foundation nodes, which is positive definite, see page 120 of reference [147], the $\overline{\mathbf{D}}$ matrix for a tensegrity is semi-definite and, due to the presence of compression elements, with $q_{ij} < 0$, several complications arise during form-finding. A practical procedure for finding a set of force densities that yield a matrix $\overline{\mathbf{D}}$ with the required rank, was presented by Vassart [175]. Further details will be given in section 3.4.

3.3.3 Energy Method

In the following, some key main findings by Connelly [22] will be summarised using as far as possible the original terminology.

A configuration of n ordered points in $\mathcal{D}$-dimensional space is denoted by

$$\mathbf{P} = \begin{bmatrix} \mathbf{p}_1 & \mathbf{p}_2 & \dots & \mathbf{p}_n \end{bmatrix}. \tag{3.21}$$

A *tensegrity framework* $G(\mathbf{P})$ is the graph on $\mathbf{P}$ where each edge is designated as either a cable, a strut or a bar; cables cannot increase in length, struts cannot decrease in length and bars cannot change length. A stress state $\boldsymbol{\omega}$ for $G(\mathbf{P})$ is a self-stress if the following condition holds at each node i:

$$\sum_j \omega_{ij} \left(\mathbf{p}_j - \mathbf{p}_i\right) = \mathbf{0}, \tag{3.22}$$

where $\omega_{ij} \geq 0$ for cables, $\omega_{ij} \leq 0$ for struts, and no condition is stipulated for the bars. Comparing (3.22) with the equilibrium equations for the same node written in terms of force densities, it is obvious that the stresses ω_{ij} are identical to the force densities q_{ij}.

Satisfying the above equilibrium condition is a necessary, but not sufficient, condition for the tensegrity framework to be in a stable equilibrium configuration. A basic principle in the analysis of the stability of structures is that the total potential energy functional should be at a local minimum for a given configuration to be stable. In analogy with the total potential, reference [21] defines the following energy form associated with the stress $\boldsymbol{\omega}$:

$$E(\mathbf{P}) = \frac{1}{2}\sum_{ij} \omega_{ij} \|\mathbf{p}_j - \mathbf{p}_i\|^2. \tag{3.23}$$

The idea is that when the end points of an element are displaced, energy builds up as a function of the square of the extension. The function in (3.23) is set up to have an absolute minimum corresponding to the rest length of the element [22]. All members are assumed to behave as linear elastic springs. Mathematically, the cables, which only take tension, have a rest length of zero while the struts, which only take compression, have an infinite rest length.

Let

$$\overline{\mathbf{p}} = \begin{pmatrix} \mathbf{x} \\ \mathbf{y} \\ \mathbf{z} \end{pmatrix} \tag{3.24}$$

be a column vector, of length $\mathcal{D}n$, containing the x-coordinates of $\mathbf{P}$, followed by the y-coordinates, etc. Then, (3.23) can be written as the quadratic form:

$$E(\mathbf{P}) = \frac{1}{2}\overline{\mathbf{p}}^{\mathrm{T}} \begin{bmatrix} \boldsymbol{\Omega} & & \\ & \boldsymbol{\Omega} & \\ & & \boldsymbol{\Omega} \end{bmatrix} \overline{\mathbf{p}}, \tag{3.25}$$

where the elements of $\boldsymbol{\Omega}$ are given by

$$\Omega_{ij} = \begin{cases} -\omega_{ij} & \text{if } i \neq j, \\ \sum_{k \neq i} \omega_{ik} & \text{if } i = j, \\ 0 & \text{if there is no connection between } i \text{ and } j. \end{cases} \tag{3.26}$$

Note that $\boldsymbol{\Omega}$ is identical to $\overline{\mathbf{D}}$, hence the above formulation provides a deeper insight into the characteristics of the force density method and how it can be used to find stable equilibrium configurations of tensegrity structures. The link between the force density method and the energy minimisation was first pointed out by Kötter [73] and later by Schek [147].

A necessary condition for the tensegrity framework to be prestress stable in configuration $\mathbf{P}$ is that the quadratic form $E(\mathbf{P})$ has a local minimum at $\mathbf{P}$. The positive definiteness of $E(\mathbf{P})$ is directly related to that of $\boldsymbol{\Omega}$, but expecting positive definiteness is unrealistic, because—as already noted above for $\overline{\mathbf{D}}$—the nullspace of $\boldsymbol{\Omega}$ contains at least the non-trivial vector $(1\ 1\ \ldots\ 1)^{\mathrm{T}}$.

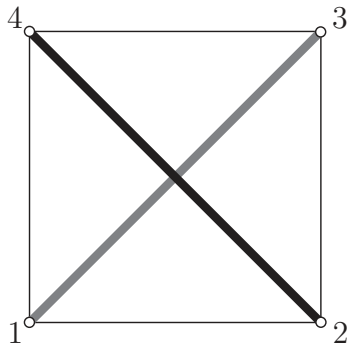

Figure 3.4: Snelson's X-frame

The strongest type of prestress stability, named *super stability* by Connelly [23], requires prestress stability with the additional condition that $\mathbf{\Omega}$ is positive semi-definite with maximal rank. The maximal rank of $\mathbf{\Omega}$ for a structure in $\mathcal{D}$-dimensional space that does not in fact lie in a subspace of smaller dimension, see examples in section 3.4.1, is $n - \mathcal{D} - 1$. Hence, to design a super stable tensegrity framework one has to find a set of force densities such that the nullity $\mathcal{N}$ of $\mathbf{\Omega}$ is $\mathcal{D} + 1$. A further condition for super stability is that there are no affine infinitesimal flexes of the tensegrity framework $G(\mathbf{P})$. Affine infinitesimal flex is another name for a linear infinitesimal mechanism. Such a mechanism can be described by the linear map $\mathbf{d}_i = \mathbf{A}\mathbf{p}_i + \mathbf{n}$, where $\mathbf{A}$ is a $\mathcal{D} \times \mathcal{D}$ matrix and $\mathbf{n}$ a translation vector [22]. When describing a rigid body motion, $\mathbf{A}$ is skew symmetric, i.e. $\mathbf{A} = -\mathbf{A}^{\mathrm{T}}$.

For example, consider the two-dimensional ($\mathcal{D} = 2$) tensegrity structure in Figure 3.4 where the outside edges are cables and the diagonals are struts. A stress equal to 1 in the cables and -1 in the struts is a self-stress for this structure. The stress, i.e. force density, matrix is [21]:

$$\mathbf{\Omega} = \begin{bmatrix} 1 & -1 & 1 & -1 \\ -1 & 1 & -1 & 1 \\ 1 & -1 & 1 & -1 \\ -1 & 1 & -1 & 1 \end{bmatrix}, \tag{3.27}$$

which is positive semi-definite with nullity 3. Hence the tensegrity structure in Figure 3.4 is super stable [23].

Connelly and Back [24] analyse tensegrity structures with different types of symmetry using this method. Their initial assumption is that there is a symmetric state of self-stress with a force density of 1 in each cable and $-\omega_s$ in each strut. A further assumption is that there are two types of cables but only one type of strut, arranged such that satisfying equilibrium at only one node of the structure implies, by symmetry, that it is satisfied also at all other nodes. The force density in the strut is chosen such that the structure is super stable [23, 24].

A complete catalogue of all the tensegrity structures that are possible for each symmetry group is produced, using group theory. Although some of the structures in the catalogue have struts that go through each other, and therefore are of limited practical interest, the catalogue contains many solutions that were previously unknown.

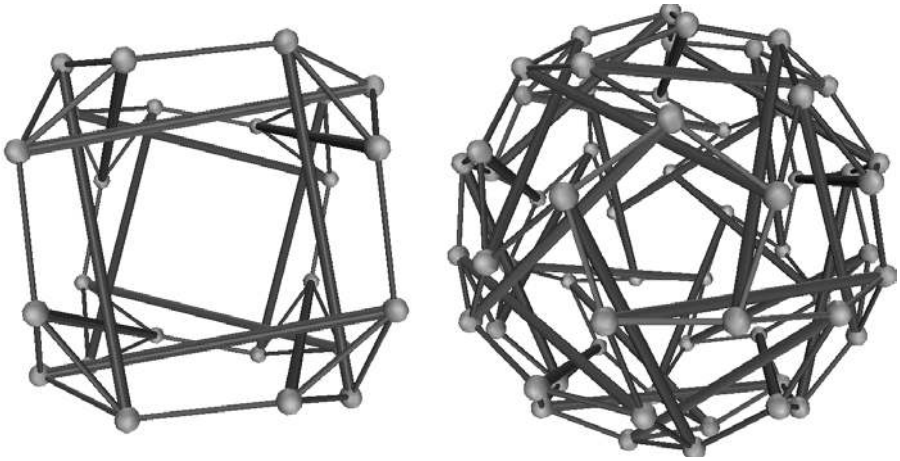

(a) (b)

Figure 3.5: Symmetric tensegrities from Connelly and Back's catalogue.

See Figure 3.5 for some structures from their catalogue.

3.3.4 Reduced Coordinates

This method was introduced by Sultan *et al.* [160]. Consider a tensegrity structure whose b elements consist of M cables and O struts. The struts are considered as a set of bilateral constraints acting on the cable structure. Hence, a set of N independent, generalised coordinates $\mathbf{g} = (g_1 \ g_2 \ \dots \ g_N)^{\mathrm{T}}$ is defined, which define the position and orientation of these struts.[2]

Consider a state of self-stress for the structure and let t_j be the axial force in a generic cable element j; the cable forces $\mathbf{t} = (t_1 \ t_2 \ \dots \ t_M)^{\mathrm{T}}$ are in equilibrium with appropriate forces in the struts and zero external loads. A set of equilibrium equations relating the forces in the cables, but without showing explicitly the forces in the struts, can be obtained from virtual work.

Consider a virtual displacement $\delta\mathbf{g}$ of the structure that involves no extension of the struts. The change of length of cable j is

$$\delta l_j = \sum_{i=1}^{N} \frac{\partial l_j}{\partial g_i} \delta g_i. \tag{3.28}$$

Considering all cables, (3.28) gives

$$\delta\mathbf{l} = \mathbf{A}^{\mathrm{T}} \delta\mathbf{g}, \tag{3.29}$$

[2]If $\mathcal{D} = 2$ three generalised coordinates are required for each struts, hence $N = 3 \times O$; if $\mathcal{D} = 3$ then $N = 5 \times O$.

where the elements of the $N \times M$ matrix $\mathbf{A}$ are

$$A_{ij} = \frac{\partial l_j}{\partial g_i}. \tag{3.30}$$

Because the extensions of the struts are zero, the virtual work in the struts is also zero and so the total internal work, from the cables only, is

$$\mathbf{t}^{\mathrm{T}} \delta \mathbf{l} = (\mathbf{A}\mathbf{t})^{\mathrm{T}} \delta \mathbf{g}. \tag{3.31}$$

For the structure to be in equilibrium, this must be zero for any virtual displacement $\delta\mathbf{g}$. This gives the following reduced equilibrium equations

$$\mathbf{A}\mathbf{t} = \mathbf{0}. \tag{3.32}$$

For this equation to have a non-trivial solution it is required that

$$\text{rank } \mathbf{A} < M, \tag{3.33}$$

where only solutions that are entirely positive are of interest, i.e.

$$t_j > 0 \quad \text{for } j = 1,\ 2,\ ...,\ M. \tag{3.34}$$

General analytical conditions that govern the form of a tensegrity structure of given topology can be obtained by analysing (3.33) and (3.34).

Sultan [159] applies this method to a tensegrity mast of which Figure 3.6 shows a simple two-stage example. The same structure had been previously considered by Snelson [151]. The mast consists of three struts per stage, held in place by three sets of cables—saddle, vertical, and diagonal—between two rigid triangular plates at the top and bottom; in Figure 3.6 note the definition of the overlap h. Having shown that a structure in which the rigid plates have been replaced by cables, has the same equilibrium configuration as the original structure, but involves a smaller number of unknown cable forces, Sultan analyses this simpler problem.

The first step in the form-finding process is to identify a set of generalised coordinates which describes the configuration of this structure. The 18 coordinates chosen by Sultan [159] for the two-stage mast are

- for each strut, the azimuth angle α_j, i.e. the angle between the vertical plane containing the strut and the x–z plane, and the colatitude δ_j, i.e. the angle between the strut and the z-axis, and
- three translation and three rotation parameters defining the position and orientation of the rigid plate at the top with respect to the bottom plate.

By using symbolic manipulation software, e.g. Maple or Mathematica, the length of each cable can be expressed in terms of the 18 coordinates and then differentiated to obtain the 18×18 matrix $\mathbf{A}$, in symbolic form. At this stage, the final shape of the structure is still unknown and the existence of a prestressable configuration is dependent on finding a suitable set of strut lengths. Sultan [159] reduces the number of

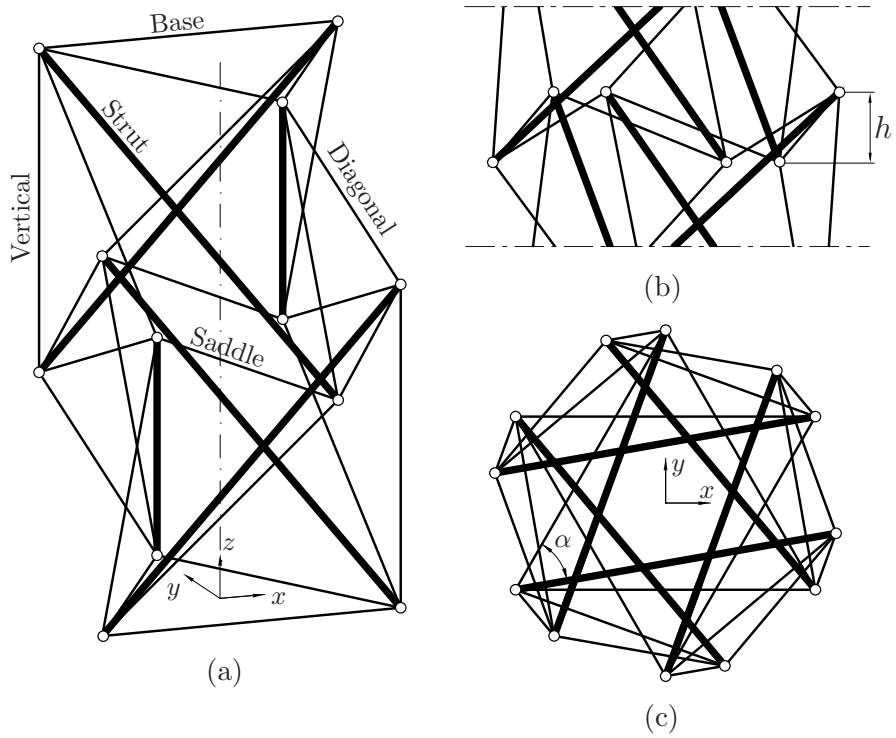

Figure 3.6: Sultan and Skelton's two stage tensegrity tower: (a) three-dimensional view, (b) side view, and (c) top view.

independent generalised coordinates by considering only symmetric configurations, with the same azimuth, α, and colatitude, δ, and by considering a fixed position of the top plate. Then, by assuming a special symmetry in $\mathbf{t}$, the problem could be reduced even further, to 3×3 with the forces in the diagonal, saddle and vertical cables remaining as the only unknowns. Finally, applying to this reduced matrix the condition for the existence of non-trivial solutions, rank $\mathbf{A} = 2$ equivalent to

$$\det \mathbf{A} = 0, \tag{3.35}$$

yields a quadratic equation that could be solved for the overlap h:

$$h = \begin{cases} \dfrac{1}{2\tan\delta\cos\left(\alpha+\dfrac{\pi}{6}\right)}\left(\sqrt{\dfrac{a^2}{3} - 3l^2\sin^2\delta\cos^2\left(\alpha+\dfrac{\pi}{6}\right)}\right. & \\ \left. -\dfrac{a}{\sqrt{3}} + l\sin\delta\cos\left(\alpha+\dfrac{\pi}{6}\right)\right) & \text{if } \alpha \neq \dfrac{\pi}{3}, \\ \dfrac{l\cos\delta}{2} & \text{if } \alpha = \dfrac{\pi}{3}. \end{cases} \tag{3.36}$$

Here, a is the side length of the equilateral triangles at the top and bottom of the mast, and l the length of each strut. A particular symmetric configuration, in which all the nodes lie on the surface of a cylinder, is defined by the following relationship between δ and α:

$$\delta = \arcsin\left[\frac{2a}{l\sqrt{3}}\sin\left(\alpha+\frac{\pi}{3}\right)\right]. \tag{3.37}$$

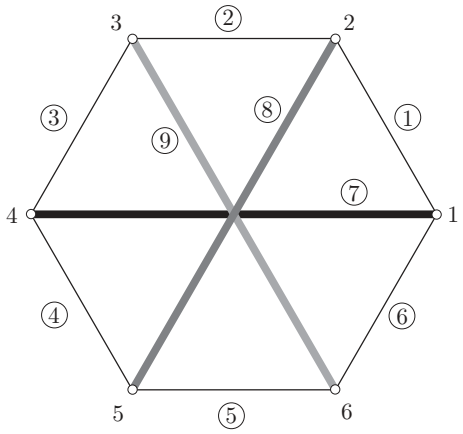

Figure 3.7: Two-dimensional hexagonal tensegrity.

For masts with more than two stages, $\mathbf{A}$ was derived using symbolic software, but (3.35) was then solved numerically. Sultan [159] successfully applied this form-finding method to masts with up to nine stages.

3.4 Implementation of the Force Density Method

The force density method has been outlined in section 3.3.2. This section will deal with procedures to actually find super-stable tensegrities, i.e. with positive semi-definite matrix $\overline{\mathbf{D}}$ with nullity $\mathcal{N} = \mathcal{D} + 1$. Vassart and Motro [177] list three techniques for finding a set of force densities that achieve the required nullity: (i) intuitive, (ii) iterative and (iii) analytical.

Of these three techniques, the first is suitable for systems with only a few members, and will be illustrated in section 3.4.1; the second technique is based on a trial-and-error, or more refined search for a set of force densities that yield the required nullity. The third technique is the most effective; $\overline{\mathbf{D}}$ is analysed in symbolic or semi-symbolic form, in the case of systems with a large number of elements [177]. The following examples show how this is done in practice, for structures of increasing complexity.

3.4.1 A Two-Dimensional Example

Consider the hexagonal tensegrity shown in Figure 3.7. For it to be super stable, the nullity of $\overline{\mathbf{D}}$ has to be three, but it is interesting to consider also the cases $\mathcal{N} = 1,\ 2$ to better understand why in section 3.3.3 it was stated that one must look for sets of force densities that make rank $\overline{\mathbf{D}} = n - \mathcal{D} - 1$.

Case $\mathcal{N} = 1$
Most sets of force densities yield a $\overline{\mathbf{D}}$ matrix with nullity one. For example, the

arbitrary set $\mathbf{q}_1 = (1 \;\; 2 \;\; 3 \;\; 4 \;\; 5 \;\; 6 \;\; -7 \;\; -8 \;\; -9)^{\mathrm{T}}$ produces

$$\overline{\mathbf{D}}_1 = \begin{bmatrix} 0 & -1 & 0 & 7 & 0 & -6 \\ -1 & -5 & -2 & 0 & 8 & 0 \\ 0 & -2 & -4 & -3 & 0 & 9 \\ 7 & 0 & -3 & 0 & -4 & 0 \\ 0 & 8 & 0 & -4 & 1 & -5 \\ -6 & 0 & 9 & 0 & -5 & 2 \end{bmatrix}. \tag{3.38}$$

The nullspace of $\overline{\mathbf{D}}_1$ is spanned by $(1 \;\; 1 \;\; 1 \;\; 1 \;\; 1 \;\; 1)^{\mathrm{T}}$—see reference [156] for further details on how to compute a basis for a nullspace—which, through (3.19) and the analogous equation in the y-coordinates, give the configuration $\mathbf{x} = (x_1 \;\; \ldots \;\; x_6)^{\mathrm{T}} = (\alpha \;\; \alpha \;\; \alpha \;\; \alpha \;\; \alpha \;\; \alpha)^{\mathrm{T}}$ and $\mathbf{y} = (y_1 \;\; \ldots \;\; y_6)^{\mathrm{T}} = (\beta \;\; \beta \;\; \beta \;\; \beta \;\; \beta \;\; \beta)^{\mathrm{T}}$. Here, α and β can take arbitrary values. This solution corresponds to configurations of the structure where all the nodes coincide and so the whole structure is reduced to a single point, which is of little practical interest.

Case $\mathcal{N} = 2$
Next, uniform force densities in all cable elements and in *two* of the struts force densities of half those in the cables were prescribed; the force density in the third cable was arbitrary. For example, for $\mathbf{q}_2 = (2 \;\; 2 \;\; 2 \;\; 2 \;\; 2 \;\; 2 \;\; -1 \;\; -1 \;\; -3)^{\mathrm{T}}$

$$\overline{\mathbf{D}}_2 = \begin{bmatrix} 3 & -2 & 0 & 1 & 0 & -2 \\ -2 & 3 & -2 & 0 & 1 & 0 \\ 0 & -2 & 1 & -2 & 0 & 3 \\ 1 & 0 & -2 & 3 & -2 & 0 \\ 0 & 1 & 0 & -2 & 3 & -2 \\ -2 & 0 & 3 & 0 & -2 & 1 \end{bmatrix}. \tag{3.39}$$

It can be readily verified that columns five and six are *dependent*, and hence that the nullspace of $\overline{\mathbf{D}}_2$ is spanned by $(-1 \;\; -1 \;\; 0 \;\; 1 \;\; 1 \;\; 0)^{\mathrm{T}}$ and $(2 \;\; 2 \;\; 1 \;\; 0 \;\; 0 \;\; 1)^{\mathrm{T}}$. Hence, denoting by α, β the x-coordinates of nodes 5, 6 respectively, and by γ, δ their y-coordinates, the configuration of the system is described by $\mathbf{x} = (-\alpha + 2\beta \;\; -\alpha + 2\beta \;\; \beta \;\; \alpha \;\; \alpha \;\; \beta)^{\mathrm{T}}$ and $\mathbf{y} = (-\gamma + 2\delta \;\; -\gamma + 2\delta \;\; \delta \;\; \gamma \;\; \gamma \;\; \delta)^{\mathrm{T}}$. This configuration corresponds to all nodes lying on a straight line, as shown in Figure 3.8(a), and is again of little practical interest.

Case $\mathcal{N} = 3$
Finally, *uniform force densities* both in the cable elements and in the struts, in a ratio of two to one, were prescribed. For example, $\mathbf{q}_3 = (2 \;\; 2 \;\; 2 \;\; 2 \;\; 2 \;\; 2 \;\; -1 \;\; -1 \;\; -1)^{\mathrm{T}}$ yields

$$\overline{\mathbf{D}}_3 = \begin{bmatrix} 3 & -2 & 0 & 1 & 0 & -2 \\ -2 & 3 & -2 & 0 & 1 & 0 \\ 0 & -2 & 3 & -2 & 0 & 1 \\ 1 & 0 & -2 & 3 & -2 & 0 \\ 0 & 1 & 0 & -2 & 3 & -2 \\ -2 & 0 & 1 & 0 & -2 & 3 \end{bmatrix}. \tag{3.40}$$

Here, columns four, five and six are dependent, hence the nullspace of $\overline{\mathbf{D}}_3$ is spanned by $(1 \;\; 2 \;\; 2 \;\; 1 \;\; 0 \;\; 0)^{\mathrm{T}}$, $(-2 \;\; -3 \;\; -2 \;\; 0 \;\; 1 \;\; 0)^{\mathrm{T}}$, and $(2 \;\; 2 \;\; 1 \;\; 0 \;\; 0 \;\; 1)^{\mathrm{T}}$. Denoting

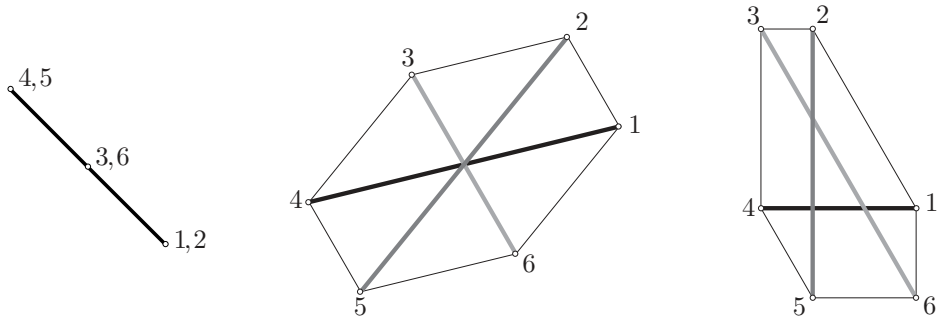

(a) $\mathcal{N} = 2$ (b) $\mathcal{N} = 3$ (c) $\mathcal{N} = 3$

Figure 3.8: Configurations of two-dimensional hexagonal tensegrities.

by α, β, γ the free x-coordinates of nodes 4, 5, 6, respectively, and δ, ϵ, ζ their y-coordinates, the system configuration is given by $\mathbf{x} = (\alpha - 2\beta + 2\gamma \;\; 2\alpha - 3\beta + 2\gamma \;\; 2\alpha - 2\beta + \gamma \;\; \alpha \;\; \beta \;\; \gamma)^{\mathrm{T}}$ and $\mathbf{y} = (\delta - 2\epsilon + 2\zeta \;\; 2\delta - 3\epsilon + 2\zeta \;\; 2\delta - 2\epsilon + \zeta \;\; \delta \;\; \epsilon \;\; \zeta)^{\mathrm{T}}$.

The original solution in Figure 3.7 is re-obtained for $\alpha = -1$, $\beta = -1/2$, $\gamma = 1/2$, $\delta = 0$, $\epsilon = -\sqrt{3}/2$, and $\zeta = -\sqrt{3}/2$. However, note that, despite the force densities $\mathbf{q}_3$ being symmetric, this solution also produces the configuration shown in Figure 3.8(b), which has only two-fold symmetry, for $\alpha = -1$, $\beta = -1/2$, $\gamma = 1$, $\delta = 0$, $\epsilon = -\sqrt{3}/2$, and $\zeta = -1/2$. The reason why it is possible to find less symmetric or even asymmetric configurations for a given, symmetric state of force densities is because the element lengths are not explicitly set in the force density formulation.

In concluding, it is noted that the particular $\mathbf{q}_3$ considered above was obtained after noticing that in the configurations shown in Figure 3.7 the force densities must have a particular distribution, to satisfy nodal equilibrium. However, by carrying out a symbolic analysis of the force density matrix other solutions were subsequently found. For example, an alternative choice was $\mathbf{q}_4 = (1 \;\; 2 \;\; 1 \;\; 2 \;\; 1 \;\; 2 \;\; -2/3 \;\; -2/3 \;\; -2/3)^{\mathrm{T}}$, for which a particular configuration (with α, β, etc. as in the original configuration) is that shown in Figure 3.8(c).

3.4.2 Tensegrity Prisms

Consider a structure with the topology shown in Figure 3.9. A set of force densities with three-fold symmetry is prescribed as follows. The force densities in the cable forming the bottom and top triangles are q_b and q_t, respectively; they are q_l in the lateral cables and q_s in the struts. Assuming that the top and bottom triangles are parallel, equilibrium perpendicular to the planes of the triangles gives $q_s = -q_l$, cf. (3.10).

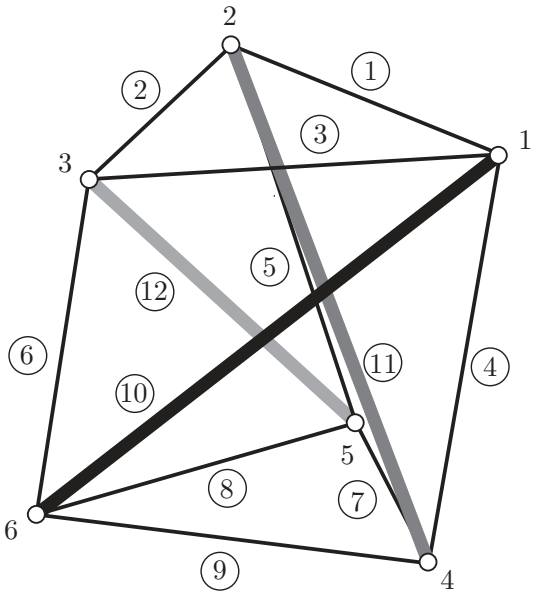

Figure 3.9: Tensegrity prism.

Hence, the $\overline{\mathbf{D}}$ matrix can be set up in terms of only three force densities

$$\overline{\mathbf{D}} = \begin{bmatrix} 2q_t & -q_t & -q_t & -q_l & 0 & q_l \\ -q_t & 2q_t & -q_t & q_l & -q_l & 0 \\ -q_t & -q_t & 2q_t & 0 & q_l & -q_l \\ -q_l & q_l & 0 & 2q_b & -q_b & -q_b \\ 0 & -q_l & q_l & -q_b & 2q_b & -q_b \\ q_l & 0 & -q_l & -q_b & -q_b & 2q_b \end{bmatrix}. \tag{3.41}$$

By Gaussian elimination $\overline{\mathbf{D}}$ is reduced to the upper echelon form [156]

$$\mathbf{U} = \begin{bmatrix} q_l & 0 & -q_l & -q_b & -q_b & 2q_b \\ 0 & q_l & -q_l & q_b & -2q_b & q_b \\ 0 & 0 & 0 & -q^* & 0 & q^* \\ 0 & 0 & 0 & 0 & q^* & -q^* \\ 0 & 0 & 0 & 0 & 0 & 0 \\ 0 & 0 & 0 & 0 & 0 & 0 \end{bmatrix}, \tag{3.42}$$

where $q^* = (q_l^2 - 3q_bq_t)/q_l$. Since $q_l \neq 0$, rank $\overline{\mathbf{D}}$ is either four, if $q^* \neq 0$, or two, if $q^* = 0$. If super stability is required, then $\mathcal{N} = 4$, i.e. rank $\overline{\mathbf{D}} = 2$ and so $q^* = 0$.

Any set of positive cable force densities that satisfies the condition

$$q_l^2 - 3q_bq_t = 0 \tag{3.43}$$

is possible, but Vassart [175] presents two interesting cases: (i) $q_t = q_b$ and (ii) $q_t = q_l$. In both cases, the last four coordinates can take arbitrary values; denoting those x-coordinates, for example, by α, β, γ, δ, in case (i) the configuration of the structure is described by $\mathbf{x} = (\alpha+(\beta+\gamma-2\delta)/\sqrt{3}\ \ \alpha+(-\beta+2\gamma-\delta)/\sqrt{3}\ \ \alpha\ \ \beta\ \ \gamma\ \ \delta)^{\mathrm{T}}$, similarly for y and z. In case (ii) the configuration of the structure is described by

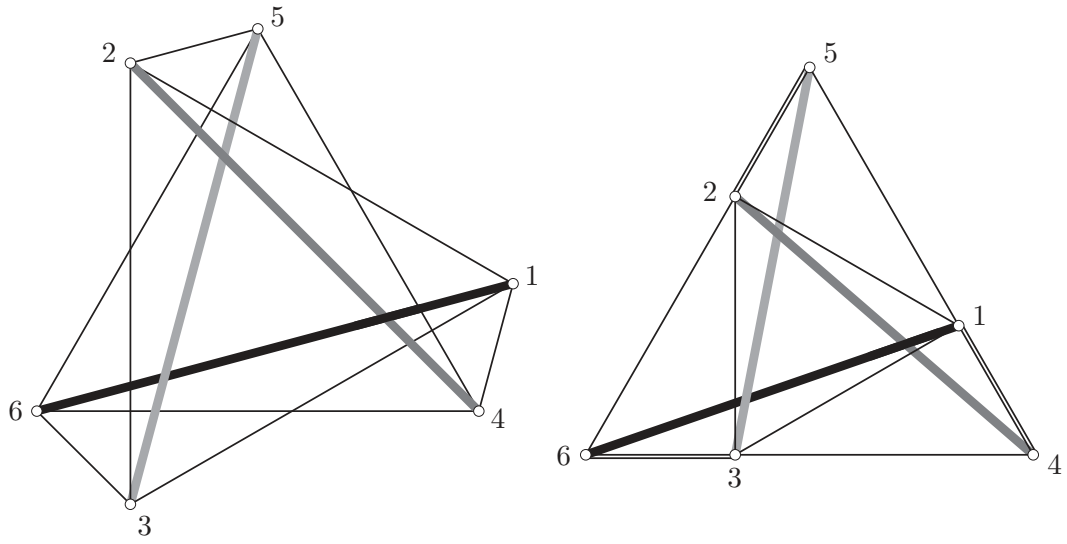

(a) $q_t = q_b$, $q_l = \sqrt{3}q_b$, and $q_s = -q_l$ (b) $q_t = q_l$, $q_b = q_l/3$, and $q_s = -q_l$

Figure 3.10: Top views of two different rotationally symmetric tensegrity prisms

$\mathbf{x} = (\alpha + (\beta + \gamma - 2\delta)/3 \quad \alpha + (-\beta + 2\gamma - \delta)/3 \quad \alpha \quad \beta \quad \gamma \quad \delta)^{\mathrm{T}}$. The rotationally symmetric configurations, obtained by giving appropriate values to α, etc. are shown in Figure 3.10.

Changing the relationship between q_t and q_b while keeping q_l fixed, changes the relative sizes of the top and bottom triangles. Again, many geometrically non-symmetric configurations may be found by appropriate choices of the free nodes.

3.4.3 Spherical Tensegrities

The earlier part of this section has shown applications of the force density method to the form-finding of some relatively straightforward tensegrity structures; several symmetric configurations that had already been found by other methods were thus re-obtained. Further applications of the same method, to slightly more complex systems will be presented next.

Expandable octahedron
For the expandable octahedron, Figure 3.2, there is only one type of cable and one type of strut. Earlier analysis, cf. [70], has shown that the distance between parallel struts is half the length of the strut, equilibrium in the strut direction yields $q_s = -3q_c/2$. An analysis of $\overline{\mathbf{D}}$ produces two possible solutions for $\mathcal{N} = 4$: $q_s = -3q_c/2$ and $q_s = -2q_c$, but $\overline{\mathbf{D}}$ is positive semi-definite only for the first one. In addition to the symmetric configuration of Figure 3.2, many asymmetric configurations can be found.

Truncated tetrahedron
An equilibrium configuration for the truncated tetrahedron, Figure 3.1, was found

in reference [121]. For that configuration, the single state of self-stress was computed by the force method described in section 3.5. For a force of 1 in the cable elements forming the triangle faces, there is a force of 1.3795 in the remaining cables, and −1.5016 in the struts. Since the strut and cable lengths are 2.2507 and 1, respectively, the corresponding force densities are 1, 1.3795 and −0.6672.

As shown in Figure 3.1, the nodes of the truncated tetrahedron lie in four different horizontal planes. An independent form-finding study showed that, unlike the structures analysed so far, no relationships between the force densities could be obtained from equilibrium statements without considering the geometric symmetry conditions. Hence, the general state of self-stress is characterised by three different force density values: q_t for cables forming the triangles, q_l for the other cables, and q_s for the struts.

By setting $q_l = \gamma q_t$, and after carrying out a Gaussian elimination on the matrix $\overline{\mathbf{D}}$, the condition for $\mathcal{N} = 4$ was found to be

$$2\left(1+\gamma\right)\left(\frac{q_s}{q_t}\right)^2 + \left[3+2\gamma\left(3+\gamma\right)\right]\frac{q_s}{q_t} + \gamma\left(3+2\gamma\right) = 0. \tag{3.44}$$

To re-obtain the earlier results $\gamma = 1.3795$ and thus $q_s/q_t = -0.6672$, and also a second solution $q_s/q_t = -2.5022$. However, for that solution the $\overline{\mathbf{D}}$ matrix has negative eigenvalues, and hence the corresponding configurations are unstable.

For different values of γ, e.g. $\gamma = 1$ as in reference [24], different configurations, with unequal cable lengths, of the truncated tetrahedron were obtained. However, it was difficult to specify the ratio γ to find a configuration with a particular ratio between the lengths of the cables. Therefore, it is concluded that the force density method is an excellent method for finding the configuration of new tensegrities, but less than ideal for structures with some known, or desired element lengths.

To complete the form-finding of spherical tensegrities it should be mentioned that Nishimura [117] uses the force method together with group theory to find the initial equilibrium configurations of such structures. This method resembles the approach used by Connelly and Back [24]. With Nishimura's contribution, the form-finding of tensegrities corresponding to the truncated versions of the following regular polyhedra: tetrahedron, octahedron, cube, icosahedron, and dodecahedron, is finally solved analytically. In the case of the truncated tetrahedron, the condition for a non-trivial self-stress is [117]

$$\begin{aligned} 4\kappa^2\left[\cos\alpha + 4\cos\alpha\left(1+\cos^2\alpha\right) + 4\sqrt{3}\sin\alpha\left(\cos\alpha - 1\right)\right] \\ - 12\kappa\left(\cos^2\alpha + \cos\alpha\left(\sqrt{3}\sin\alpha + 2\right) - 2\sqrt{3}\sin\alpha\right) \\ + 9\left(\cos\alpha - \sqrt{3}\sin\alpha\right) = 0, \end{aligned} \tag{3.45}$$

where κ is the ratio of the side length of the truncating tetrahedron and the side length of the original tetrahedron, a, and α is the angle of rotation of the triangles with respect to an inertial system xyz. Nishimura [117] notes that as $\kappa \to 0$,

$\alpha \to \pi/6$, and as $\kappa \to 1/2$, $\alpha \to 0$. The lengths of the cables forming the truncating triangles, the cables connecting the triangles, and the struts are

$$l_t = \kappa a, \tag{3.46}$$

$$l_l = \frac{a}{3}\sqrt{9 + 24\kappa(\kappa - 1) - 4\kappa\left[(3 - 4\kappa)\cos\alpha + \kappa\cos 2\alpha\right]}, \tag{3.47}$$

$$l_s = \frac{a}{\sqrt{18}}\sqrt{9 + \left[3 - 4\kappa - 2\kappa\left(\cos\alpha - \sqrt{3}\sin\alpha\right)\right]^2}, \tag{3.48}$$

respectively. The specific case where the lengths of the cables are equal is considered. Simultaneously solving (3.46)–(3.48) for a, κ, and α subject to $l_l = l_t = 1$ yields $a = 2.9873$, $\kappa = 0.3348$, and $\alpha = 0.1127$. Substituting these value into (3.48) yields the strut length $l_s = 2.256274$. This value is very close to 2.2507, found by Pellegrino [121]. The state self-stress of the truncated tetrahedron, expressed in terms of force densities, is

$$q_t = -q_s\frac{3 - 4\kappa\,(1 - \cos\alpha)}{6\kappa\cos\alpha}, \tag{3.49}$$

$$q_l = -q_s\frac{\left(\cos\alpha + \sqrt{3}\sin\alpha\right)\left[3 - 4\kappa\,(1 - \cos\alpha)\right]}{\cos\alpha\left[6 - 4\kappa\left(2 + \cos\alpha + \sqrt{3}\sin\alpha\right)\right]}. \tag{3.50}$$

Inserting the present values into (3.49) and (3.50) gives $q_l/q_t = 1.379421$ and $q_s/q_t = -0.667142$, again in accordance with the previous analysis.

3.5 The Force Method for Analysis of Bar Frameworks

Once the prestress stable form of the tensegrity structure has been found its kinematic and static properties are sought. As described in Chapter 1, a framework of pin-jointed bars, with three degrees of freedom at each joint, can be completely characterised by the extended Maxwell's rule, (1.2). Three of the five parameters, the number of bars, joints and kinematic constraints, are prescribed but the other two, the number of self-stress states and internal mechanisms, depend on the geometrical configuration of the framework.

A method to investigate the properties of a general framework of pin-jointed bars is developed by Pellegrino and Calladine in a series of articles [14–16, 122, 124, 127]. The method, which is now known as the force method, is first described in [127]. Kuznetsov [74] found that the method, as presented, was incomplete as it failed to correctly analyse relatively simple frameworks. It included the matrix rank conditions that are necessary, but not sufficient, for prestress stability; the basic positive definitiveness conditions, however, were missing. Following the criticism, a refined version of the method was presented in [15]. Kuznetsov [75] came up with what looked as a counterexample to the improved method, but the questions around that were finally resolved in [16]. In reference [127], the computational scheme to find the

number of self-stress states and mechanisms was based on Gaussian elimination, but such a scheme will have problems with ill-conditioned equilibrium matrices. Pellegrino [124] presents a scheme based on the *Singular Value Decomposition* (SVD) of the equilibrium matrix. The SVD scheme is computationally more expensive than the Gaussian elimination scheme, but has several advantages which will be explained later.

Another method of analysing the properties of bar frameworks is presented by Kuznetsov in [76], based on a series of articles by him over the past three decades. In comparison, the method does not lend itself to efficient numerical analysis as well as the previous one. Therefore, the previous method seems more advantageous, because what really is needed in the static and kinematic analysis of very large frameworks, involving several hundred elements, is a robust and efficient numerical method. In the next five sections the method by Pellegrino and Calladine [14–16, 122, 124, 127] is described.

3.5.1 Equilibrium and Compatibility Matrices

Consider a three-dimensional pin-jointed bar framework with j joints and b bars acted upon by external forces at the joints. The framework is in its deployed state and restrained in the three-dimensional space by c kinematic constraints. If the structural deformations under the external loads are small, a linear analysis is sufficient. The set of equilibrium equations for the framework is written as

$$\mathbf{Ht} = \mathbf{f}, \tag{3.51}$$

where $\mathbf{H}$ is the $3j - c \times b$ equilibrium matrix containing the direction cosines, in the x, y and z directions, of each element, $\mathbf{t}$ is the internal force vector of length b, and $\mathbf{f}$ is the external force vector of length $3j - c$. The external forces give rise to displacements which must be compatible with the elongations of the bars. The set of linear compatibility equations is

$$\mathbf{Cd} = \mathbf{e} \tag{3.52}$$

where $\mathbf{C}$ is the $b \times 3j - c$ compatibility matrix, $\mathbf{d}$ is the joint displacement vector of length $3j - c$, and $\mathbf{e}$ is the bar elongation vector of length b. The work done by the external loads is $\frac{1}{2}\mathbf{f}^{\mathrm{T}}\mathbf{d}$ and the strain energy stored in the framework is $\frac{1}{2}\mathbf{t}^{\mathrm{T}}\mathbf{e}$. Equating the external work and strain energy yields

$$\mathbf{H}^{\mathrm{T}} = \mathbf{C}. \tag{3.53}$$

Equation (3.53) expresses the static–kinematic duality of bar frameworks [124, 155].

3.5.2 Static and Kinematic Properties

The equilibrium and compatibility matrices contain essential information about the framework. Well-known in the linear-algebraic treatment of matrices are the four

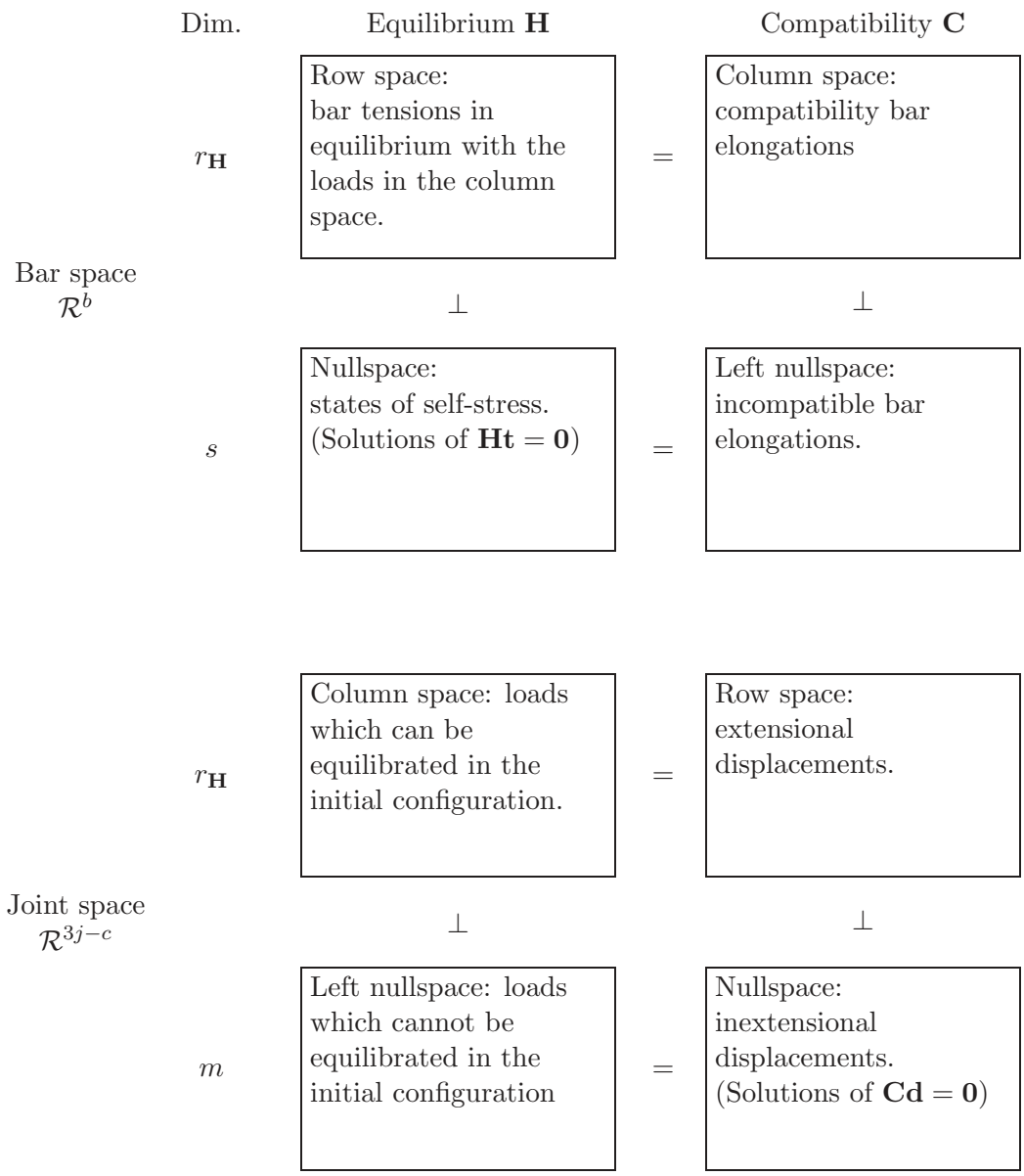

Figure 3.11: The four fundamental subspaces associated with **H** and **C** [122].

vector subspaces. The physical significance of the four vector subspaces associated with **H** and **C** are briefly explained in Figure 3.11; for further information on subspaces see [156]. The standard way to find the bases for the four subspaces is through Gaussian elimination. Another approach, suggested by Pellegrino [124], is the SVD, in which the equilibrium matrix **H** is factorised as

$$\mathbf{H} = \mathbf{U}\mathbf{\Sigma}\mathbf{W}^{\mathrm{T}}, \tag{3.54}$$

where **U** is a $3j - c \times 3j - c$ orthogonal matrix, **W** is a $b \times b$ orthogonal matrix, and $\mathbf{\Sigma}$ is a $3j - c \times b$ matrix with $r_{\mathbf{H}}$ positive elements σ_{ii} $(i = 1,\ ...,\ r_{\mathbf{H}})$ on the leading diagonal and all other elements zero. The coefficients of $\mathbf{\Sigma}$ are the singular values of **H**, which are the square roots of the eigenvalues of $\mathbf{H}\mathbf{H}^{\mathrm{T}}$ and $\mathbf{H}^{\mathrm{T}}\mathbf{H}$. The rank $r_{\mathbf{H}}$ of the equilibrium matrix **H** is the number of non-zero diagonal elements in $\mathbf{\Sigma}$, cf. the number of pivots after a Gaussian elimination of **H**. In practice, the diagonal of

Table 3.2: Classification of structural assemblies.

Assembly type	Static and kinematic properties
I	$s = 0$ $m = 0$ Statically determinate and kinematically determinate
II	$s = 0$ $m > 0$ Statically determinate and kinematically indeterminate
III	$s > 0$ $m = 0$ Statically indeterminate and kinematically determinate
IV	$s > 0$ $m > 0$ Statically indeterminate and kinematically indeterminate

$\mathbf{\Sigma}$ often contains up to $\min(3j - c, b)$ singular values of decreasing magnitude; none of these values are actually equal to zero, but some are much smaller than others. Values smaller than a set tolerance have to be treated as zero. Pellegrino [124] sets the tolerance to $10^{-3} \cdot \sigma_{11}$ for most structural assemblies, but notes that a lower tolerance may be required near critical points where the rank of the equilibrium matrix drops. A wide gap in an otherwise continuous range of singular values is another sign to look for. Once $r_{\mathbf{H}}$ has been decided the number of self-stress states and mechanisms are

$$s = b - r_{\mathbf{H}} \tag{3.55}$$

and

$$m = 3j - c - r_{\mathbf{H}}. \tag{3.56}$$

A basis $\mathbf{S}$ for the states of self-stress is given by the last s columns of $\mathbf{W}$,

$$\mathbf{S} = \begin{bmatrix} \mathbf{w}_{r_{\mathbf{H}}+1} & \dots & \mathbf{w}_b \end{bmatrix}. \tag{3.57}$$

Similarly, a basis $\mathbf{D}$ for the mechanisms is given by the last m columns of $\mathbf{U}$,

$$\mathbf{D} = \begin{bmatrix} \mathbf{u}_{r_{\mathbf{H}}+1} & \dots & \mathbf{u}_{3j-c} \end{bmatrix}. \tag{3.58}$$

Pellegrino [122] classify structural assemblies into four groups depending on their degree of static and kinematic indeterminacy, Table 3.2. What matters in the classification is only if s or m is zero or not.

3.5.3 Rigid-Body Mechanisms

The mechanisms in $\mathbf{D}$ can either be internal mechanisms or rigid-body mechanisms, arising from inadequate kinematic restraints of the structure. These two types of mechanisms are fundamentally different but the SVD algorithm makes no distinction between them. In a case when the structure is not fully restrained, $\mathbf{D}$ generally contains combinations of the two mechanism types. It is therefore not possible to just pick out the rigid-body mechanisms from $\mathbf{D}$. A scheme to separate the internal

mechanisms from the rigid-body ones was proposed by Pellegrino [121, 127]. It can cope with up to six rigid-body mechanisms.

Any rigid-body displacement in three-dimensional space may be described by a translation $\mathbf{n}$ and a rotation $\mathbf{r}$, where

$$\mathbf{n} = \begin{pmatrix} n_x & n_y & n_z \end{pmatrix}^{\mathrm{T}}, \tag{3.59a}$$

$$\mathbf{r} = \begin{pmatrix} r_x & r_y & r_z \end{pmatrix}^{\mathrm{T}}. \tag{3.59b}$$

The displacement $\mathbf{d}_i$ of a point i in such a rigid-body motion is given by

$$\mathbf{d}_i = \mathbf{n} + \mathbf{r} \times \mathbf{p}_i, \tag{3.60}$$

where $\mathbf{p}_i$ is the position vector of point i in the original configuration. If the structure has a total of c constrained degrees of freedom, the system of c equations in six unknowns is

$$\mathbf{R} \begin{pmatrix} \mathbf{n} \\ \mathbf{r} \end{pmatrix} = \mathbf{0}, \tag{3.61}$$

where $\mathbf{R}$ has size $c \times 6$. The rank $r_{\mathbf{R}}$ of $\mathbf{R}$ counts how many of the c kinematic constraints that suppress the rigid-body degrees of freedom. Thus, the number of rigid-body mechanisms is

$$m_{\mathrm{rb}} = 6 - r_{\mathbf{R}}. \tag{3.62}$$

A basis for the nullspace of $\mathbf{R}$ is an independent set of m_{rb} rigid-body motions in terms of $\mathbf{n}$ and $\mathbf{r}$. The corresponding set of rigid-body mechanisms to those motions is found by (3.60). A matrix $\mathbf{D}_{\mathrm{rb}}$ of size $m_{\mathrm{rb}} \times 3j - c$ containing the rigid-body mechanisms is formed. Now each of the rigid-body mechanisms of $\mathbf{D}_{\mathrm{rb}}$ has to be removed from each column of $\mathbf{D}$. This is done by the Gram-Schmidt orthogonalisation procedure [156]: for each mechanism $\mathbf{d}_j$ ($j = 1,\ ...,\ m$) each independent rigid-body mechanisms $\mathbf{d}_{\mathrm{rb},k}$ ($k = 1,\ ...,\ m_{\mathrm{rb}}$) is removed by use of the formula

$$\mathbf{d}_j := \mathbf{d}_j - \sum_{k=1}^{m_{\mathrm{rb}}} \frac{\mathbf{d}_{\mathrm{rb},k}^{\mathrm{T}} \mathbf{d}_j}{\mathbf{d}_{\mathrm{rb},k}^{\mathrm{T}} \mathbf{d}_{\mathrm{rb},k}} \mathbf{d}_{\mathrm{rb},k}. \tag{3.63}$$

$\mathbf{D}$ is now transformed into a set of internal mechanisms, but only $m - m_{\mathrm{rb}}$ of them are independent. A subsequent Gaussian elimination step can be used to remove those dependent on others [121].

When dealing with complex frameworks it is important to be able to differentiate between rigid-body mechanisms and internal mechanisms. However, the main aim here is to efficiently restrain any structure so that $\mathbf{D}$ does not contain any rigid-body motions.

3.5.4 Internal Mechanisms

Once the structure has been adequately fixed, the remaining mechanisms are only the internal ones. Physically, there are two types of internal mechanisms: *infinitesimal* and *finite*. In a finite mechanism the joints can move with no change in lengths of

the bars, while in an infinitesimal mechanism there are some small length changes of the bars when the joints move. In terms of displacements, this change in length is, generally, of second or higher order. Hence, infinitesimal mechanisms tighten up when activated, as shown in the simple example in section 1.3. Also shown in that example was that a state of self-stress gave the assembly a positive first-order stiffness. If a state of self-stress can impart positive first-order stiffness to every mechanism of a structure, then the mechanisms are *first-order infinitesimal*. Such infinitesimal mechanisms are associated with second-order changes of bar lengths. However, mechanisms which cannot be stabilised by a state of self-stress are of second or higher order or are finite. Thus, if an assembly has some mechanisms they must be first-order infinitesimal to ensure the stability of the structure.

Despite the stability issues related to second- and higher-order mechanisms, they have been given some attention; Connelly and Servatius [25] discuss the various definitions of order of rigidity and mechanisms in literature and redefine higher-order rigidity. Vassart *et al.* [176] present an analytical method in two steps, i.e. geometry and energy characterisation, which can determine the order of the mechanisms and identify finite mechanisms. Now if the only objective is to determine if the mechanisms are first-order infinitesimal or not there is a better approach proposed by Calladine and Pellegrino [15, 122]. For each state of self-stress $\mathbf{t}_i$ and each mechanism $\mathbf{d}_j$ a vector of geometric loads $\mathbf{g}_{ij}$ can be computed as

$$\mathbf{g}_{ij} = \mathbf{B}_{\mathbf{d}_j}\mathbf{t}_i, \tag{3.64}$$

where $\mathbf{B}_{\mathbf{d}_j}$ is similar to the equilibrium matrix $\mathbf{H}$ but with coefficients of type $(d^j_{kx} - d^j_{lx})/l_{kl}$ instead of $(x_k - x_l)/l_{kl}$, i.e. displacements of mechanism j instead of nodal coordinates. The m geometric loads for self-stress state i form the columns of the geometric load matrix $\mathbf{G}_i$ of size $3j - c \times m$. Each state of self-stress has its own matrix $\mathbf{G}$. For assemblies with $s = 1$ and $m > 0$, the test for first-order mechanisms is to check that the symmetric matrix $\mathbf{G}^{\mathrm{T}}\mathbf{D}$ is positive or negative definite. A negative definite $\mathbf{G}^{\mathrm{T}}\mathbf{D}$ corresponds to a self-stress $-\mathbf{t}$. For assemblies with $s > 1$, the test becomes slightly more complicated as a linear combination of all matrices $\mathbf{G}^{\mathrm{T}}\mathbf{D}$, each corresponding to a self-stress state, which is positive definite has to be found. For simple problems this can be done symbolically, but for larger problems, an automatic numerical routine is required. Such a routine is presented by Calladine and Pellegrino [15]. However, they later found a certain framework with two states of self-stress and two internal mechanisms, one of first-order and one of higher-order. This framework is classified as a first-order infinitesimal mechanisms but still cannot be stabilised by a state of self-stress [16].

At this point, the tools to completely classify a pin-jointed bar framework have been provided. What is left is to analyse the response of the framework to external loads. This is normally done by the *Finite Element Method* (FEM) but can, for certain frameworks, be done by the present method. In many cases this method gives more insight into the problem.

3.5.5 Structural Computations

Pellegrino [122,124] presents a method for computing the forces and displacements of a pin-jointed bar framework due to external loads. The assumptions of the method, as it is presented below, are that geometrical and material non-linearities can be neglected. Hence, the method is linear and relates to the initial configuration of the assembly, which in the case of a deployable structure is equal to the deployed one. This method has been found to be very accurate for assemblies of type II, Table 3.2. Assemblies of type IV, however, undergo significant increases of prestress during loading and deform less than predicted by the linear method. Nevertheless, the linear method is presented below with respect to a type IV assembly.

First, the force and displacement systems have to be connected: assuming linear-elastic material, the element forces $\mathbf{t}$ are related to the bar elongations $\mathbf{e}$ by the flexibility matrix $\mathbf{\Phi}$ as

$$\mathbf{e} = \mathbf{e}_0 + \mathbf{\Phi}\mathbf{t}, \tag{3.65}$$

where $\mathbf{e}_0$ is the vector of initial bar elongations. The $b \times b$ diagonal flexibility matrix $\mathbf{\Phi}$ has $\phi_i = l_i/A_iE_i$ as its entry of position (i, i).

Before starting the computations of the internal bar forces $\mathbf{t}$, the bar elongations $\mathbf{e}$, and the displacements $\mathbf{d}$ one has to check that the framework can carry the load $\mathbf{f}$; the external load $\mathbf{f}$ must be zero in the subspace of loads which cannot be equilibrated, cf. Figure 3.11:

$$\mathbf{D}^{\mathrm{T}}\mathbf{f} = \mathbf{0}. \tag{3.66}$$

If the framework passes this test, the general solution to (3.51) is

$$\mathbf{t} = \mathbf{t}_\mathbf{f} + \mathbf{S}\boldsymbol{\alpha}, \tag{3.67}$$

where $\mathbf{t}_\mathbf{f}$ contains the internal forces in equilibrium with the load $\mathbf{f}$ and $\boldsymbol{\alpha}$ is a vector of s free parameters. $\mathbf{t}_\mathbf{f}$ is efficiently computed as

$$\mathbf{t}_\mathbf{f} = \sum_{i=1}^{r_\mathbf{H}} \frac{\mathbf{u}_i^{\mathrm{T}}\mathbf{f}}{\sigma_{ii}}\mathbf{w}_i. \tag{3.68}$$

The value of $\boldsymbol{\alpha}$ is determined by the following compatibility condition

$$\mathbf{S}^{\mathrm{T}}\mathbf{e} = \mathbf{0}, \tag{3.69}$$

stating that the elongation $\mathbf{e}$ must vanish in the subspace of incompatible strains. Substituting (3.65) and (3.67) into (3.69) and solving for $\boldsymbol{\alpha}$ yields

$$\boldsymbol{\alpha} = -(\mathbf{S}^{\mathrm{T}}\mathbf{\Phi}\mathbf{S})^{-1}\mathbf{S}^{\mathrm{T}}(\mathbf{e}_0 + \mathbf{\Phi}\mathbf{t}_\mathbf{f}) \tag{3.70}$$

Finally, substituting $\boldsymbol{\alpha}$ into (3.67) gives the resulting internal forces $\mathbf{t}$.

In analogy with (3.67) the general solution to (3.52) is

$$\mathbf{d} = \mathbf{d}_\mathbf{e} + \mathbf{D}\boldsymbol{\beta}, \tag{3.71}$$

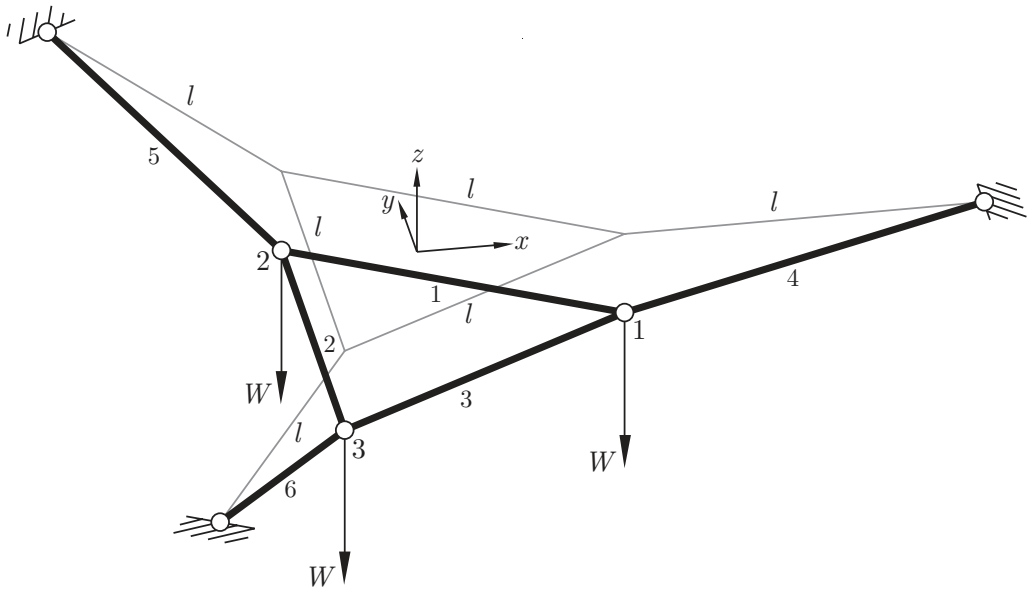

Figure 3.12: Hanging triangular net

where $\mathbf{d_e}$ is any vector of displacements compatible with $\mathbf{e}$ and $\boldsymbol{\beta}$ is a vector of m free parameters. Similarly to $\mathbf{t_f}$, $\mathbf{d_e}$ is computed as

$$\mathbf{d_e} = \sum_{i=1}^{r_\mathbf{H}} \frac{\mathbf{w}_i^\mathrm{T}\mathbf{e}}{\sigma_{ii}}\mathbf{u}_i. \tag{3.72}$$

Note that the term $\mathbf{D}\boldsymbol{\beta}$ in (3.71) represents a general inextensional displacement satisfying $\mathbf{Cd} = \mathbf{0}$. $\boldsymbol{\beta}$ is determined by the orthogonality between the matrix of geometric loads $\mathbf{G}$ and $\mathbf{d}$,

$$\mathbf{G}^\mathrm{T}\mathbf{d} = \mathbf{0}, \tag{3.73}$$

which is obtained from virtual work considerations. Substituting (3.71) into (3.73) and solving for $\boldsymbol{\beta}$ yields

$$\boldsymbol{\beta} = -(\mathbf{G}^\mathrm{T}\mathbf{D})^{-1}\mathbf{G}^\mathrm{T}\mathbf{d_e}. \tag{3.74}$$

Substituting $\boldsymbol{\beta}$ back into (3.71) gives the resulting joint displacements $\mathbf{d}$.

3.5.6 Example: Hanging Triangular Net

Consider the hanging triangular net in Figure 3.12 with six pin-jointed bars. Three nodes are fully fixed in space. The horizontal projections of the members all have equal length l and the middle triangle lies a distance $h = l/4$ beneath the plane of the supports. A weight W hangs in each of the unconstrained nodes. The set of equilibrium equations for the hanging net is written as:

$$\begin{bmatrix} \sqrt{3}/2 & 0 & \sqrt{3}/2 & -4/\sqrt{17} & 0 & 0 \\ -1/2 & 0 & 1/2 & 0 & 0 & 0 \\ 0 & 0 & 0 & -1/\sqrt{17} & 0 & 0 \\ -\sqrt{3}/2 & 0 & 0 & 0 & 2/\sqrt{17} & 0 \\ 1/2 & 1 & 0 & 0 & -2\sqrt{3}/\sqrt{17} & 0 \\ 0 & 0 & 0 & 0 & -1/\sqrt{17} & 0 \\ 0 & 0 & -\sqrt{3}/2 & 0 & 0 & 2/\sqrt{17} \\ 0 & -1 & -1/2 & 0 & 0 & 2\sqrt{3}/\sqrt{17} \\ 0 & 0 & 0 & 0 & 0 & -1/\sqrt{17} \end{bmatrix} \begin{pmatrix} t_1 \\ t_2 \\ t_3 \\ t_4 \\ t_5 \\ t_6 \end{pmatrix} = \begin{pmatrix} 0 \\ 0 \\ -W \\ 0 \\ 0 \\ -W \\ 0 \\ 0 \\ -W \end{pmatrix}, \tag{3.75}$$

where t_i is the tension force in bar i and the right hand side the external loads. An SVD of the equilibrium matrix gives $s = 0$ and $m = 3$, hence assembly type II. The mechanisms in $\mathbf{D}$ are orthogonal but not necessarily symmetric with respect to the geometry. To find the symmetric mechanisms a special approach is needed, cf. [69], but this will not be used here. The computation of the internal forces are straightforward as $\mathbf{S} = \mathbf{0}$; (3.68) gives

$$\mathbf{t} = W \begin{pmatrix} 2.31 & 2.31 & 2.31 & 4.12 & 4.12 & 4.12 \end{pmatrix}^{\mathrm{T}}. \tag{3.76}$$

Using $AE/W = 10^3$, (3.74) gives $\boldsymbol{\beta} \approx \mathbf{0}$ in the present numerical precision. Thus, the displacements of the assembly are due to extensional deformation only: the displacements are

$$\mathbf{d} = \frac{l}{10^3} \begin{pmatrix} 1.33 & 0 & -22.9 & -0.667 & 1.15 & -22.9 & -0.667 & -1.15 & -22.9 \end{pmatrix}^{\mathrm{T}}. \tag{3.77}$$

If the level of the triangular middle platform is set to zero, i.e. all bars lie in one plane, the numbers of self-stress states and mechanisms change to $s = 1$ and $m = 4$ using the recommend tolerance $10^{-3} \cdot \sigma_{11}$ for the small singular values. Figure 3.13 shows the variation of the two lowest singular values with the height h of the triangular platform. Theoretically, the assembly has a state of self-stress only for $h = 0$ but with the present tolerance for the singular values the range of prestressability is about $-0.01 < h/l < 0.01$. It appear that a lower tolerance must be used if the geometry has to be accurately determined. This need to be considered when analysing the tensegrities in the following chapters.

3.6 Discussion

Seven form-finding methods for tensegrity structures have been reviewed and classified into two categories. The first category contains kinematic methods, which determine the configuration of either maximal length of the struts or minimal length of the cable elements, while the length of the other type of element is not allowed to vary. The second category contains static methods, which search for equilibrium configurations that permit the existence of a state of prestress in the structure

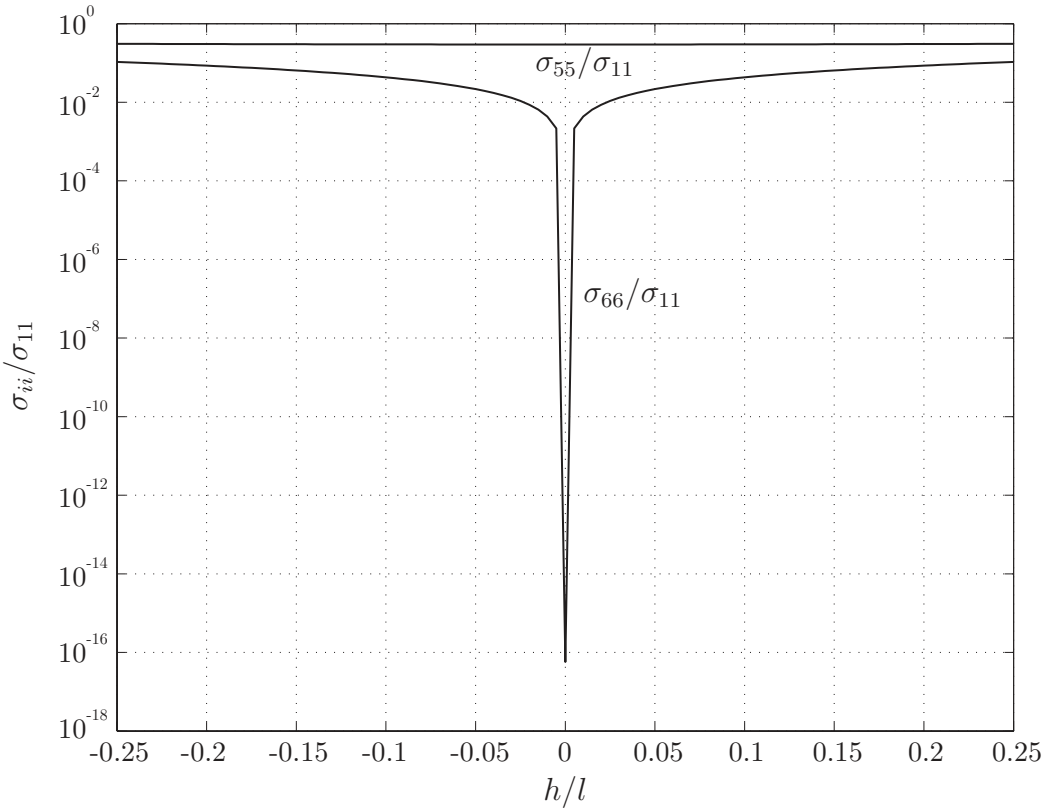

Figure 3.13: The variation of the two lowest singular values, σ_{55} and σ_{66}, with the height h.

with certain required characteristics. Each category includes an analytical method, suitable only for simple or very symmetric structures.

The non-linear optimisation approach and the method of pseudo dynamical relaxation have both successfully been used to determine configuration details, i.e. nodal coordinates, of structures that were already essentially well known. However, neither of the two can be applied to problems that are not completely defined, e.g. when the lengths of all cables are not known in the formulation where the lengths of the struts are maximised.

The three remaining static methods, sections 3.3.2–3.3.4, are in fact only two, since the force density method and the energy method are equivalent. The main strength of the force density method is that it is well suited to situations where the lengths of the elements of the structure are not specified at the start. Thus, new configurations can be easily produced, but it is difficult to control the variation in the lengths of the elements, as the set of force densities is varied. The reduced coordinates method offers a greater control on the shape of the structure, but involves more extensive symbolic computations.

The linear force method, for analysis of the structure subsequent to form-finding, is an efficient numerical method which makes use of the advantages of the SVD. It should be emphasised that the method, as it is presented here, is useful only for

structures that behave linearly. As will be seen later, this is sufficient for many problems, but not all. In cases where the structures undergo large displacements, a geometrically non-linear FEM must be used. A FEM, suitable for cable structures where cable slackening can occur, is presented in reference [171]. This will be used in some of the following analyses.

Now that the necessary tools to analyse a general tensegrity structure have been provided it is time to move on to the development of deployable tensegrity structures for space applications.

Chapter 4

Deployable Tensegrity Masts

4.1 Background

In Snelson's US patent "Continuous tension, discontinuous compression structures" from 1965, [151], the construction of highly complex tensegrity structures by simple modules is described. One of these structures is a mast with three struts per stage. This mast is created by assembling triangular prisms on top of each other. The direction of rotation of the prisms vary so that every second prism is rotated clockwise and every other counter-clockwise. This procedure is illustrated in Figure 4.1 for a three-stage mast. They merge into a mast by substituting their individual base cables by the saddle cables. The height of each module is H, but the height of the mast is lower than $3H$ due to the overlap h of the saddle cables. It can be shown that for a cylindrical mast this overlap can be expressed as a ratio of the module height, $\eta = h/H$, cf. [117].

An important characteristic of Snelson's tensegrity structures is that they have a single state of self-stress. Hence, the length of only one element has to be adjusted to prestress the structure. This is a key property to the practical implementation of tensegrity structures, as has been shown by Snelson.

Fuller presents a tetrahedral mast in his patent from 1962, [44]. This mast has struts that are connected to each other and is, therefore, less interesting from the point of deployability.

4.2 Static and Kinematic Properties

The first step in the analysis of any bar framework is the determination of its static and kinematic properties. Consider an n-stage tensegrity mast with v struts per stage, constructed according to the scheme in Figure 4.1. Counting the number of joints and bars in the mast yields

$$j = 2vn \tag{4.1}$$

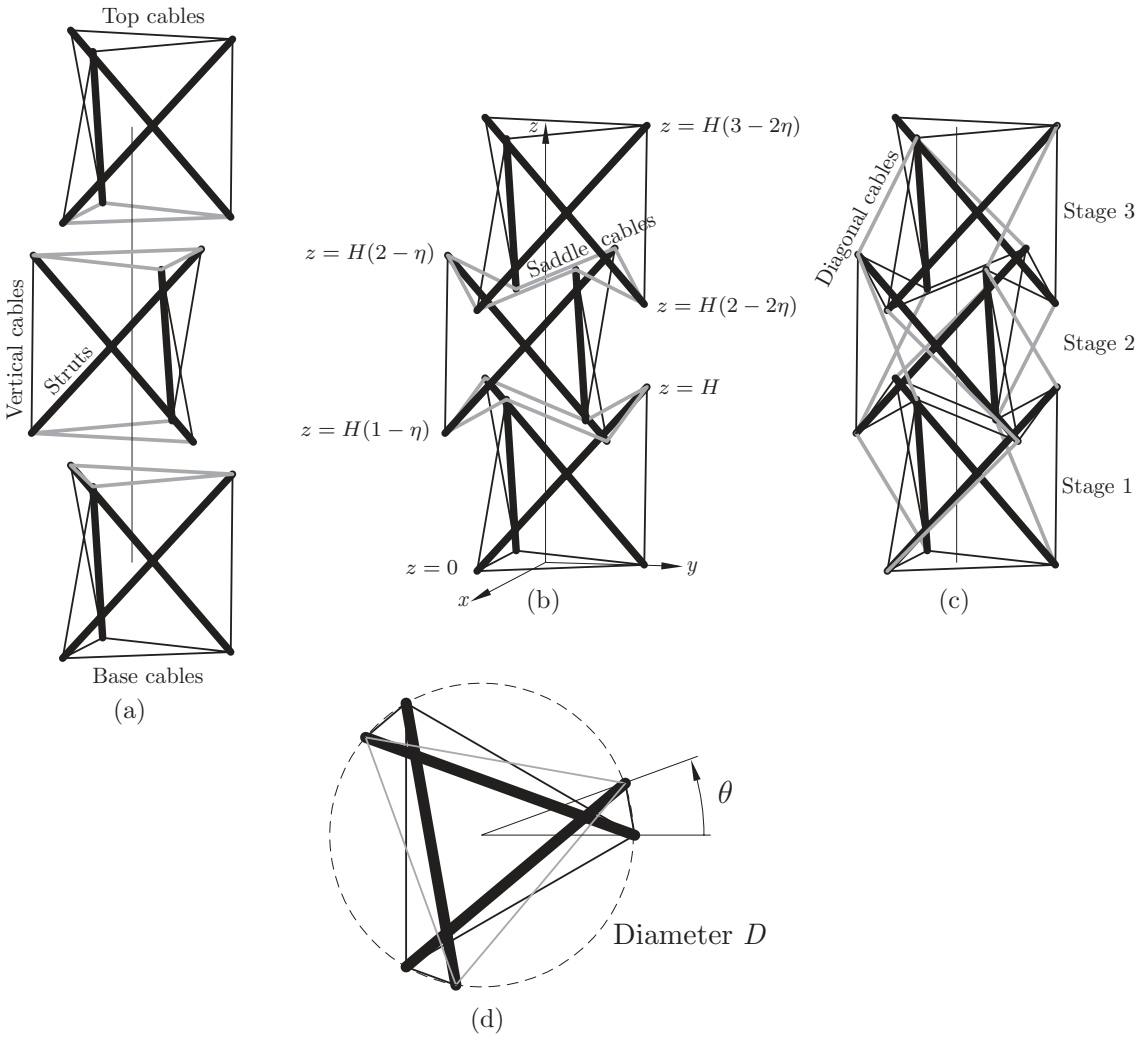

Figure 4.1: Assembling a three-stage tensegrity tower with three struts per stage from basic tensegrity modules: (a) three modules are (b) assembled by replacing the cables of the bases with saddle cables and finally (c) adding diagonal cables to prestress the structure. The top base of the upper and lower modules is rotated an angle θ w.r.t. the bottom base. The middle module is rotated counter-clockwise the same angle.

and

$$b = 2v(3n - 1). \tag{4.2}$$

Substituting (4.1), (4.2) and $c = 6$ into the extended Maxwell's rule, (1.2), yields

$$m - s = 2v - 6, \tag{4.3}$$

which is independent of the number of stages n. Hence, under the assumption of only one state of self-stress, $s = 1$, the number of mechanisms is

$$m = 2v - 5. \tag{4.4}$$

For most applications the stiffness is important, hence the masts with three struts per stage are preferable as they have the lowest number of internal mechanisms.

Another aspect is to keep the total number of struts low as they will comprise the major part of the mass of the mast. Therefore, one might think that the masts with two-struts per stage would be better. However, closer examination of the masts with $v = 2$ yielded $j = 4n$, in accordance with (4.1), but $b = 6(2n - 1)$ as the bottom and top bases now only consist of a single cable each. The extended Maxwell's rule for this mast yielded $m - s = 0$, hence the same number of mechanisms as the masts with three struts per stage. From a practical viewpoint it would be more difficult to provide adequate restraints at the base, for this case with two struts per stage. The masts with three struts per stage have triangular bases which can easily be constrained. In the following, the focus will, therefore, be on masts with three struts per stage.

4.3 Form-Finding

Snelson [151] has built highly complex tensegrity masts for several decades. The mathematical conditions for the existence of a prestressable configuration have, for the majority of these masts, been unknown. Sultan [159] presents the first mathematical treatment of Snelson's multi-stage tensegrity mast with three struts per stage. Shortly thereafter, Nishimura [117] presents closed-form solutions for the equilibrium configuration of multi-stage tensegrity masts with v struts per stage.

4.3.1 Two-Stage Tensegrity Mast

Sultan, [159], shows that the initial equilibrium solution of a cylindrical two-stage tensegrity mast with three struts per stage and equal stage height, reduces to a quadratic equation in η with θ as the only remaining variable. Following the pioneering work by Sultan, Nishimura [117], derives the following general equation for the overlap ratio η of a two-stage tensegrity mast with v-struts per stage:

$$\frac{R_1}{R_1'}\cos\left(\frac{\pi}{v}+\theta\right)=\frac{\eta\left(1-(1-\eta)\cos\frac{\pi}{v}\right)}{2\left(1-\cos\frac{\pi}{v}\right)(1-\eta)+\eta^2}, \tag{4.5}$$

where R_1' and R_1 are the base and top radii of the first stage, respectively, and θ the angle of relative rotation. Symmetry implies $R_1' = R_2$ and $R_1 = R_2'$. Some special cases of (4.5) are noted: (i) for $\theta = 0$ and $R_1 = R_1'$, the overlap is

$$\eta=\frac{2\cos\frac{\pi}{v}}{1+2\cos\frac{\pi}{v}}, \tag{4.6}$$

and (ii) for $v = 3$ and $R_1 = R_1'$, (4.5) simplifies to

$$\eta^2\left(\cos\left(\frac{\pi}{3}+\theta\right)-\frac{1}{2}\right)-\eta\left(\cos\left(\frac{\pi}{3}+\theta\right)+\frac{1}{2}\right)+\cos\left(\frac{\pi}{3}+\theta\right)=0. \tag{4.7}$$

Equation (4.6) indicates that the overlap span of the two-stage mast is quite small: $\eta = 1/2$ for $v = 3$, and $\eta \to 2/3$ as $v \to \infty$.

4.3.2 Multi-Stage Tensegrity Masts

Sultan [159] uses a symbolic approach to find the overlap of multi-stage masts. As the number of stages increases, the computations becomes too complex for the symbolic mathematical softwares, even though symmetry conditions are used to reduce the size of the matrices; masts with up to nine stages are analysed in [159].

In order to analyse masts with a very large number of stages, say 100, a numerical approach based on the force method is suggested here. The initial equilibrium configuration of the tensegrity mast is the solution to (3.51) in the absence of external forces, $\mathbf{f} = \mathbf{0}$. Hence, the task is to find the overlap η which renders the equilibrium matrix singular, i.e. $\det \mathbf{H}(\eta) = 0$. This approach, which was implemented by the author and H. Y. E. Pak, starts with an initial value for η. The mast configuration was then generated by the scheme in [159]. The determinant of the $6(3n-1)\times 6(3n-1)$ equilibrium matrix $\mathbf{H}$ was then computed (*N.B.* $v = 3$). The Matlab [89] function `fsolve`, which solves a system of non-linear equations by the method of least squares,

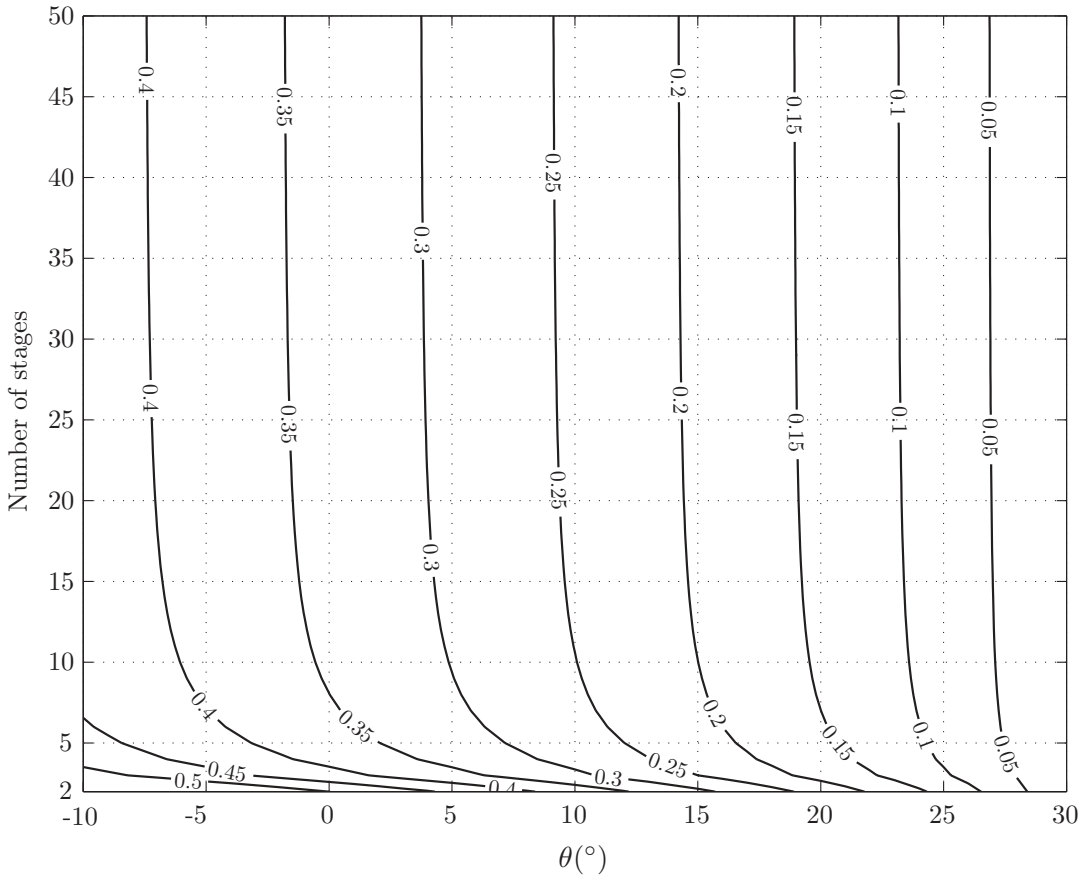

Figure 4.2: Contour lines of the dimensionless overlap η for multi-stage tensegrity masts with three struts per stage.

was used to solve $\det \mathbf{H}(\eta) = 0$ for η. With the `fsolve` function, masts with up to 15 stages could be solved, but the termination tolerance `TolFun` had to be set as low as 10^{-40} to achieve convergence. To analyse masts with more stages, another approach was needed. Instead of implementing a sophisticated line-search routine, which also may fail, a more rudimentary routine, based on successive interval bi-sectioning, was implemented, cf. [29]. The convergence was slow but stable. Several overlap values may exist, which give a zero determinant, but only one with the correct prestress. Care must therefore be taken in choosing the initial interval. This approach may not be the most elegant way of finding the initial equilibrium configurations, but it nevertheless yields the correct solution. The equilibrium configurations for masts with up to 50 stages were computed by this improved numerical method. The overlap values of these masts are given in Appendix A and Figure 4.2 shows a graphical representation of these values. It is observed that the overlap diminishes with the number of stages. The state of self-stress also changes with n and θ. The fact that the overlap decreases with the number of stages may not be ideal from a manufacturing point of view as new stages cannot be added without changing the geometry of the complete mast.

Investigating multi-stage tensegrity masts, Nishimura [117] finds that even though all symmetry groups are used to simplify the prestressability condition, no analytical solution could be obtained for masts with more than four stages using current symbolic software. Nishimura then investigates a class of tensegrity masts with the same self-stress for the interior stages independent of the number of stages. An interior stage is defined as any stage but the first and the last stage in a mast [117]. Recall that for a given relative rotation θ, the overlap ratio η decreased as the number of stages increased, Figure 4.2. By having different rotation angles for the interior and the first and last stages, Nishimura shows that it is possible to keep a constant overlap ratio for any number of stages. The geometry of a cylindrical multi-stage tensegrity mast with the same self-stress for interior stages and constant stage height ($H = H^*$) is thus described by three parameters [117]: the rotation angle of the first and last stages θ, the rotation angle of the interior stages θ^*, and the overlap ratio η ($= \eta^*$). Note that the rotation angle of the second and second to last stages is the same as that of the interior stages. For the interior stages, the relationship between the overlap ratio η^* and relative rotation θ^* is [117]

$$\begin{aligned}\eta^{*2}\left[\cos\frac{\pi}{v}-\cos\left(\frac{\pi}{v}+\theta^*\right)\right]+\eta^*\left(1-\cos\frac{\pi}{v}\right)\left[1+\cos\left(\frac{\pi}{v}+\theta^*\right)\right]\\ -\cos\left(\frac{\pi}{v}+\theta^*\right)\left(1-\cos\frac{\pi}{v}\right)=0.\end{aligned} \tag{4.8}$$

If $\theta^* = 0$,

$$\eta^* = \frac{\cos\dfrac{\pi}{v}}{1+\cos\dfrac{\pi}{v}}, \tag{4.9}$$

while if $\eta^* = 0$,

$$\theta^* = \pi\left(\frac{1}{2}-\frac{1}{v}\right), \tag{4.10}$$

which is identical to the relative rotation of a tensegrity prism with $i = 1$, (3.4).

After finding the interior overlap ratio η^* by (4.8), the relative rotation of the first and last stages is subsequently determined by solving, symbolically or numerically, the characteristic equation of a 7×7 matrix (Equation (41) in [116]). However, Micheletti [93, 94] shows that the rotation of the end stages is actually found using the prestressability condition for the two-stage mast, (4.5). To find the geometry of a cylindrical tensegrity mast with uniform interior self-stress, one specifies θ^* to find η^* by (4.8). Then θ is computed by (4.5) with $R_1 = R_1'$. Note that it is possible to design multi-stage masts with $\theta = \theta^*$ and constant η, but the nodes of these masts do not all lie on the surface of a cylinder; the base and top radii have to change according to (4.5), i.e., $R_1/R_1' \neq 1$. For example, $\theta = \theta^* = 0$ gives

$$\frac{R_1}{R_1'} = \frac{2}{3 - \cos\dfrac{\pi}{v}}. \tag{4.11}$$

The multi-stage tensegrity masts by Nishimura are better suited for applications as the forces are relatively uniform through the mast.

4.4 Manufacturing Technique

The practical implementation of tensegrity masts requires an efficient and accurate manufacturing technique. Conceptually, the structure is easy to make since the compression members do not touch each other, which otherwise would require complicated joint designs. The present manufacturing technique was inspired by Pugh's [132] illustration of the diamond pattern system, Figure 4.3. However, because of the intrinsic difference between the cables and struts in terms of material properties, it was decided to separate the construction of the tension and compression members. This is in contrast to the conventional way of construction, where, e.g., a mast is built from node to node and stage by stage. An obvious disadvantage of the conventional method is the difficulty in retaining the required precision when the whole structure has to be constructed in three dimensional space, which in the case with flexible structures, is especially awkward. A direct analogy to the proposed manufacturing method is the separation of tensile and compression members in the construction of tension roof structures, cf. [171].

The separation of the tension and compression members would result in more freedom in the manipulation of the flexible cables. The first step in the manufacturing procedure is to map the three-dimensional net of cables onto a two-dimensional plane, as done by Pugh, without changing any cable lengths. Since the cable net is composed mainly of triangles connected to each other in a special way, the number of net configurations is restricted. It was found that only two cable net configurations, which preserve all cable lengths, exist. These configurations are shown in Figures B.2(a) and (b) for a two-stage mast and in Figures B.3(a) and (b) for a three-stage mast. At first, net 1 and 2 for the two-stage mast seemed equal. However, close scrutiny of net 1 showed that the diagonal cables had changed place with the vertical cables, which means that the saddle cables had been inverted. Net 2 agrees

more with the layout of three-dimensional version of the cable net, Figure B.1(a). The two key aspects of the manufacturing method required to obtain good precision are to ensure accurate element lengths and to make certain that the angles in the two-dimensional net do not differ too much from the corresponding angles in three dimensions. Net 1 may satisfy the first requirement but certainly not the latter one. In this respect net 2 is better, but still not ideal. The horizontal distance between the nodes along the saddles is identical to the length of the base cables, which produces an overlap in two dimensions that is larger than that in three dimensions. For a three-stage mast, this layout has overlapping triangles, Figure B.3(b), which is highly undesirable. By relaxing the length preservation condition slightly, the saddle overlap in the two-dimensional cable net was set equal to ηH, Figures B.2(c) and B.3(c). This setting yielded that the distance between the nodes at the bases was too long and, thus, could not be constructed along with the rest of the net. However, the angles between the members in net 3 should agree better with those in three dimensions. Considering accuracy issues, net 3 is the preferred layout. It was identified as sensible to have as few open-ends of the cables as possible, so an attempt was made to find a way of completing the entire tracing of the net with only one or two separate cables. However, it was soon realised that because there existed more than two nodes with an odd number of cables connected to them, by simple *Graph Theory*, it was impossible to use one cable only.

The construction of three tensegrity masts by Pak and the author is described in reference [118]. It is reported that these masts suffer from large cable length inaccuracies, despite accurate cable nets. These nets were constructed by first gluing the plotted cable net to a wooden board. Holes were then drilled at all intersection points and small threaded rods were positioned in the holes. Stiff Kevlar cords were strung between the intersection points and fastened by looping the cords once around each threaded rod. Subsequent to the tracing of the net, the connections were secured by epoxy resin. According to [118], the length errors were caused by uneven lengthening or shortening of individual cables. The changes in length seemed to depend on the way the cables were looped around the nodes. In hindsight, the looping direction decided if the cable lengthened or shortened, but it was not the heart of the problem. The direct cause was the use of net 1, which forces the nodes to rotate to adopt to the three-dimensional configuration. Unfortunately, the deficiencies of net 1 was not recognised until all three masts had been constructed.

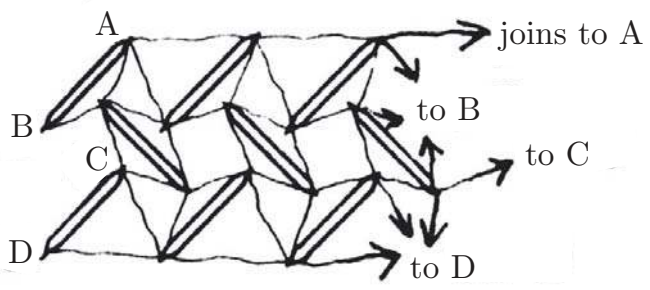

Figure 4.3: Illustration of the Pugh's diamond pattern systems for a three-stage, three struts per stage mast, [132].

To examine the feasibility of net 3, an eight-stage mast was constructed by the author, using almost the same method as the previous masts. However, the experience from the previous constructions indicated that the connections must be manufactured to a higher precision. Preferably, the cables of the two-dimensional cable net should lie in the same plane and go through the centre of the nodes; looping of the cables around the nodes must be avoided. The net for the eight-stage mast was plotted on an A0 paper (1189×841 mm^2), which was fastened on a 40 mm thick *Medium Density Fibreboard* (MDF). Holes of 4 mm in diameter, approximately normal to the board, were drilled through the board at the cable net intersections. Threaded 4 mm rods (M4), 44 mm in length, were positioned in the holes. To the parts of the rods sticking up from the board, 14 mm long aluminium tubes of 6 mm outer and 4 mm inner diameter were glued. The aluminium tubes had been pre-drilled with eight 1 mm co-planar holes, in the direction of the cables through the centre of the tube. Thus, all the cables in the final net would lie in the same plane and each cable would go through the centre of the node. The cables were made of a 0.45 mm diameter stainless steel cable composed of 49 individual wires for maximum flexibility. After the tracing of the cables, the connections were secured by filling the aluminium cylinders with high-strength epoxy resin, which efficiently bonded to the thin steel cable.

The struts were made of the same aluminium tubes as the connections. Two nuts were placed on the threaded rods to enable length adjustment. One of the initial aims was to make a mast with the minimum number of adjustment mechanisms, since they are usually large, difficult to design and will easily fail. However, from the experience from earlier models, it was considered necessary to include some adjustment possibility. It was immediately recognised that the eight-stage mast was far more accurate than the previous models. Nevertheless, surprisingly large length adjustments were needed to prestress the nets. One reason for the inaccuracies is shown in Figure 4.4. In the two-dimensional net, the cables connected to a node lie in the same plane and go through the same point, Figure 4.4(a). However, in the three-dimensional net they do not necessarily intersect, Figure 4.4(b). Thus, the geometry of the mast will change to a configuration where they intersect, i.e. where the forces can be in equilibrium. To eliminate this error source it is necessary to manufacture joints, preferably spherical, with holes drilled in the directions of the cables in the three-dimensional net configuration. By adjusting the distance between the nodes in the two-dimensional net according to the layout of the holes in the spherical joint it would still be possible to construct the net in two dimensions, but the cables will no longer lie in the same plane[1]. No net was, however, constructed according to this principle.

To summarise, the basic idea of the construction scheme, which was to separate the construction of the cable net and that of the bars, worked well after some early mistakes. The modification of the struts to enable mast folding and deployment will be presented next.

[1]This solution was pointed out to the author by R. E. Skelton at "Colloquium Lagrangianum—Strutture Tensegrity: Analisi e Progetti" (Tensegrity Structures: Analysis and Design) in Rome, 6–8 May 2001.

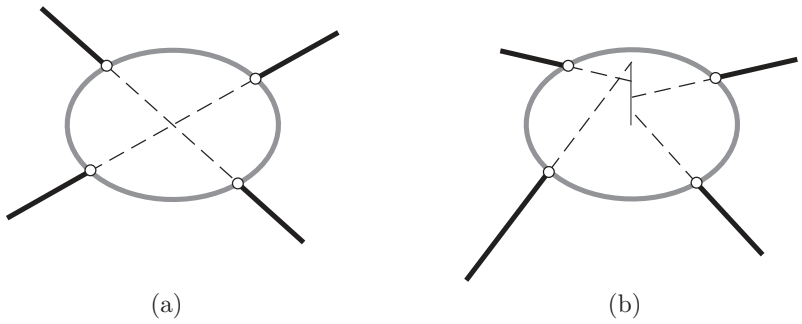

(a) (b)

Figure 4.4: Cables which coincide in two dimensions (a) may not coincide in three dimensions (b).

4.5 Deployment

An n-stage tensegrity mast with three struts per stage has $5-2/n$ times more cables than struts. In addition, the struts are the only stiff members and also the longest ones. Concerning deployment and packaging efficiency, the focus would therefore be on the struts. In the few studies on foldable or deployable tensegrities, this has not always been the case.

Bouderbala and Motro [11] analyse different approaches to tensegrity folding: (i) strut mode, (ii) cable mode and (iii) mixed mode. In the first mode, only the lengths of the strut are changed and in the second one, only the cable lengths. In the third mode both lengths are changed. The folding of expandable octahedron assemblies are studied. The cable mode is found to be less complex than the strut mode, although the latter one produces a more compact package.

Furuya [45] analyses three approaches for the deployment of a tensegrity mast with connected struts: (i) fixed lateral cable length, (ii) fixed strut length and (iii) fixed base cable length. For modes (i) and (ii), the size of the triangular bases changes simultaneously during deployment. Only in mode (iii) is it possible to deploy the mast sequentially, which usually is more convenient for space applications. Telescopic struts are suggested for realising the mechanisms of this mode.

In the deployment approach by Skelton and Sultan [159, 162], the lengths of the cables are changed in a way so that the structure at every step is in an initial equilibrium configuration. Hence, the structure is in stable equilibrium throughout the deployment.

There are, however, a few disadvantages with this approach. First, using a cable-activated deployment means that the diameter of the mast will increase if the struts are stacked horizontally on top of each other in the stowed configuration. As observed in section 2.2.4, the popular masts for space applications have a constant diameter during deployment. If the struts are stacked vertically the diameter need not change, but such a scheme will probably lead to problems as it is no longer obvious how the struts should be stacked for a trouble-free deployment. Second, a large number of devices is needed to control the lengths of the cables; each strut

has one electric motor to control the length of the saddle cables and three reels on which the vertical and diagonal cables are stored to prevent entanglement [149]. The motors and the reels produce a very reliable cable-activated deployment, but they add complexity to the mast. As described in reference [149], this deployment procedure is neither synchronous nor sequential but rather a combination of both.

In the search for a deployment procedure that is simpler than the cable-activated approach, but hopefully equally reliable, a procedure based on strut deployment will be proposed.

4.5.1 Strut Deployment

If the strut length is equal to the diameter and folded by a midpoint hinge, the struts can fit horizontally beside each other in a canister with a diameter equal to that of the mast. If the struts are longer, some parts of them will lie on top of each other and, thereby, increase the stack height. This is a drawback, although not too serious. Telescopic struts can be collapsed into shorter lengths. A telescopic alternative, however, would require a motor on each of the $3n$ struts in the mast. Having so many motors presents too large a risk. The failure of only one motor would end the deployment. Thus, a hinge with self-deployable characteristics would be preferable.

Tape-Spring Rolling (TSR) Hinge

The use of carpenter tapes, or tape-springs, i.e. the curved metal tape found in tape measures has been considered for a long time in the design of self-deploying hinges [128]. In order to fold these tapes, a large moment is required to initially buckle the tape. Subsequent to buckling, a much lower moment is required to continue folding the tape. During deployment, the tapes provide a small but constant restoring moment to eventually lock into the straight position. A key property of the tape-spring is that it can be significantly deformed several times without permanent damage. To increase the buckling moment, and also the restoring moment, two tape-springs can be placed a certain distance apart with the concave sides facing each other. The resulting hinge will be quite stiff in bending but weaker in torsion. A tape-spring hinge, which also is torsionally stiff, has been developed at DSL, Figure 4.5. Its basic components are two tape-springs and two Rolamite hinges[2], one on each side of the tape-springs. The Rolamite hinges are made of steel cables and *Delrin*[3], a space qualified acetal resin, with approximately half the density of aluminium. The overall weight of the hinge depicted in Figure 4.5 is 0.105 kg [181]. Including attachments to the struts the TSR hinge has a total mass of 0.2 kg. Other advantages of this hinge is simple assembling and low friction, the

[2]The Rolamite, or the rolling-band, concept was invented by D. F. Wilkes of the Atomic Energy Commission's Sandia Laboratory, Albuquerque, NM, USA. In its basic form, the device consists of a metal band looped around two rollers, [19]

[3]Delrin is a registered trademark of E. I. du Pont de Nemours and Company.

(a) (b)

Figure 4.5: The tape spring rolling hinge: (a) deployed and (b) folded (Courtesy of A. M. Watt).

latter eliminates the need for lubrication. More information about the TSR hinge is found in [180, 181].

Bi-Stable Tube Hinge

A well-known property of tape-springs is that they are stable only in the straight position. Once folded into a bent configuration, they need external restraints to keep them in that position, e.g. the cassette containing the rolled-up carpenter tape. Recently, the BRC tube, which is stable in both the bent and straight positions, was invented by Daton-Lovett [30, 65]. The bi-stability is obtained by a special layout of the fibres in the composite material. In the straight configuration the tube is unstrained, while it is strained in the rolled-up configuration. To move the tube from the rolled-up position to the straight position requires only a small quantity of energy.

A strut with a hinge made of a bi-stable tube is shown in Figure 4.6. A four-stage tensegrity mast, with bi-stable hinges, was built by H. Y. E. Pak and the author. Another, more distant, alternative to bi-stable hinges is to manufacture the whole strut as a bi-stable tube. The torsional stiffness can be increased by closing the open cross-section with velcro [30].

4.5.2 Demonstrator Masts

As mentioned earlier, three tensegrity masts, two with three stages and one with four stages, were built at DSL, cf. [118]. The first three-stage mast was not foldable and was only made to gain some experience with the manufacturing procedure. The mast was prestressed by two adjustable plastic ties, one on the top base cable and the other on the bottom cable. The second three-stage mast had struts made of aluminium rods and single-blade tape-springs as hinges. When the mast was

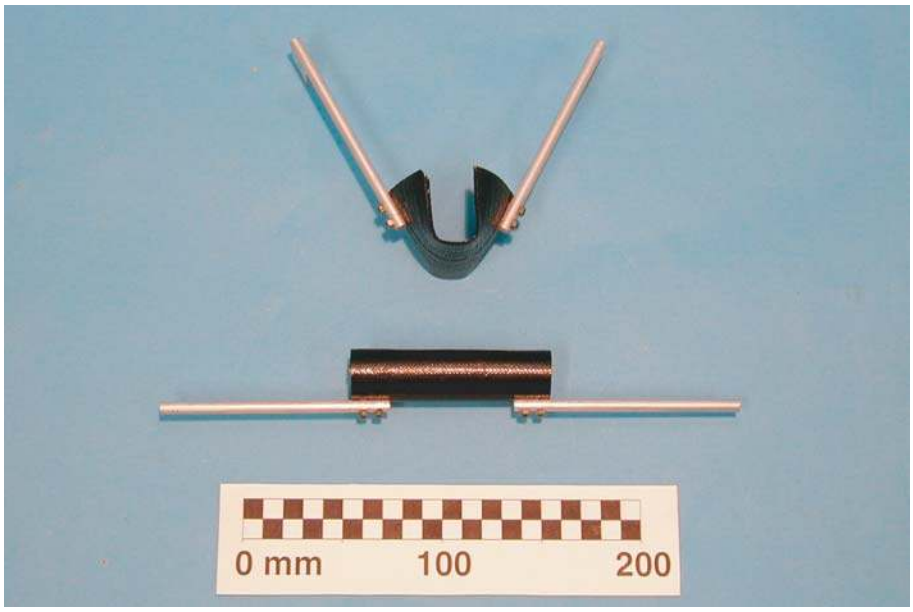

Figure 4.6: Strut with a bi-stable hinge in straight and bent configurations.

prestressed, by shortening the top and bottom cables, several struts buckled in torsion. Closer examination revealed that the blades had been flattened by the pop-rivets which connected the blades with the rods. This flattening significantly reduced the stiffness of the curved tape and yielded the mast useless. For the following masts, a heavier bolt-and-nut alternative was used instead of pop-rivets.

Four-Stage Mast

The four-stage mast, which was the third tensegrity mast built at DSL [118], was the first one that could be folded in a satisfactory way. The struts were made of solid 6.35 mm diameter aluminium rods and bi-stable tubes were used as hinges, Figure 4.6. The torsional buckling problems with the previous model was eliminated by the bi-stable tubes. In order to achieve increased axial stiffness, the rods were attached to the outside of the tubes. The struts, which had a length accuracy of ± 1 mm, had turn-buckles at the ends that enabled length adjustment. The deployed mast is shown in Figure 4.7. The mast was reasonably straight considering the accuracy problems of the cable net discussed earlier. However, high local stresses were induced at the connections between bi-stable composite tubes and the aluminium rods, which led to local buckling of the tubes. This significantly reduced the compressive strength of the struts and the mast could not be prestressed to the desired level. Compared to the mast with tape-spring hinges, the mast with the bi-stable struts was much heavier which led to cable slackening. The mast could easily be folded by hand, thanks to the bi-stability of the hinges. The folded mast is shown in Figure 4.8. The bi-stable tubes are disproportionately large in comparison to the complete mast. However, no bi-stable tubes of smaller diameter, that functioned well, were available at the time.

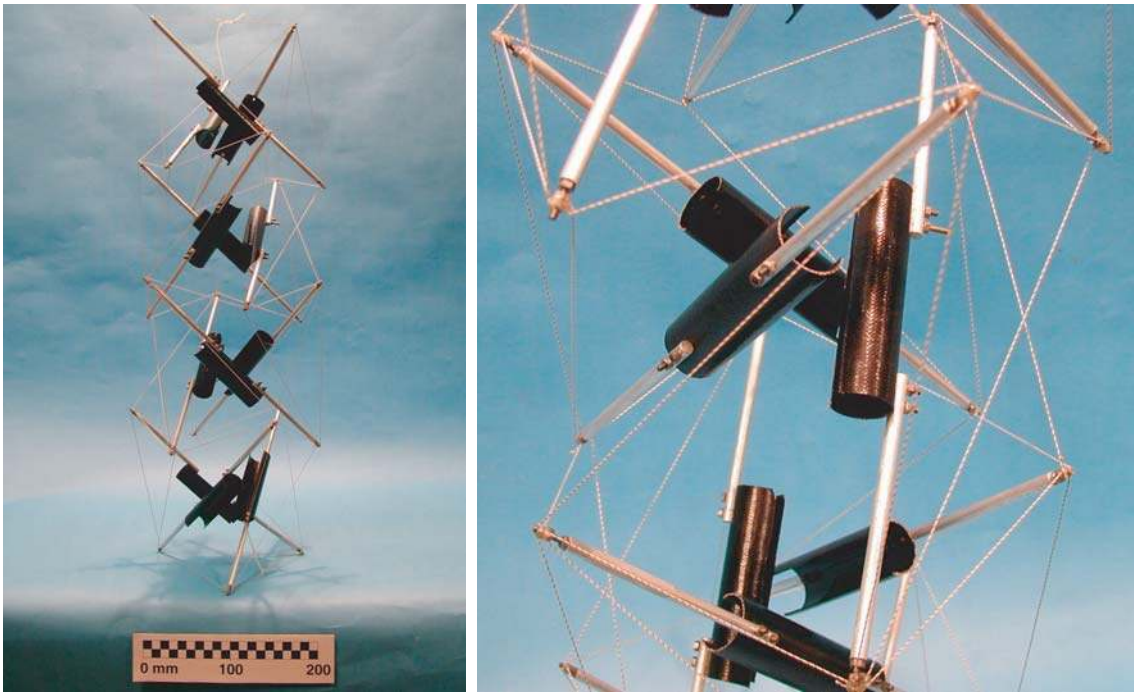

(a) (b)

Figure 4.7: The deployed four-stage mast with bi-stable struts.

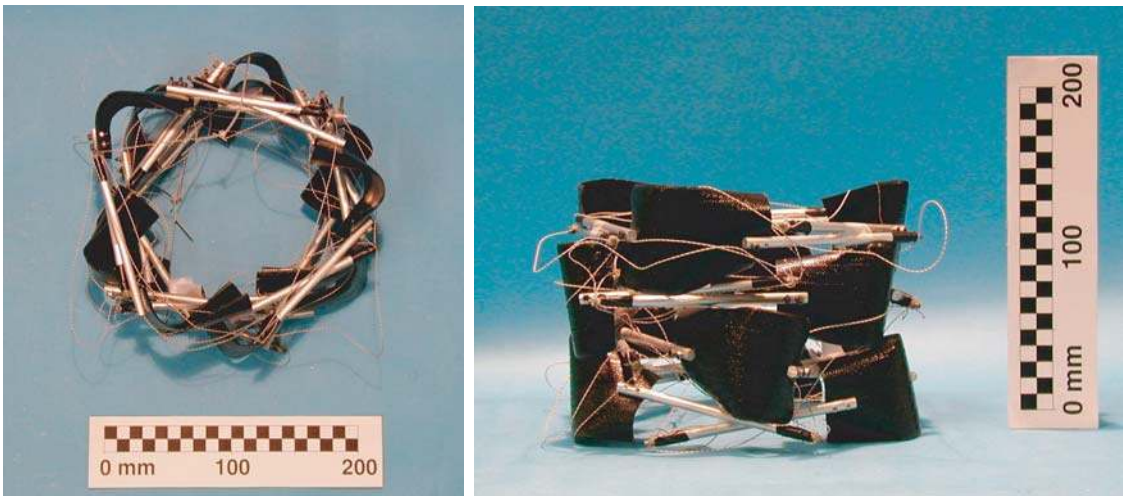

(a) (b)

Figure 4.8: The stowed four-stage mast with bi-stable struts.

Eight-Stage Mast

To fully evaluate the concept of self-deployable struts, the eight-stage mast was equipped with tape-spring hinged struts. Two tape-springs (19 mm wide) were

connected to two aluminium tubes, with the concave sides of the tape-springs facing each other. Compared with the tape-spring hinges of the second three-stage model, the new hinges were much stiffer in both torsion and bending. The mast could thus be given the necessary prestress to reduce the effects of gravity. One immediate problem was how to keep the struts in the folded configuration. This was solved by enclosing the stowed package by a canister, Figure 4.9, similar to that used for the CM, Figure 2.4. Another problem was how to control the deployment of the mast. An approach suggested by Pellegrino [126] was to use an inflatable tube inside the mast. The tube would activate the deployment and stabilise the unstressed mast during deployment. For the present mast, the inflatable tube was replaced by an aluminium rod through the base of the canister and connected to the three nodes at the top of the mast. When the rod was pushed from underneath the base, it deployed the mast sequentially. The complete deployment of the eight-stage mast is shown in Figures 4.10 and 4.11. The mast was not fully prestressed until the bottom stage was fully deployed. However, the slender aluminium rod could not provide enough force and the tape-spring hinges could not provide sufficient moment to deploy the bottom stage, i.e. to prestress the whole structure. A final prestressing of the mast can be obtained by allowing one of the base cables to be a little longer during deployment. All the tape-spring hinges can then be deployed since they do not have to prestress the mast. Finally, the longer base cable is shortened by a motorised turn-buckle and the mast is prestressed. Hence, only two motors would be needed: one that shortens the base cable and one that deploys the structure by actuating and controlling the mast deployment. Twice the deployment had to be stopped to resolve some entanglement problems. This must be regarded as very satisfactory considering no precautions had been taken to avoid entanglement.

4.6 Structural Analysis

Several studies, e.g. [45, 117, 159], talk about the potential of the tensegrity masts as lightweight, deployable structures, but none do a comparison with existing deployable masts. To satisfactorily prove the applicability of tensegrity masts as efficient deployable structures, they must be compared to a realised and successful mast. The current state-of-the-art mast is the primary deployable structure for the STRM—the 60 m long ADAM. The ADAM supports a 360 kg antenna at its tip and carries 200 kg of electric and fibre-optic cables and a gas line along its length [1]. Data for the STRM ADAM is given in Table 4.1. Recall that the tensegrity masts with three struts per stage are kinematically indeterminate to one degree. Their stiffness is therefore dependent on the prestress level. The stiffness of the ADAM is presumably higher than that of the tensegrity mast, as it uses stiff square frames between each bay, Figure 2.7. However, it is possible to remove the infinitesimal mechanisms of the tensegrity mast by adding cables in such a way that completely triangulates the bottom stage. This stiffening approach will be tested here.

(a) (b)

Figure 4.9: Eight-stage mast stowed in a canister: (a) side view and (b) top view.

In order to facilitate an accurate comparison, the tensegrity mast should have the same diameter, length and number of bays as the ADAM. First, a tensegrity mast with struts of equal lengths was studied. Then, a mast with uniform interior forces was analysed.

In the present mast generation routine, cf. [118], one of the input values is the strut length. To generate a mast with a given bay length, the relationship between the bay and strut length must be found. For an n-stage mast with three struts per stage, the length of the struts, l_s, for given values of the mast diameter D, bay length H_{bay}, rotation angle θ and overlap η, is computed as:

$$l_s = \left(\frac{D^2}{4} \left(2 + \cos\theta^* + \sqrt{3} \sin\theta^* \right) + \frac{H_{\text{bay}}^2}{\left[1 - \eta \left(1 - \frac{1}{n} \right) \right]^2} \right)^{1/2} . \tag{4.12}$$

The length of the struts at the end stages for a mast with uniform interior forces is found by setting $\theta^* := \theta$.

4.6.1 Initial Equilibrium Element Forces

An appropriate initial equilibrium mast configuration should have fairly uniform internal forces.

For $D = 1.12$ m and $H_{\text{bay}} = 0.6975$ m, the maximum and minimum cable and strut forces versus the number of stages, for a mast with equal-length struts, are shown

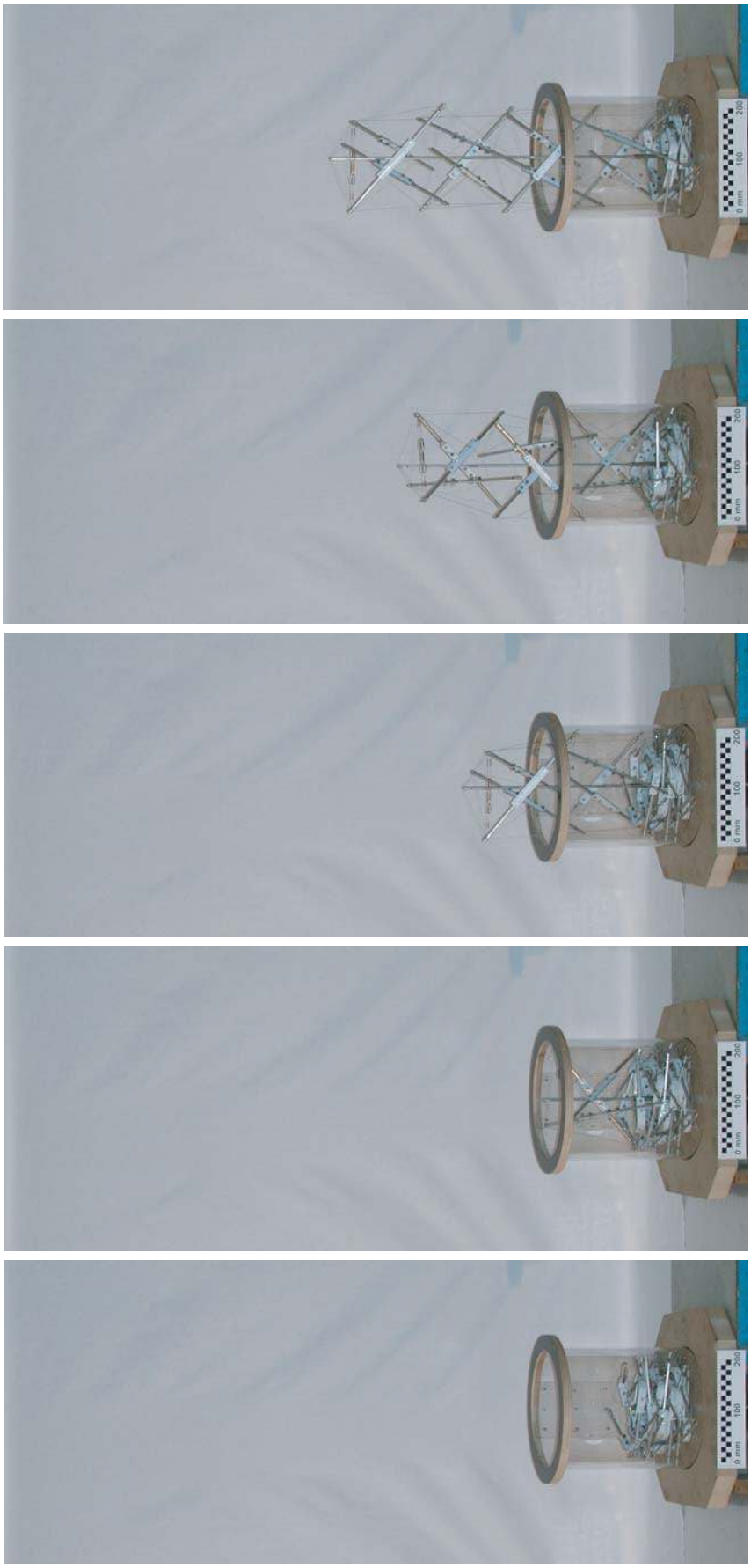

Figure 4.10: Rod-controlled deployment of the eight-stage mast: first four stages.

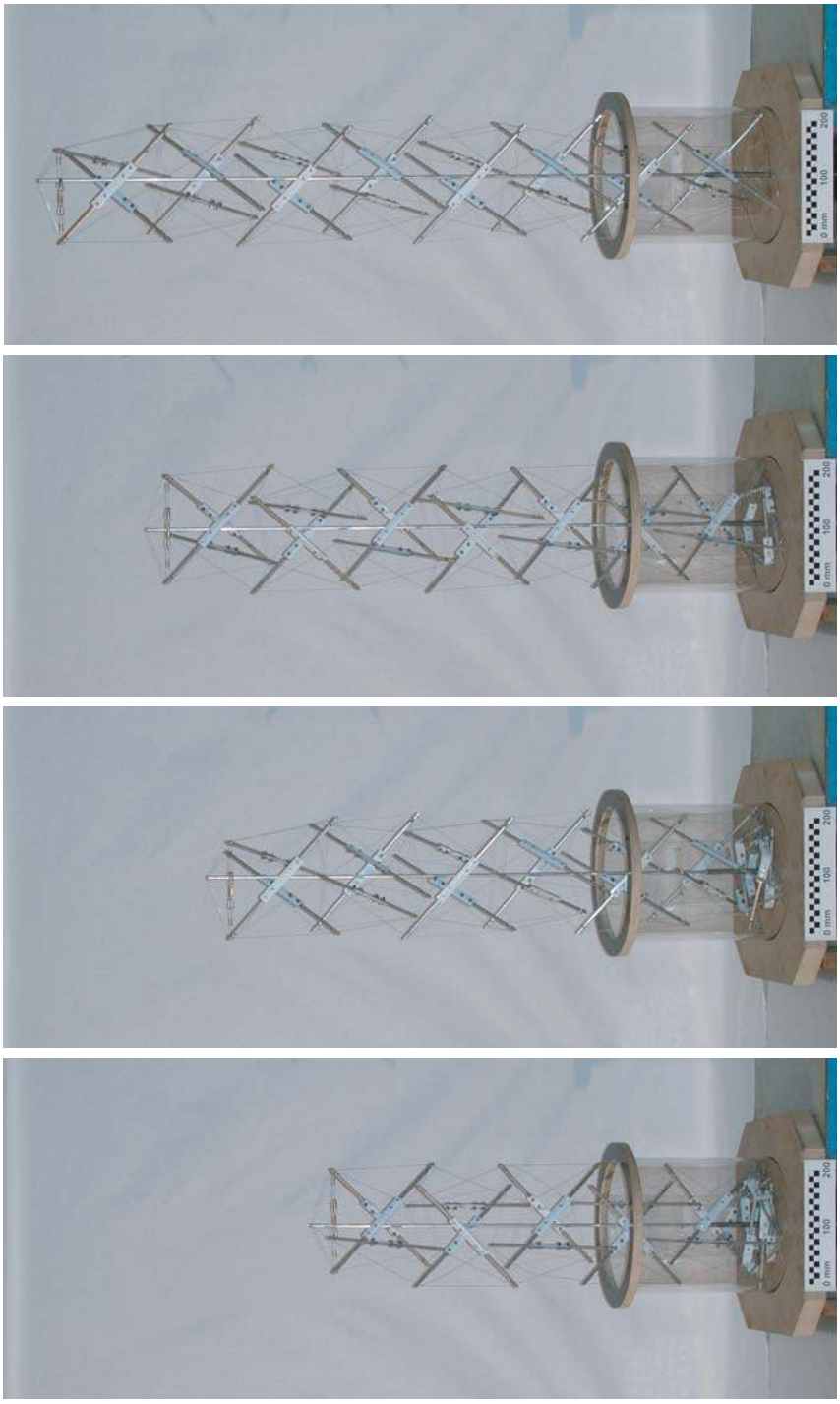

Figure 4.11: Rod-controlled deployment of the eight-stage mast: last four stages.

Table 4.1: Data for the 60 m long STRM ADAM, [1].

Geometry			Stiffness		
Length	(m)	60.68	Bending stiffness	(MNm^2)	13
Diameter	(m)	1.12	Torsional stiffness	(MNm^2)	0.15
Bay length	(m)	0.6975	Shear stiffness	(MN)	0.49
Number of bays		87	First bending mode	(Hz)	0.10
Mass	(kg)	290	First torsion mode	(Hz)	0.17
Mechanical stability			**Strength**		
Bending	(°/N)	0.0059	Bending strength	(Nm)	8140
Twist	(°/Nm)	0.0228	Torsional strength	(Nm)	305
Axial	(μm/N)	0.7	Shear strength	(N)	400

in Figure 4.12. The overlap values were taken from Appendix A. The maximal and minimal forces were normalised by the force in the base cables. The maximum cable and strut force increased linearly with the number of stages while the minimum cable force decreased only slightly. Already for seven stages, the maximum strut force was ten times the force in the base cables at $\theta^* = -10°$. Hence, in a multi-stage mast with equal-length struts, the relationships between element forces are undesirably large. This is a serious disadvantage and the only conclusion must be that long masts with equal-length struts are unfeasible for applications.

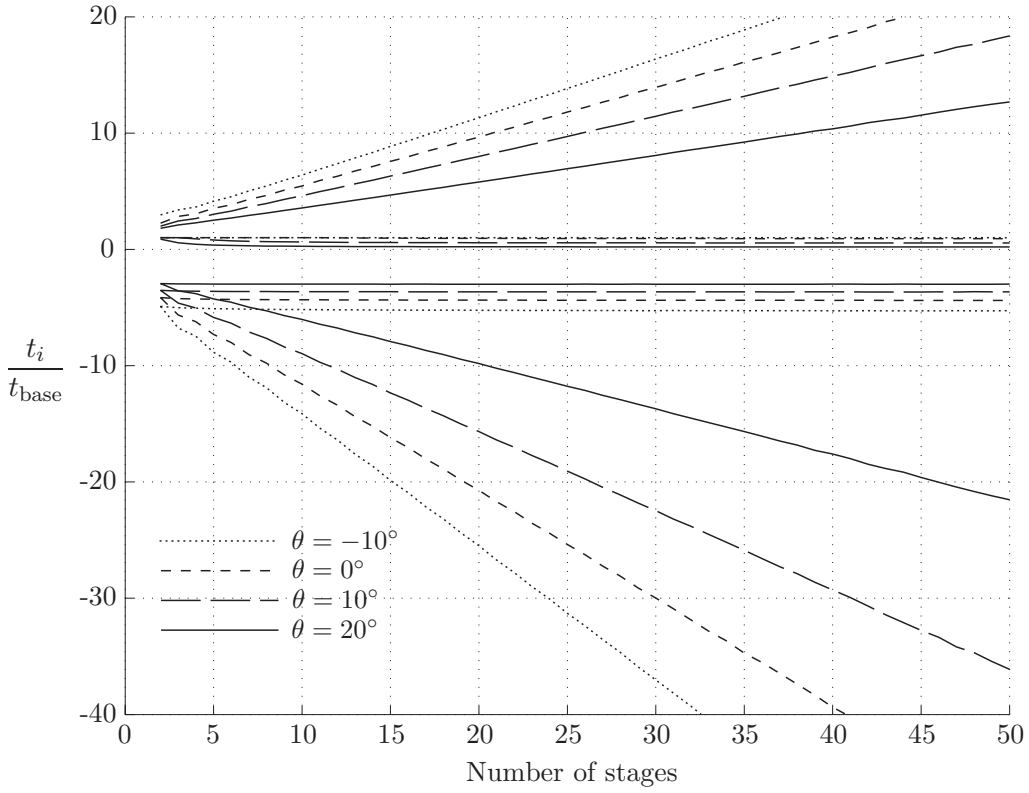

Figure 4.12: Maximum and minimum forces in the cables and struts in a multi-stage mast with struts of equal length.

The mast configuration by Nishimura [117], which has uniform forces for the interior stages, is probably more suitable for practical uses. In the following analysis of the Nishimura mast it was assumed that each stage had the same radius, $R_i' = R_i$, height, $H^* = H$ and overlap ratio, $\eta^* = \eta$. For a given value of the interior stage rotation θ^*, η was found by (4.8). Subsequently, the rotation of the end stages, θ, was computed by (4.5). As (4.5) and (4.8) are valid for any number of stages, the element forces in an n-stage mast ($n \geq 5$) was generated by two sets of element forces; the first set corresponds to stages 1 and n and the second set corresponds to the intermediate stages. The total number of different force values is ten. Set 1 is the struts and base, vertical, diagonal, and saddle cables (*N.B.* two values) at the first (or last) stage and set 2 the struts and vertical, diagonal and saddle cables at the interior stages. Hence, the forces in an n-stage mast were determined by analysing a five-stage mast. This remarkable characteristic significantly simplified the analysis of multi-stage masts. The variations of the normalised forces with θ^* are shown in Figure 4.13. It was immediately noted that the forces were lower than those of the equal-length strut masts. As before, a suitable configuration should have uniform element forces. Therefore, the magnitudes of the forces in the mast were restricted: (i) no cable force was allowed to be lower than that in the base cables and (ii) the maximum compressive force in the struts could not be larger than five times the tension force in the base cables. These requirements restricted the interval of possible solutions to $\theta^* = 0$–10°.

4.6.2 Preliminary Design of Struts and Cables

The struts of the mast with uniform interior forces were subjected to the largest forces; their design is therefore of most importance. As the struts most likely would be slender, their load bearing capacity is governed by buckling. Consider a perfectly straight column of two rigid bars and a rotational spring at the connecting hinge, Figure 4.14(a). The buckling load of the column is [36]

$$P_{\text{cr}} = \frac{C_M}{l}, \tag{4.13}$$

where C_M is the spring stiffness and l the column length. Now consider that the column has an initial imperfection, ψ_{ini}, with the corresponding lateral mid-point displacement $\Delta \approx \psi_{\text{ini}} l/2$. The mid-point moment $M_{l/2}$ in the imperfect column due to the compressive load P is

$$M_{l/2} = P\Delta \frac{1}{1 - \dfrac{P}{P_{\text{cr}}}}, \tag{4.14}$$

where P_{cr} the buckling load according to (4.13). Rearranging (4.14) yields

$$P = \frac{1}{\dfrac{\Delta}{M_{l/2}} + \dfrac{1}{P_{\text{cr}}}}. \tag{4.15}$$

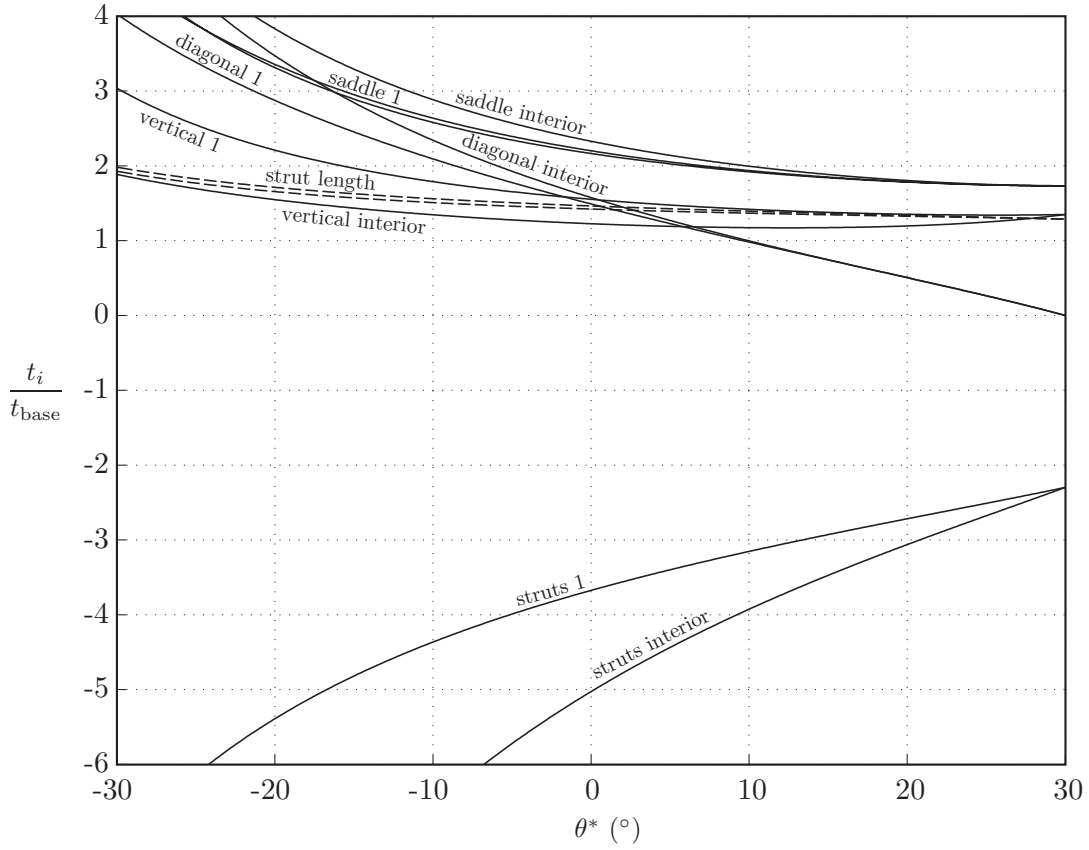

Figure 4.13: Cable and strut forces in the first (and last) and interior stages in a multi-stage mast with uniform interior forces. $D = 1.12$ m, $H_{\text{bay}} = 0.6975$ m and $n = 87$ in (4.12).

In reference [181], the buckling moment, M_{cr}, and rotational stiffness, C_M, of the TSR hinge are measured to 13 Nm and 480 kNmm/rad, respectively. The test for the rotational stiffness was done with a hinge of slightly different geometry than that which was tested for the buckling moment. Formulae for predicting the stiffness indicate that the latter hinge has higher stiffness than the former one. Nevertheless, in the following calculation of the load bearing capacity of the hinged strut, the measured values were used. In order to obtain a high load capacity, the manufactured strut must be as close to straight as possible. While the two bars of the strut can be made nearly straight, the error arising from the alignment of the hinge attachments is probably more severe. Considering the extremely high cost of launching a spacecraft, high manufacturing tolerances are justified; the aim for the strut crookedness was $\Delta \leq l/400$.

At $\theta^* = 0°$, the strut length at the first stage is $l_{s,1} = 1.46$ m, which yields $P_{\text{cr}} = 328$ N using (4.13). Substituting the buckling load, $\Delta = 3.65$ mm and $M = 13$ Nm into (4.15) yielded $P = 300$ N. As this value is very low, no safety factor against buckling was considered in the following analyses and sometimes the compression load was allowed to be higher than the buckling load in order to study the effects of increased prestress. The tubes connected to the hinge were made of CFRP with $E = 210$ GPa and $\rho = 1660$ kg/m^3 [96]. The minimum wall thickness of the tubes

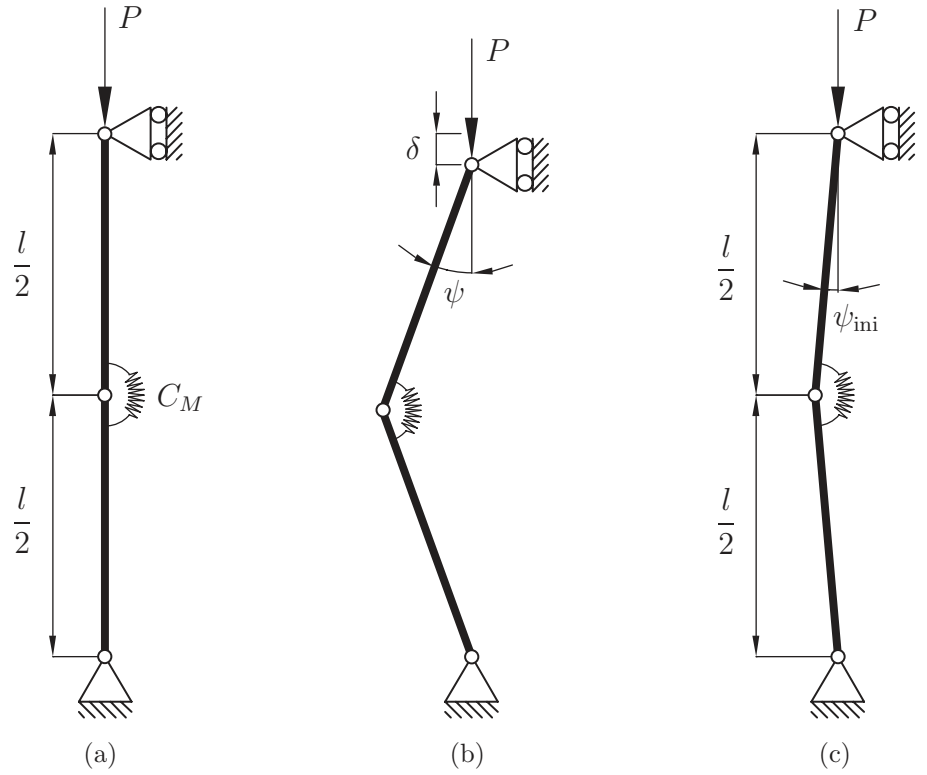

Figure 4.14: Buckling of a two-link column: (a) initial state, (b) buckled state and (c) initial, imperfect state.

was set to 1 mm to ensure adequate toughness for handling and assembly [96]. With regard to length precision requirements, the struts cannot be too slender. A strut diameter of 25 mm yielded, for a pin-ended strut of constant tubular cross-section and length $l_{\mathrm{s},1}$, $P_{\mathrm{Eu}} = 5.28$ kN or about $17P$. The effective axial stiffness of the strut was computed as

$$\left(\frac{AE}{l}\right)_{\mathrm{eff}} = \frac{\left(\frac{AE}{l}\right)_{\mathrm{TSR}} \left(\frac{AE}{l}\right)_{\mathrm{CFRP}}}{\left(\frac{AE}{l}\right)_{\mathrm{TSR}} + \left(\frac{AE}{l}\right)_{\mathrm{CFRP}}}, \tag{4.16}$$

where $(AE/l)_{\mathrm{TSR}}$ is the stiffness of the TSR hinge and $(AE/l)_{\mathrm{CFRP}}$ the stiffness of the CFRP tubes. The measured TSR hinge stiffness is 7223 N/mm, with $l = 88$ mm, [181], and the computed stiffness of the CFRP tubes, with $l = 1460 - 88 = 1372$ mm, is 11540 N/mm. By (4.16) the effective axial stiffness of the strut was 4442 N/mm or 6.485 MN for a length of 1460 mm.

The cables were assumed to be made of thin CFRP tape 5 mm wide and 0.5 mm thick. Its properties were the same as for the tubes above. The allowable stress was set to 200 MPa with safety factor between 5 and 10, which gave an allowable force of 500 N. The axial stiffness of the cables was 0.525 MN.

4.6.3 Vibration Analysis

A few earlier studies have been concerned with the vibrational characteristics of tensegrity masts. Furuya [45] analyses a five-stage mast with contacting struts made of simple triangular prisms. An n-stage mast of this type has $s = m = n$. The prestress, therefore, plays an important part in providing the mast with geometric stiffness. Not surprisingly, the frequencies of the zero energy modes increase with the level of prestress. Murakami [115] performs a modal analysis of a six-stage mast with $v = 3$. The fundamental mode is the one corresponding to the internal mechanism, which is characterised by adjacent counter-twisting of each stage, i.e. a global axial mode. The second mode is a bending mode and its frequency is much higher than the first one. While the frequency of the first mode can be increased by increasing the prestress, the frequency of the flexural mode, which has a non-zero elastic energy, does not change significantly with the prestress level.

The natural frequencies are computed by the classical eigenvalue problem of the homogeneous linear systems

$$\mathbf{K}\mathbf{d} = \omega^2\mathbf{M}\mathbf{d}, \tag{4.17}$$

where $\mathbf{K}$ is the tangent stiffness matrix, $\mathbf{M}$ the mass matrix, $\mathbf{d}$ the displacement vector and ω the angular frequency. For problems with a small number of degrees of freedom, e.g. ten-stage mast, the Matlab function `eig` was used. For larger problems, such as the 87-stage mast, the function `eigs` was used instead. The `eigs` function computes the N largest eigenvalues and their corresponding eigenvectors, where N is a user-defined value. Since the lowest eigenvalues were sought for the present problem, (4.17) was re-written as [47]:

$$\widetilde{\mathbf{K}}\tilde{\mathbf{d}} = \varpi\tilde{\mathbf{d}}, \tag{4.18}$$

where

$$\widetilde{\mathbf{K}} = \mathbf{L}^{\mathrm{T}}\mathbf{K}^{-1}\mathbf{L}, \tag{4.19}$$

$$\tilde{\mathbf{d}} = \mathbf{L}^{\mathrm{T}}\mathbf{d}, \tag{4.20}$$

and

$$\varpi = \frac{1}{\omega^2}. \tag{4.21}$$

The lower triangular matrix $\mathbf{L}$ was obtained by a Choleski factorisation of $\mathbf{M}$:

$$\mathbf{M} = \mathbf{L}\mathbf{L}^{\mathrm{T}}. \tag{4.22}$$

Although not optimised for efficiency, this approach required significantly less computer time when analysing larger problems.

In the present study, the mast and element dimensions were those determined in the previous section. For simplicity, the mass of each hinge, 0.2 kg, was evenly distributed along the length of each strut. The joints between the struts and the cables were assumed to be 25 mm diameter aluminium spheres, each weighing 0.025 kg. The total mass of these joints was evenly distributed along the total length of the cables and the struts.

To gain some understanding of the vibrational characteristics of the tensegrity masts, a ten-stage mast was first analysed. This mast had the same diameter and bay length as the former one, but slightly shorter struts by (4.12). First, the mast was analysed for different values of θ^* between 0 and 10° and a constant prestress of 50 N in the base cables. This analysis yielded, as anticipated, that only the frequency of the mode corresponding to the "axial" internal mechanism, Figure 4.15(a), varied with the prestress in the structure (which changes with θ^*). The frequencies of the flexural modes, Figures 4.15(b) and (c), were unaffected by a change of θ^*. These observations agrees with the ones by Murakami [115]. One configuration, $\theta^* = 10°$, was chosen for further studies on the effects of the prestress level. Note that this particular configuration did not have the highest frequencies but had the lowest internal forces and lowest total mass. The ten-stage mast was analysed for four levels of prestress: 50, 100, 200 and 500 N. The buckling load of the struts, 300 N, was disregarded in this analysis. As before, the flexural modes were not affected by the increased prestress. However, a continuous increase of the prestress eventually resulted in that the frequency of the fundamental, axial mode becoming higher than those of the two first flexural modes. This shift in fundamental mode can be seen in Table 4.2 when going from 200 to 500 N. From the opposite point of view, the axial mode was the fundamental mode up to 24 stages for $t_{\text{base}} = 50$ N. Increasing t_{base} to 100 N gave a fundamental mode shift at 16 stages. Thus, for very long masts the fundamental mode is a bending mode and its frequency is independent of the level of prestress.

The results for the 87-stage mast are shown in Table 4.3. The first two modes were flexural modes with frequencies of 0.037 Hz, which can be compared with 0.10 Hz for the STRM ADAM. The frequency of the axial mode was 0.13 Hz for the lowest prestress. For a cantilever beam, the lowest bending frequency is [120]

$$f_{1,\text{cb}} \approx \frac{3.516}{2\pi}\sqrt{\frac{EI}{ml^4}}. \tag{4.23}$$

Substituting the data for the STRM ADAM, $f_{1,\text{cb}} = 0.10$ Hz, $m = 4.80$ kg/m and $l = 60.68$ m, into (4.23) and solving for EI yielded $EI = 2.1$ MNm^2, which is about 6 times lower than the value given in Table 4.1. However, the frequency given in

Table 4.2: Data and results from the modal analysis of the ten-stage mast. Axial mode frequencies in bold face.

n	θ^* (°)	η	Length (m)	Mass (kg)	m_c (kg/m)	m_s (kg/m)	$\sum l_c$ (m)	$\sum l_s$ (m)
10	10	0.2412	6.975	13.1	0.0136	0.2819	118.2	40.7

t_{base}	f_1	f_2	f_3	f_4	f_5	$t_c^{\max}$	$t_c^{\min}$	$t_s^{\max}$	$t_s^{\min}$
50	**1.1787**	2.8214	2.8468	4.1371	12.0952	99	48	−194	−156
100	**1.6442**	2.8224	2.8478	5.2359	12.6260	199	97	−388	−312
200	**2.3006**	2.8245	2.8499	6.8581	13.5714	397	194	−776	−623
500	2.8307	2.8562	**3.6006**	9.9618	15.6138	994	484	−1939	−1559

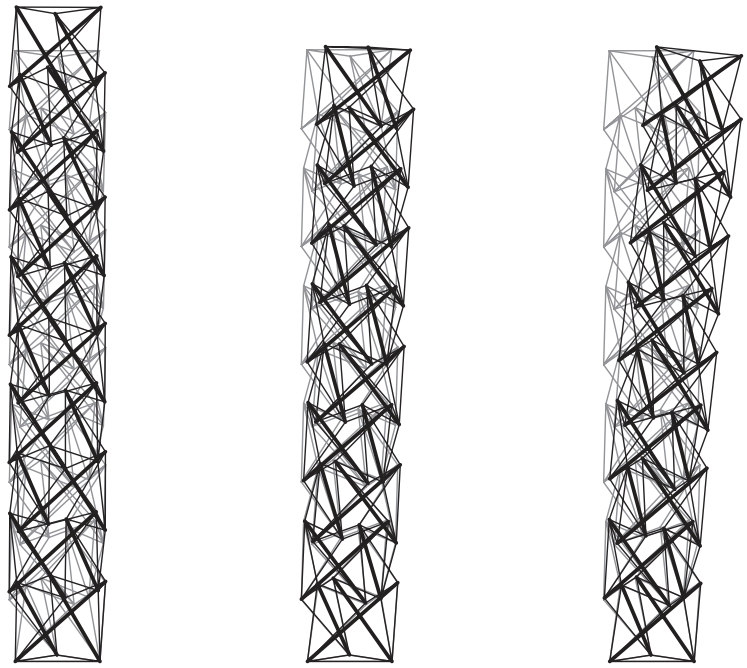

(a) (b) (c)

Figure 4.15: First three eigenmodes of a ten-stage tensegrity mast ($t_{\text{base}} = 50$ N and $\theta^* = 10°$): (a) $f_1 = 1.179$ Hz, (b) $f_2 = 2.821$ Hz and (c) $f_3 = 2.847$ Hz.

Table 4.3: Data and results from the modal analysis of the 87-stage mast. Axial mode frequencies in bold face.

n	θ^* (°)	η	Length (m)	Mass (kg)	m_c (kg/m)	m_s (kg/m)	$\sum l_c$ (m)	$\sum l_s$ (m)
87	10	0.2412	60.683	114.2	0.0134	0.2805	1047.9	357

t_{base}	f_1	f_2	f_3	f_4	f_5	$t_c^{\max}$	$t_c^{\min}$	$t_s^{\max}$	$t_s^{\min}$
50	0.0374	0.0374	**0.1324**	0.2339	0.2340	100	49	−196	−158
100	0.0374	0.0374	**0.1872**	0.2340	0.2341	199	98	−393	−315
200	0.0374	0.0374	0.2342	0.2342	**0.2646**	399	196	−785	−631
500	0.0375	0.0375	0.2347	0.2348	**0.4174**	997	490	−1963	−1577

Table 4.1 may include the 360 kg antenna attached to the tip. By Raleigh's method the first frequency of a cantilever beam with a point mass M at its tip can be written as [120]:

$$f_{1,\text{cb,pm}} \approx \frac{1}{2\pi}\sqrt{\frac{3EI}{l^3\left(M + \frac{33}{140}ml\right)}}. \tag{4.24}$$

Substituting $M = 360$ kg into (4.24) yielded $EI = 12.6$ MNm^2, which is much closer to the stated value. Inserting the values of the 87-stage (or the ten-stage) tensegrity mast in (4.23) produced $EI = 0.11$ MNm^2. Hence, the STRM ADAM is more than 100 times stiffer than the tensegrity mast in bending.

4.6.4 Static Analysis

For a complete analysis of the tensegrity mast, its static properties must be investigated. Static analyses of tensegrity masts with three struts per stage have previously been performed by several researchers. Skelton and He [149] compute the axial stiffness and the buckling load of a 186 m long, six-stage tensegrity mast for a deep sea project. Sultan and Skelton [161] analyse the axial and torsional stiffness of a two-stage mast. As anticipated, the stiffness increases with the prestress level. A more thorough study of the two-stage mast stiffness is presented by Skelton *et al.* [150]. The axial stiffness increases as the struts become more vertical, i.e. decreasing colatitude, and the prestress increases the axial stiffness in the case of small external forces; as the external forces increase, the effects of prestress can be neglected. The bending stiffness is constant until one or more cables go slack. After a cable has gone slack, the bending stiffness drops and becomes a non-linear monotonically decreasing function of the applied loading. As the colatitude increases, i.e. the struts become more horizontal, the bending stiffness increases. Their final observation is that prestress does not affect the bending stiffness of the mast provided the cables are taut, but does delay the onset of cable slackening. Pak [118] analyses the axial, bending and torsional stiffness of a four-stage mast. Again it is found that the axial stiffness is almost equal in tension and compression and increases with the external loading. The bending stiffness of the four stage mast is constant until a cable goes slack. The torsional stiffness is identical in the clockwise and counter-clockwise directions.

The studies above clearly show that the strength and stiffness in bending are the critical properties of tensegrity masts. Therefore, the focus of this study was on the bending properties of the ten- and 87-stage masts, but the axial stiffness was also computed. As this analysis was not intended to be a parametric study, only configurations with $\theta^* = 10^\circ$ were considered. Following the approach in reference [150], four load cases were considered, Figure 4.16.

The masts were analysed by a geometrically non-linear FEM, with the struts modelled by two-node bar elements and the cables by no-compression catenary elements, cf. [171]. The special catenary element is advantageous in problems where cable

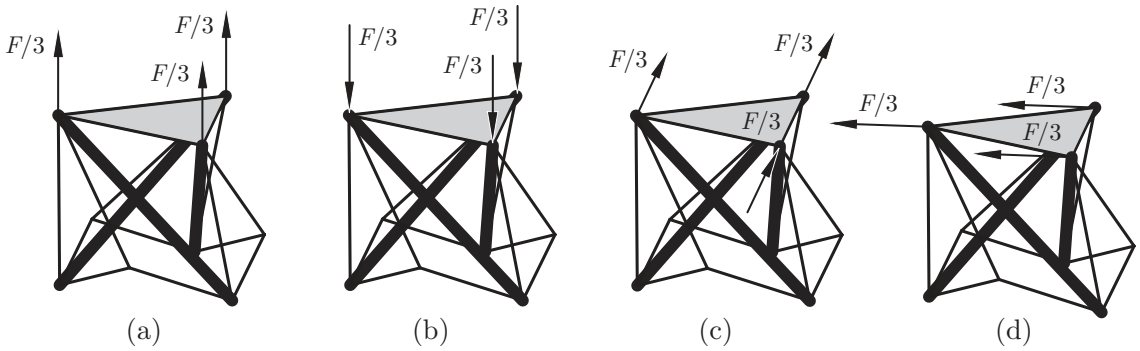

Figure 4.16: Load cases for the tensegrity mast: (a) tension, (b) compression, (c) bending in direction B1 and (d) bending in direction B2.

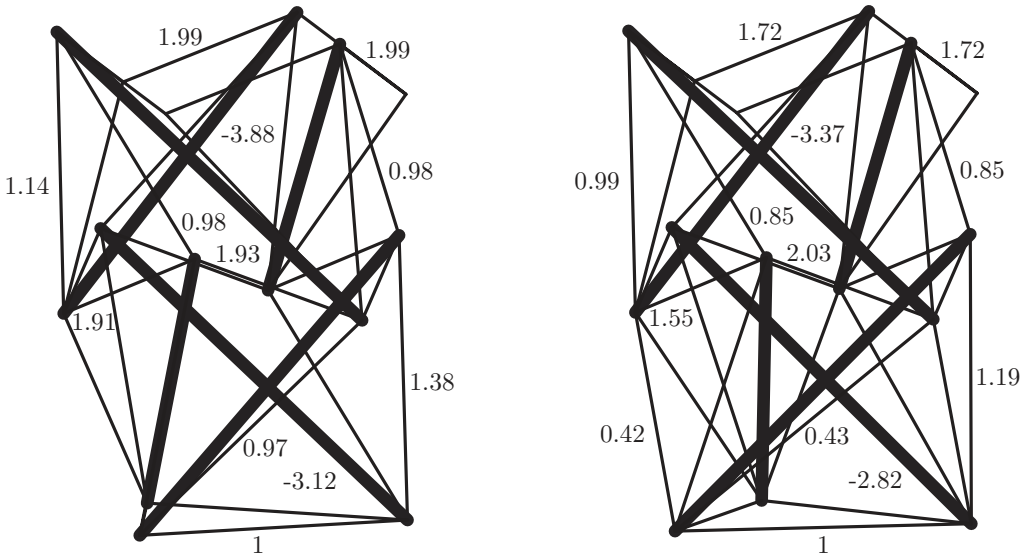

Figure 4.17: Normalised forces in the two lowest stages of ten-stage tensegrity masts: (a) un-stiffened and (b) stiffened.

slackening may occur.

Since the internal mechanism of the masts makes them weak in the axial direction, a way of stiffening the mast was investigated. Three additional cables were added to the first stage so that it became fully triangulated, Figure 4.17. In the original configuration, these cable were unstressed, which cannot be accepted. One way to prestress the cables was to further rotate the first stage so that the struts became longer. The resulting mast now had three independent states of self-stress, $s = 3$, and no internal mechanism. Among these states of self-stress a rotationally symmetric combination $\mathbf{s}_{\text{sym}}$ was sought,

$$\mathbf{s}_{\text{sym}} = \alpha_1 \mathbf{s}_1 + \alpha_2 \mathbf{s}_2 + \alpha_3 \mathbf{s}_3. \tag{4.25}$$

The α's were found by equating the element forces in the base cables to unity. The element forces in the mast now changed. For the ten-stage mast the element forces in the first two stages are shown in Figure 4.17, both for a normal and a stiffened mast with an additional 15° rotation of the first stage. The results for the ten-stage masts are shown in Figures 4.18 and 4.19.

The behaviour of the un-stiffened mast under axial loading was about the same in tension and compression. In compliance with the findings by others, the mast got stiffer as the load increased. The initial stiffness of the un-stiffened mast was 275 kN/m. The response of the stiffened mast differed slightly in tension and compression. Generally, the stiffened mast was stiffer in tension although the initial stiffness was about the same, 420 kN/m. However, at a loading of 16.3 N three diagonal cables on stage 2 went slack (marked as a discontinuity in the curve) and the stiffness decreased. Under compression no cable became slack.

In bending, the diagonal cable on the compressed side at the second stage became

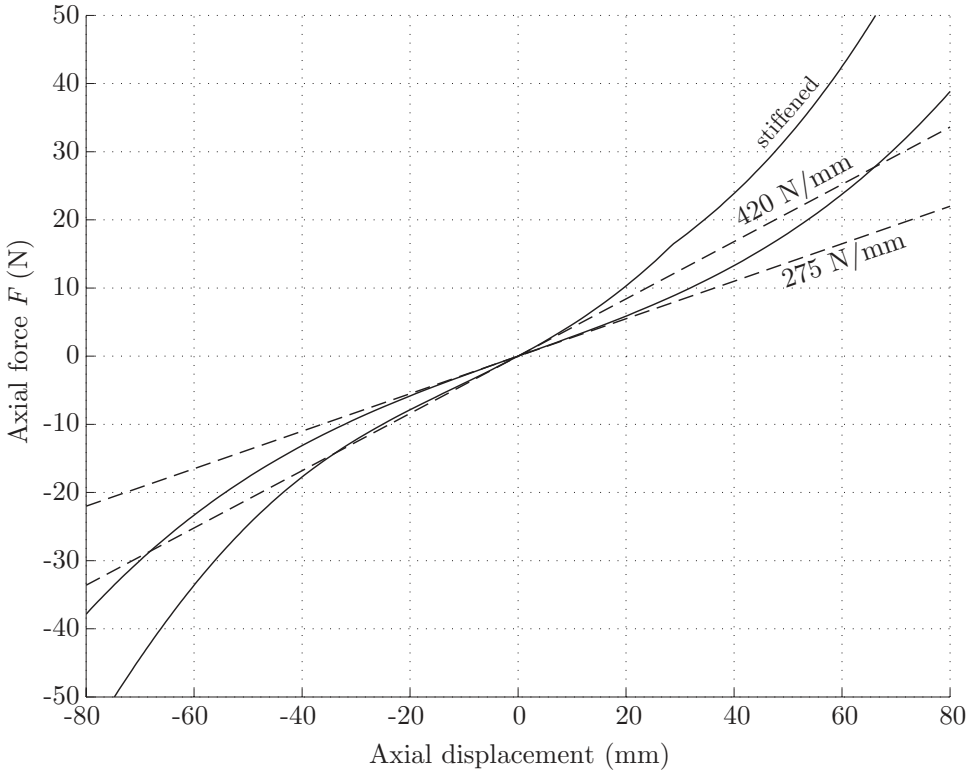

Figure 4.18: Load–displacement curves for an un-stiffened and a stiffened ten-stage tensegrity mast subjected to axial loading.

slack at $F = 11.2$ N for load direction B1. For direction B2, the same cable went slack at 11.0 N. The bending stiffness was about the same in each direction before and after cable slackening. The bending stiffness of the mast with no slack cables was 110 kNm^2, as determined by the vibration analysis. After a cable went slack, the bending stiffness immediately dropped to 22 kNm^2. The case of the stiffened mast was a bit different. For direction B1, one of the additional cables on the compressed side of the mast already went slack at 3.9 N; for direction B2 it happened at 4.2 N. For B1 the next cable to go slack was a diagonal cable at stage 3 and this occurred at 9.8 N. For B2 it was a diagonal cable at stage 1 at the load of 8.6 N. A further increase of the load resulted in more and more cables becoming slack and the bending stiffness dropped suddenly at every occurrence as noted in Figure 4.19.

As regards the low bending stiffness of the ten-stage mast, it was not necessary to perform a complete analysis of the 87-stage mast. For example, a lateral load $F = 1$ N would give a tip displacement of 677 mm, hence the mast is much too flexible.

4.7 Discussion

Using the remarkably simple relationship by Nishimura [117], the form-finding of straight, multi-stage tensegrity masts with an adequate prestress distribution is no

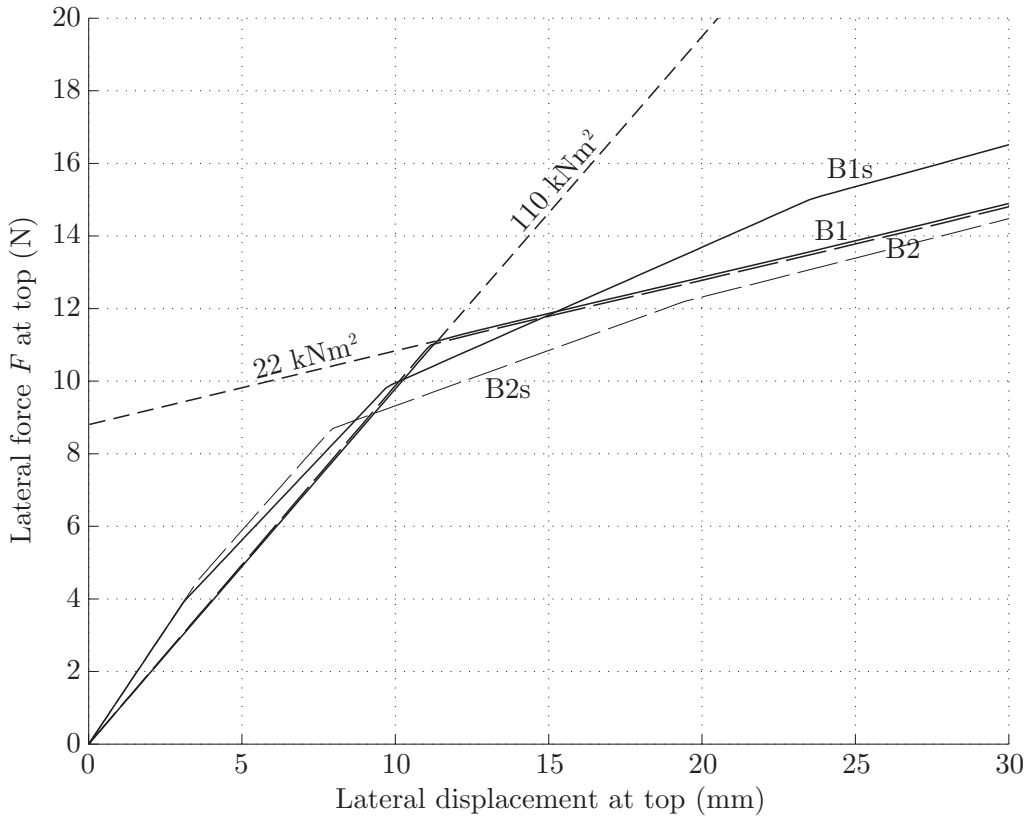

Figure 4.19: Load–displacement curves for an un-stiffened and a stiffened ten-stage tensegrity mast subjected to lateral loading. Each discontinuity indicates that yet another cable has become slack.

longer an obstacle in design.

The proposed manufacturing scheme eventually turned out to be satisfactory when all the early mistakes had been eliminated. The use of joints, with holes drilled to the correct three-dimensional angles, should eliminate the last obvious source of inaccuracy.

The suggested strut deployment approach worked well. One inherent problem with tensegrity masts are that they do not reach full stiffness until the last stage is deployed. This seriously limits the applicability of these masts. However, it might not be that difficult to provide the deployed portion of the mast full stiffness. Since most of the stages are equal, with nodes lying on a regular hexagon, it must be possible to give the saddle cables the correct prestress and the saddle nodes the proper restraints in order to prestress the deployed part of the mast. These restraints must take on the role of the struts and the cables of the stage that is next in line to be deployed.

One approach to reduce the risk of the cables getting tangled up in the struts is to use tape-like instead of cord-like cables. Tapes have a natural folding direction and it is presumably attainable to arrange the cables such that they do not get caught by struts during deployment. This needs to be studied further.

The structural behaviour of the multi-stage mast concur with the predictions of studies by other researchers; namely, the masts are relatively stiff axially but very weak in bending. The removal of the internal mechanism did not improve the behaviour significantly; the initial axial stiffness increased by about 50%, but the bending stiffness cannot be said to have increased at all as the first cable went slack at a very low load level.

Chapter 5

Design Prerequisites for a Deployable Reflector Antenna

This and the following two chapters will provide an in-depth description of the development of a deployable reflector antenna aimed for small satellites. In the present chapter, the background and motivation behind the new concept are described along with examples of other small satellites using deployable structures. State-of-the-art antenna concepts, which may be suitable for the present application, are studied. Then, the new antenna structure is introduced.

A parabolic reflector antenna can be given two different configurations: axi-symmetric or offset; the geometries of these configurations will be presented. One particular aspect, the required smoothness of the reflector surface, will significantly affect the choice of structural concept. The effects of the surface accuracy on the antenna performance, accuracy characteristics of different concepts, and surface accuracies of existing deployable antennas will be presented. Finally, suitable materials for the antenna structure will be selected.

This chapter can be seen as an introduction to reflector antennas with a requirement specification for the particular antenna, which will be developed in Chapters 6 and 7. This background information is necessary to fully appreciate decisions and judgments made later on in the thesis.

5.1 Small Satellites and Deployable Structures

Conventional satellite technology has for several decades been focused on a small number of large, complex spacecraft. Recently these satellites have been complimented by systems which use several smaller satellites in *Low Earth Orbit*[1] (LEO) [39]. Micro-satellites, i.e., with a mass less than 50 kg, have been used for technology tests and amateur radio for almost two decades, but they were not

[1] A LEO often has an altitude below 1,000 km, where the radiation from the Van Allen belt is low (p. 181 in [183]).

viewed as useful for space science research because of their small size [48]. In the 1980s, micro-satellites in LEO were recognised due to their advantage in digital communication. Users send a message to the satellite during its passage and the message could then be delivered throughout the world, thereby providing global mail service, which even a large satellite in a *Geosynchronous Orbit*[2] (GEO) cannot provide [39].

Today, small satellites are developed for short-time missions and quickly put together by small teams. The use of fewer and more contemporary components also helps to reduce the cost of the spacecraft [39]. Small satellites are therefore an affordable way to space for the military, universities and industry. Modern small satellites are launched at low cost as secondary payloads, or so-called piggyback passengers, along with a large spacecraft payload. NASA's *Space Shuttle* has several ways of accommodating payloads in its payload bay. Two of the carrier systems are the *Get Away Special* and *Hitchhiker*, using cylindrical containers of different sizes mounted on the bay wall [39]. In Europe, Arianespace developed the *Ariane Structure for Auxiliary Payloads* (ASAP) to accommodate secondary payloads on the Ariane rockets. Mounted on the Ariane-4 rocket the ASAP can carry six small satellites, each with a mass of up to 50 kg. The ASAP on the Ariane-5 rocket, Figure 5.1, can accommodate eight satellites, each weighing less than 120 kg [3, 39]. Launch resources for secondary payloads often have a single price for payloads under a certain mass limit, but, in general, they are volume rather than mass constrained. However, it should be kept in mind that these secondary payloads do not have a guaranteed launch date [39].

Deployable structures have been used on small satellites since the beginning of the space programme. In recent years they have fallen into disfavour due to their higher risk, complexity, and several failures [136], e.g. the high-gain antenna on Galileo. In order to facilitate the design of reliable mechanisms, it is important to recognise the risk associated with such structures from the onset of the mission programme [136]. A few examples of small and micro-satellites with deployable structures are given below.

5.1.1 Micro-Satellites Astrid-1 and -2

Sweden's first micro-satellite, Astrid-1, Figure 5.2(a), was launched on January 24, 1995 from the Plesetsk Cosmodrome in Russia as a piggyback passenger on a Kosmos-3M launch vehicle to an altitude of about 1,000 km. Astrid-1 was designed and developed by *Swedish Space Corporation* (SSC). The total mass of Astrid-1 was 27 kg. With solar panels stowed, the dimensions was approximately $0.45 \times 0.45 \times 0.29$ m^3, and with solar panels deployed $1.1 \times 1.1 \times 0.46$ m^3 (including antennas). The mass and dimensions were chosen because they represented about half the maximum permitted values of a micro-satellite on the Ariane-4 ASAP [48]. In total, the four solar panels, each 0.39×0.29 m^2, produced 42 W.

[2]The period of a GEO is 23 hours 56 minutes and 4 seconds, matching the Earth's rotational motion.

Figure 5.1: DERA's small satellites STRV-1 C and D on Ariane-5 ASAP for launcher fit check (Courtesy of DERA).

The second Swedish micro-satellite, Astrid-2, Figure 5.2(b), also designed by SSC, was launched on December 8, 1998 from the same site, on a similar launch vehicle, and to a similar altitude as Astrid-1. The total mass of Astrid-2 was 29 kg. With solar panels stowed, the size was $0.95 \times 0.45 \times 0.30$ m^3, and with solar panels deployed $1.7 \times 1.1 \times 0.3$ m^3. The total power of the six solar panels, each 0.39×0.29 m^2, was 80 W. The design lifetime for Astrid-2 was one year, but on July 24, 1999 contact with the satellite was lost and never re-established despite several attempts [163].

On Astrid-1, the solar panels are the only deployable structures. The design is simple and reliable; one pair of hinges with a common axis of rotation on each solar panel. On Astrid-2, a similar deployment technique was used for four of its six solar panels, while the remaining two panels were non-deployable. Astrid-2 also had a two-hinged deployable boom, oriented along its spin axis, which carried a device for attitude determination plus one of the scientific payloads. It appears from Figure 5.2(b) that the boom unfolds in a plane and that a cable is used to stop the unfolding and to correctly position the boom.

5.1.2 Small Satellite Odin

Another satellite developed by the SSC is the small satellite Odin. The primary payload on Odin is a 1.1 metre non-deployable, solid surface, offset reflector antenna. The mass of the main reflector is 5.5 kg, and the total antenna mass, including the sub-reflector and supporting structure, is 9.9 kg. Odin has a total mass of 250 kg, a height of 2.0 m, and a base area of 1.1×1.1 m^2 with stowed solar panels,

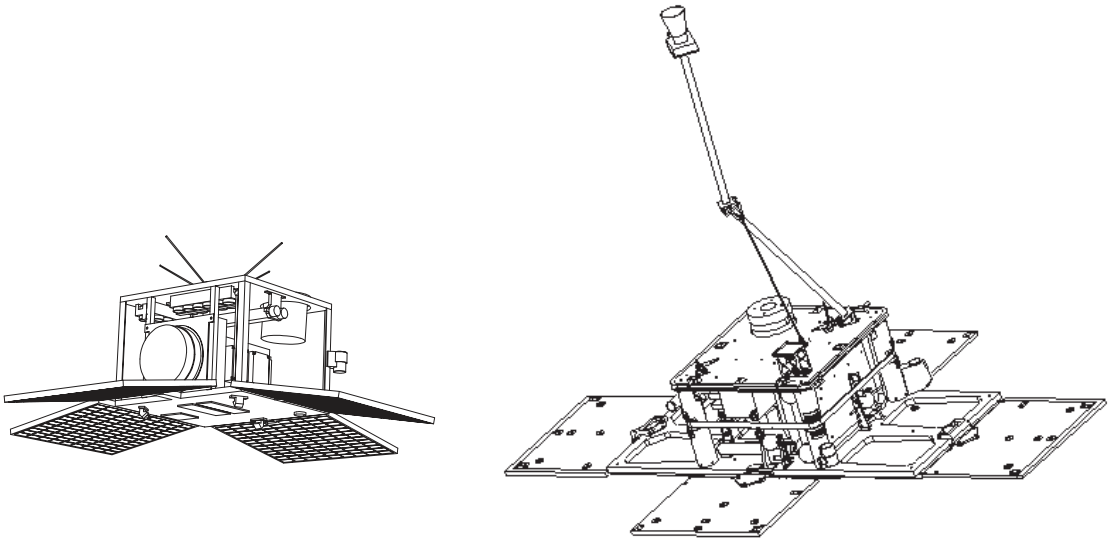

(a) (b)

Figure 5.2: The Swedish micro-satellites (a) Astrid-1 and (b) Astrid-2 with solar panels deployed (Courtesy of Swedish Space Corporation).

Figure 5.3(a), and 3.8×3.8 m^2 with deployed solar panels, Figure 5.3(b). Odin was launched on February 20, 2001 from Svobodny, Russia, as the only payload on a Start-1 launch vehicle to an altitude of 600 km. A piggyback launch would have been a more economically viable alternative, but that would have compromised the scientific objectives and led to a more complex satellite design [164]. The four solar panels, each approximately 1.4×0.75 m^2, provided 340 W of power. The design lifetime for Odin is two years.

The Odin satellite is significantly larger than the Astrid satellites in order to accommodate the reflector antenna, solar reflectors and other scientific instruments. Further, given the high operating frequency of the antenna (580 GHz), only a solid reflector surface can give the required surface accuracy (10 μm). However, a deployable solid surface antenna could have been used instead, but at a higher mission risk.

5.1.3 Space Technology Research Vehicles

In 1989, the *Defence Evaluation and Research Agency* (DERA) at Farnborough[3] in United Kingdom started the *Space Technology Research Vehicle* (STRV) programme as a single micro-satellite project. The project objectives were to show that small, low cost satellites could offer affordable space-based research to civil government, industry, and academic organisations, and also provide support to military defence research objectives [32].

[3]DERA Farnborough was renamed QinetiQ on July 2, 2001, but will in this thesis still be referred to as DERA.

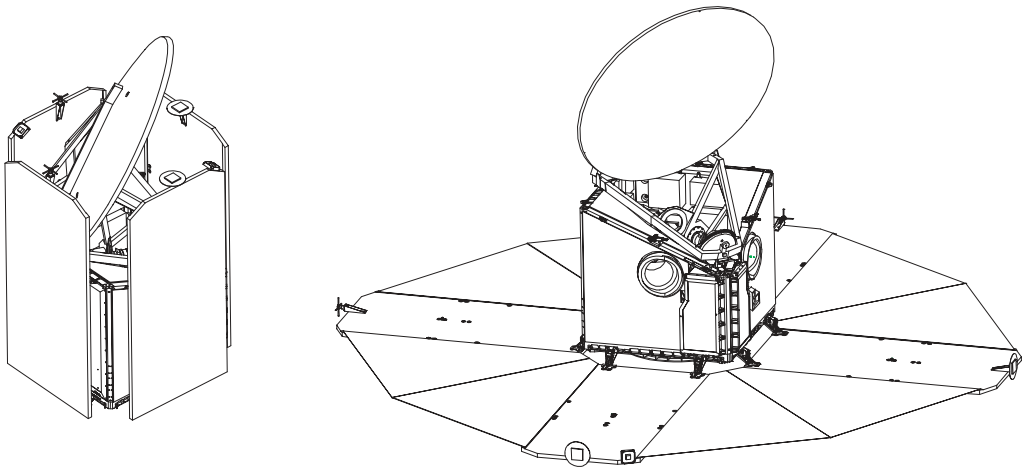

(a) (b)

Figure 5.3: The Swedish small satellite Odin with solar panels (a) stowed, and (b) deployed (Courtesy of Swedish Space Corporation).

The first two micro-satellites of the programme, STRV-1 A and B, were launched on June 17, 1994 from the *Guiana Space Centre*, Kourou in French Guiana. They were piggyback passengers on an Ariane-4 launch vehicle to a *Geosynchronous Transfer Orbit* (GTO) [32]. The dimensions of both STRV-1 A and B were $0.45 \times 0.45 \times 0.47$ m^3, while the mass was 50 and 53 kg, respectively, due to different scientific payloads. The satellites had solar panels on four of its sides, each approximately 0.40×0.45 m^2, providing a total power of 31 W [32]. Unlike the Astrid satellites, STRV-1 A and B had no deployable structures, e.g. solar panels. The design lifetime of STRV-1 A and B was one year, but they continued conducting orbital operations until September 1998 when they were donated to the University of Colorado at Boulder, USA, allowing students to operate the satellites [32].

Following the success of STRV-1 A and B, DERA designed two new satellites, STRV-1 C and D, which could accommodate more scientific payloads and thereby widen the scope of mission objectives [32]. The new payload required a larger spacecraft structure, capable of generating 80 W, which is more than twice the power available on STRV-1 A and B. The dimensions of STRV-1 C and D were $0.7 \times 0.6 \times 0.7$ m^3, Figure 5.4. Each satellite weighed about 100 kg. STRV-1 C and D were launched on November 15, 2000 from the same site as their precursors, again as auxiliary payloads, but this time on an Ariane-5 launch vehicle to a GTO. However, only two weeks after launch, the mission was brought to a premature ending when the receivers of both satellites were cut from their power source because of a design mistake. This means that the satellites cannot receive anything sent from the ground, including recovery commands [145].

5.1.4 Future STRV Missions

In the spring of 2000, DERA started the plans for future STRV missions. The main areas of interest include a space based *Global Positioning System* (GPS) for attitude and orbit determination, and miniature remote sensing [32]. These tasks would necessitate the use of deployable structures and outline requirements are formulated for a range of such structures by DERA in reference [136]. These requirements can be divided into three categories:

1. Booms for space based GPS applications,
2. *Synthetic Aperture Radar* (SAR) antenna for remote sensing, and
3. Solar arrays of 1.5–2 kW, needed to run the SAR antenna.

In remote sensing, a high image resolution is the primary goal. Generally, a higher resolution is obtained using a larger antenna, but placing a large antenna in space is extremely expensive. By using the motion of the spacecraft and advanced signal processing techniques, a larger antenna can be simulated. This is, in very simple terms, the principle behind the SAR technology. The performance of a SAR antenna is affected by a number of parameters but one especially important is its size. Hence, one of the biggest limitations in performing a SAR mission using a small satellite, is the problem of stowing a large antenna in a small volume. Various SAR antenna options are available [136]:

- Parabolic reflector,
- Planar array, or
- Reflect array.

In DERA's requirements, no specific mission had been identified, so the stowage constraints for the deployable structures were assumed to be defined by the envelope around the STRV-1 C and D satellites on the Ariane-5 ASAP [136], Figure 5.4.

DSL was given the task of designing deployable structures to meet the requirements by DERA. As most of the existing technologies of deployable structures are aimed for large spacecraft applications, it was soon found that new technology was needed to meet the requirements by DERA. In response to these requirements, three novel deployable structures, related to categories 2 and 3 above, were developed. These are presented in reference [130]. In that study, the author was involved in the development of a 3 m diameter parabolic reflector SAR. The operating frequency for this antenna is assumed to be in the X-band (9.65 GHz) as most recent systems use this frequency. The mass goal for the main reflector alone is 20 kg. Including electronics, feed, support, etc. the total payload mass goal is 150 kg [136].

The preliminary study of the SAR reflector antenna, performed by Pellegrino and the author, is presented in references [130] and [169]. This study will now be significantly

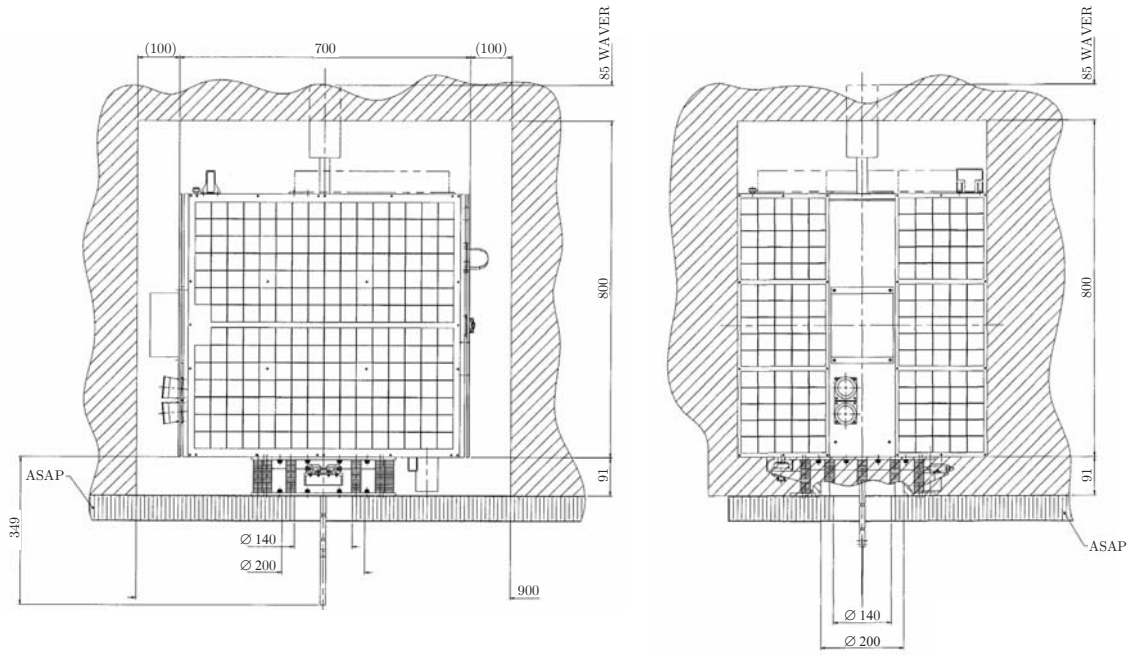

(a) Front view (b) Side view

Figure 5.4: Envelope of the STRV on ASAP ring (Courtesy of DERA).

expanded. The aim of the following and the next two chapters is to provide a thorough feasibility study of the new reflector concept.

5.2 New Reflector Concept for Small Satellites

The main difficulty in meeting the requirements by DERA is the very stringent constraints on the dimensions of the packaged envelope, $800 \times 200 \times 100$ mm^3. A concept which would easily conform to these dimensions is the inflatable reflector. Much work is currently being done on inflatable reflectors, mainly in the USA, cf. [42, 67], but still they cannot be regarded as a mature technology. An inflatable antenna is therefore not considered as an alternative for the present application. In addition, the required stowed size immediately rule out all umbrella-type mesh antennas as the hubs of these are too large. The stowed size of these antennas also tend to be more cubic than oblong that is needed here, e.g. the *Collapsible Rib-Tensioned Surface* (CRTS) reflector [78]. Many umbrella-type antennas also rely on active control of the surface shape which complicates the overall design, e.g. the HRA. A better design would be one that passively, i.e. without active control, provides the required surface accuracy. This naturally leads us to the concept of the tension truss, briefly described in section 2.3.1.

5.2.1 Existing Concepts with Passive Structure

The research on antennas which passively, i.e. without active control, achieve the required surface accuracy started in the early 1980s with NASA's *Large Deployable Reflector* (LDR) programme, cf. [96].

The current state-of-the-art of high precision antennas with a passive structure is the AstroMesh antenna. The stowed height of the AstroMesh is given by the length of one vertical plus one horizontal strut. For a given aperture and number of bays it is not possible to change the length of the horizontal struts. It is, however, possible to shorten the vertical struts by making the rear net shallower, say half the depth of the front net, if larger forces in the ring are accepted. For example, a 3 m diameter reflector with $F/D = 0.4$ and a ring truss divided into 18 bays would, with identical front and rear nets and no separation between the nets, have a stowed height of 1.46 m. If the height of the rear net is halved, the stowed height is 1.22 m. In general, an AstroMesh reflector with small F/D requires a high ring truss with too high stowed height for the present application. An alternative ring structure based on a pantograph concept, cf. [188], with, again, 18 bays would have a packaged height of about 0.9 m. However, this requires a large number of joints which add a significant mass to the structure. The tension truss antenna for the HALCA satellite, Figure 2.14, has, like the umbrella-type antennas, a large hub and is therefore not suitable for the present application.

Although none of the existing designs are directly applicable, it is considered that an adaptation of the AstroMesh concept offers the greatest potential for meeting the requirements with a low-cost system. The main parts of the new concept is presented below.

5.2.2 Tensegrity Reflector Concept

The new reflector antenna concept, Figure 5.5, is based on the tensegrity and tension truss concepts. Like the AstroMesh antenna, it is composed of three main parts:

- a deployable ring structure, Figure 5.5(b),
- two identical cable nets (front and rear nets), Figure 5.5(b), connected by tension ties, Figure 5.5(c), and
- the reflecting mesh, attached to the front net, Figure 5.5(a).

The complete antenna structure is composed of a large number of tension elements, i.e. the net cables and constant-tension springs, and only six compression elements, i.e. the struts. The deployable ring structure is a one-stage tensegrity module with six struts which has one state of self-stress and seven internal mechanisms of inextensional deformation. The tensegrity module alone is very flexible, but as will be shown in the next chapters, the complete antenna structure is quite stiff.

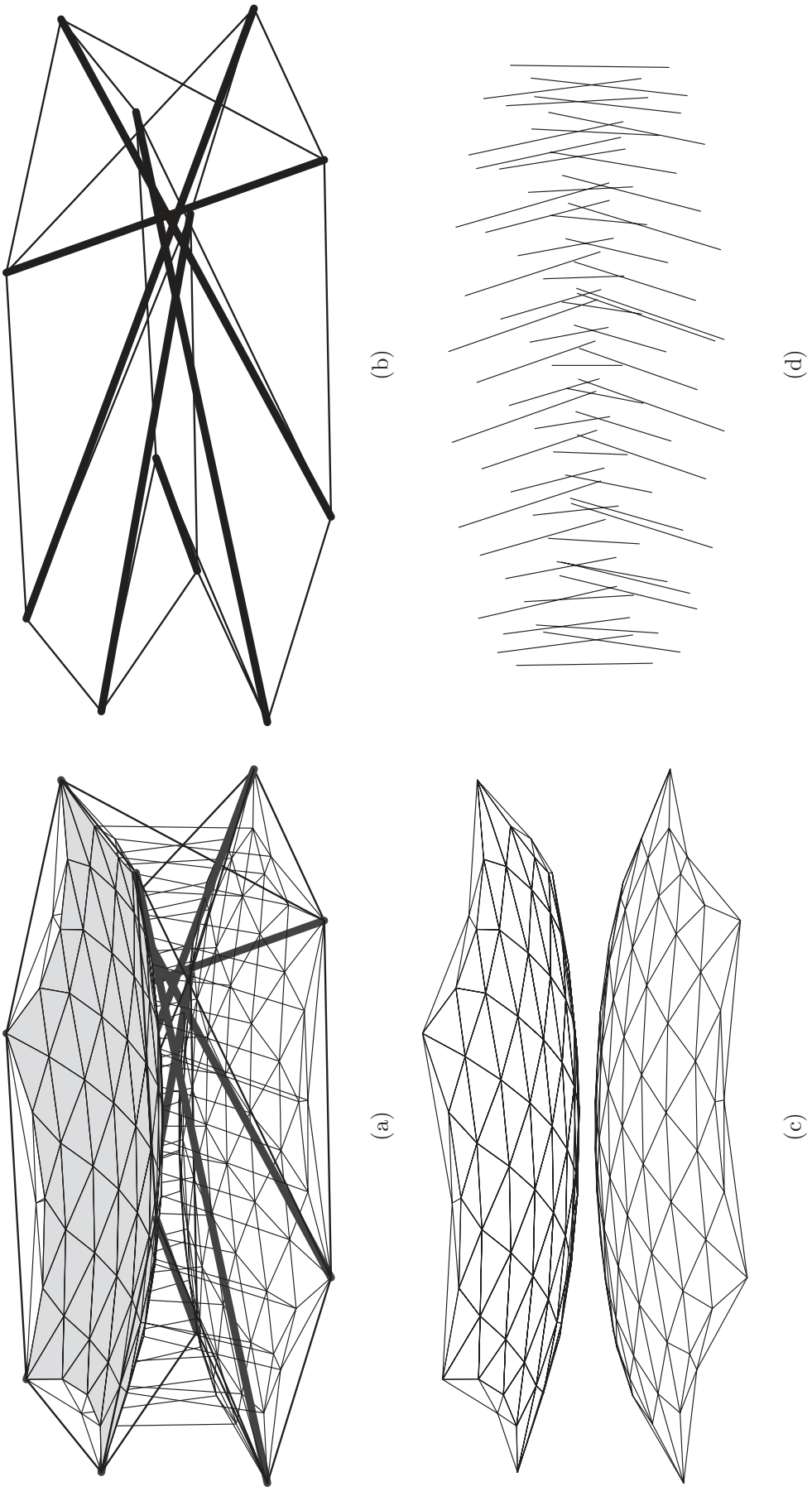

Figure 5.5: The new tensegrity reflector concept for small satellites: (a) the complete structure with RF reflective mesh attached to the front net, (b) the tensegrity ring structure, (c) the front and rear nets, and (d) the tension ties connecting the nets.

Although the concept above is new, it consists of several known substructures put together to meet the requirements of stowage size. The main difference compared to previous concepts must be the deployable ring structure. The present ring structure was inspired by new ideas of using tensegrity for deployable space antennas, cf. [71].

5.3 Geometry of Parabolic Reflector Antennas

Reflector systems are the basic types for satellites because of their low mass, low complexity and cost, and design maturity. Two important properties make the parabolic reflector, where the reflecting surface is a paraboloid of revolution, especially useful as an antenna [158]:

- Incident rays parallel to the reflector axis converge to a spot known as the focal point. Conversely, all rays leaving the focal point are parallel to the reflector axis after reflection from the parabolic surface.
- All path lengths from the focal point to the reflector and onto the aperture plane are the same and equal to $2F$, where F is the focal length, i.e. the distance from the apex of the paraboloid to the focal point, Figure 5.6.

Basically, a reflector antenna consists of two components: a reflecting surface that is large relative to the operating wavelength and a much smaller sub-reflector, placed close to the focal point of the main reflector. The role of the sub-reflector is to re-direct the rays reflected in the main reflector to the feed.

5.3.1 Axi-Symmetric Reflector

The simplest antenna has an axi-symmetric parabolic reflecting surface. In a Cartesian coordinate system, xyz, this surface is described by

$$z = \frac{x^2 + y^2}{4F}. \tag{5.1}$$

It is most common to specify the reflector in terms of the diameter D and focal-length-to-diameter ratio F/D, which give the size and curvature, respectively [158]. The angle θ_0 from the Z-axis to the reflector rim is

$$\theta_0 = 2 \arctan \frac{D}{4F}. \tag{5.2}$$

As $F/D \to \infty$, the reflector becomes planar and when $F/D = 0.25$, the focal point lies in the plane passing through the reflector rim. It is sometimes useful to know the height of the reflector H_0, which is computed as:

$$H_0 = \frac{D^2}{16F}. \tag{5.3}$$

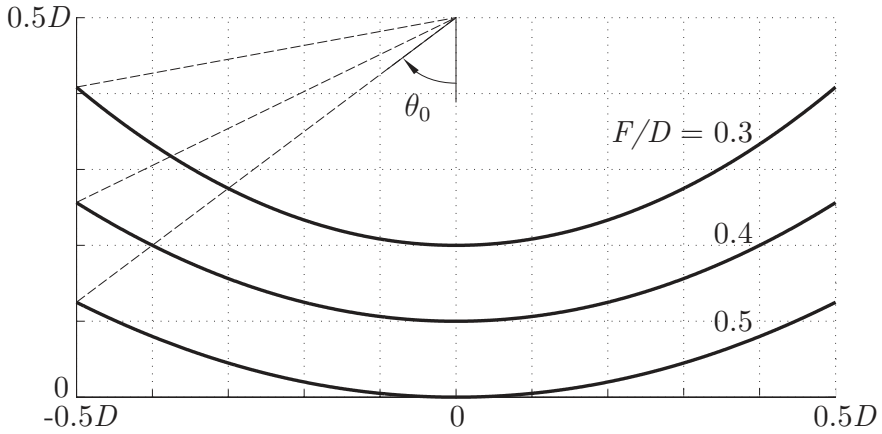

Figure 5.6: Parabola shapes for $F/D = 0.3,\ 0.4,\ 0.5$.

A disadvantage of axi-symmetric reflectors is that the feed antenna and its support structure in many cases are bulky and block the incident rays, resulting in reflector performance degradation. To eliminate or reduce aperture blocking reflector antennas with offset feeds are used [158]. An offset parabolic reflector may also simplify the satellite design as the feed can be contained within the satellite structure, without the need of a support structure [183].

5.3.2 Offset Reflector

The offset parabolic antenna is constructed by considering a parent paraboloid with diameter D_p, Figure 5.7. Then a cylinder of radius R_a, whose axis is parallel to the Z-axis, is defined in the first and fourth quadrants of the XY-plane. The intersection of this cylinder and the parent paraboloid is a plane ellipse which defines the rim of the offset reflector. In Figure 5.7, the surface of the offset reflector is visualised by the intersections of several concentric cylinders and the parent paraboloid. Also shown are the coordinate systems xyz and $x'y'z'$, both with origins at O in the centre of the offset reflector. Referring to Figure 5.8, the following relations are derived [78]:

$$\phi_a = \arctan \frac{X_O}{2F}, \tag{5.4}$$

$$\begin{pmatrix} x \\ z \end{pmatrix} = \begin{pmatrix} X \\ Z \end{pmatrix} - \begin{pmatrix} X_O \\ X_O^2/4F \end{pmatrix}, \tag{5.5}$$

and

$$\begin{pmatrix} x' \\ z' \end{pmatrix} = \begin{bmatrix} \cos\phi_a & \sin\phi_a \\ -\sin\phi_a & \cos\phi_a \end{bmatrix} \begin{pmatrix} x \\ z \end{pmatrix}. \tag{5.6}$$

Note that $Y = y = y'$. For a given point (x', y') the z' coordinate is found by substituting (5.5) and (5.6) into (5.1). Simplifying gives the following quadratic

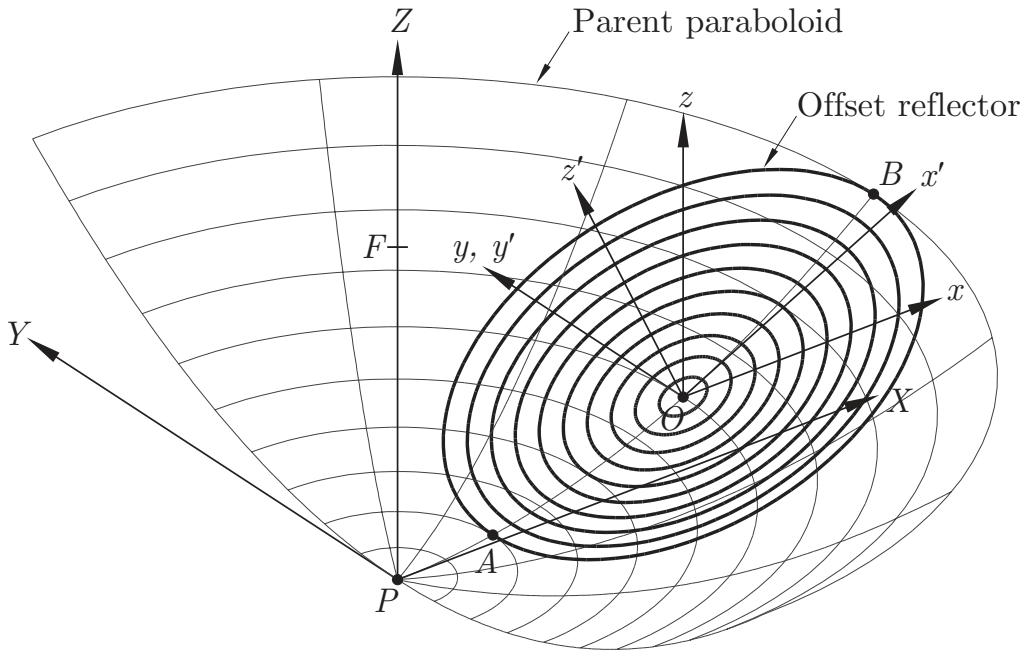

Figure 5.7: Three-dimensional view of the offset reflector antenna on parent paraboloid.

equation [78]:

$$\underbrace{\sin^2\phi_a}_{A}(z')^2 - \underbrace{\left[4F\cos\phi_a + 2\sin\phi_a\left(X_O + x'\cos\phi_a\right)\right]}_{B} z' + \underbrace{\left[(y')^2 + x'\left(2X_O\cos\phi_a + x'\cos^2\phi_a - 4F\sin\phi_a\right)\right]}_{C} = 0, \tag{5.7}$$

with the solutions

$$z'_{1,2} = \frac{-B \pm \sqrt{B^2 - 4AC}}{2A}. \tag{5.8}$$

Only the "$-$" solution is of interest as the other, much larger value, corresponds to the intersection of the z'-axis and the part of the parent paraboloid in the second and third quadrants, i.e., $X < 0$. The depth of the offset reflector, H_a, can be found by (5.5) and (5.6) as:

$$H_a = \frac{D_a^2}{16\xi F}, \tag{5.9}$$

where ξ is the ellipticity, i.e., the ratio of the major and minor axis of the reflector aperture, calculated as:

$$\xi = \sqrt{1 + \left(\frac{D_a + 2X_A}{4F}\right)^2}. \tag{5.10}$$

Note that the height of the axi-symmetric reflector, (5.3), is re-obtained for $X_A = -D_a/2$.

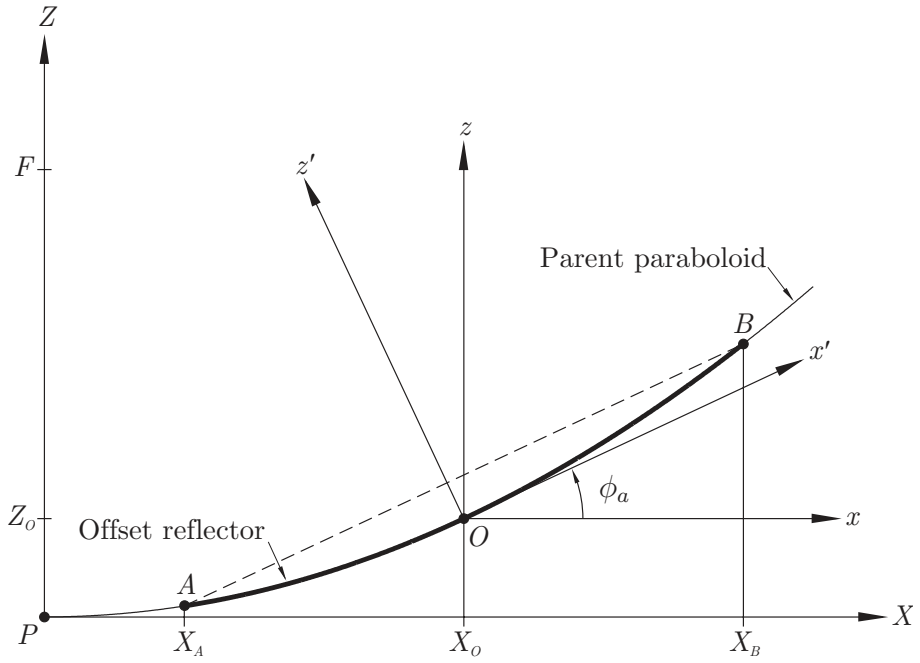

Figure 5.8: Offset reflector geometry definitions.

Standard Configuration

The normal choice for O is $X_O = (X_B + X_A)/2 = X_A + R_a$. This reflector configuration is therefore called the *standard configuration* [78]. In the xyz system, the coordinates of a point C on the reflector rim, Figure 5.9, are

$$x_C = R_a \cos\varphi, \tag{5.11a}$$

$$y_C = R_a \sin\varphi, \tag{5.11b}$$

$$z_C = \frac{R_a}{4F}\left(R_a + 2X_O\cos\varphi\right). \tag{5.11c}$$

The coordinates of point C in the $x'y'z'$ system are obtained by (5.6). Two views of the standard configuration are shown in Figure 5.9. The first view, Figure 5.9(a), is along the z-axis; the second view, Figure 5.9(b), is along the z'-axis. Note that in Figure 5.9(b) the reflector centre O does not coincide with the centre of the elliptic rim. For the CRTS reflector, Lai [78] observed that the standard configuration is not ideal and therefore proposed a new configuration, the *central hub configuration*, with two axis of symmetry.

Central Hub Configuration

For this configuration point O is in the centre of the elliptic reflector rim. The position of the central hub, X_O, is determined by the following relation, Figure 5.9(b):

$$x'_A + x'_B = 0, \tag{5.12}$$

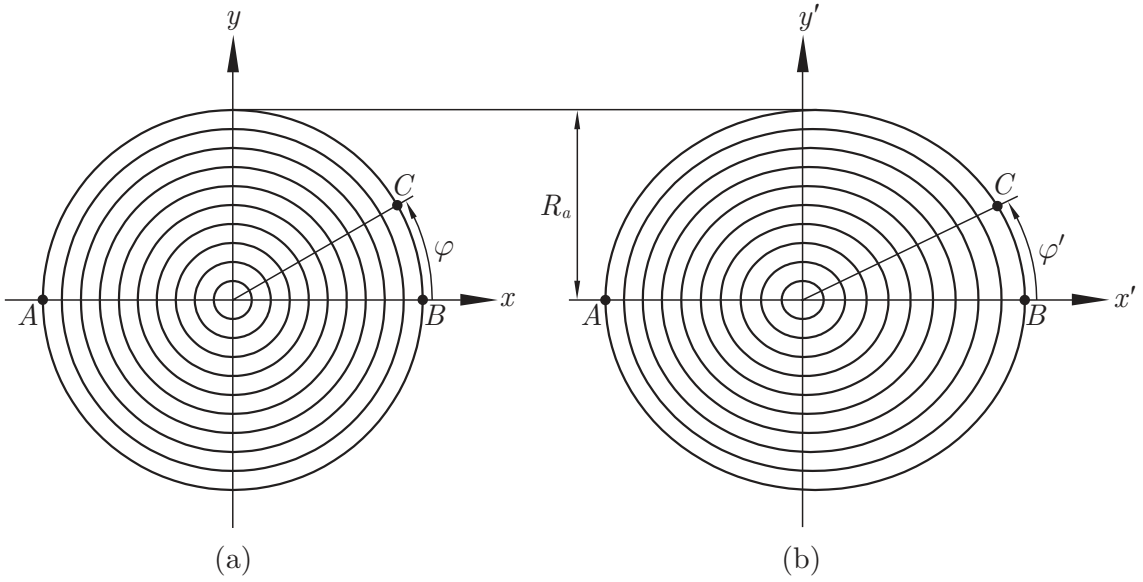

Figure 5.9: Standard offset configuration projected onto (a) xy plane and (b) $x'y'$ plane.

where

$$x'_A = (X_A - X_O)\cos\left(\arctan\frac{X_O}{2F}\right) + \frac{X_A^2 - X_O^2}{4F}\sin\left(\arctan\frac{X_O}{2F}\right) \tag{5.13}$$

and

$$\begin{aligned} x'_B = (2R_a + X_A - X_O)\cos\left(\arctan\frac{X_O}{2F}\right) \\ + \frac{(2R_a + X_A)^2 - X_O^2}{4F}\sin\left(\arctan\frac{X_O}{2F}\right), \end{aligned} \tag{5.14}$$

see [78] for further details. Equation (5.12) is solved numerically for X_O using e.g. the function `fzero` in Matlab [89]. In the $x'y'z'$ coordinate, system the x' and y' coordinates of a point on the elliptic reflector rim are

$$x' = x'_A\cos\varphi', \tag{5.15}$$

$$y' = R_a\sin\varphi', \tag{5.16}$$

while the z'-coordinate is found by (5.7). As anticipated by Lai [78], the central hub configuration produces a better membrane prestress distribution in the CRTS reflector than the standard configuration. Note that for the central hub configuration, the z'-axis is not normal to the elliptic aperture plane which is the case for the standard configuration. To make it normal, the local system must be rotated an angle $\Delta\phi_a$, which is the difference between ϕ_a for the standard configuration and ϕ_a for the central hub configuration.

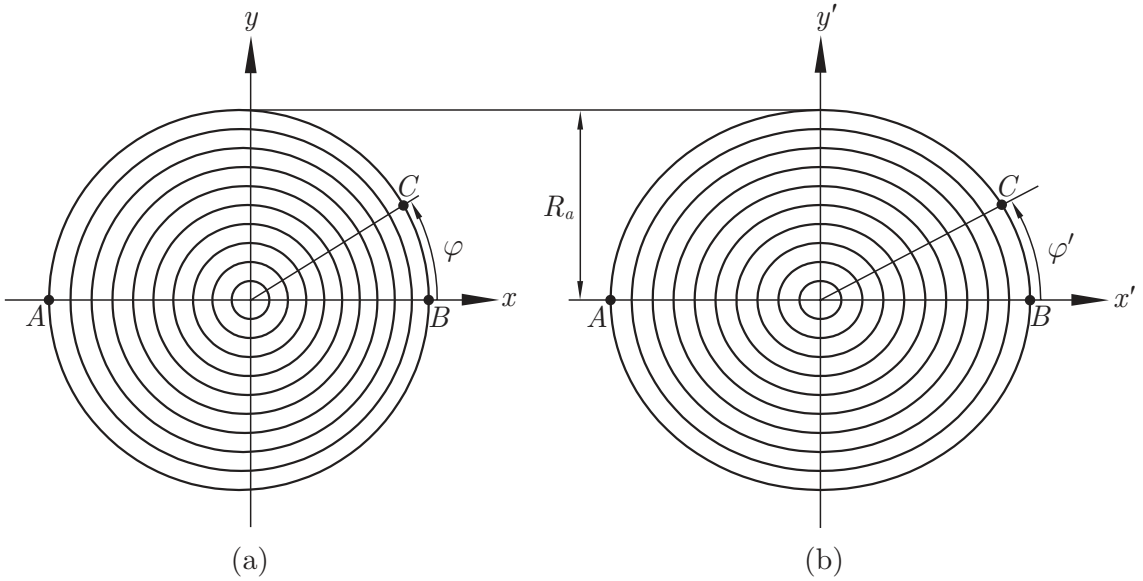

Figure 5.10: Central hub offset configuration projected onto (a) xy plane and (b) $x'y'$ plane.

Circular Configuration

Lai [78] also considered a third configuration where the aperture projection on the $x'y'$ plane is a circle instead of an ellipse. This configuration, called the *circular configuration*, was chosen for the CRTS reflector as it produces a better membrane prestress distribution and more uniform loading of the ribs, than the two previous configurations. For the circular configuration, the reflector rim is not coplanar as in the other configurations. While this aspect was not a problem for the CRTS umbrella-type reflector, it is probably undesirable for a deployable reflector with a supporting ring structure. The circular configuration will therefore not be further considered in this study.

5.3.3 Values for F/D and X_A

The values for the antenna diameter, focal length and offset distance are determined by taking a number of aspects, both electrical and structural, into account. It is always desirable to have as large a diameter as possible for increased gain. When it comes to the F/D ratio and offset distance X_A, it seems that these are determined by special optimisation routines not immediately accessible to structural engineers [12, 84]. From a structural viewpoint, a large F/D ratio means a bulky supporting structure for the sub-reflector which unnecessary adds weight to the whole assembly. Regarding the offset distance, X_A, it should be large enough to eliminate the feed blockage. However, a larger offset means a larger ellipticity factor which may have some implications for the present concept concerning the prestressability of the tension truss. The simplest way to get an idea of the appropriate values for these antenna parameters is to look at values used for other deployable space antennas.

Table 5.1: Geometrical data for some axi-symmetric and offset deployable reflector antennas.

Type[a]	Structure/satellite	D (m)	F (m)	X_A (m)	F/D[b]	ξ	Ref.
M	Aerospatiale	5.00	1.90	0.70	0.167	1.307	[141]
	AstroMesh[c] antenna	23.56	15.70	3.92	0.286	1.118	[62]
	Fan rib antenna	3.40	2.50	0.04	0.363	1.059	[66]
	BAe/Surrey antenna	5.00	3.00[d]	0.50	0.273	1.120	[141]
S	ODIN radiometer	1.10	0.61	0.05	0.265	1.115	[148]
	SSDA	1.48	0.62	—	0.423	—	[51]
I	ARISE antenna	25.00	11.55	0.00	0.231	1.137	[20]
	Space rigidised antenna	5.53	2.13	—	0.385	—	[174]

[a]M: mesh, S: solid, and I: inflatable.
[b]For offset reflectors the diameter of the parent reflector, $D_p = 2(D + X_A)$, is used.
[c]Values for the AstroMesh onboard the Thuraya satellite is not known, so the values for the antenna from the first study, [62], is used instead.
[d]The value of 1.5 m given in Table 3 in [141] is corrected to 3.0 m stated elsewhere.

This was, however, not such a simple task as in many cases only parts of the sought information were provided. It is likely that such information is classified and cannot be made public. The antennas for which all parameters were available are listed in Table 5.1. The F/D ratio varies between 0.167 and 0.363 for the parent paraboloid, which means that they are quite deep. The ellipticity interval is 1.056–1.307, with most values around 1.1. X_A/D_a varies from 0, which is the absolute minimum, to 0.166.

5.4 Reflector Antenna Theory

Despite the title, this section will not aim at describing the complete theory of reflector antennas, as it is well beyond the scope of this thesis. Nevertheless, within that theory there are some aspects directly related to the structural design of the antenna. These aspects will be presented here.

5.4.1 Antenna Gain

In communication systems, an increase in aperture size means an increase in the amount of information that can be sent or received. In sensing systems, however, it means that a finer ground resolution can be obtained. The factor describing the performance of the antenna is its gain. High gain antennas allow for high transmission data rates at low power and improve the signal to noise ratio [158].

For a reflector antenna, the theoretical maximum gain is

$$G_{\text{th}} = \left(\frac{\pi D}{\lambda}\right)^2. \tag{5.17}$$

where λ is the wavelength of the operating frequency. This maximum gain is reduced by a number of factors, e.g. aperture blockage and phase errors, to

$$G_0 = \eta_a G_{\text{th}} \tag{5.18}$$

where η_a is the product of all antenna efficiency factors η_i, $0 < \eta_i \leq 1$.

The efficiency factor due to aperture blockage, η_b, can be estimated as [158]:

$$\eta_b = \left(1 - \frac{1}{\eta_t}\frac{A_b}{A_a}\right)^2 \tag{5.19}$$

where A_b is the blockage area projected onto the aperture area A_a, and η_t the aperture taper efficiency factor. This takes into account that the central part of the aperture usually is more affected by the blockage. For optimum antenna performance, it is shown that $\eta_t \approx 0.89$ [158].

Phase errors arise due to surface deviations from the ideal paraboloid. Considering their impact on the antenna radiation pattern, Pontoppidan [131] divides the surface deviations into the following three groups:

1. *Deviations which change the desired paraboloid into another best-fit paraboloid.*
   Deviations due to slowly varying distortions, like thermal distortions, and their effect on the performance are completely described by a de-focus. The best-fit paraboloid, i.e. a paraboloid which in a least-square sense best approximates to the ideal one, may deviate from the ideal one up to about one wavelength without seriously affecting the performance of the antenna.

2. *Other systematic errors.*
   Systematic surface deviations are inherent in the construction of the antenna and can be predicted. In general, systematic deviations cannot be considered similar to random errors, but have to be treated separately.

3. *Other random errors.*
   Random errors are caused by the fabrication tolerances in the manufacturing process and are unpredictable within given statistical limits.

According to Stutzman and Thiele [158], many applications have $\eta_a \approx 0.65$. Values of η_a between 0.43 and 0.72, depending on the frequency, are reported by van 't Klooster *et al.* [174]. The influence of random errors on the antenna performance is treated in the following section.

5.4.2 Effects of Random Surface Errors

An approximate method to compute the effects of random surface deviations on the antenna gain is presented by Ruze [142]. He assumed that the surface deviation at any point is a random sample from a single Gaussian distribution with zero mean and a standard deviation equal to the root-mean-square (rms) of the surface deviation of the reflector. A further assumption is that the surface deviations are correlated in small regions. Under these assumptions, the random error efficiency factor, η_r, can be written as:

$$\eta_r = \exp\left[-\left(\frac{4\pi\delta_{\text{rms}}}{\lambda}\right)^2\right], \tag{5.20}$$

where δ_{rms} is the radiometric rms surface deviation [50, 142]. The radiometric rms surface deviation is defined as [50]:

$$\delta_{\text{rms}} = \left[\frac{1}{A_a}\iint_{A_a}\left(\frac{\Delta\wp}{2}\right)^2 \mathrm{d}A\right]^{1/2}, \tag{5.21}$$

where $\Delta\wp$ is the phase error, i.e. path-length difference of a reflected ray due to the surface imperfections, and A_a the aperture area. Usually, the surface deviations are measured in a direction axial or normal to the reflector surface for reasons of simplicity. The relation between the deviation in the axial direction, Δz, and $\Delta\wp$ is [50, 142, 184]

$$\Delta\wp = \frac{2\Delta z}{1+(r/2F)^2}, \tag{5.22}$$

while for the deviation in the normal direction, Δn, it is

$$\Delta\wp = \frac{2\Delta n}{\sqrt{1+(r/2F)^2}}, \tag{5.23}$$

where r is the distance from the centre of the axi-symmetric reflector to the point of measure. For shallow reflector surfaces, the factor $1+(r/2F)^2$ is close to unity and even for deeper ones it is small, e.g., $F/D = 0.4$ and $r = D/2$ gives $1+(r/2F)^2 = 1.39$. Assuming that the denominator can be set to unity, (5.21) simplifies to

$$\delta_{\text{rms},z} = \left[\frac{1}{A_a}\iint_{A_a}(\Delta z)^2 \,\mathrm{d}A\right]^{1/2}. \tag{5.24}$$

Equation (5.24) is simpler than (5.21) and frequently used to predict the performance of a reflector antenna, cf. [2,50]. Using $\delta_{\text{rms},z}$ in (5.20), will overestimate the gain loss as $\delta_{\text{rms},z} \geq \delta_{\text{rms}}$. However, later studies [184, 189] show that the assumptions related to (5.20) in general underestimate the gain and therefore can be considered to be a worst case. Although (5.20) relates only to random surface deviations, it is with good approximation found to be valid for any type of deviation measured relative to the best fit paraboloid [131]. Thus, (5.24) is likely to give a good approximation

of the radiometric rms surface deviation and antenna gain loss and can therefore safely be used.

An important result from (5.20) is that if a given reflector operates at increasing frequency, the gain, at first, increases as the square of the frequency until the surface deviation effect takes over and then a gain deterioration occurs. Maximum gain is obtained at the wavelength of

$$\lambda_{\max} = 4\pi\delta_{\text{rms}}, \tag{5.25}$$

Substituting $\lambda_{\max}$ into (5.20) gives the maximum gain

$$G_{\max} \approx \frac{\eta_a}{43}\left(\frac{D}{\delta_{\text{rms}}}\right)^2, \tag{5.26}$$

which is proportional to the square of the manufacturing accuracy D/δ_{rms} [142].

5.4.3 Systematic Surface Error of Faceted Paraboloids

Many reflector antennas, e.g. AstroMesh [165] and ETS-VIII [107], divide the reflector surface into flat facets rather than gores as is the case for umbrella-types. Figure 5.11 shows a shallow spherical cap approximated by triangular and hexagonal flat facets. Faceting introduces a systematic deviation of the actual surface from the desired surface which degrade the performance of the reflector. As shown in the previous section, the parameter governing the performance degradation is the rms surface deviation. Thus, the maximum facet size required to meet a specific surface accuracy is sought.

In general, it is not possible to map regular polygons onto a curved surface. To find an expression for the relation between the surface error and the facet size some assumptions have to be made [2, 58]. For a shallow reflector, with focal length F, a six bay triangular division, Figure 5.11(a), results in nearly equilateral triangles. If the reflector is shallow, it can be closely approximated by a sphere with radius $2F$. Thus, the $\delta_{\text{rms},z}$ calculation for an equilateral triangle on a spherical surface is assumed to be a good approximation for the actual geometry. This assumption was checked by Agrawal *et al.* [2] and found to be valid.

Hedgepeth [56,58] provides the first and most thorough study of rms errors of faceted mesh antennas. Beside the surface deviation due to the facet size, this study also includes effects of *mesh saddling*. With no lateral loading an isotropic uniformly tensioned membrane must have zero Gaussian curvature, i.e. saddle shape. At the intersection between adjacent facets on the paraboloid, the mesh tension changes direction. The resulting lateral loading tends to curve the supporting element inwards, Figure 5.12. The corresponding normalised rms surface deviation $\delta_{\text{rms},z}$ of the best-fit facet and a sphere of radius $2F$ is, [56],

$$\frac{\delta_{\text{rms},z}}{D} = 0.01614\frac{(\ell/D)^2}{F/D}\left(1 + 0.33\frac{p\ell}{t}\right), \tag{5.27}$$

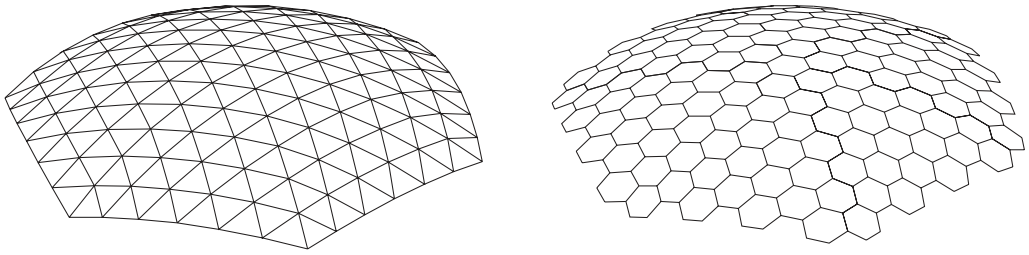

(a) (b)

Figure 5.11: Approximating a shallow spherical dish with flat facets of (a) triangular and (b) hexagonal shape.

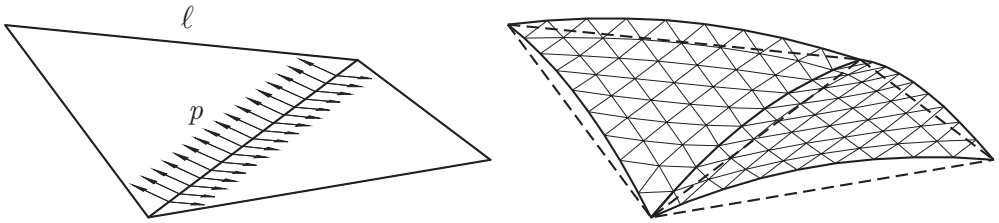

(a) (b)

Figure 5.12: Mesh saddling of triangular facets on a synclastic surface.

where ℓ is the side length of the triangle, p the mesh tension, and t the force in the supporting element. To minimise the effects of mesh saddling, i.e., allow the largest facet size, the tendon force must be large compared to the mesh tension.

The rms deviation of facets including mesh saddling was recently re-analysed by Tanizawa *et al.*, as reported in [106]. By applying a Fourier series solution, instead of a polynomial as Hedgepeth [56], for the deformation of the supporting tension element, Figure 5.12, the rms deviation of the equilateral triangle was found to be

$$\frac{\delta_{\mathrm{rms},z}}{D} = 0.01614\frac{(\ell/D)^2}{F/D}\sqrt{1 + 0.660\frac{p\ell}{t} + 0.133\left(\frac{p\ell}{t}\right)^2} \tag{5.28}$$

for $p\ell/t < 1$. A Taylor series expansion of the square root part of (5.28) around $p\ell/t = 0$ gives $1 + 0.33p\ell/t + \mathcal{O}[(p\ell/t)^2]$, which is similar to the corresponding part of (5.27). For practical values of $p\ell/t$, the difference between (5.28) and (5.27) is negligible.

Agrawal *et al.* [2] compute the rms surface deviation between best-fit flat facets of triangular, square, and hexagonal shape and a sphere. For equilateral triangles it is

$$\frac{\delta_{\mathrm{rms},z}}{D} = \frac{1}{16\sqrt{15}}\frac{(\ell/D)^2}{F/D}, \tag{5.29}$$

i.e., identical to (5.27) as $p\ell/t \to 0$. For a given value of $\delta_{\mathrm{rms},z}$ the required side length ℓ is

$$\frac{\ell}{D} = 7.872\sqrt{\frac{F}{D}\frac{\delta_{\mathrm{rms},z}}{D}}. \tag{5.30}$$

For squares and regular hexagons, the value 7.872 is substituted by 6.160 and 4.046, respectively. Hence, the triangles have the largest side length for a given rms deviation tolerance. Agrawal *et al.* [2] also analyse the electrical performance of a proposed large reflector antenna ($D = 660$ m and $F = 573$ m) with an operation frequency of 1 GHz and an allowable surface error, $\delta_{\text{rms},z}$, of 12 mm ($\lambda/25$). It is found that hexagonal facets provide a slightly better radiation pattern than triangular facets. A reflector surface made out of square facets with identical $\delta_{\text{rms},z}$ yield a worse radiation pattern, which is explained by the variation of the surface deviation over the reflector. Although hexagonal facets yield a better radiation pattern, triangular facets are structurally desirable and require the fewest number of structural members to meet a given surface tolerance. Considering all factors, their conclusion is that triangles appear to be the best option for approximating a paraboloidal reflector surface.

Referring to the research by Agrawal *et al.* [2], Fichter [38] proposes a method of changing the boundary shape of the facets so that the total rms error could be improved. For congruent facets with a boundary radius of $2F$, it is found that $\delta_{\text{rms},z} = 0.0082\ell^2/F$, which is about 49% below the flat facet rms error. The minimum rms deviation was found to be $\delta_{\text{rms},z} = 0.0069\ell^2/F$ for a boundary radius of $1.4F$. This optimum solution can also be re-obtained by minimising (5.28) with respect to $p\ell/t$, which yields $p\ell/t = -2.474$. Hence, to realise this optimum facet as well as the congruent one, the boundary members must be in compression which requires elastic rods rather than cables along the facet boundaries. The optimum solution for a cable supported facet is, therefore, the flat facet.

Hedgepeth [56] also studies the rms surface deviation of umbrella-type reflectors having gores rather than facets. Including the mesh saddling between the parabolic ribs, the rms surface deviation is

$$\frac{\delta_{\text{rms},z}}{D} = 0.01076\frac{(\ell/D)^2}{F/D}\left(1 + \frac{p_1}{p_2}\right), \tag{5.31}$$

where ℓ is the gore width at the reflector rim, and p_1 and p_2 the membrane tensions in the radial and circumferential directions, respectively. For isotropic mesh tension, $p_1 = p_2$, the required gore width is

$$\frac{\ell}{D} = 6.817\sqrt{\frac{F}{D}\frac{\delta_{\text{rms},z}}{D}}. \tag{5.32}$$

A very large number of ribs is needed to obtain a high surface accuracy.

5.4.4 Allowable Surface Error of Reflector Antennas

The main design points for deployable reflector antennas are deployment feasibility and high surface accuracy. Only the surface accuracy can be considered at this point. In this section, an acceptable value of rms surface distortion will be identified. The requirement report by DERA [136] does not directly specify the required surface

accuracy for the present reflector but states that an rms accuracy of at least $\lambda/20$–$\lambda/10$ is necessary.

The allowable surface accuracy is somewhat dependent on the antenna type; for symmetrical reflectors the peak gain is the most important parameter [138]. From (5.18) and (5.20) it is evident the there can be a trade-off in the choice of reflector diameter and rms surface accuracy. A larger, less accurate reflector can provide the same peak gain as a smaller more accurate one. For offset reflectors, the choice of reflector diameter is also constrained by aspects related to the radiation pattern [138]. It is generally not sufficient to specify a total rms surface accuracy. Different surface error distributions with the same total rms surface accuracy can give different radiation patterns. A study of these radiation patterns is, however, well beyond the scope of this thesis.

Roederer and Rahmat-Samii [138] observe that rms surface accuracy goals lie typically in the interval $\lambda/100$–$\lambda/25$. In the extensive and more recent review of the precision of deployable antennas by Hachkowski and Peterson [52], the rms surface deviation ranges from[4] $\lambda/353$ to $\lambda/6$. Both of these studies include values from antennas at different stages of development: in orbit, flight models, engineering models, and engineering feasibility studies.

The tension truss concept was earlier identified as the most viable solution for passively achieving a reflector surface with high accuracy. A closer look at the practical surface accuracy of structures based on this concept is therefore of great value in determining an allowable rms surface accuracy for the present reflector.

Miyasaki *et al.* [107] uses $\lambda/50$ (2.4 mm at S-band) as the allowable surface deviation for the 13 m ETS-VIII antenna. Analysis and test of a 3-module assembly result in an rms surface accuracy of 0.4 mm and 0.5 mm, respectively. Using these results, the rms surface deviation for the entire reflector is estimated to less than 1.3 mm.

In [62], where the concept of the AstroMesh reflector is introduced, the design of a 23.56 m diameter offset reflector antenna ($F/D_p = 0.286$) is described. The allowable rms surface deviation is taken as $\lambda/50$, or 1 mm at C-band. The first contribution to the total surface error comes from the faceting of the reflector surface. The acceptable rms deviation error due to faceting is set to $\lambda/200$ or 0.25 mm for the operating frequency. The required side length ℓ of the triangles, (5.29), is 0.5 m, requiring a tension truss with 27 rings. Hedgepeth *et al.* [62] also note that an umbrella-type antenna would require 170 ribs to yield the same accuracy, (5.32), again showing the advantage of the tension truss concept. Other systematic contributions to the total surface error are distortions due to

- Gravity during ground testing,
- Centrifugal forces due to satellite spinning,
- Loading of the tension ties, and

[4] Values computed from 24 of the 50 listed antenna structures for which both λ and $\delta_{\mathrm{rms},z}$ are given.

Table 5.2: Surface distortions for the 6 m AstroMesh reflector [166].

Error source	$\delta_{\mathrm{rms},z}$	
	(mm)	(%)[a]
Surface faceting	0.33	32.7
Manufacturing	0.41	50.4
Mesh saddling	< 0.10	3.0
Deployment repeatability	< 0.08	1.9
Thermal extremes	0.20	12.0
Total root-sum-square	< 0.6	100.0

[a]Computed as $\delta^2_{\mathrm{rms},i} / \sum_i \delta^2_{\mathrm{rms},i}$

- Large strains arising due to systematic error in net fabrication, from a large temperature change, or from pre-tensioning.

The computed rms error estimates for these sources are: 0.4 mm if the rim is supported during ground testing, 0.12 mm at a spinning rate of 3.2 rpm, 0.6 mm with a tension tie force of 4.5 N, and around 0.2 mm for a strain of 254.4 μm/m in each net element. The rms surface error due to random member length errors in fabrication and thermal expansion coefficient variation are evaluated by the *Monte Carlo* technique and found to be less than 0.5 mm. Random errors due to uncertainty in the tension tie loading yield an rms error of 0.2 mm. A total rms surface error estimate is not given for the reflector but this extensive study clearly shows the influences of different error sources.

More recent results on the surface accuracy are available for the 6 m AstroMesh reflector [165, 166]. The rms surface distortion due to gravity during ground testing is smaller than the resolution of the photogrammetry measuring system, which is 0.07 mm. The rms surface error due to mesh saddling, section 5.4.4, is less than $\lambda/500$, thus having very little influence on the total error. The total root-sum-of-squares (rss) error from all sources is less than 0.6 mm or $1.0 \cdot 10^{-4} D$, Table 5.2. A total surface distortion of $2.5 \cdot 10^{-5} D$, is believed to be achievable with existing materials and manufacturing technology. For a 12 m reflector operating at 40 GHz, that would give an rms surface accuracy equal to $\lambda/20$.

5.4.5 Ground Resolution

The gain is not the only factor deciding the antenna diameter. For Earth observing systems the ground resolution is of significant importance [18]. The ground resolution is expressed as the size of an object that can be distinguished from the background. For a satellite at altitude, h, the ground resolution, χ, at *nadir*[5] is

$$\chi = 2.44 \frac{h\lambda}{D} \tag{5.33}$$

[5]Nadir is the direction from the spacecraft to the centre of the Earth.

where h can be replaced by the slant range to determine the ground resolution away from nadir. It should be noted, however, that a SAR can provide ground resolutions similar to visual systems, $\lambda = 0.5$ μm, independent of the range and wavelength by synthesising the required aperture. For the present antenna, $D = 3$ m, $f = 9.65$ GHz, and $h = 550$ km, the ground resolution would be $\chi = 13.9$ km and with the ground resolution goal of $\chi = 1.5$ m [136], the SAR antenna will be able to simulate an aperture with $D = 27.8$ km.

5.4.6 Accuracy Goals for the Present Antenna

This review of surface accuracies of deployable mesh antennas shows that a high, but realistic, surface accuracy goal for the present application would be a total rms error of $\lambda/50$ with a budget of $\lambda/100$ for the faceting rms surface deviation. However, since the present reflector will use SAR technology, which uses signal processing to achieve a high resolution, a lower surface accuracy can be accepted [4, 183]. Therefore, a lower accuracy goal of $\lambda/25$, with a budget of $\lambda/50$ for the facet error, will also be considered.

5.5 Selection of Materials

The space environment is extremely harsh with very low vacuum levels, high doses of thermal and particle radiation, micro-meteoroids and debris, magnetic and gravitational fields, and temperatures as low as 4 K [144, 183]. The selection of materials is of cardinal importance to the survivability of a spacecraft in this environment. Spacecraft structures typically contain both metallic and non-metallic materials. Most metals are isotropic while non-metals, i.e. composites, normally are anisotropic. The selection of materials is based on several factors [183]: strength, stiffness, density, thermal expansion, cost, etc. For precision structures, such as reflector antennas, the relevant material properties are high modulus of elasticity and low *Coefficient of Thermal Expansion* (CTE).

5.5.1 Materials for the Antenna Structure

Aluminium alloy is the most commonly used metal for spacecraft structures. Advantages of aluminium are low density, high strength-to-weight ratio, availability, low cost, and machinability. The main disadvantage of aluminium is its high CTE, $22\mu/°$C [183]. Other metals, e.g. titanium or magnesium, have lower CTE but provide other disadvantages.

CFRP offer better material properties than metals and can be tailored for high strength, high stiffness, and extremely low CTE. By controlling the direction of the graphite fibres, very high stiffness-to-weight ratios are obtained. Material with a modulus of 115–124 GPa is readily available [62, 141]. According to Hedgepeth *et*

al. [62], CFRP with a modulus of 227.5 GPa can be produced at extra cost which for high-precision antenna applications may be justified. For example, using the less stiff CFRP for the 23.5 m reflector in reference [62] would have resulted in doubled rms surface errors due to ground testing and pre-tensioning, and lower vibration frequencies. Typical tensile strength for high-modulus CFRP is about 1500 MPa, but higher strengths are available [133]. As CFRP is a very brittle material, it can be assumed that the proportional limit is above 90% of the ultimate strength. CFRP is also very light; densities between 1660 and 1740 kg/m^3 are available [62, 96]. These densities are a little higher than raw CFRP, to allow for an impermeable coating of the struts [96]. CFRP with a CTE less than 1.0μ/°C can easily be procured.

Although the main antenna structure will be composed of composite material, details such as end fittings are made of metal. These details are preferably attached by bonding as bolting would give rise to undesirable stress concentrations. Other more complex moving details, e.g. hinges, can be made of several different materials where each material affect the overall performance of the detail. For example, the TSR hinge, section 4.5.1, contains tapes of spring steel, thin steel cables, aluminium alloy spacers, steel bolts, and a main body of Delrin.

5.5.2 Materials for the RF Reflective Surface

First of all, the material used for the RF reflective surface must be easy to compactly fold and require a low density. The most common surface material for space reflectors of moderate precision is a mesh knitted from metallic or synthetic fibres that have been plated with RF reflective material. A mesh provides the compliance necessary to conform to the doubly curved surface without wrinkling. A high compliance also means that the mesh can be connected directly to the net structure without any special interface [61]. Because of its openings, the mesh is limited to frequencies up to 40 GHz. At higher frequencies, the losses through the mesh are too great. Solid membrane surfaces have been developed for higher frequency applications, but without success. The very low in-plane compliance of membrane means that it will not easily conform to a doubly curved surface without developing wrinkles, which degrade the antenna performance [95]. For the present antenna, it is assumed that the mesh is knitted from gold-plated molybdenum wires, which are readily available. This mesh has a surface density of 25 g/m^2 [62].

To assure good electrical conductivity between the mesh wires, the tension in the mesh must be fairly isotropic and uniform. Mesh tensions of 2.0–2.5 N/m were reported in earlier studies [61,62]. Recently, values of 10–11 N/m have been used [34, 165]. A higher mesh tension will more effectively smooth out the creases formed in the mesh during folding and, thereby, give a better antenna performance. In addition, it has been shown, [61, 62], that the strength of a structure designed for a mesh tension value of 2.5 N/m is sufficient to withstand lateral accelerations many times greater than those experienced in orbit without severe distortion of the reflector surface.

Chapter 6

Analysis of Tension Trusses

In the previous chapter it was found that a new reflector antenna concept is needed in order to meet the stowage requirements of a future STRV mission. Ideally, the required accuracy of the reflector surface should be achieved with a passive structure, i.e. without active control. Miura's tension truss [104] was identified as the best candidate for this task as its surface accuracy can be altered without major changes to the supporting structure. As the performance of the antenna is a function of the condition of the reflecting surface, it was considered necessary to analyse the behaviour of tension trusses separately from that of the antenna structure.

A tension truss is basically a geodesic dome with elements that are flexible rather than stiff. In that way, it can easily be folded. External forces are applied at the nodes to provide a state of tensile forces in the assembly, Figure 6.1. In practice, the external forces are provided by springs, called tension ties. The key feature of the tension truss is that its shape is more or less predetermined by the lengths and arrangement of its elements. The elastic deformation effects on the shape are of secondary importance. For this to hold, the assembly must be kinematically determinate.

Despite the clear advantages of the tension truss for lightweight, high-precision deployable structures, only a few studies consider its fundamental characteristics, cf. [100,104]. Other studies are mainly concerned with the implementation of the tension truss in various deployable structures, cf. [99,106,165]. Recently, basic research on the characteristics and applicability of the tension truss with different types of support conditions has been undertaken at the DSL, cf. [34,79,80,169]. These studies provide new insight into the prestressability of the tension truss. In this chapter, the preliminary study of references [168,169] is significantly expanded. First, a way of making an n-ring tension truss kinematically determinate is presented. Then, studies on the prestressability of axi-symmetric and offset net configurations are undertaken. Finally, the effects of systematic and random manufacturing errors on the antenna performance parameters are investigated.

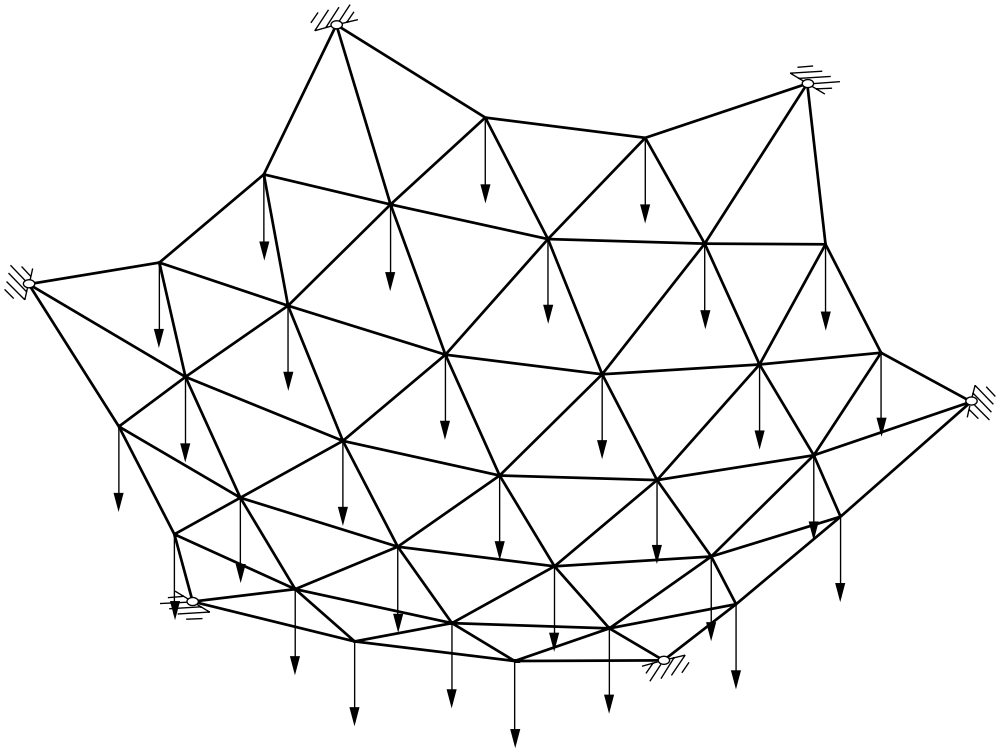

Figure 6.1: Tension truss prestressed by external loads acting approximately normal to the net surface.

6.1 Static and Kinematic Properties

Consider an axi-symmetric tension truss generated according to the scheme in Appendix C. The number of elements b and joints j in the assembly are

$$b = v\frac{n(1+3n)}{2}, \tag{6.1}$$

$$j = 1 + v\frac{n(1+n)}{2}, \tag{6.2}$$

respectively. Substituting (6.1) and (6.2) into the extended Maxwell's rule, (1.2), yields the following number of kinematic constraints required for static determinacy:

$$c = 3 + vn. \tag{6.3}$$

Along the boundary there are $3vn$ degrees of freedom, which is more than sufficient. However, in both the HALCA antenna, Figure 2.14, and the present one, Figure 5.5, supports are provided only at the v outermost vertices, Figure 6.1. Inserting $c = 3v$ into (1.2) yields

$$m - s = v(n-3) + 3. \tag{6.4}$$

As a state of self-stress generally cannot exist in a net of synclastic shape, i.e. bowl shape, $s = 0$. Thus, the number of internal mechanisms in the tension truss is

$$m = v(n-3) + 3. \tag{6.5}$$

Note that for $n < 3$, several states of self-stress can exist in the synclastic net, thus disproving the statement $s = 0$ above. However, none of the self-stress combinations produced tension in all elements. It is therefore correct to say that no feasible state of self-stress can exist in a synclastic net.

With a limited number of supports, the only way to remove the internal mechanisms is to add more bars, and possibly more nodes, to the assembly. Preferably, the additional nodes and bars should be located along the boundary and connected in a manner that preserves the v-fold symmetry of the original tension truss. Denoting the number of additional nodes and bars per bay by j_{an} and b_{an}, respectively, (1.2) yields for kinematic determinacy, assuming $s \neq 0$,

$$s = v(n-3) + 3 + v(3j_{\text{an}} - b_{\text{an}}). \tag{6.6}$$

Solving (6.6) for b_{an} gives

$$b_{\text{an}} = \frac{3+s}{v} + 3(j_{\text{an}} - 1) + n. \tag{6.7}$$

For $v > 3$, it is not possible to construct a statically determinate assembly. For the case $v = 6$ and $s = 3$, the minimum number of extra bars is $b_{\text{an}} = n - 2$. However, a quick study showed that the resulting configurations are not ideal. Setting $j_{\text{an}} = 1$ gives $b_{\text{an}} = n+1$. This alternative is far better considering that there are $n+1$ nodes along the boundary of each bay to which the added bars can be connected directly. A further increase of j_{an} produces more complicated configurations involving crossing elements. The above analysis provide an indication of the feasibility of the new configuration. If it can be shown that all of the mechanisms can be removed, the tension truss is a type III assembly, cf. Table 3.2, which can be accurately analysed by the linear force method described in section 3.5.

6.2 Axi-Symmetric Configurations

The main advantage of the tension truss is its ability to conform to a multitude of shapes. Here, it approximates an axi-symmetric reflector. For a given diameter D and curvature F/D, the first task for a designer is to specify the remaining parameters in the mesh generation routine. Most important of these is the number of rings n, which is given by the required surface accuracy. Other parameters are the sag of the boundaries and the position of the additional nodes for the best internal force distribution.

6.2.1 Sag-to-Span Ratio

The sag-to-span ratio of the edge cables is the first property to be determined. A small ratio will give rise to undesirably large forces in the edge elements, while a large ratio cuts away too much of the reflector surface and distorts the boundary triangles. In tensile roof applications, a sag-to-span ratio of 8–12% is common,

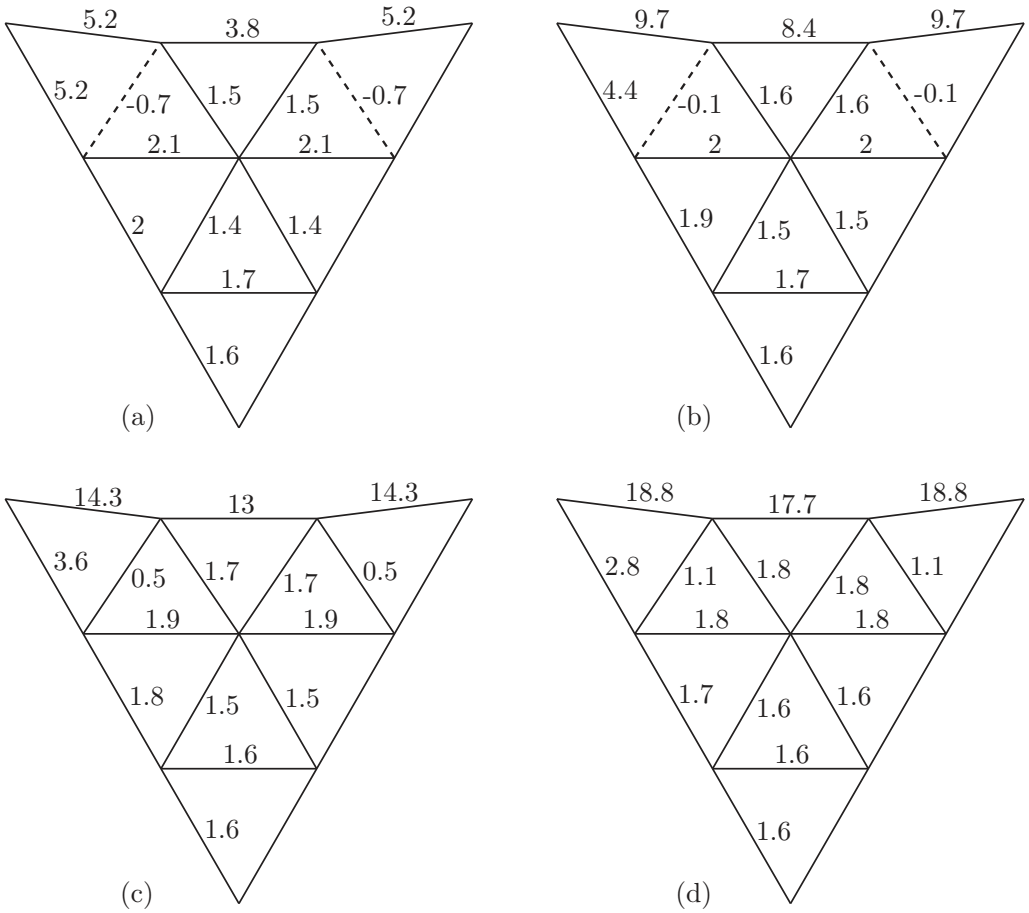

Figure 6.2: Forces in a 3 m diameter three-ring net with 5% sag-to-span ratio (only one sixth of the complete net is shown). Loads on the inner nodes are 1 N and loads on the edge nodes are: (a) 1 N, (b) 2 N, (c) 3 N and (d) 4 N.

cf. [171]. The analysis of the edge sag will be done with a three-ring tension truss ($D = 3$ m, $F/D = 0.4$) were the additional nodes and elements have been taken out. This is done to remove the influence of the additional nodes on the net forces. The resulting net is kinematically indeterminate with $m = 3$. However, it can be shown that each of the three mechanisms is orthogonal to the particular sets of tension tie forces used in the analysis, cf. (3.66). The three-ring tension truss was analysed for three sag-to-span ratios: 5, 10 and 15%. For each ratio, the initial setting of the tension tie forces was 1 N throughout, which is most practical as identical constant-tension springs would be used in all of the tension ties. If the force pattern in the net is irregular or, worse, some elements are in compression, the tension tie forces have to be adjusted. The results for a 5% sag-to-span ratio are shown in Figure 6.2. For the case where the tension tie forces are all equal to 1 N, Figure 6.2(a), some members are in compression. By increasing the edge forces, the compression forces gradually become smaller and then tensile, Figures 6.2(b)–(d). An almost uniform force distribution was obtained for edge forces of 4 N. However, the largest force along the edge was over 15 N. When the sag-to-span ratio was increased to 10% there was still compression for tension tie forces of 1 N, Figure 6.3(a). As the force

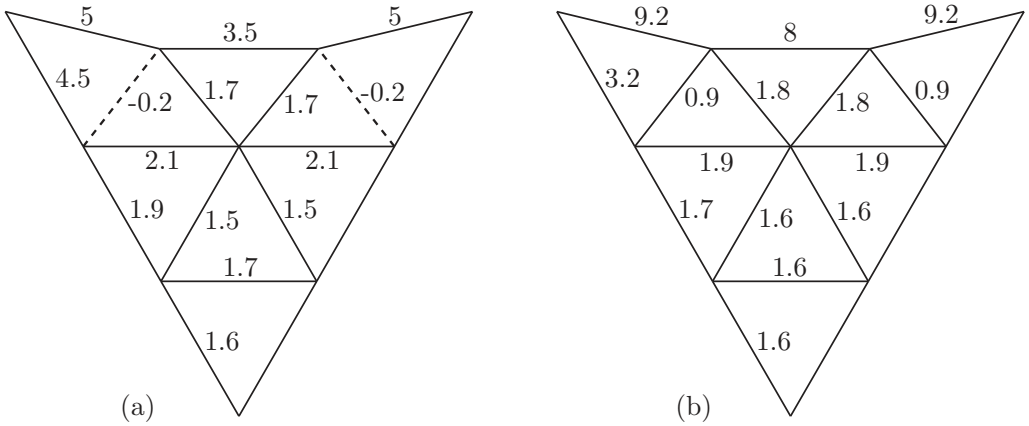

Figure 6.3: Forces in a 3 m diameter three-ring net with 10% sag-to-span ratio. Loads on inner nodes: 1 N; loads on edge nodes: (a) 1 N and (b) 2 N.

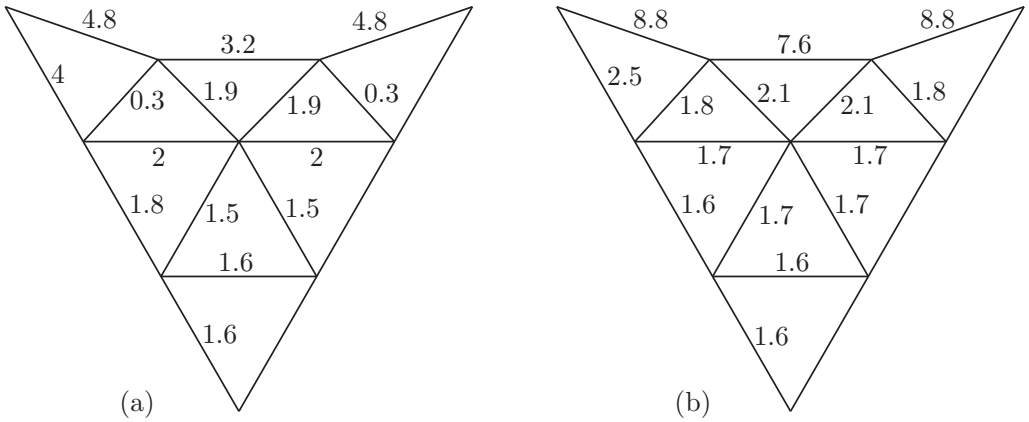

Figure 6.4: Forces in a 3 m diameter three ring net with 15% sag-to-span ratio. Loads on inner nodes: 1 N; loads on edge nodes: (a) 1 N and (b) 2 N.

in the edge ties was increased to 2 N an acceptable distribution of net forces was obtained and the edge forces were smaller than for the 5% ratio, Figure 6.3(b). A further increase of the sag-to-span ratio to 15% yielded no compressed elements even for the case of uniform 1 N tension tie loads, Figure 6.4(a). When increased to 2 N, the forces in the edge ties gave an almost uniform force pattern, in the range 1.6–2.5 N, and the forces in the edge elements were slightly smaller than for 10%. Although a sag-to-span ratio of 15% produced a better force pattern than the 10% ratio, the further loss of reflecting area was not justified. Note also that with the present mesh generation routine there is a limit to the maximum number of rings n, for a certain value of the sag-to-span ratio ρ. According to Appendix C, the maximum sag-to-span ratio is

$$\rho_{\max} = \frac{1}{2(n-1)\tan(\pi/v)}. \tag{6.8}$$

This can be rewritten as

$$n = 1 + \frac{1}{2\rho\tan(\pi/v)}. \tag{6.9}$$

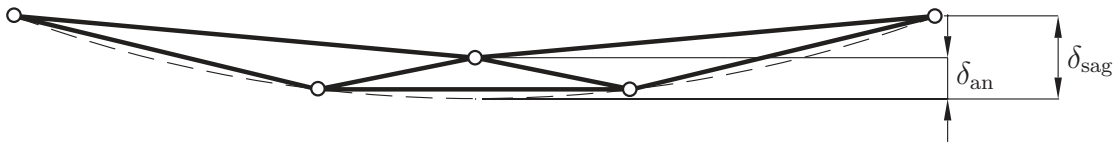

Figure 6.5: The position of the extra node in the radial direction.

The maximum number of rings n_{max} for a given sag-to-span ratio is

$$n_{max} = \left\lfloor 1 + \frac{1}{2\rho \tan(\pi/v)} \right\rfloor, \tag{6.10}$$

where the floor function $\lfloor x \rfloor$ yields the largest integer $\leq x$. For $v = 6$, $\rho = 0.15$ yields $n_{max} = 6$ and $\rho = 0.10$ yields $n_{max} = 9$. Hence, a sag-to-span ratio of 10% was selected for the tension truss in the analyses that follow. The outer diameter D of the tension truss was fixed to 3 m, so with $\rho = 0.10$, the effective aperture diameter was 2.32 m using (C.7).

6.2.2 Position of Additional Nodes

Another benefit of a larger sag-to-span ratio, is that it leaves more room for the additional elements along the boundary. Vertically, the additional nodes lay on the paraboloid. Tangentially, they were positioned in the middle of the supports. Radially the position varied; theoretically, any value between 0 and δ_{sag} from the edge cable was possible, Figure 6.5. To determine the best position of the additional nodes, three-ring trusses with different focal lengths were analysed. The tie forces were equal to 1 N on interior nodes and 2 N on the edge and additional nodes. The ratios between the maximum and minimum forces in the interior and all elements, respectively, were used to identify the best configuration, Figure 6.6. The aim was an interior force ratio close to unity and a fairly low ratio for all forces. It appears that for all the three F/D ratios, the best configurations were obtained for δ_{an}/δ_{sag} between 0.4 and 0.5.

6.2.3 Tension Tie Force Distribution

It was shown for the three-ring tension truss that the tension ties on the edges had to provide twice the force of the interior ties to give a desirable internal force pattern. As the number of rings increases, it is likely that more than two different tie forces are needed to obtain an adequate prestress. For practical purposes, however, it is necessary to restrict the number of different ties and their differences in force. If possible, only four different types of ties should be used within a structure and the minimal difference in force was set to 0.5 N. Also, the position of the additional nodes should not be too close to the edge cable in order to avoid problems that

may arise when connecting many members to a single node; a minimum value of 0.4 of the total sag seemed appropriate. Hence, the problem of prestressing an n-ring tension truss has been reduced to finding (i) a tension tie force combination on the edge and additional nodes and (ii) a position for the additional nodes. Throughout this analysis, $D = 3$ m and the sag-to-span ratio was fixed to 10%. The tie force combinations on the edge and additional nodes were, for each number of rings, found by a trial-and-error procedure. After a few tests on a tension truss with four rings it became clear which edge ties affected certain elements. The results from the trial analysis are shown in Figures 6.7–6.10. The corresponding element forces and their ratios for three different positions of the additional nodes are shown in Table 6.1. In all cases, the best ratios were obtained for $\delta_{\text{an}}/\delta_{\text{sag}} = 0.4$. The maximum number of rings in the analysed tension trusses was seven. The prestressing problems became significantly severe for more than seven rings, so this was taken as a limit. Another issue that will limit the number of rings is that the struts of the ring structure in the antenna concept, Figure 5.5, pass through the tension tie forest.

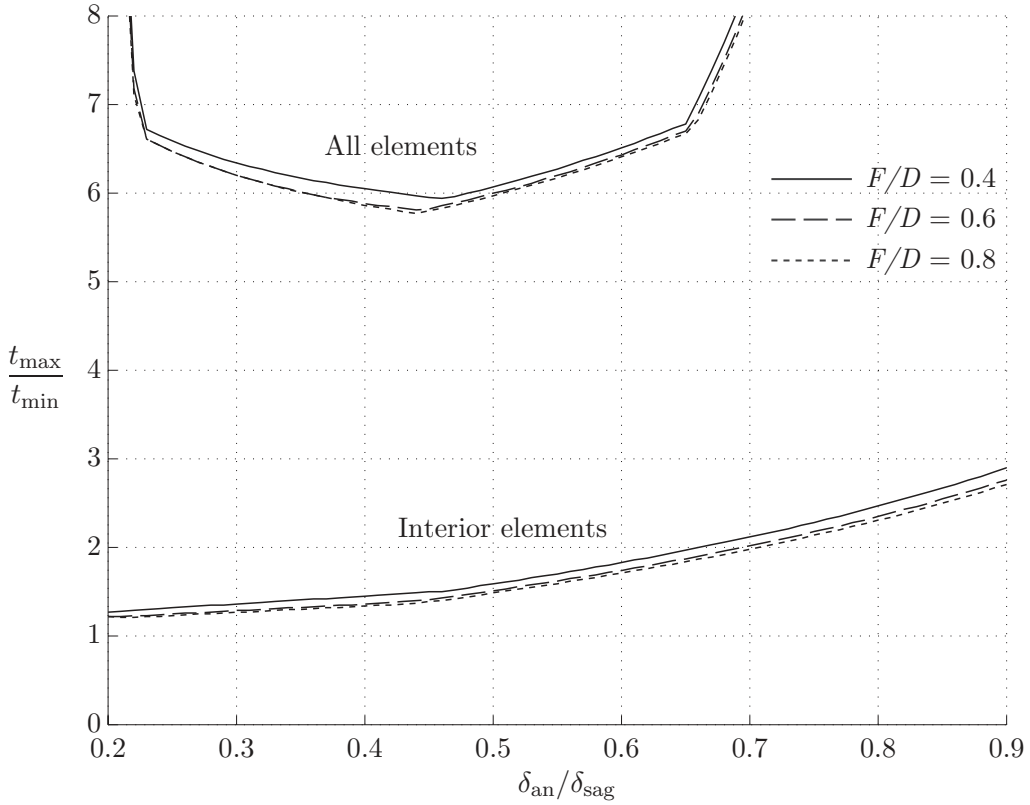

Figure 6.6: Ratios of the maximum and minimum forces in the tension truss. Two cases: interior elements and all elements.

Table 6.1: Tension truss element forces and their ratios (axi-symmetric configuration). The best ratios are in bold face.

n	F (m)	$\frac{F}{D_p}$	H_a (m)	$\frac{\delta_{an}}{\delta_{sag}}$	t_{min}^{int} (N)	t_{max}^{int} (N)	$\frac{t_{max}^{int}}{t_{min}^{int}}$	t_{min}^{all} (N)	t_{max}^{all} (N)	$\frac{t_{max}^{all}}{t_{min}^{all}}$
3	1.2	0.4	0.469	0.4	1.59	2.31	**1.45**	1.59	9.62	**6.05**
				0.5	1.45	2.45	1.59	1.55	9.38	6.07
				0.6	1.42	2.60	1.83	1.42	9.26	6.51
	1.8	0.6	0.313	0.4	2.39	3.25	**1.36**	2.39	14.04	**5.88**
				0.5	2.28	3.46	1.51	2.28	13.70	5.99
				0.6	2.10	3.66	1.74	2.10	13.52	6.43
	2.4	0.8	0.234	0.4	3.16	4.23	**1.34**	3.16	18.53	**5.86**
				0.5	3.03	4.50	1.49	3.03	18.08	5.97
				0.6	2.79	4.77	1.71	2.79	17.85	6.41
4	1.2	0.4	0.469	0.4	1.35	4.24	**3.14**	1.30	15.81	**12.18**
				0.5	1.30	4.33	3.34	0.92	15.83	17.25
				0.6	1.24	4.43	3.58	0.56	15.86	28.18
	1.8	0.6	0.313	0.4	2.00	5.94	**2.97**	1.84	22.93	**12.49**
				0.5	1.92	6.07	3.16	1.30	22.96	17.69
				0.6	1.83	6.21	3.39	0.80	23.01	28.91
	2.4	0.8	0.234	0.4	2.65	7.72	**2.91**	2.40	30.20	**12.61**
				0.5	2.55	7.88	3.09	1.69	30.24	17.86
				0.6	2.43	8.06	3.32	1.04	30.30	29.21
5	1.2	0.4	0.469	0.4	1.92	5.26	**2.74**	1.92	27.20	**14.17**
				0.5	1.91	5.32	2.78	1.57	27.21	17.33
				0.6	1.70	5.40	3.17	0.78	27.23	34.92
	1.8	0.6	0.313	0.4	2.84	7.34	**2.58**	2.84	39.30	**13.82**
				0.5	2.83	7.43	2.63	2.34	39.30	16.80
				0.6	2.51	7.53	3.00	1.16	39.34	33.97
	2.4	0.8	0.234	0.4	3.77	9.52	**2.52**	3.77	51.67	**13.70**
				0.5	3.75	9.63	2.57	3.11	51.67	16.60
				0.6	3.33	9.77	2.93	1.54	51.72	33.62
6	1.2	0.4	0.469	0.4	2.69	5.79	**2.16**	1.48	43.21	**29.11**
				0.5	2.64	5.89	2.23	0.75	43.28	57.69
				0.6	2.59	6.00	2.32	0.10	43.36	417.97
	1.8	0.6	0.313	0.4	3.98	8.07	**2.03**	2.10	62.24	**29.63**
				0.5	3.92	8.21	2.10	1.06	62.34	58.75
				0.6	3.83	8.36	2.18	0.15	62.46	425.90
	2.4	0.8	0.234	0.4	5.28	10.46	**1.98**	2.74	81.75	**29.84**
				0.5	5.20	10.64	2.05	1.38	81.88	59.18
				0.6	5.09	10.83	2.13	0.19	82.04	429.13
7	1.2	0.4	0.469	0.4	2.49	7.76	**3.12**	1.45	57.00	**39.24**
				0.5	2.44	7.86	3.22	1.38	57.09	41.40
				0.6	2.39	7.97	3.34	1.00	57.19	57.37
	1.8	0.6	0.313	0.4	3.68	10.80	**2.93**	2.17	81.94	**37.78**
				0.5	3.62	10.93	3.02	2.06	82.07	39.82
				0.6	3.54	11.08	3.13	1.47	82.22	56.07
	2.4	0.8	0.234	0.4	4.89	13.98	**2.86**	2.89	107.55	**37.24**
				0.5	4.80	14.16	2.95	2.74	107.71	39.25
				0.6	4.70	14.35	3.06	1.94	107.91	55.58

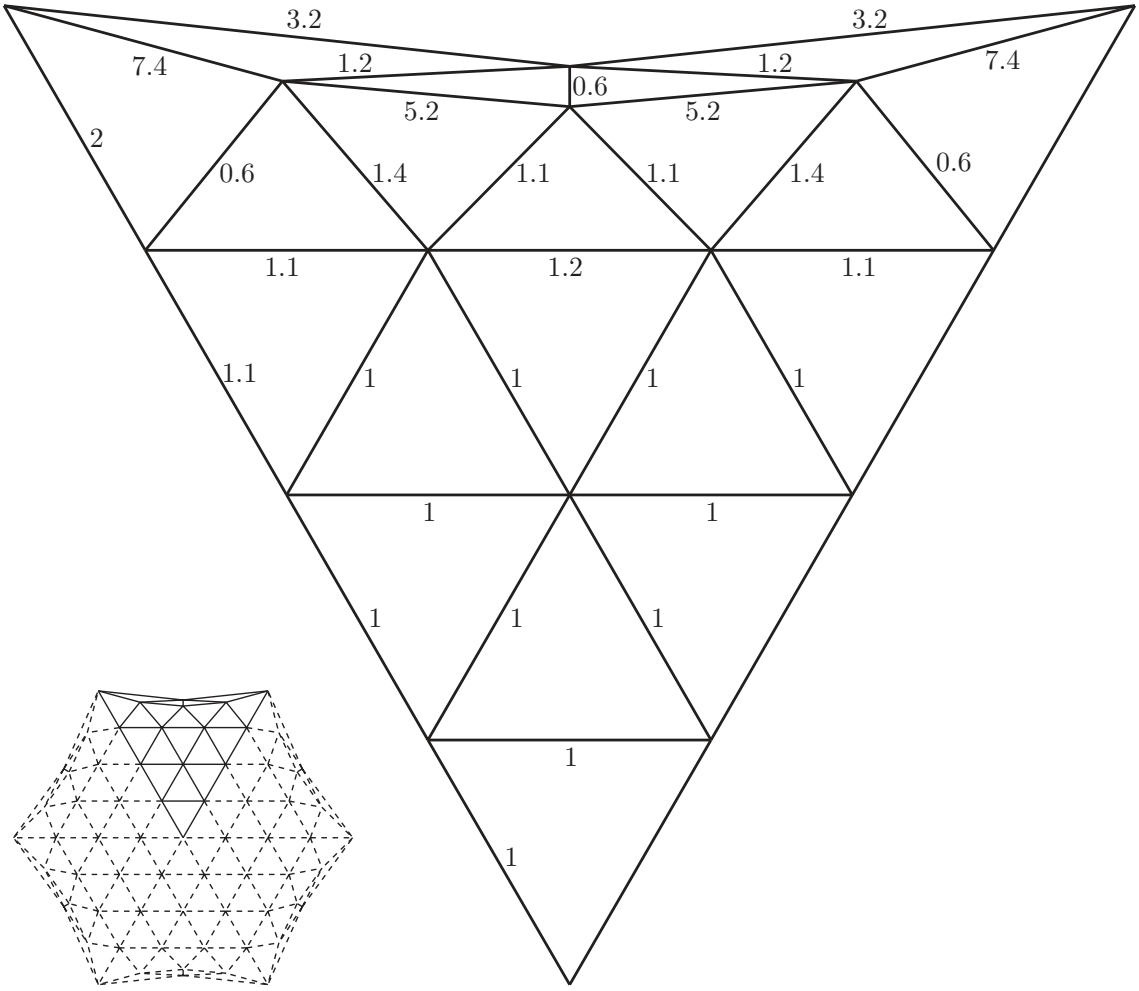

(a)

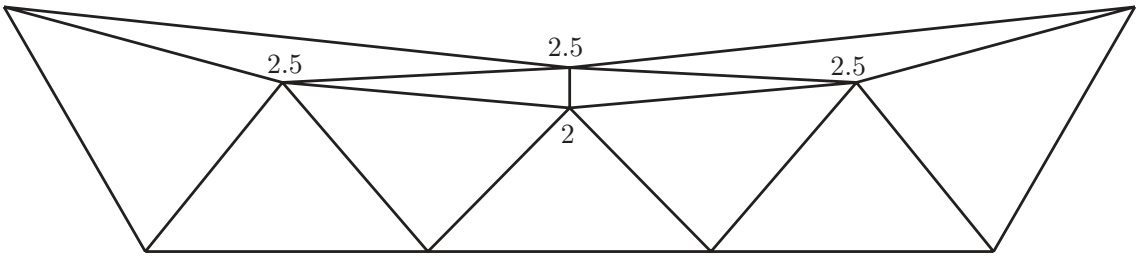

(b)

Figure 6.7: Normalised prestress distribution (a) under tension tie forces (b). Multiplication factor for element forces was 2.1. $D = 3$ m, $F/D = 0.4$, $\rho = 0.10$ and $\delta_{\text{an}}/\delta_{\text{sag}} = 0.4$.

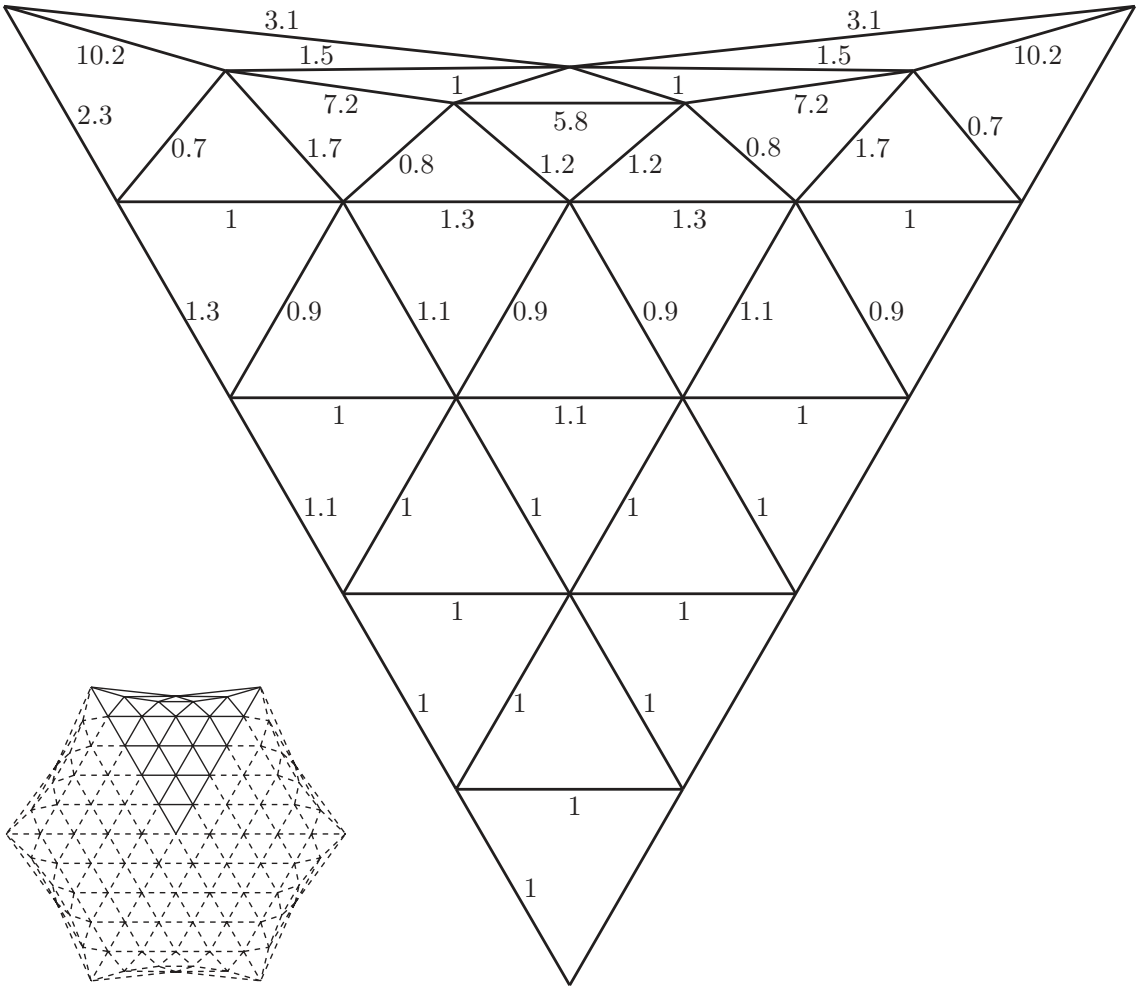

(a)

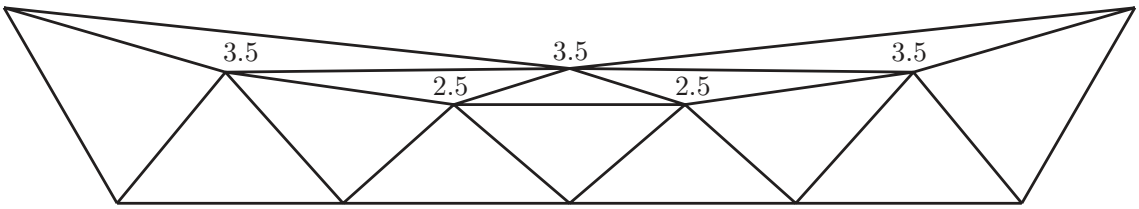

(b)

Figure 6.8: Normalised prestress distribution (a) under tension tie forces (b). Multiplication factor for element forces was 2.7. $D = 3$ m, $F/D = 0.4$, $\rho = 0.10$ and $\delta_{\text{an}}/\delta_{\text{sag}} = 0.4$.

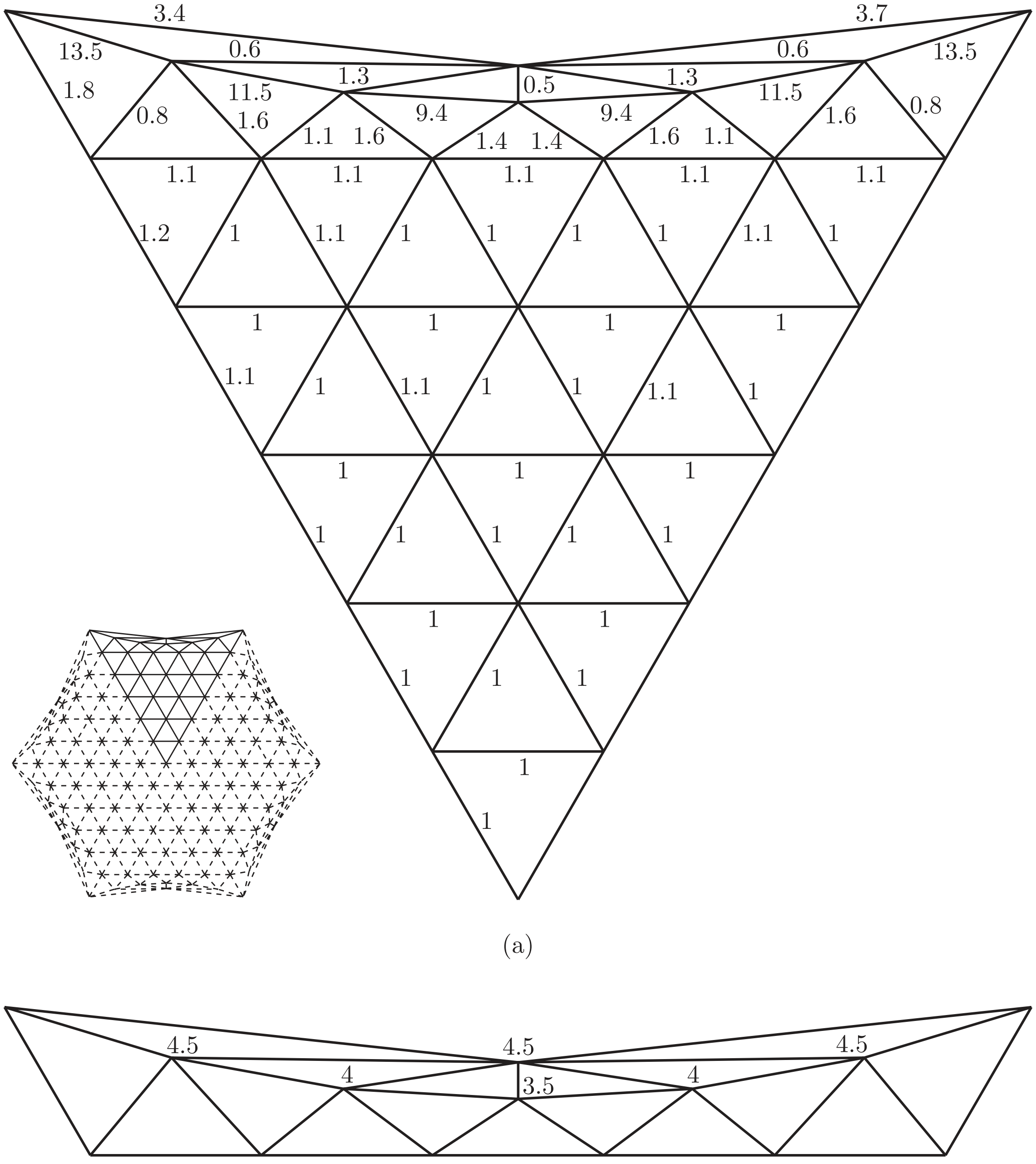

(a)

(b)

Figure 6.9: Normalised prestress distribution (a) under tension tie forces (b). Multiplication factor for element forces was 3.2. $D = 3$ m, $F/D = 0.4$, $\rho = 0.10$ and $\delta_{\rm an}/\delta_{\rm sag} = 0.4$.

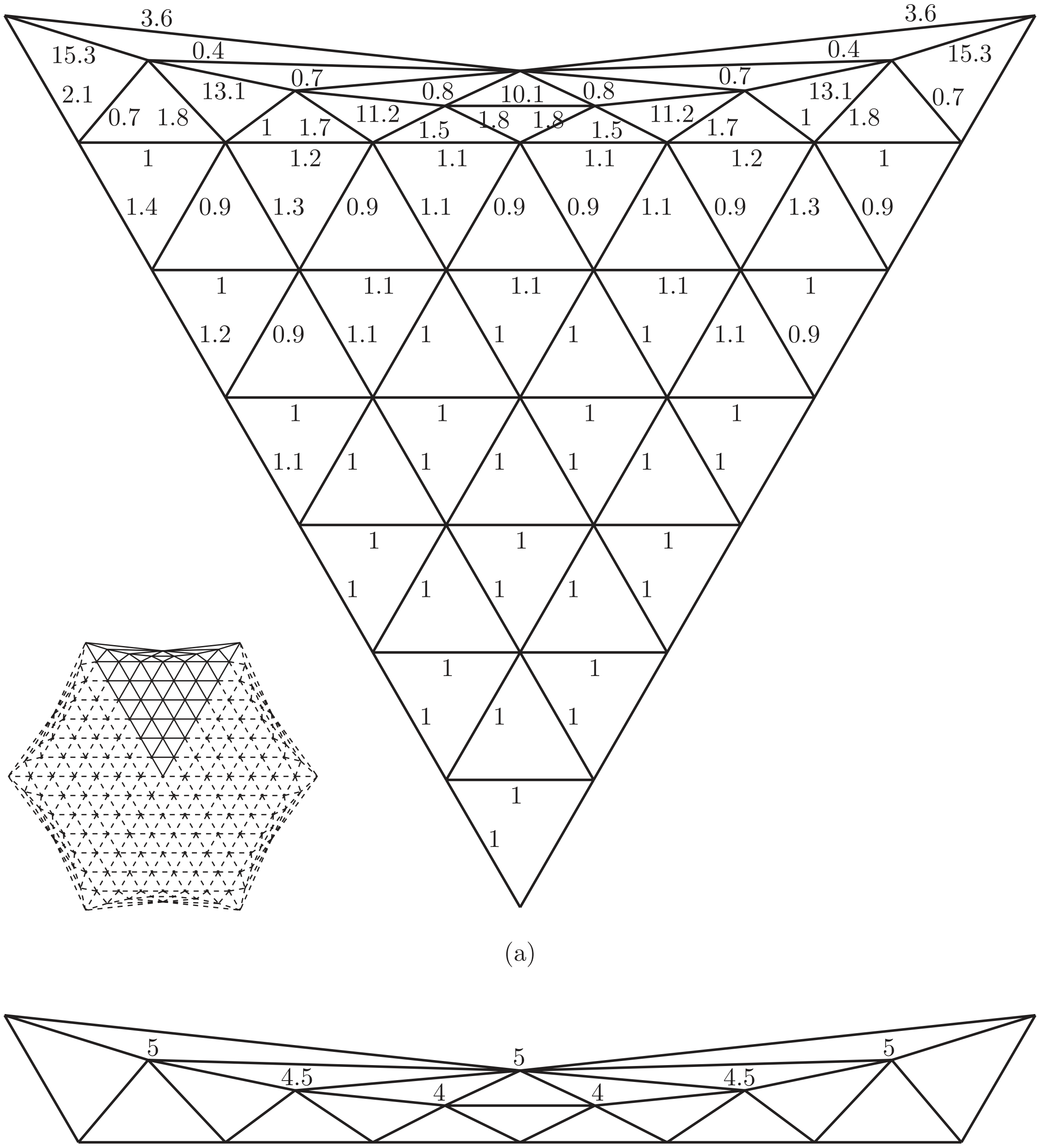

(a)

(b)

Figure 6.10: Normalised prestress distribution (a) under tension tie forces (b). Multiplication factor for element forces was 3.7. $D = 3$ m, $F/D = 0.4$, $\rho = 0.10$ and $\delta_{\text{an}}/\delta_{\text{sag}} = 0.4$.

6.3 Offset Configurations

The offset version of the tension truss is created by simply mapping the positions of the joints of the circular aperture onto an elliptic one. Thus, in the present case where the minor axis of the ellipse is equal to D, only the x-coordinate needs changing, $x := \xi x$, where ξ is the ellipticity, (5.10). The vertical joint positions are re-calculated using (5.8).

6.3.1 Focal Length and Offset Distance

For the offset antennas in Table 5.1, F/D_p varies between 0.167 and 0.363 and X_A/D_a varies between 0 and 0.17. From a blockage viewpoint, a larger value of X_A is better. Other issues, e.g. the size of the spacecraft bus and the antenna support structure, may prescribe both the focal length and offset distance. To determine the sensitivity of the force distribution in the tension truss to the ellipticity, ξ, three different realistic values of X_A/D_a were used: 0, 0.1 and 0.2. Three different focal length were also used: 1.5, 1.8 and 2.1 m. A preliminary analysis of a three-ring offset tension truss showed that a focal length less than 1.5 m was more difficult to prestress. Initially, the tension tie forces applied to the edge and additional nodes of the offset tension trusses were identical to those of the axi-symmetric cases, Figures 6.7–6.10. If, however, some of the elements ended up in compression, due to the change in geometry, the tension tie forces were changed.

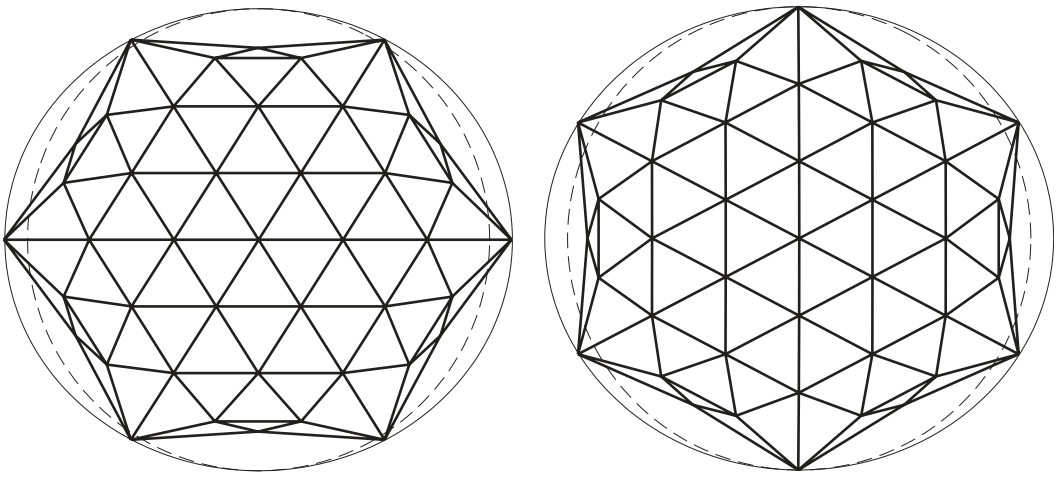

(a) (b)

Figure 6.11: Two symmetric offset configurations for the tension truss: (a) configuration 1 and (b) configuration 2.

6.3.2 Two Symmetric Offset Configurations

There are only two ways of arranging the tension truss in the offset configuration which preserve a certain symmetry, Figure 6.11. The first alternative, Figure 6.11(a), is to let two opposite support nodes lie along the major axis of the elliptic aperture. The second alternative, Figure 6.11(b), differs from the first by a 90° rotation so that the opposite nodes now lie along the minor axis. A preliminary analysis with a three-ring net showed that, in terms of prestressability, no configuration could be said to be better than the other. From a more practical reasoning, configuration 1 may be easier to attach to the spacecraft with nodes along the major ellipse axis, but this is only an assumption. Since there was hardly any difference in the force distribution between the two configurations, only configuration 1 will be used in the following analyses, based on the assumed simpler attachment. The results for the offset tension trusses are given in Table 6.2. The tension tie forces on the edge and additional nodes had to be changed slightly to give a satisfactory force pattern in the truss. The new values for three to seven rings are given in Figure 6.12. The value $X_A = 0$ gives the lowest ratio for the internal forces, but not necessarily the lowest for all forces.

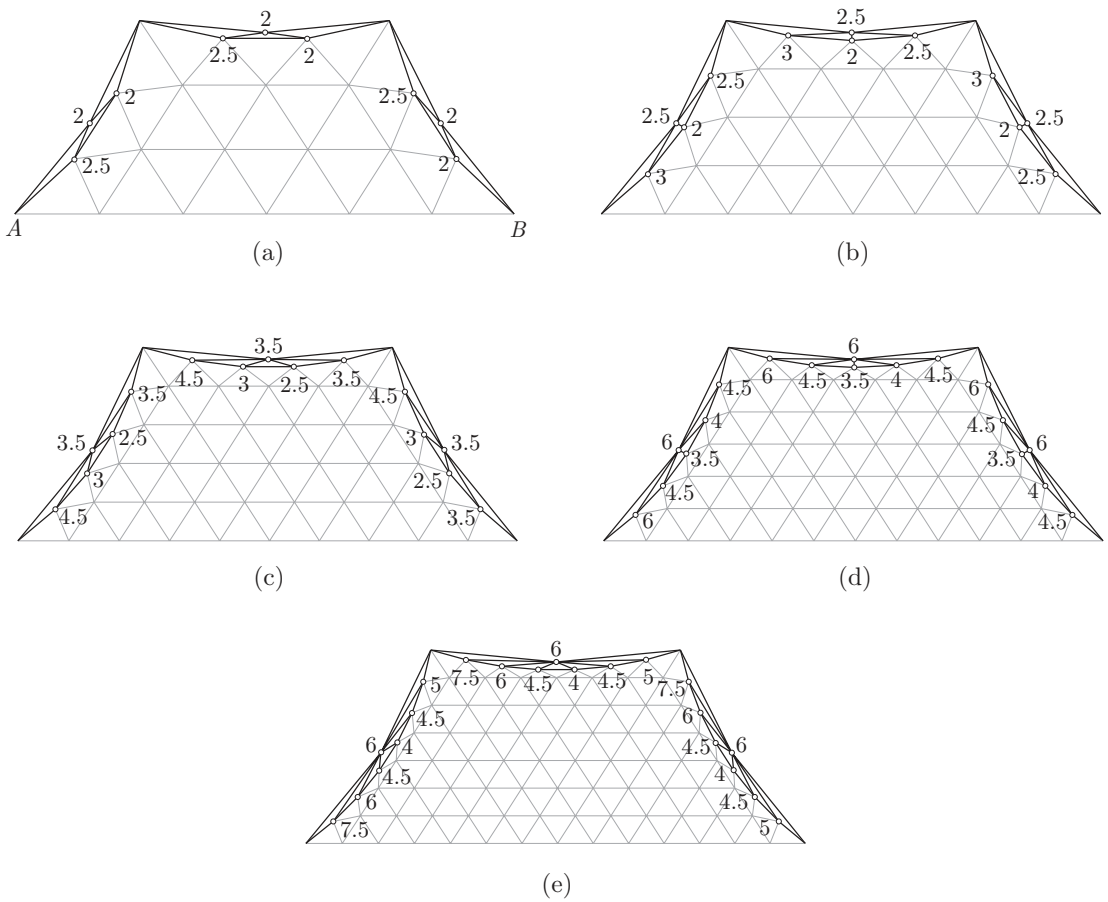

Figure 6.12: Tension tie force distribution along the edges and on the extra nodes to obtain an adequate internal force distribution in the tension truss of configuration 1: (a) three, (b) four, (c) five, (d) six, and (e) seven rings. Interior elements are drawn thinner for clarity.

Table 6.2: Tension truss element forces and their ratios (offset configuration 1). The best ratios are in bold face.

n	F (m)	X_A (m)	ξ	$\frac{F}{D_p}$	H_a (m)	$t^{\text{int}}_{\text{min}}$ (N)	$t^{\text{int}}_{\text{max}}$ (N)	$\frac{t^{\text{int}}_{\text{max}}}{t^{\text{int}}_{\text{min}}}$	$t^{\text{all}}_{\text{min}}$ (N)	$t^{\text{all}}_{\text{max}}$ (N)	$\frac{t^{\text{all}}_{\text{max}}}{t^{\text{all}}_{\text{min}}}$
3	1.5	0	1.118	0.250	0.335	1.62	4.05	**2.50**	1.62	18.44	**11.38**
		0.3	1.166	0.227	0.322	1.71	4.40	2.58	1.71	19.50	11.41
		0.6	1.221	0.208	0.307	1.64	4.79	2.93	1.64	20.66	12.61
	1.8	0	1.083	0.300	0.288	2.00	4.45	**2.22**	2.00	20.69	**10.33**
		0.3	1.118	0.273	0.280	2.05	4.75	2.32	2.05	21.63	10.56
		0.6	1.158	0.250	0.270	2.00	5.08	2.53	2.00	22.64	11.30
	2.1	0	1.062	0.350	0.252	2.39	4.90	**2.05**	2.39	23.10	**9.66**
		0.3	1.088	0.318	0.246	2.38	5.16	2.16	2.38	23.93	10.03
		0.6	1.118	0.292	0.240	2.36	5.45	2.31	2.36	24.83	10.54
4	1.5	0	1.118	0.250	0.335	1.20	6.37	**5.29**	1.20	28.34	**23.53**
		0.3	1.166	0.227	0.322	1.05	6.91	6.56	1.05	31.27	29.71
		0.6	1.221	0.208	0.307	0.95	7.52	7.93	0.95	34.57	36.44
	1.8	0	1.083	0.300	0.288	1.93	6.86	**3.56**	1.55	31.60	**20.33**
		0.3	1.118	0.273	0.280	1.78	7.31	4.10	1.60	32.96	20.61
		0.6	1.158	0.250	0.270	1.67	7.82	4.67	1.65	35.39	21.43
	2.1	0	1.062	0.350	0.252	2.60	7.47	**2.88**	1.76	35.33	**20.03**
		0.3	1.088	0.318	0.246	2.46	7.85	3.19	1.81	36.54	20.21
		0.6	1.118	0.292	0.240	2.35	8.28	3.52	1.86	37.87	20.38
5	1.5	0	1.118	0.250	0.335	2.20	7.88	**3.57**	2.20	50.40	**22.87**
		0.3	1.166	0.227	0.322	2.27	8.49	3.74	2.27	54.17	23.88
		0.6	1.221	0.208	0.307	2.20	9.17	4.16	2.20	59.91	27.18
	1.8	0	1.083	0.300	0.288	2.88	8.67	**3.01**	2.63	56.81	21.59
		0.3	1.118	0.273	0.280	2.93	9.18	3.14	2.90	59.18	**20.41**
		0.6	1.158	0.250	0.270	2.92	9.75	3.34	2.92	61.79	21.18
	2.1	0	1.062	0.350	0.252	3.54	9.59	**2.71**	2.60	63.61	24.48
		0.3	1.088	0.318	0.246	3.55	10.02	2.82	2.82	65.70	23.30
		0.6	1.118	0.292	0.240	3.53	10.51	2.98	3.01	68.02	**22.59**
6	1.5	0	1.118	0.250	0.335	2.60	9.88	**3.80**	1.69	78.83	**46.63**
		0.3	1.166	0.227	0.322	2.64	10.55	4.00	1.81	86.46	47.83
		0.6	1.221	0.208	0.307	2.13	11.27	5.30	1.95	95.63	48.92
	1.8	0	1.083	0.300	0.288	3.34	11.08	**3.31**	2.01	88.95	44.35
		0.3	1.118	0.273	0.280	3.40	11.63	3.42	2.10	92.57	44.11
		0.6	1.158	0.250	0.270	3.22	12.25	3.80	2.21	97.20	**43.87**
	2.1	0	1.062	0.350	0.252	4.07	12.38	**3.04**	2.31	99.67	43.14
		0.3	1.088	0.318	0.246	4.11	12.85	3.12	2.39	102.86	43.06
		0.6	1.118	0.292	0.240	4.10	13.39	3.27	2.49	106.41	**42.78**
7	1.5	0	1.118	0.250	0.335	1.99	14.12	**7.10**	1.99	114.40	**57.52**
		0.3	1.166	0.227	0.322	2.06	15.02	7.30	2.06	120.33	58.46
		0.6	1.221	0.208	0.307	1.90	16.00	8.41	1.64	126.84	77.52
	1.8	0	1.083	0.300	0.288	2.63	15.86	**6.03**	2.21	129.23	58.51
		0.3	1.118	0.273	0.280	2.68	16.61	6.20	2.62	134.38	51.36
		0.6	1.158	0.250	0.270	2.74	17.44	6.38	2.74	140.08	**51.21**
	2.1	0	1.062	0.350	0.252	3.26	17.75	**5.44**	2.03	144.92	71.32
		0.3	1.088	0.318	0.246	3.29	18.39	5.59	2.38	149.45	62.75
		0.6	1.118	0.292	0.240	3.37	19.11	5.67	2.74	154.50	**56.45**

6.4 Effects of Manufacturing Errors on the Reflector Accuracy

As described in section 5.4, the performance of a reflector antenna is mainly determined by the manufactured surface accuracy of the reflecting surface. For the tension truss, the systematic deviation due to surface faceting, (5.29), can be said to represent the minimum theoretical error. Unavoidably, the minimum achievable surface error is higher due to errors in the manufacturing process. These errors are randomly distributed in the structure and their influence on the surface accuracy can, in most cases, not be determined analytically. In such cases the alternative approach is the Monte Carlo technique, cf. [97].

Despite the significant importance of manufacturing errors, only a few studies are available in the literature. Hedgepeth [59] develops an equivalence between the statistical errors and the natural frequencies of a reflector antenna structure assembled by tetrahedral truss elements. Hedgepeth's analysis results in formulae which can be used for the preliminary design of such antennas. An interesting case of his analysis is when the height of the truss structure approaches zero, thus becoming a geodesic dome. The rms surface error of a geodesic dome, with an error-free rim, is [59]:

$$\delta_{\mathrm{rms},z} = 2F\sigma_\varepsilon, \tag{6.11}$$

where σ_ε is the standard deviation of the member length imperfections. It should be noted that (6.11) is based on a continuum approach and valid only for a large number of facets. Greene [49] continues the analysis of the tetrahedral truss structure using the Monte Carlo technique and a linear *Finite Element* (FE) model to obtain results for a reflector with a low number of facets. Greene finds that the surface deviation increases as the number of facet rings decreases. For two and four rings it is about three and two times higher than that predicted by (6.11), respectively. In addition to the surface accuracy, Greene also analyses the reflector de-focus and variation of the forces in the tetrahedral truss. It is found that the de-focus, like the surface accuracy, increases with a decreasing number of facet rings. More recently, Hedgepeth *et al.* [62] uses the Monte Carlo technique for a nine ring geodesic dome ($F = 15.7$ m) fixed at its rim. The rms surface error is computed for two error sources: member length imperfection and tension tie force variation. The average rms surface error of 100 simulations is 0.394 mm for the former case. Inserting $F = 15.7$ m and $\sigma_\varepsilon = 10^{-5}$ in (6.11) gives $\delta_{\mathrm{rms},z} = 0.314$ mm, which agrees well with their simulated value. The average rms surface deviation due to a tension tie force variation of 0.1 N is 0.160 mm. These three studies provide important information on the effects of manufacturing errors on different reflector parameters.

The element length imperfection and tension tie load variation are not the only manufacturing errors. Random errors related to the present antenna are:

- Member length imperfections,
- Ring structure distortion,

- Tension tie load variation, and
- Random thermal strains.

First, it is important to find how each of these errors alone affects the surface accuracy and de-focus in order to establish the manufacturing tolerance level. Then, the combined effect of all the random errors has to be determined to conclude on the achievable surface accuracy of the reflector. Other sources that affect the accuracy of the reflector are gravity during ground testing, attitude accelerations, etc.

6.4.1 Monte Carlo Technique for the Tension Truss

The technique used to calculate the effects of manufacturing errors makes use both of the force method and of the FEM. First, the configuration of the error-free tension truss was generated by the routine in Appendix C. Then, the element forces under the prescribed tension tie loading were computed by the force method. These forces were used to compute the unstrained length ℓ_0 of element i as:

$$\ell_{0,i} = \frac{\ell_i}{1 + t_i/AE_i}, \tag{6.12}$$

where t is the force in each element and AE the axial stiffness. To account for length errors in the assembly of the tension truss, the unstrained length of element i was modified as

$$\tilde{\ell}_{0,i} = \ell_{0,i}(1 + \varepsilon), \tag{6.13}$$

where

$$\varepsilon \sim \mathrm{N}(0, \sigma_\varepsilon), \tag{6.14}$$

i.e. normally distributed with a zero mean value and standard deviation σ_ε. The normally distributed random strain ε was generated by the Matlab [89] routine `randn`, which will theoretically produce over $2^{1492} \approx 10^{449}$ values before repeating itself. Then, the tension truss with the imperfect element lengths and unchanged tension tie loads was analysed by a finite element program using no-compression catenary cable elements, cf. [171]. These catenary elements require a small self-weight to avoid numerical problems. However, its influence was neglected as it was chosen to be much smaller than the tension tie loads. In the FE analysis it was assumed that all elements have the same properties, although the edge elements most likely have to be stiffer to sustain the higher forces.

6.4.2 Best-Fit Paraboloid Analysis

In section 5.4, the best-fit paraboloid, which minimises the rms surface deviation, was introduced. The computation of the best-fit paraboloid to a set of points on the reflector surface can be separated into two parts [49, 140]:

1. a rigid body fit, where a fitted paraboloid of fixed focal length undergoes translation along the Z-axis and rotates about the X- and Y-axis, followed by
2. a re-adjustment ΔF of the equivalent focal length.

Some results of best-fit paraboloid computations are given in [62] and [140]. They show that the rotations about the X- and Y-axes are very small; one is about $5 \cdot 10^{-4}$ and the other about one order lower. Therefore, the rotations about the X- and Y-axes were assumed to be negligible in the present analysis. As a result, the Z-axis of the best-fit paraboloid was always parallel to that of the ideal paraboloid. These simplifications may also be warranted by the use of (5.24), instead of (5.21), when calculating the rms surface error. Lai [78] uses a similar approach to compute the surface error for the CRTS reflector.

For a reflector surface represented by a discrete set of points, the equation of the best-fit paraboloid is

$$Z = \frac{X^2 + Y^2}{4F} + \Delta Z_P, \tag{6.15}$$

where F denotes the best-fit focal length and ΔZ_P the translation of the apex of the ideal paraboloid in the XYZ system. Let $(X_1, Y_1, Z_1), (X_2, Y_2, Z_2), ..., (X_n, Y_n, Z_n)$ be the coordinates of n points on the reflector surface. If the n points are not equally distributed over the aperture, the contribution of each point in the computation of the best-fit paraboloid will vary. This is taken care of by weighting each point by its associated area. Thus, dense points are given lower weights than sparse points. A more refined weighting can be done by also taking into account the radiation pattern over the aperture [178]. However, this will not be included here considering the simplifications already made. Substituting each of the n points into (6.15) and multiplying with the horizontal projection of the surface area associated to each point lead to the following over-determined system of linear equations:

$$\begin{bmatrix} A_1(X_1^2 + Y_1^2) & A_1 \\ A_2(X_2^2 + Y_2^2) & A_2 \\ \vdots & \vdots \\ A_n(X_n^2 + Y_n^2) & A_n \end{bmatrix} \begin{pmatrix} 1/4F \\ \Delta Z_P \end{pmatrix} = \begin{pmatrix} A_1 Z_1 \\ A_2 Z_2 \\ \vdots \\ A_n Z_n \end{pmatrix}. \tag{6.16}$$

Equation (6.16) is solved by a standard least squares solution technique, cf. [156]. In the present best-fit analysis the sides of each triangular facet were divided into N parts of equal length $\Delta\ell = \ell/N$, thereby creating N^2 sub-triangles. The centre of gravity of each sub-triangle was taken as a point in the best-fit paraboloid computation and the horizontal projection of the sub-triangle area was taken as its weight factor. Subsequently, the axial rms surface deviation is computed as:

$$\delta_{\mathrm{rms},z} = \left[\frac{1}{\sum_{i=1}^{n} A_i} \sum_{i=1}^{n} A_i \left(\tilde{Z}_i - Z_i \right)^2 \right]^{1/2}. \tag{6.17}$$

Note that for offset reflectors the points should be measured in the coordinate system of the parent paraboloid, XYZ. Another important parameter for the performance of the reflector is the de-focus, which is simply the total translation of the focal point, $\Delta F + \Delta Z_P$ [49].

6.4.3 Extracting the Random Surface Deviations

The routine for computing the best-fit paraboloid, rms surface deviation and defocus does not distinguish systematic errors from random errors, but computes the total rms surface error. However, the systematic error due to faceting will always exist so the contribution from the random rms surface error must be extracted from the total rms surface error. A technique to extract a single or several random errors from the total error will now be introduced. First, assume that the total error is caused by one systematic and one random error source. In the following, z_{sy} denotes the z-coordinate of the reflector surface with only the systematic error present, z_{bf} the z-coordinate of the best-fit paraboloid (to both errors), and ϵ_z the additional contribution of the random error in the z-direction. Equation (5.24) can be expanded as follows:

$$\begin{aligned}
\delta^2_{\mathrm{rms},z} &= \frac{1}{A_a}\iint\limits_{A_a} (\Delta z)^2 \,\mathrm{d}A \\
&= \frac{1}{A_a}\iint\limits_{A_a} \left((z_{\mathrm{sy}}+\epsilon_z) - z_{\mathrm{bf}}\right)^2 \mathrm{d}A \\
&= \underbrace{\frac{1}{A_a}\iint\limits_{A_a} \left(z_{\mathrm{sy}} - z_{\mathrm{bf}}\right)^2 \mathrm{d}A}_{\mathrm{I}} + \underbrace{\frac{1}{A_a}\iint\limits_{A_a} \epsilon_z^2 + 2\epsilon_z(z_{\mathrm{sy}} - z_{\mathrm{bf}})\mathrm{d}A}_{\mathrm{II}}\,.
\end{aligned} \tag{6.18}$$

Integral I is approximately equal to the squared systematic rms surface deviation due to the facet approximation. It is not exactly equal since the calculation of the best-fit paraboloid also includes ϵ_z. Integral II is the square of the additional surface deviation due to manufacturing tolerances. For $\epsilon_z \to 0$, the rms surface deviation approaches that of the ideal faceted reflector antenna. With some further simplifications it is also possible to approximately find the separate effects of different random deviations. For the case of two random deviations, $\epsilon_z = \epsilon_{z,1} + \epsilon_{z,2}$, (5.24) is written as:

$$\begin{aligned}
\delta^2_{\mathrm{rms},z} = \frac{1}{A_a}\iint\limits_{A_a} \left(z_{\mathrm{sy}} - z_{\mathrm{bf}}\right)^2 + \frac{1}{A_a}\iint\limits_{A_a} 2\epsilon_{z,1}(z_{\mathrm{sy}} - z_{\mathrm{bf}})\mathrm{d}A \\
+ \frac{1}{A_a}\iint\limits_{A_a} 2\epsilon_{z,2}(z_{\mathrm{sy}} - z_{\mathrm{bf}})\mathrm{d}A + \frac{1}{A_a}\iint\limits_{A_a} (\epsilon_{z,1}+\epsilon_{z,2})^2\mathrm{d}A.
\end{aligned} \tag{6.19}$$

Terms of type $\epsilon_{z,i}\epsilon_{z,j}$ are very small and can be neglected, which means that the fourth integral vanishes. Thus, the second and third integrals are the influences of $\epsilon_{z,1}$ and $\epsilon_{z,2}$, respectively. If the individual random error $\epsilon_{z,i}$ is small this technique can be extended to an arbitrary number of random errors. Thomson [166] uses a similar technique to compute the total rms surface deviation, or the rss surface deviation as he calls it, from several error sources. Thomson's results are reproduced in Table 5.2.

6.4.4 Systematic Facet Surface Deviation

Before the influence of the random errors can be computed the systematic rms surface deviation and de-focus have to be determined. Although it was possible to get a good estimate of the rms surface error by (5.29) it was necessary for the following analyses to compute the error by the best-fit computation described above. In this, and the following analyses of the surface deviation, the parameters of the antenna were: $D = 3$ m, $F/D = 0.4,\ 0.6$ and 0.8, and $\delta_{\text{an}}/\delta_{\text{sag}} = 0.6$. The analysis of the systematic rms error were done for three to nine rings. The nodal positions of the tension truss were the ones generated by the mesh generation routine in Appendix C. As the tension truss is six-fold symmetric, only one sixth needed to be analysed. The systematic rms surface error was computed for 5^2, 10^2, 20^2, 25^2 and 40^2 sub-triangles in each triangular facet. The results from all except the 25^2 case were used in a Richardson extrapolation scheme, cf. [29], to determine the asymptotic values of the rms surface error. They were then compared to those by Agrawal *et al.*, (5.29). The 25^2 sub-division was chosen to be used in the subsequent computations of the random error as it produced values close to the asymptotic values and required less computation time when the entire tension truss has to be analysed. The results of the systematic error computations are shown in Table 6.3, where superscripts $^{\text{Ag}}$ and ^{25} indicate the values by (5.29) and a 25^2 sub-division, respectively. Values without superscript are the Richardson-extrapolated ones. Throughout the range of rings, both of the computed rms surface errors agree well with the one by (5.29). The de-focus decreased with increasing number of rings as it should, thus the reliability of the best-fit routine was confirmed.

6.4.5 Influence of Tension Tie Loading

While the computation of the systematic surface errors was done for three to nine rings, the analyses concerned with the random errors were only done for three rings. Since this is a feasibility study, although a quite extensive one, an estimation of the required manufacturing tolerances can be done by analysing a representative antenna configuration. For example, Hedgepeth *et al.* [62] perform Monte Carlo simulations on a nine ring geodesic dome with flexible members in order to get accuracy estimates for the real one with 27 rings. It was further assumed that the dependency of the rms surface error and de-focus on the number of rings was similar to that of the tetrahedral truss structure studied in [49, 59]. Thus, a smaller number of rings would produce a larger rms surface error and more severe de-focus. Note, however, that the validity of this assumption was not put to test in this thesis.

The computations of the systematic errors in the previous section were based on the generated nodal positions. When the equilibrium configuration of the tension truss was computed using the FEM, the nodal positions differed due to load deformations. For significant differences, the previously computed systematic error cannot be used when extracting the random errors from the total error. To determine if the elastic deformation was large enough to affect the systematic error, the three-ring tension truss was analysed for two different interior tension tie loads: 1 and 10 N. The results

Table 6.3: Surface deviation (rms) and de-focus of a paraboloid due to triangular faceting.

n	F/D	$\delta^{\mathrm{Ag}}_{\mathrm{rms},z}$ (mm)	$\delta_{\mathrm{rms},z}$ (mm)	$\delta^{25}_{\mathrm{rms},z}$ (mm)	$\Delta F + \Delta Z_P$ (mm)	$\Delta F^{25} + \Delta Z^{25}_P$ (mm)
3	0.4	3.3620	3.3496	3.3417	22.4630	22.4728
	0.6	2.2413	2.2331	2.2278	22.6142	22.6233
	0.8	1.6810	1.6748	1.6709	24.9814	24.9909
4	0.4	1.8911	1.9305	1.9261	13.6208	13.6272
	0.6	1.2607	1.2870	1.2841	14.0371	14.0435
	0.8	0.9456	0.9652	0.9630	15.7322	15.7392
5	0.4	1.2103	1.2629	1.2601	8.4811	8.4852
	0.6	0.8069	0.8419	0.8401	8.6046	8.6086
	0.8	0.6052	0.6315	0.6301	9.5516	9.5559
6	0.4	0.8405	0.8897	0.8877	5.4803	5.4830
	0.6	0.5603	0.5931	0.5918	5.3715	5.3740
	0.8	0.4202	0.4448	0.4439	5.8324	5.8349
7	0.4	0.6175	0.6569	0.6555	3.6903	3.6921
	0.6	0.4117	0.4379	0.4370	3.4574	3.4589
	0.8	0.3088	0.3285	0.3277	3.6399	3.6416
8	0.4	0.4728	0.5011	0.5000	2.5954	2.5967
	0.6	0.3152	0.3341	0.3333	2.3142	2.3153
	0.8	0.2364	0.2506	0.2500	2.3489	2.3499
9	0.4	0.3736	0.3919	0.3910	1.9075	1.9085
	0.6	0.2490	0.2613	0.2607	1.6223	1.6231
	0.8	0.1868	0.1959	0.1955	1.5849	1.5856

are shown in Table 6.4. The higher tension tie load gave slightly lower values for the de-focus. This was due to the increased vertical deformation of the net. However, the rms surface deviation was unaffected by the higher tie load. In the studies which follow, an interior tie load of 5 N was used to further reduce the effects of the small self-weight of the catenary elements. In a zero-gravity environment, a smaller tie load can be used.

Table 6.4: Influence of deformation due to tension tie loading (three-ring tension truss).

F/D		0.4		0.6		0.8	
$t^{\mathrm{int}}_{\mathrm{tie}}$	(N)	1	10	1	10	1	10
$\delta_{\mathrm{rms},z}$	(mm)	3.3417	3.3417	2.2279	2.2279	1.6710	1.6710
$\Delta F + \Delta Z_P$	(mm)	22.4801	22.4695	22.6253	22.6115	24.9765	24.9575

6.4.6 Statistical Considerations

The statistical treatment of the results from the Monte Carlo trials was more or less straightforward. The mean value of a parameter p is denoted $\bar{p}$ and its standard deviation σ_p. Here, the parameters are the rms surface error and de-focus. From the trials, the maximum and minimum values of p were also extracted. However, since the number of trials was quite small the maximum computed value $p_{\max}$ could not be taken as the highest value likely to occur. To find a representative maximum value of the parameter, a probability limit had to be set. A maximum value often used is $\widehat{p} = \bar{p} + 3\sigma_p$, which corresponds to a probability of 0.00135 that any simulated value will be larger. This value was chosen to represent the worst possible value of the studied parameter. The quality of the simulated values was estimated by the standard deviation of all the values generated with `randn`, which should be close to one. The standard deviation of S simulations was approximatively computed as

$$\sigma_{\texttt{randn}} = \left(\frac{1}{S} \sum_{i=1}^{S} \sigma_{\texttt{randn},i}^2 \right)^{1/2}, \tag{6.20}$$

where $\sigma_{\texttt{randn},i}$ is the standard deviation for simulation number i.

Another important statistical aspect is the required number of Monte Carlo simulations. Hedgepeth *et al.* [62] use 100 simulations for their two cases. Greene [49] also uses 100 simulations for the rms surface error but finds it necessary to increase the number of trials to 200 to determine the de-focus with reasonable accuracy. To determine how the surface error and de-focus vary with the number of Monte Carlo simulations, a tension truss with member length imperfections was chosen as a test example. The rms surface error and de-focus, and their corresponding standard deviations, were computed for 100 to 500 simulations, Table 6.5. Overall, the differences were very small; only the standard deviation of the surface error had differences of more than 1%. Hence, it was concluded that 100 simulations was sufficient for the Monte Carlo analysis of the tension truss.

6.4.7 Influence of Member Length Imperfections

The first of the random error sources is the individual lengths of the elements. The fabrication tolerance that can be achieved depends highly on the manufacturing costs that can be accepted. Hedgepeth [58] finds that "a value of σ_ε of 10^{-3} is representative of ordinary careful practice, 10^{-4} is characteristic of a high-quality machine shop, 10^{-5} is achievable with well-designed and operated hard tooling, and 10^{-6} is very difficult and costly." However, length tolerances σ_ε as low as $3 \cdot 10^{-7}$ has recently been achieved for the AstroMesh [166]. It was decided to analyse the present three-ring tension truss for three tolerances: $\sigma_\varepsilon = 10^{-4}$, 10^{-5} and 10^{-6}.

The results for the rms surface error and de-focus are given in Table 6.6. Of importance to the performance of the antenna is also to maintain a sufficient stress level in the tension truss. The lowest net element force was therefore sought for each

simulation. For $F/D = 0.4$ and $\sigma_\varepsilon = 10^{-4}$, 10^{-5} and 10^{-6} the interval and mean value (in parenthesis) of the lowest element force were 0.0463–5.97 N (1.18 N), 5.57–6.97 N (6.43 N), and 6.95–7.09 N (7.03 N), respectively. For $F/D = 0.6$ they were 0.0635–8.63 N (3.38 N), 8.82–10.4 N (9.78 N), and 10.3–10.5 N (10.4 N), respectively. For $F/D = 0.8$ they were 0.0642–11.8 N (6.57 N), 12.4–13.8 N (13.2 N), and 13.8–13.9 N (13.8 N). Apparently, a tolerance of $\sigma_\varepsilon = 10^{-4}$ cannot be accepted.

6.4.8 Influence of Tension Tie Load Variation

The tension ties are so-called constant-force springs with relatively low stiffness so that an elongation results only in a small change of force. Compared to the length imperfections, the achievable force accuracy is much lower. Hedgepeth *et al.* [62] use a standard deviation of 0.1 N for a magnitude of 1 N. In the following analysis, two tie force variations were used: 0.1 and 0.05. The case of the lower accuracy, $\sigma_\tau = 0.1$, yielded unsatisfactory results and therefore the higher accuracy was required.

The interval and mean value (in parenthesis) of the lowest element force for $F/D = 0.4,\ 0.6$, and 0.8 with $\sigma_\tau = 0.1$ were 0.177–5.85 N (3.52 N), 0.218–8.16 N (5.56 N), and 1.04–11.7 N (8.18 N). There was a risk, although slim, that some cables become slack. For $F/D = 0.4$ the lowest force was lower than 0.25 N in only two cases of the 100 simulations, otherwise it was higher than 1.25 N. Using the smaller tolerance, $\sigma_\tau = 0.05$, gave intervals and mean values 3.51–6.54 N (5.56 N), 5.46–9.87 N (8.62 N), and 9.26–13.4 N (11.7 N), for the same values of F/D. Clearly, $\sigma_\tau = 0.05$ provided a better chance of keeping a good prestress in all elements, which is necessary to avoid severe mesh saddling.

Table 6.5: Surface accuracy and de-focus for a three-ring tension truss as a function of the number of Monte Carlo simulations ($D = 3$ m, $F/D = 0.4$, $\rho = 0.1$ and $\sigma_\varepsilon = 10^{-6}$).

Number of simulations		100	200	300	400	500
$\bar{\delta}_{\mathrm{rms},z}$	(mm)	3.341749	3.341747	3.341744	3.341743	3.341743
Difference	(%)	—	−0.000070	−0.000150	−0.000185	−0.000191
$\sigma_{\delta_{\mathrm{rms},z}}$	(mm)	0.000055	0.000059	0.000060	0.000060	0.000062
Difference	(%)	—	7.43	9.56	9.23	11.56
$\overline{\Delta F + \Delta Z_P}$	(mm)	22.470104	22.469671	22.469767	22.469752	22.469726
Difference	(%)	—	−0.000019	−0.000015	−0.000016	−0.000017
$\sigma_{\Delta F+\Delta Z_P}$	(mm)	0.004709	0.005031	0.005107	0.005186	0.005233
Difference	(%)	—	0.068	0.084	0.10	0.11

Table 6.6: Influence of member length imperfection on the rms surface deviation and de-focus (three-ring tension truss, 100 Monte Carlo simulations).

F/D		0.4			0.6			0.8		
σ_ε		10^{-4}	10^{-5}	10^{-6}	10^{-4}	10^{-5}	10^{-6}	10^{-4}	10^{-5}	10^{-6}
$\widehat{\delta}^{\varepsilon}_{\mathrm{rms},z}$	(mm)	0.4112	0.1127	0.03921	0.4388	0.1013	0.03656	0.4989	0.1035	0.03469
$\bar{\delta}^{\varepsilon}_{\mathrm{rms},z}$	(mm)	0.2195	0.0259	0.01828	0.2658	0.0299	0.02003	0.3322	0.0409	0.02239
$\sigma^{\varepsilon}_{\Delta F+\Delta Z_P}$	(mm)	0.4896	0.0470	0.00471	1.4521	0.1424	0.01375	3.4273	0.3048	0.03065
$\overline{\Delta F+\Delta Z_P}$	(mm)	22.4397	22.4721	22.47010	22.3806	22.5946	22.61259	23.9639	24.9716	24.96371
$\sigma^{\varepsilon}_{\texttt{randn}}$		1.0110	1.0069	1.00263	0.9957	0.9982	1.00263	1.0019	1.0026	1.00434
$\bar{\delta}_{\mathrm{rms},z}$	(mm)	3.3489	3.3418	3.34175	2.2436	2.2280	2.22789	1.7036	1.6714	1.67100
$\delta^{\max}_{\mathrm{rms},z}$	(mm)	3.3693	3.3431	3.34191	2.2691	2.2303	2.22810	1.7310	1.6739	1.67121
$\delta^{\min}_{\mathrm{rms},z}$	(mm)	3.3371	3.3400	3.34162	2.2286	2.2258	2.22772	1.6754	1.6694	1.67085
$\sigma_{\delta_{\mathrm{rms},z}}$	(mm)	0.0060	0.0006	0.00006	0.0090	0.0007	0.00007	0.0134	0.0009	0.00007
$\overline{\Delta F}$	(mm)	9.1397	9.1693	9.16810	13.5284	13.7298	13.74633	17.3476	18.3245	18.31619
$\Delta F^{\max}$	(mm)	10.2548	9.2569	9.17654	17.7177	14.1251	13.77194	25.5796	18.9141	18.38325
$\Delta F^{\min}$	(mm)	8.2079	9.0621	9.15601	10.4594	13.3359	13.70852	8.7774	17.4652	18.24982
$\sigma_{\Delta F}$	(mm)	0.4219	0.0401	0.00403	1.3528	0.1323	0.01277	3.2783	0.2922	0.02917
$\overline{\Delta Z_P}$	(mm)	13.3000	13.3028	13.30200	8.8521	8.8648	8.86626	6.6164	6.6471	6.64752
$\Delta Z_P^{\max}$	(mm)	13.5273	13.3211	13.30380	9.2139	8.9002	8.86875	7.0597	6.6791	6.65139
$\Delta Z_P^{\min}$	(mm)	13.1494	13.2856	13.29985	8.6061	8.8307	8.86319	6.2262	6.6073	6.64370
$\sigma_{\Delta Z_P}$	(mm)	0.0770	0.0079	0.00079	0.1142	0.0115	0.00112	0.1590	0.0146	0.00161

Table 6.7: Influence of tension tie force variation on the rms surface deviation and de-focus (three-ring tension truss, 100 Monte Carlo simulations).

F/D		0.4		0.6		0.8	
σ_τ		0.1	0.05	0.1	0.05	0.1	0.05
$\widehat{\delta}^\tau_{\mathrm{rms},z}$	(mm)	0.1656	0.11030	0.1854	0.12845	0.2274	0.14592
$\bar{\delta}^\tau_{\mathrm{rms},z}$	(mm)	0.0366	0.02711	0.0790	0.05704	0.1281	0.06173
$\sigma^\tau_{\Delta F+\Delta Z_P}$	(mm)	0.0765	0.03707	0.2968	0.14942	0.7357	0.43429
$\overline{\Delta F+\Delta Z_P}$	(mm)	22.4641	22.47280	22.5509	22.61540	24.8709	24.91352
$\sigma^\tau_{\texttt{randn}}$		1.0027	1.00001	0.9957	1.00810	0.9986	0.99714
$\bar{\delta}_{\mathrm{rms},z}$	(mm)	3.3419	3.34181	2.2292	2.22853	1.6758	1.67199
$\delta^{\max}_{\mathrm{rms},z}$	(mm)	3.3451	3.34319	2.2340	2.23053	1.6875	1.67601
$\delta^{\min}_{\mathrm{rms},z}$	(mm)	3.3379	3.34065	2.2240	2.22572	1.6684	1.66735
$\sigma_{\delta_{\mathrm{rms},z}}$	(mm)	0.0013	0.00057	0.0021	0.00099	0.0035	0.00174
$\overline{\Delta F}$	(mm)	9.1629	9.17070	13.6891	13.74996	18.2262	18.26742
$\Delta F^{\max}$	(mm)	9.3482	9.24285	14.2461	14.06349	19.9889	19.23906
$\Delta F^{\min}$	(mm)	8.9964	9.08753	13.0219	13.41423	16.2504	17.19885
$\sigma_{\Delta F}$	(mm)	0.0680	0.03307	0.2798	0.14064	0.7116	0.41983
$\overline{\Delta Z_P}$	(mm)	13.3012	13.30211	8.8618	8.86544	6.6447	6.64610
$\Delta Z_P^{\max}$	(mm)	13.3253	13.31591	8.9073	8.88727	6.7302	6.68603
$\Delta Z_P^{\min}$	(mm)	13.2816	13.29318	8.8138	8.84171	6.5870	6.59766
$\sigma_{\Delta Z_P}$	(mm)	0.0096	0.00470	0.0190	0.00994	0.0282	0.01703

6.4.9 Influence of Ring Structure Distortion

In the following analysis of the influence of the ring structure distortion, it was assumed that the random distortions in x-, y-, and z-directions were normally distributed with a zero mean value and the same standard deviation, σ_ρ. In the real antenna structure this type of error arises due to length errors in the members of the ring structure, which are of two different types: cables and struts. It is likely that one of these can be manufactured to a higher precision than the other. Hence, the least accurate of the types will give rise to the largest error at the ring nodes; this was the basis of the assumption of using a single standard deviation. The member length imperfection influence analysis indicated that the accuracy level 10^{-4} could produce cable slackening. Therefore, only the two higher accuracy levels, 10^{-5} and 10^{-6}, were used in the ring structure distortion analysis. For each node, the nodal distortion in each of the x-, y- and z-directions was computed as $D\epsilon_\rho$, where $\epsilon_\rho \sim \mathrm{N}(0, \sigma_\rho)$.

The results from the ring distortion analysis are shown in Table 6.8. The interval and mean value (in parenthesis) of the lowest element force for $F/D = 0.4,\ 0.6,$ and 0.8 with $\sigma_\rho = 10^{-5}$ were 0.0387–5.26 N (0.716 N), 0.0342–8.08 N (0.725 N), and

Table 6.8: Influence of ring structure distortion on the rms surface deviation and de-focus (three-ring tension truss, 100 Monte Carlo simulations).

F/D		0.4		0.6		0.8	
σ_ρ		10^{-5}	10^{-6}	10^{-5}	10^{-6}	10^{-5}	10^{-6}
$\widehat{\delta}^{\rho}_{\mathrm{rms},z}$	(mm)	0.4442	0.08298	0.8320	0.09032	0.6798	0.09899
$\bar{\delta}^{\rho}_{\mathrm{rms},z}$	(mm)	0.2454	0.04088	0.4439	0.01156	0.3608	0.06146
$\sigma^{\rho}_{\Delta F+\Delta Z_P}$	(mm)	0.7685	0.00945	1.2530	0.04909	1.1724	0.04861
$\overline{\Delta F+\Delta Z_P}$	(mm)	21.5504	22.46750	23.6198	22.65153	24.5268	24.91198
$\sigma^{\rho}_{\texttt{randn}}$		0.9861	0.98562	1.0027	0.98153	0.9723	1.00060
$\bar{\delta}_{\mathrm{rms},z}$	(mm)	3.3507	3.34195	2.2716	2.22783	1.7094	1.67198
$\delta^{\max}_{\mathrm{rms},z}$	(mm)	3.3623	3.34252	2.3308	2.22889	1.7707	1.67288
$\delta^{\min}_{\mathrm{rms},z}$	(mm)	3.3392	3.34130	2.2262	2.22673	1.6710	1.67054
$\sigma_{\delta_{\mathrm{rms},z}}$	(mm)	0.0068	0.00026	0.0355	0.00060	0.0315	0.00060
$\overline{\Delta F}$	(mm)	8.5018	9.16349	14.6794	13.77344	17.6941	18.27448
$\Delta F^{\max}$	(mm)	9.2674	9.18197	17.1475	13.84509	19.9586	18.37599
$\Delta F^{\min}$	(mm)	7.3351	9.14827	12.7152	13.71798	13.7381	18.19524
$\sigma_{\Delta F}$	(mm)	0.5959	0.00695	1.1382	0.03537	1.2003	0.03994
$\overline{\Delta Z_P}$	(mm)	13.0486	13.30401	8.9405	8.87810	6.8327	6.63750
$\Delta Z_P^{\max}$	(mm)	13.3672	13.31591	9.1928	8.90543	7.3125	6.66412
$\Delta Z_P^{\min}$	(mm)	12.7981	13.29415	8.7002	8.85469	6.4979	6.62382
$\sigma_{\Delta Z_P}$	(mm)	0.1832	0.00510	0.1364	0.01408	0.2301	0.00955

0.0368–10.4 N (1.85 N), respectively. With $\sigma_\rho = 10^{-6}$, the corresponding intervals and mean values were 5.53–7.02 N (6.49 N), 5.16–10.4 N (7.77 N), and 10.9–13.7 N (11.8 N), respectively. Evidently, the tension truss is more sensitive to distortions of the supporting ring than to member length imperfections. Nevertheless, it is possible to adjust the ring structure during the assembly process, which is not the case with the individual member lengths.

6.4.10 Combined Influence of Manufacturing Imperfections

In the previous sections, the individual influences of member length imperfection, tension tie force variation, and distortion of the supporting ring structure on the rms surface deviation and de-focus were examined. The manufacturing accuracy of the real reflector surface is determined by the combined effect of all these imperfections. An estimate of the surface accuracy can be obtained by computing the total rms surface deviation from all error sources as

$$\delta_{\mathrm{rms},z} = \left(\sum_i \delta^2_{\mathrm{rms},z,i} \right)^{1/2} . \tag{6.21}$$

It was shown above that a low tolerance may result in cable slackening even though the decrease in surface accuracy is small; the algorithm used for computing the rms surface deviation does not take cable slackening into account. The combined effect of the random errors will increase the risk of cable slackening, so high accuracy levels are needed. Two tolerance levels were tested:

- I: $\sigma_\varepsilon = 10^{-5}$, $\sigma_\rho = 10^{-5}$, and $\sigma_\tau = 0.1$.
- II: $\sigma_\varepsilon = 10^{-6}$, $\sigma_\rho = 10^{-6}$, and $\sigma_\tau = 0.05$.

The results are given in Table 6.9. For level I, the interval and mean values of the lowest element force were 0.0181–2.72 N (0.125 N), 0.0283–5.58 N (1.07 N), and 0.0728–10.5 N (5.27 N), for $F/D = 0.4,\ 0.6$ and 0.8, respectively. Thus, level I does not achieve a sufficient level of accuracy as the combined effect of the manufacturing tolerances resulted in cable slackening. For level II, the intervals and mean values were 0.938–6.00 N (3.99 N), 5.61–9.98 N (8.10 N), and 8.28–12.9 N (11.2 N), using the same order as above. Hence, level II is the tolerance goal for an accurate reflector antenna.

6.4.11 Influence of Thermal Strains

Another error source, that is somewhat related to the manufacturing accuracy, is the straining of the elements due to thermal loading. During a mission, the spacecraft will be both in and out of the Earth's shadow and, thus, subjected to extreme temperatures. To analyse the influence of thermal strains on the surface accuracy, the maximum and minimum equilibrium temperatures of the in-orbit tension truss have to be found. The equilibrium temperature of a body in space is estimated by an energy balance. Conservation of energy yields that the absorbed energy is equal to the emitted energy. Each element of the tension truss is treated as a *thin flat plate* with no side insulated and whose surface normal is parallel to the solar rays and passes through the centre of the Earth. In the energy balance of a body in space, the heat inputs are the direct solar flux, Earth-reflected solar flux (albedo), and Earth-emitted *infrared* (IR) flux. The heat output is the emitted radiation energy from the body. Setting up this energy balance, assuming the same IR emissivity and solar absorptivity on the top and bottom surfaces of the net bands, and solving for the worst-case hot temperature yields [119]

$$T_{\max} = \left[\frac{q_{\mathrm{IR}} \varepsilon_{\mathrm{IR}} \sin^2 \rho + G_S \alpha_S (1 + a K_a \sin^2 \rho)}{2 \varepsilon_{\mathrm{IR}} \sigma} \right]^{1/4}, \tag{6.22}$$

where q_{IR} is the Earth IR emission (237 ± 21 W/m^2), $\varepsilon_{\mathrm{IR}}$ the IR emissivity on the band surface, ρ the angular radius of the Earth ($\sin \rho = R_E/(h+R_E)$), R_E the radius of the Earth (6,378,140 m), h the altitude of the body, α_S the solar absorptivity on the band surface, G_S the solar flux (1326–1418 W/m^2 depending on season), a the albedo of direct solar flux (0.30 ± 0.05), K_a a correcting factor for the reflection of the

Table 6.9: Combined influence of manufacturing imperfections on the rms surface deviation and de-focus (three- ring tension truss, 100 Monte Carlo simulations).

F/D		0.4		0.6		0.8	
Tolerance level		I	II	I	II	I	II
$\widehat{\delta}^{\mathrm{c}}_{\mathrm{rms},z}$	(mm)	0.6339	0.15472	0.4490	0.13489	0.6092	0.13946
$\bar{\delta}^{\mathrm{c}}_{\mathrm{rms},z}$	(mm)	0.3902	0.08536	0.2846	0.05896	0.4143	0.03420
$\sigma^{\mathrm{c}}_{\Delta F+\Delta Z_P}$	(mm)	0.5271	0.04887	0.6758	0.15815	0.9932	0.45069
$\overline{\Delta F+\Delta Z_P}$	(mm)	21.8707	22.41913	22.3707	22.60387	24.0263	25.22523
$\sigma^{\varepsilon}_{\texttt{randn}}$		1.0039	0.99641	1.0042	1.00835	0.9951	1.00447
$\sigma^{\rho}_{\texttt{randn}}$		0.9945	1.01713	1.0084	0.98381	1.0254	0.98031
$\sigma^{\tau}_{\texttt{randn}}$		1.0028	1.00164	1.0010	0.99887	0.9908	1.00538
$\bar{\delta}_{\mathrm{rms},z}$	(mm)	3.3644	3.34279	2.2459	2.22858	1.7215	1.67120
$\delta^{\max}_{\mathrm{rms},z}$	(mm)	3.3963	3.34456	2.2813	2.23157	1.7743	1.67657
$\delta^{\min}_{\mathrm{rms},z}$	(mm)	3.3424	3.34066	2.2278	2.22500	1.6788	1.66679
$\sigma_{\delta_{\mathrm{rms},z}}$	(mm)	0.0123	0.00083	0.0089	0.00110	0.0190	0.00182
$\overline{\Delta F}$	(mm)	8.7067	9.14152	13.4875	13.73870	17.5499	18.53619
$\Delta F^{\max}$	(mm)	9.4895	9.23777	16.0529	14.02969	20.2019	19.47404
$\Delta F^{\min}$	(mm)	7.4097	9.04804	11.8542	13.30536	14.4719	17.29273
$\sigma_{\Delta F}$	(mm)	0.4414	0.03721	0.6164	0.14884	0.9334	0.42772
$\overline{\Delta Z_P}$	(mm)	13.1640	13.27761	8.8833	8.86517	6.4763	6.68904
$\Delta Z_P^{\max}$	(mm)	13.3538	13.31202	9.0786	8.89629	6.6566	6.76164
$\Delta Z_P^{\min}$	(mm)	12.9545	13.25132	8.7021	8.83677	6.2391	6.62063
$\sigma_{\Delta Z_P}$	(mm)	0.1013	0.01571	0.0801	0.01155	0.0877	0.03455

solar energy off the spherical Earth ($K_a = 0.664 + 0.521\rho - 0.203\rho^2$), and σ Stefan-Boltzmann's constant ($5.67051 \cdot 10^{-8}$ W/m^{2}K^4). The worst-case cold temperature occurs when the body is in the shadow of the Earth and out of view of any portion of the sunlit parts of the Earth. For this condition there is no direct solar flux, $G_S = 0$, or albedo, $a = 0$. The worst-case cold temperature is [119]

$$T_{\min} = \left[\frac{q_{\mathrm{IR}} \sin^2 \rho}{2\sigma}\right]^{1/4}. \tag{6.23}$$

Note that the $T_{\min}$ is independent of the surface properties. The above equation give estimates of the equilibrium temperature for the worst-case conditions. For the net elements, the angle between the solar rays and the surface normal of the bands varies over the reflector surface resulting in different equilibrium temperatures, which further degrades the surface. A correction of the equilibrium temperature for each individual band due to the angle of the solar rays was not made here as this analysis serves only as an estimate.

The net elements are made of CFRP and it was assumed that their surface properties were that of carbon black paint, [119], $\alpha_S = 0.96$ and $\varepsilon_{\text{IR}} = 0.88$. The altitude of the spacecraft to which the antenna is attached was $h = 550$ km, which gave $\sin\rho = 0.9206$. The worst-case hot temperature of the net bands, using $q_{\text{IR}} = 258$ W/m^2, $G_S = 1418$ W/m^2, and $a = 0.35$, was computed to $T_{\max} = 374$ K or $\vartheta_{\max} = +101$ °C. The worst-case cold temperature, using $q_{\text{IR}} = 216$ W/m^2, was $T_{\min} = 200$ K or $\vartheta_{\min} = -73$ °C. If the antenna was mounted on a satellite in a GEO ($H = 35{,}786$ km, $\sin\rho = 0.1513$), like the 12.25 m diameter AstroMesh antenna on Thuraya, the worst case temperatures would be $\vartheta_{\max} = +69$ °C and $\vartheta_{\min} = -192$ °C, using the same surface properties as above. According to Panetti [119], a typical operating temperature range of a parabolic reflector is -160 to $+95$ °C. The distortion test of a 6 m diameter AstroMesh uses worst-case temperatures of -160 °C and $+120$ °C [166]. In the present analysis, the following temperatures were used:

- Assembling temperature $\vartheta_{\text{ref}} = +20$ °C,
- Worst case cold temperature $\vartheta_{\min} = -80$ °C, and
- Worst case hot temperature $\vartheta_{\max} = +110$ °C.

If the equilibrium temperature variation due to the incident solar rays is neglected, the influence of the thermal strains on the antenna accuracy is mainly characterised by a change in average temperature [58]. The unstrained length of an element i after a change in temperature is

$$\ell_{0,\vartheta,i} = \ell_{0,i}\,(1 + \varepsilon_\vartheta) \tag{6.24}$$

where ℓ_0 is the unstrained length at the reference temperature ϑ_{ref}, and the ε_ϑ the thermal strain. The thermal strain at a temperature ϑ is

$$\varepsilon_\vartheta = \alpha_T\,(\vartheta - \vartheta_{\text{ref}})\,, \tag{6.25}$$

where α_T is the CTE. One of the advantages of CFRP is that it is possible to theoretically achieve zero CTE by an appropriate choice of material and layup parameters. In reality, manufacturing imperfections and variations in material properties result in non-zero CTE. CFRP with α_T less than 1.0μ/°C is readily available, but without costly testing it is difficult to make the variation of the CTE, σ_{α_T}, less than 0.4μ/°C, [62]. This variation results in a random thermal strain, even under a uniform change in temperature over the tension truss. In an early study, Hedgepeth [56] uses $\alpha_T = 0.5\mu$/°C for the CFRP. More recently, thin-walled composite tubes with near zero CTE are developed [157]; depending on the layup of the carbon fibre sheets, the CTE of the tubes varies from -0.20μ to 0.16μ/°C. Following this brief study of the achievable CTE of CFRP for space structures, the following values for the mean value and standard deviation of the CTE were used in the present analysis: $\bar{\alpha}_T = 0.5\mu$/°C and $\sigma_{\alpha_T} = 0.4\mu$/°C.

Before computing the random errors of the thermal strains, it is necessary to examine how a uniform temperature change affects the rms surface error and de-focus. In

Table 6.10: Influence on the rms surface deviation and de-focus of a uniform deterministic thermal strain in the three-ring tension truss.

F/D		0.4		0.6		0.8	
Temperature		$\vartheta_{\min}$	$\vartheta_{\max}$	$\vartheta_{\min}$	$\vartheta_{\max}$	$\vartheta_{\min}$	$\vartheta_{\max}$
$\delta^{\vartheta}_{\mathrm{rms},z}$	(mm)	—	0.2220	—	0.2085	—	0.2029
$\Delta F + \Delta Z_P$	(mm)	22.8387	22.1382	23.5076	21.8072	26.8721	23.2415
$\delta_{\mathrm{rms},z}$	(mm)	3.3338	3.3491	2.2176	2.2375	1.6585	1.6831
ΔF	(mm)	9.3448	9.0088	14.3755	13.1798	19.8796	16.9042
ΔZ_P	(mm)	13.4939	13.1294	9.1321	8.6274	6.9925	6.3373
$t^{\min}_{\mathrm{all}}$	(N)	7.14	7.07	10.58	10.41	14.10	13.75
$t^{\max}_{\mathrm{all}}$	(N)	46.46	46.35	67.92	67.57	89.83	89.05

this study, the CTE was assumed to be deterministic and equal to $\bar{\alpha}_T$. The results of this analysis are shown in Table 6.10. The net forces were more or less unaffected by a uniform temperature change. Note that $\vartheta_{\min}$ produced a smaller systematic rms surface deviation due to an increased focal length.

The results from the thermal analysis with a random CTE are given in Table 6.11. For the worst-case cold temperature the interval and mean values (in parenthesis) of the lowest element force for $F/D = 0.4,\ 0.6$, and 0.8 were 0.470–6.76 N (4.44 N), 4.30–9.95 N (7.89 N), and 8.28–13.3 N (11.1 N). For the worst-case hot temperature, the intervals and mean values were 2.04–6.68 N (4.44 N), 4.91–10.0 N (7.86 N), and 8.32–13.2 N (11.1 N) in the same order as above. There is a slight possibility that some cables go slack, but the average minimal forces are acceptable.

6.4.12 Achievable Reflector Accuracy

A comparison of the rms surface deviation results for member length errors with (6.11) showed that $\bar{\delta}^{\varepsilon}_{\mathrm{rms},z}$ was about the same as the corresponding value of (6.11) for 10^{-4} and 10^{-5}, but differed by approximately one order in magnitude for 10^{-6}. This was a bit puzzling since $\sigma_{\delta_{\mathrm{rms},z}}$ always differed with about one order of magnitude. However, this anomaly was not considered to be a major problem as the surface errors for $\sigma_{\varepsilon} = 10^{-6}$ were lower than the resolution of common measuring systems[1]. For $\sigma_{\varepsilon} = 10^{-5}$ and 10^{-6}, $\widehat{\delta}^{\varepsilon}_{\mathrm{rms},z}$ was almost constant at 0.11 and 0.04 mm, respectively. As anticipated, the rms surface deviation was relatively insensitive to a variation of the tension tie forces. This would not be the case with a kinematically indeterminate network. For the lower tolerance, $\sigma_{\tau} = 0.1$, $\widehat{\delta}^{\tau}_{\mathrm{rms},z}$ varied between 0.17 and 0.23 mm, while for the higher one, $\sigma_{\tau} = 0.05$, it varied between 0.11 and 0.15 mm. These errors were about the same order as the member length errors. The effects of ring distortions were more severe than the previous two manufacturing errors. For $\sigma_{\rho} = 10^{-5}$, $\widehat{\delta}^{\rho}_{\mathrm{rms},z}$ varied between 0.44 and 0.83 mm, where the highest magnitude was

[1]The video photogrammetry system used for the AstroMesh had a resolution of 0.07 mm rms, [166].

Table 6.11: Influence on the rms surface deviation and de-focus of a random thermal strain (three-ring tension truss, 100 Monte Carlo simulations).

F/D		0.4		0.6		0.8	
Temperature		$\vartheta_{\min}$	$\vartheta_{\max}$	$\vartheta_{\min}$	$\vartheta_{\max}$	$\vartheta_{\min}$	$\vartheta_{\max}$
$\widehat{\delta}^{\vartheta}_{\mathrm{rms},z}$	(mm)	0.2282	0.2182	0.1898	0.2221	0.2402	0.2326
$\bar{\delta}^{\vartheta}_{\mathrm{rms},z}$ [a]	(mm)	0.0895	0.0732	0.1173	0.1079	0.1400	0.1285
$\sigma^{\vartheta}_{\Delta F+\Delta Z_P}$	(mm)	0.1851	0.1808	0.5575	0.4946	1.2298	1.0949
$\overline{\Delta F+\Delta Z_P}$	(mm)	22.8507	22.1311	23.4806	21.8259	27.0176	23.2851
$\sigma^{\vartheta}_{\texttt{randn}}$		1.0009	1.0009	1.0027	1.0004	0.9994	0.9990
$\bar{\delta}_{\mathrm{rms},z}$	(mm)	3.3350	3.3499	2.2207	2.2401	1.6644	1.6880
$\delta^{\max}_{\mathrm{rms},z}$	(mm)	3.3401	3.3550	2.2294	2.2480	1.6755	1.6981
$\delta^{\min}_{\mathrm{rms},z}$	(mm)	3.3290	3.3427	2.2149	2.2340	1.6556	1.6807
$\sigma_{\delta_{\mathrm{rms},z}}$	(mm)	0.0022	0.0021	0.0027	0.0028	0.0038	0.0037
$\overline{\Delta F}$	(mm)	9.3529	9.0032	14.3502	13.1987	20.0154	16.9481
$\Delta F^{\max}$	(mm)	9.8201	9.4572	15.7129	14.1209	23.4995	19.0815
$\Delta F^{\min}$	(mm)	8.9989	8.5603	13.2259	11.8385	16.4306	13.8639
$\sigma_{\Delta F}$	(mm)	0.1582	0.1536	0.5148	0.4595	1.1769	1.0493
$\overline{\Delta Z_P}$	(mm)	13.4978	13.1280	9.1303	8.6272	7.0023	6.3371
$\Delta Z_P^{\max}$	(mm)	13.5803	13.2154	9.2769	8.7171	7.1456	6.4529
$\Delta Z_P^{\min}$	(mm)	13.4224	13.0506	9.0143	8.5167	6.8232	6.1939
$\sigma_{\Delta Z_P}$	(mm)	0.0310	0.0300	0.0474	0.0405	0.0585	0.0526

[a] Note that the effect of CTE variation is computed by (6.18) as before, but now with the systematic error from Table 6.10.

obtained for $F/D = 0.6$. For $\sigma_\rho = 10^{-6}$, $\widehat{\delta}^{\rho}_{\mathrm{rms},z}$ varied between 0.08 and 0.10 mm, where the higher value corresponded to $F/D = 0.8$.

As the rms surface error was very sensitive to the ring distortion, the ring structure must be very accurately constructed; it may be necessary to provide some kind of adjustability, to fine tune its shape during ground testing. The combined effects of the three manufacturing errors was at most 0.64 mm at level I and 0.16 mm at level II. Considering the slack cables at level I, it is obvious that level II must be the manufacturing tolerance goal. However, it may be possible to use the lower tolerance of the tension tie forces, $\sigma_\tau = 0.1$ and still have a high accuracy. The effects of the thermal loading, $\widehat{\delta}^{\vartheta}_{\mathrm{rms},z}$, were about the same for the three focal lengths: 0.19–0.24 mm. These values were computed with respect to the systematic error of a network with deterministic thermal strains. Taking the rss value of the systematic and random thermal rms errors, the resulting maximum error was approximately 0.31 mm.

Taking all the random error sources above into account, the upper bound of the rms surface deviation was about 0.35 mm, or $1.2 \cdot 10^{-4} D$. This value can be compared

with Table 5.2, where the rss surface deviation of a 6 m diameter AstroMesh, due to random error sources, is about 0.46 mm, or $7.7 \cdot 10^{-5} D$.

At tolerance level II, the de-focus, $\overline{\Delta F + \Delta Z_P}$, varied between 22.4 and 25.2 mm depending on the focal length. Its variation, $\sigma_{\Delta F + \Delta Z_P}$, at the same level, varied between 0.05 and 0.45 mm. Since a de-focus of up to one wavelength (31 mm at 9.65 GHz) can be accepted without seriously affecting the performance of the antenna, [131], it cannot be considered a problem for the present antenna. In fact, the de-focus decreased significantly as the number of net rings increased.

Chapter 7

Tensegrity Reflector Antennas

7.1 Introduction

A preliminary study of the new antenna concept is presented in references [168,169]. The present chapter will provide a more complete study of the concept starting from the simple initial studies with the stiffened tensegrity module to the vibration characteristics of a full scale offset reflector antenna. It was apparent from Figure 5.5 that the AstroMesh concept, Figure 2.15, is a major source of inspiration in the development of the new concept. To better understand the similarities and differences between the two concepts, this chapter will start with a closer study of the AstroMesh.

7.2 The AstroMesh Concept

Most details of the AstroMesh are found in the US patent [167] and in a technical report from Astro Aerospace [62]. The main parts of the AstroMesh are the triangular nets and the deployable ring structure.

7.2.1 Net Generation

The triangular nets of the AstroMesh have a configuration similar to that of the tension truss with three sets of bands oriented approximately 60° apart. Ideally, the bands should follow the geodesic lines of the surface, as a lateral loading on the surface would not tend to shift the bands in that position. However, with equally spaced nodes along the circumference, the intersection of a set of three geodesic bands, connected to the boundary, would not necessarily coincide. To minimise the number of intersections, a quasi-geodesic net, with coinciding three-band intersections, is used instead of a true geodesic net. This quasi-geodesic net is called *geotensoid*. The generation of the geotensoid starts with a hexagonal array of equilateral triangles, in this case with six rings, Figure 7.1(a). For a circular

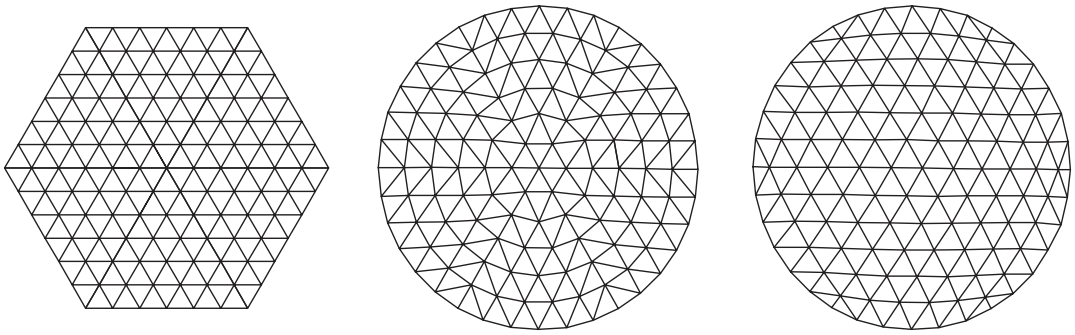

(a) (b) (c)

Figure 7.1: Geotensoid generation: (a) six-ring tension truss, (b) initial six-ring geotensoid, and (c) converged six-ring geotensoid (redrawn from [62]).

aperture, the nodes of the six-ring array are then mapped to lie on equally spaced concentric circles, Figure 7.1(b). Finally, the free nodes are iteratively adjusted so that the total length of the net bands is minimised, Figure 7.1(c).

7.2.2 Deployable Ring Structure

The deployable ring structure of the AstroMesh, shown in Figure 7.2(a), is composed of a series of upper and lower bars which, when connected, form upper and lower rings. The upper and lower rings, each composed of B segments, are separated by vertical and diagonal bars. A bar and joint count for the ring truss yields $b_{\text{ring}} = 4B$ and $j_{\text{ring}} = 2B$. As it is obvious that this ring truss cannot be prestressed, $s = 0$, the number of internal mechanisms is, (1.2),

$$m_{\text{ring}} = 2B - 6. \tag{7.1}$$

Only for $B = 3$, when the ring becomes a triangular prism, is the structure kinematically determinate. Usually the ring is divided into several bays, hence, the number of internal mechanisms is quite large. The main purpose of the two triangular networks is to eliminate the internal mechanisms of the ring truss. Ultimately, the complete assembly should be statically determinate for easy prestressing.

7.2.3 Static and Kinematic Properties

Initially, the nodes on the circumference connect directly to the ring truss, Figure 7.1(c); the number of bays is therefore equal to the number of net rings. The total numbers of bars and joints of such an assembly, with $6n$ bays, are

$$b_{6n} = \underbrace{6n(3n-1)}_{b_{\text{nets}}} + \underbrace{24n}_{b_{\text{ring}}} \tag{7.2}$$

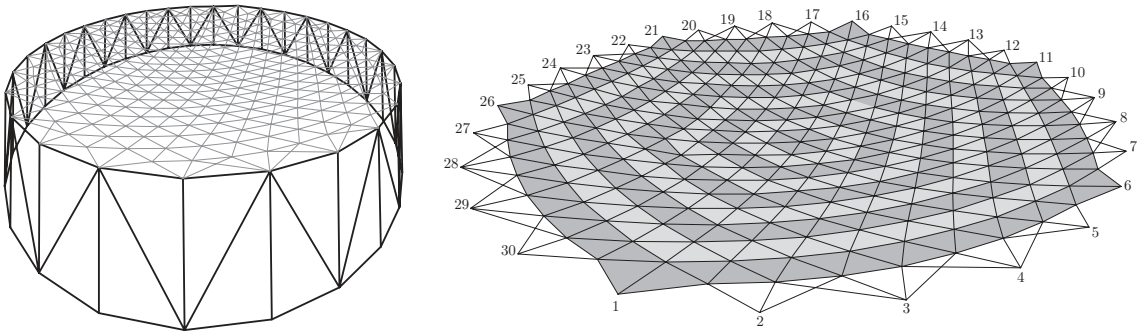

(a) (b)

Figure 7.2: Configuration of the AstroMesh onboard the Thuraya satellite: (a) line drawing created from Figure 2.15(b) and (b) highlighted rings of the top net.

and

$$j_{6n} = 6n(n+1) + 2, \tag{7.3}$$

respectively. Substituting (7.2) and (7.3) into the extended Maxwell's rule, (1.2), yields $m - s = 0$. As neither the ring truss nor the synclastic triangular nets can sustain a state of self-stress, the resulting assembly is statically determinate. A 2.5 m diameter AstroMesh reflector ($n = 4$) is built according to this approach and set up for various tests [165]. However, this approach will work only for small values of n as the ring truss composes the major part of the reflector mass; for large values of n, the antenna is too heavy. Schemes for connecting nets with many rings to trusses with less than $6n$ bays must be developed. These schemes are presumably available within TRW Astro Aerospace, but not in the open literature.

Figure 7.2(a) shows the deployable ring truss and complete top net of the 12.25 m diameter AstroMesh reflector. This ring truss has 30 bays. To better see the configuration of the top net and compare it with the tension truss, the ring truss is removed and the net rings highlighted in Figure 7.2(b). Each net has nine rings and is connected to the ring structure at 30 nodes. Referring to Figure 7.2(b), the configuration of the net at connections 1, 6, 11, 16, 21, and 26 is similar to that of the tension truss. The remaining connections are similar but different from the previous ones. The net configuration at these remaining connections is chosen to render the complete reflector statically determinate. This configuration may change if the number of rings in the nets or the number of bays in the deployable ring truss changes. Generally, the number of ring segments increases with the number of net rings. Figure 7.3 shows eight configurations of five- to nine-ring nets which satisfies Maxwell's rule, (1.1). It is observed that for an odd number of rings the nets have the same type of ring truss connections. For an even number of net rings, several alternative connections are possible. This small exercise clearly illustrates the great flexibility of the AstroMesh concept and the simple theory behind it. It also emphasises the importance of static determinacy, which by virtual work implies

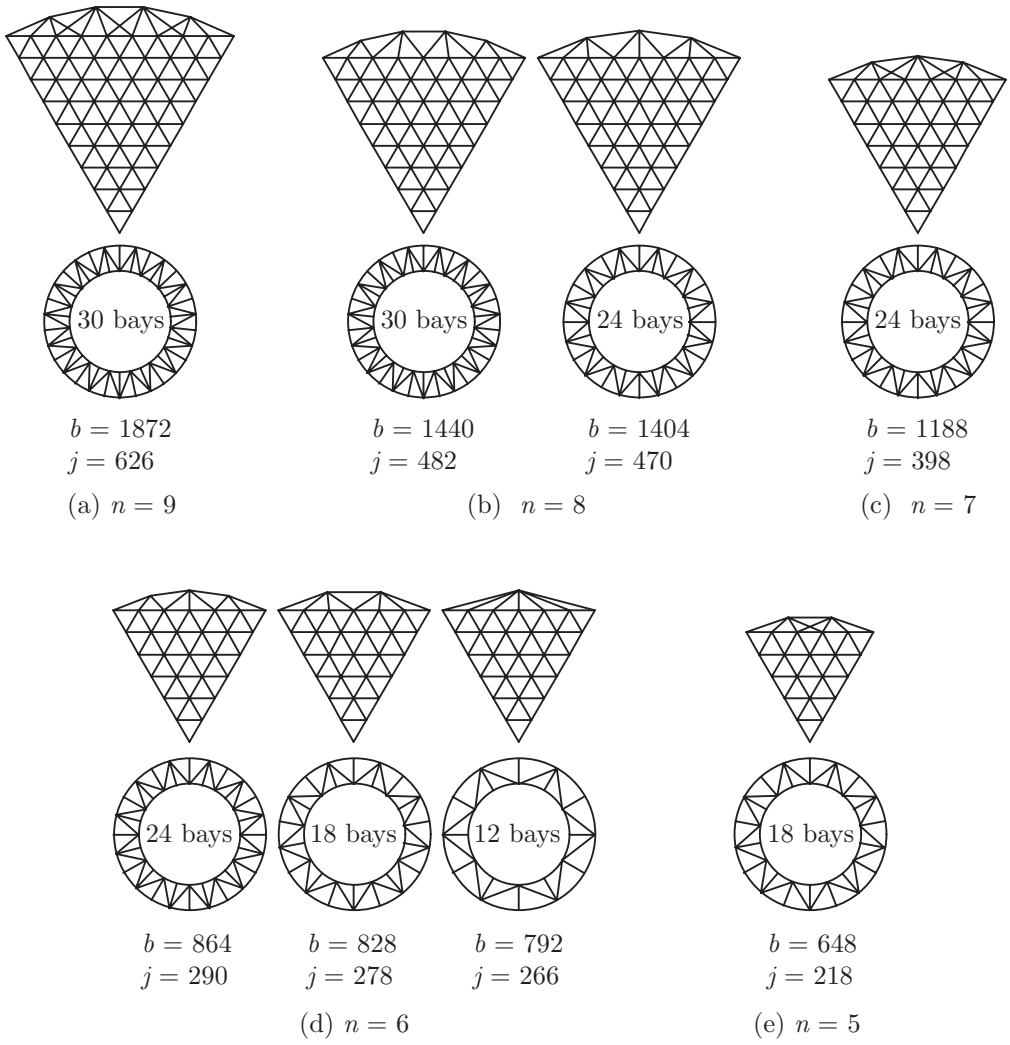

Figure 7.3: Statically determinate configurations of the AstroMesh.

kinematic determinacy, in the design of precision structures.[1] It will be seen that the new concept, to which the rest of this chapter is devoted, was designed along the lines of the AstroMesh design.

7.3 New Concept

The idea behind the new concept originates from a study by Knight *et al.* [71], where an antenna design based on tensegrity is introduced. However, no specific details about the design are given. When reference [71] was published the present author was working at DSL with tensegrity form-finding methods and tensegrity masts.

[1]The question "is static determinacy the key to the design of precision structures?" was discussed at the IUTAM-IASS Symposium on Deployable Structures (pp. 488–489 in [129]) Conclusions from that discussion are that static determinacy is desirable as these structures are easier to model than statically indeterminate ones, but it is not necessarily a solid factor to base the design on.

About the same time DERA contacted DSL for help with developing deployable structures for the STRV. As mentioned earlier, a parabolic antenna was one of the structures in which they were interested. The initial idea by Pellegrino [126] was that an antenna based on tensegrity could be developed by using a hexagonal tensegrity module and add nodes and bars inside the two hexagons to remove the internal mechanisms. The resulting structure would have a potential to meet the stringent requirements by DERA—the work with the tensegrity antenna was initiated.

7.3.1 Stiffened Hexagonal Module

Consider the regular hexagonal tensegrity module in Figure 7.4. This structure has $j = 12$ joints and $b = 24$ bars. With $c = 6$, the extended Maxwell's rule, (1.2), gives

$$m - s = 6. \tag{7.4}$$

Like all tensegrity modules, $s = 1$ with only the longer members in compression. First-order stiffness can be achieved by prestressing the structure, but this provides only a relatively small stiffness; high-precision applications require dimensionally accurate structures, i.e. kinematically determinate structures.

An improved version of the module is shown in Figure 7.5. This structure was obtained by connecting the nodes of the top and bottom hexagons to two interconnected, central joints. Note that these internal joints are not coplanar with the hexagons, thus forming two triangulated surfaces that coarsely approximate to a curved surface. The modified assembly has $j = 14$ joints and $b = 37$ bars. The extended Maxwell's rule now yields

$$m - s = -1. \tag{7.5}$$

Since the same state of self-stress of the structure in Figure 7.4 also exists for this structure and there is no other independent state of self-stress, $s = 1$ as before.

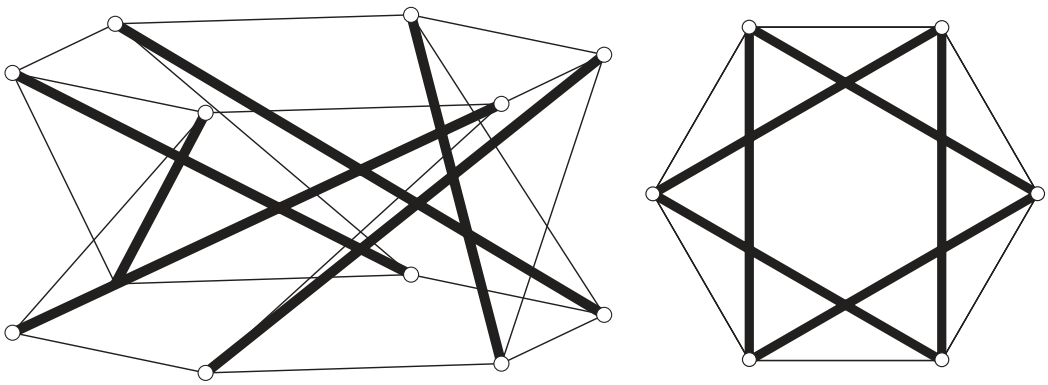

(a) (b)

Figure 7.4: Hexagonal tensegrity module: (a) three-dimensional view and (b) top view.

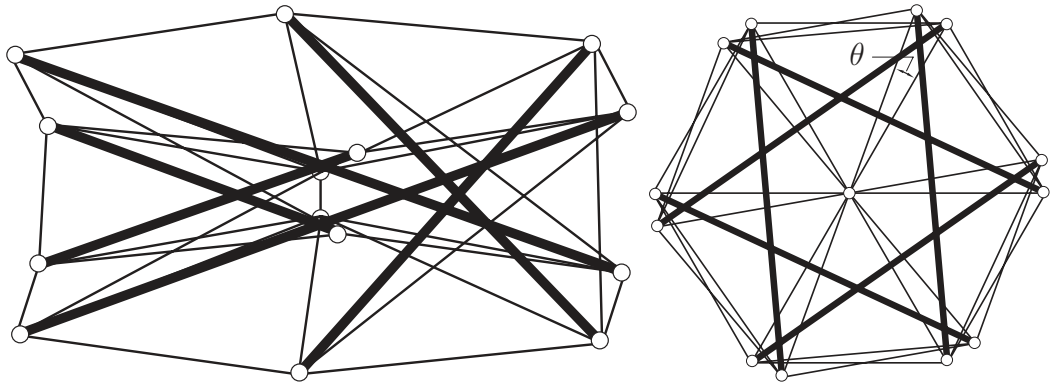

(a) (b)

Figure 7.5: Stiffened hexagonal tensegrity module: (a) three-dimensional view and (b) top view.

Hence, this structure has no internal mechanisms and is, therefore, potentially useful for the present application. Closer analysis showed that in the initial configuration, where the joints of the top hexagon lie directly above the ones of the bottom hexagon, all of the added bars were unstressed, meaning that they must be rigid. However, if the upper hexagon was rotated clock-wise with respect to the lower one by an angle θ, i.e. the compression members became longer, the state of self-stress changed such that all members became stressed. It turned out that all of the additional members ended up in tension and can be substituted by cables. Thus, the resulting structure has only six compression members and, if cables are used for the remaining members, the structure can easily be folded by collapsing the struts.

Figure 7.6 shows how the force density in the members changes with the angle of rotation θ. Four configurations, which differed in the positions of the internal interconnected joints, were analysed. The tension force in the elements forming the triangulated surfaces, called net cables, increases from its initial zero value. The compression force in the struts increases monotonically, i.e. they become more compressed. The tension force in the base cables, however, decreases and they eventually end up in compression; the angle when this happens depends on the length of the interconnected element, ΔH. The triangulated surface in this example is far too coarse to support a reflective mesh that approximates a paraboloid. To refine the surface, the simple triangulated surfaces are replaced by tension trusses.

7.3.2 Hexagonal Tensegrity Module and Tension Trusses

Consider a pin-jointed bar structure consisting of the original ring structure, i.e. the hexagonal module, plus two tension trusses. The total numbers of joints and bars for that structure are, cf. section 6.1,

$$j = 2\left(1 + 6\frac{n(1+n)}{2} + 6\right), \tag{7.6}$$

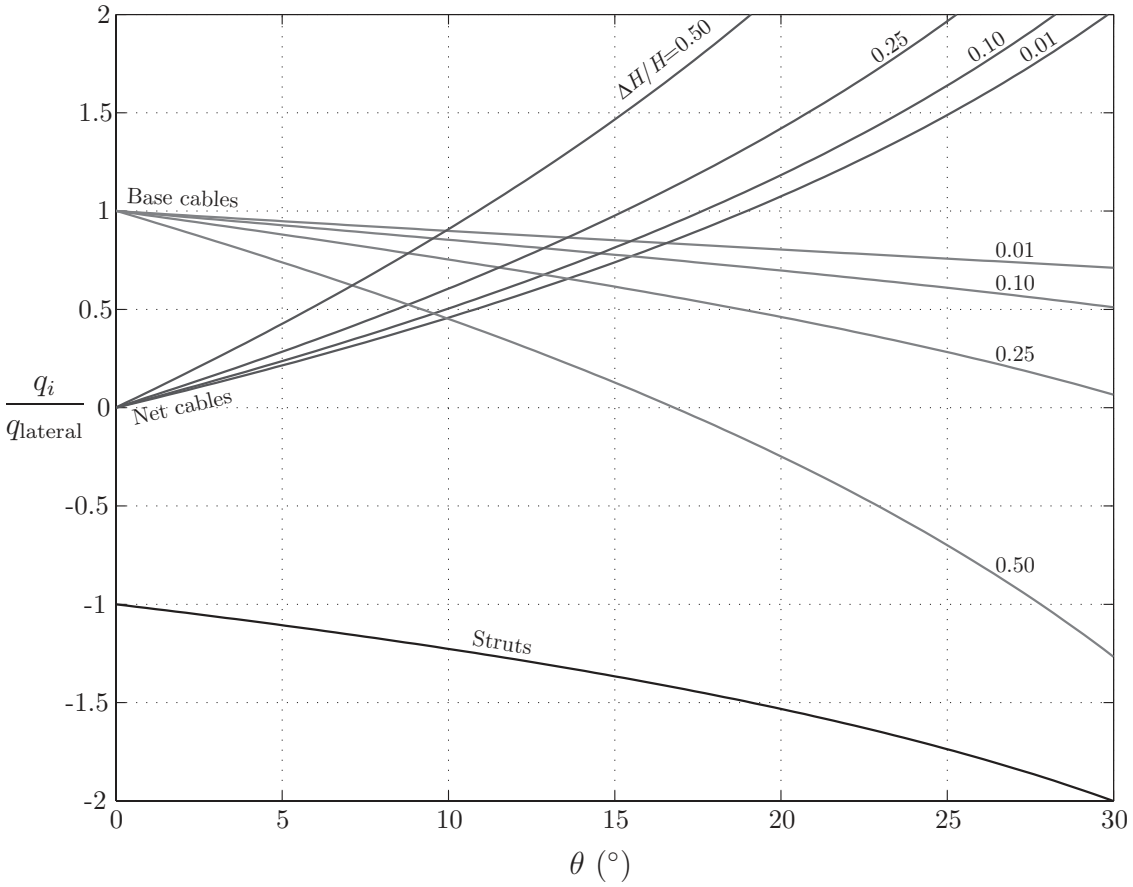

Figure 7.6: Force density values for the one-stage tensegrity reflector for various $\Delta H/H$. ΔH is the length of the interconnected element and H is the total height of the module ($q_{\text{lateral}} = 1$).

and

$$b = 6 \cdot 4 + 2\left[6\frac{n(1+3n)}{2} + 6(n+1)\right], \tag{7.7}$$

respectively. Substituting (7.6) and (7.7) into the extended Maxwell's rule gives

$$m - s = 0. \tag{7.8}$$

Again, at $\theta = 0°$ no additional states of self-stress has been created, $s = 1$. This means that there exists one internal mechanism. The immediate difference between this structure and the previous one is that the interconnected element is missing. Adding an additional bar, which connects the middle nodes of the nets, may remove this single mechanism. However, a way of prestressing the complete structure must be found. An obvious approach, based on the AstroMesh, is to connect the corresponding nodes of the two nets with tension ties. It must be emphasised that the tension ties should not be counted as bars. The tension ties are springs providing constant forces and can, therefore, be treated as external loads in an analysis. It is a common misconception that the inclusion of the tension ties would result in a structure that is highly statically indeterminate and, therefore, suffers from all sorts of prestressing difficulties; the AstroMesh is a direct proof that this is not the case.

To obtain detailed information about the static and kinematic properties of the antenna structure, its equilibrium matrix has to be analysed for different values of θ. But before an adequate configuration of the antenna can be specified, one more parameter must be determined—the separation between the nets.

7.3.3 Minimum Separation between Front and Rear Nets

The minimum distance between the closest nodes of the nets in the AstroMesh is determined by the shortest acceptable length of the tension tie connecting these nodes. For the present concept, the minimum separation depends on both the curvature of the nets, F/D, and the position of the struts, θ. Consider two paraboloids with the same F/D ratio separated by a distance ΔH at the apexes, Figure 7.7. A system xyz has its origin at the apex of the upper paraboloid. A strut connects points 1 and 2 on the rims of the paraboloids. The coordinates of these points are

$$\mathbf{p}_1 = \begin{pmatrix} \frac{D}{2}\cos\theta & \frac{D}{2}\sin\theta & \frac{D^2}{16F} \end{pmatrix}^{\mathrm{T}}, \tag{7.9}$$

$$\mathbf{p}_2 = \begin{pmatrix} \frac{D}{2}\cos 240^\circ & \frac{D}{2}\sin 240^\circ & z_2 \end{pmatrix}^{\mathrm{T}}. \tag{7.10}$$

If the paraboloids are too closely spaced the strut will intersect them. Hence, the minimum separation is when the strut lies in the tangential plane to the upper paraboloid at $\mathbf{p}_1$ (or to the lower one at $\mathbf{p}_2$). The normal to the upper paraboloid at $\mathbf{p}_i$ is

$$\mathbf{n}(\mathbf{p}_i) = \begin{pmatrix} -\frac{x_i}{2F} & -\frac{y_i}{2F} & 1 \end{pmatrix}^{\mathrm{T}}, \tag{7.11}$$

which yields the tangent plane at $\mathbf{p}_1$ as

$$z - z_1 = \frac{x_1}{2F}(x - x_1) + \frac{y_1}{2F}(y - y_1). \tag{7.12}$$

Substituting (7.9) and (7.10) into (7.12) yields the vertical position z_2 of the rim of the bottom paraboloid. Subtracting the height of the bottom paraboloid yields the minimum separation

$$\Delta H = \frac{D^2}{8F}\cos(60^\circ - \theta). \tag{7.13}$$

Thus, the minimum total height of the antenna structure is

$$H = \frac{D^2}{8F}\left[1 + \cos(60^\circ - \theta)\right]. \tag{7.14}$$

Note that even if the bottom paraboloid is made shallower than the top one, the total height of the antenna will remain constant; the coordinate z_2 is determined by the deepest paraboloid. The separation ΔH is zero at $\theta = -30^\circ$, $\Delta H = D^2/16F$ at $\theta = 0^\circ$, and $\Delta H = D^2/8F$ at $\theta = 60^\circ$; the last figure is easily verified. This means that the deployed antenna will be rather deep, e.g. $D = 3$ m, $F/D = 0.4$, and $\theta = 10^\circ$ yield $H = 1.54$ m.

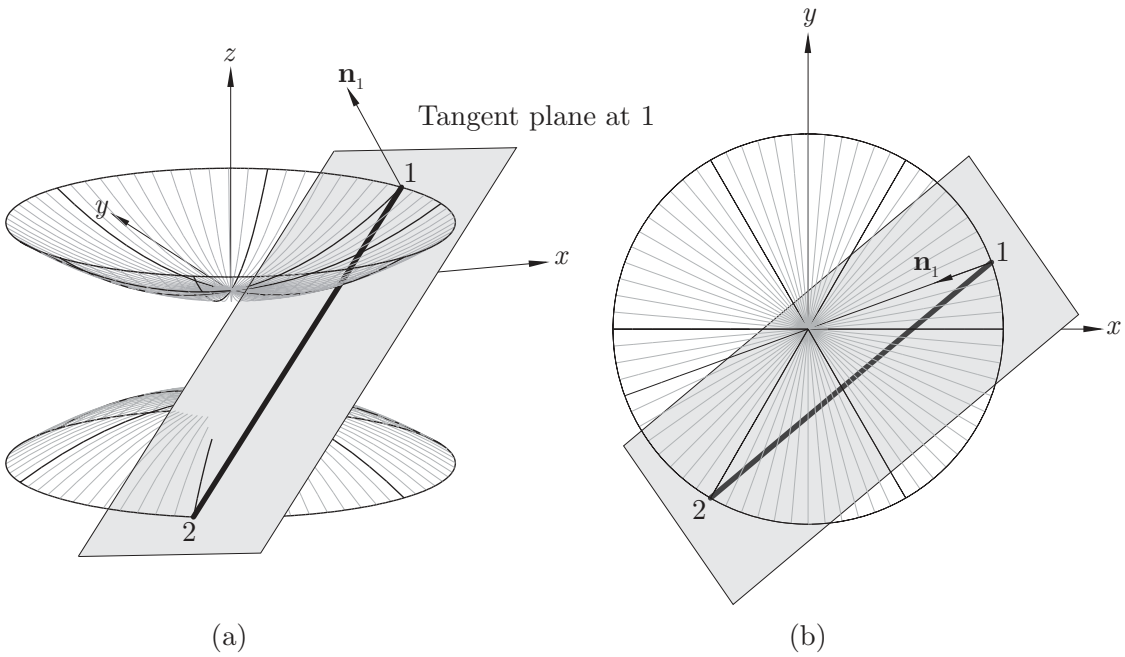

Figure 7.7: At the configuration with the theoretical minimum separation between the front and rear nets, the strut lies in the tangent planes of the paraboloids: (a) three-dimensional view and (b) top view.

7.3.4 Three-Ring Axi-Symmetric Reflector

It is now possible to describe the configuration of an axi-symmetric antenna with fixed D and F/D by only one parameter, θ. An antenna with three-ring nets was analysed. The net configuration and the tension tie forces were according to Chapter 6 for $n = 3$. The diameter $D = 3$ m and $F/D = 0.4$. Corresponding nodes of the two nets were connected by only tension ties, hence, $m-s = 0$. For $\theta = 0°$, the structure had one internal mechanism and large compressive forces were induced in the ring structure; the state of self-stress for $\theta = 0°$ was a prestressed ring structure but unstressed nets. Like the stiffened tensegrity module, the whole structure can be prestressed with $\theta > 0°$. However, contrary to the stiffened module, the static and kinematic properties of the antenna assembly changed when going from the initial to a rotated configuration. At $\theta = 0°$, $m = 1$ and $s = 1$, but for $\theta > 0°$, $m = 0$ and $s = 0$, i.e. the structure is *statically determinate*. By itself, the rotated ring structure could no longer be prestressed as $s = 0$. Nevertheless, when the complete reflector structure was considered, including the prestressing forces applied by the tension ties, it was found that only six of the 252 elements were in compression.

The variation of the internal forces in the three-ring antenna with the angle θ was analysed. Throughout the studied range, 0–30°, all of the net forces were in tension

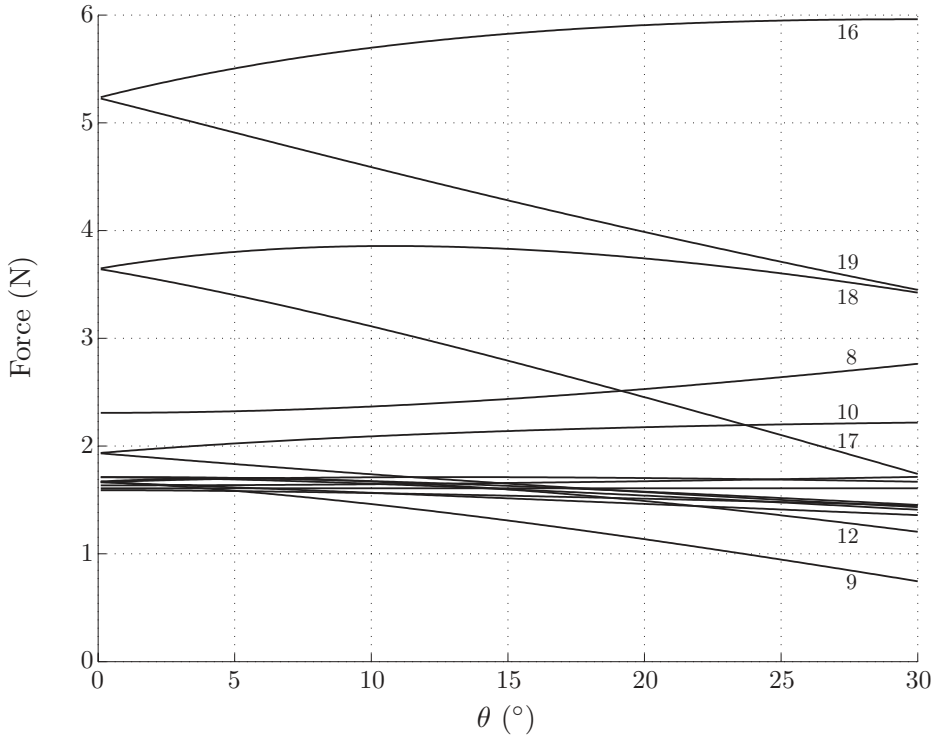

(a)

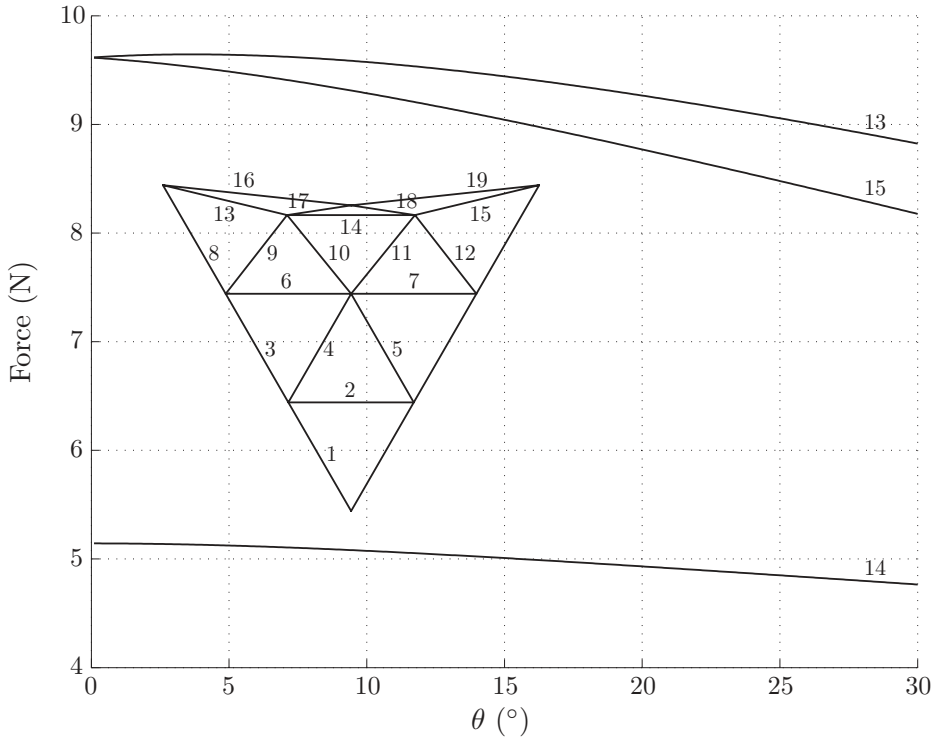

(b)

Figure 7.8: Variation of the forces in the net cables for the three-ring configuration.

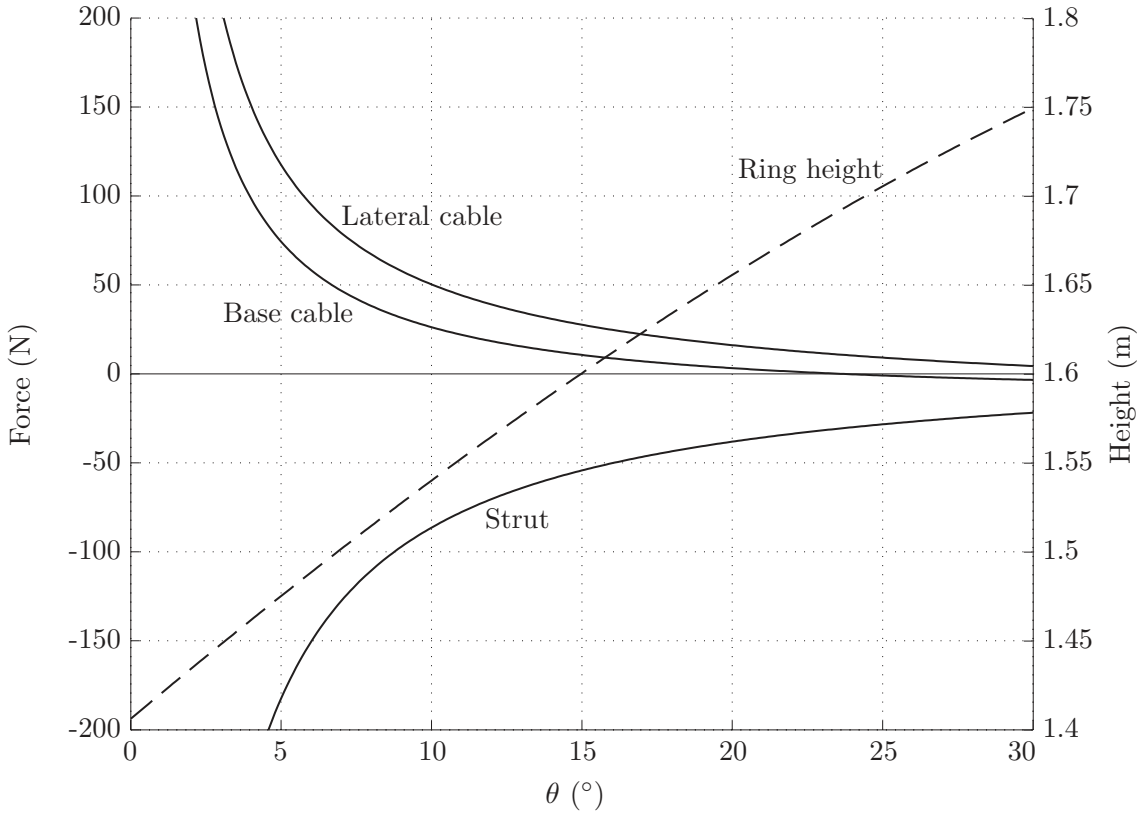

Figure 7.9: Variation of the forces in the ring structure and its height for the three-ring configuration.

with a magnitude between about 1 and 10 N for tension tie loads of 1 N on the internal joints and 2 N on the edge and additional joints, Figure 7.8. The forces in the ring structure, however, were extremely large for low values of θ, but decreased exponentially to acceptable levels at about 5°, Figure 7.9. For this particular configuration, the upper limit for θ, at which the base cables were no longer in tension, was about 24°. When looking for an adequate configuration one should not only take the magnitudes of the internal forces into account. Also shown in Figure 7.9 is the height of the ring structure from (7.14). It went from 1.41 m at 0° to 1.70 m at 24° and the goal must be to keep it as low as possible. Another issue, which might affect the choice of θ, is the possible interference between the struts and the tension ties. This problem was not considered in the present analysis, but when a physical structure is built it is of primary importance that the struts are not interfering with the tension ties, or vice versa. As the angle θ increased, the struts moved closer to the centre of the of reflector. This means not only that the struts become longer but that they are also more likely to interfere with the tension ties, at least during the deployment procedure if not at the deployed state. Therefore, θ should be kept small. Considering all of these issues, $\theta = 10°$ seems like a good choice for the present example.

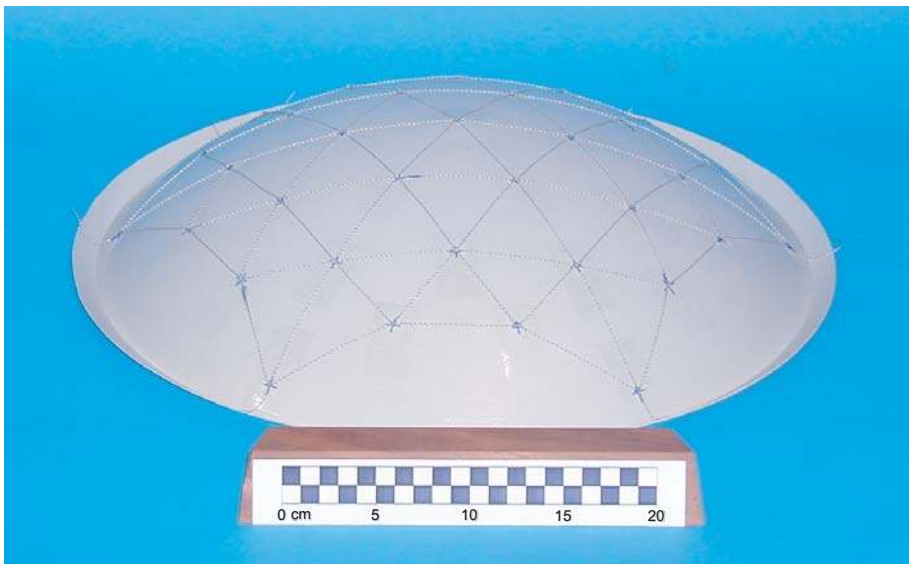

Figure 7.10: Paraboloidal plastic mold with the first of the two three-ring nets attached. The radial cables are used to connect the net to the ring structure.

7.4 Demonstration Model

To verify the feasibility of the proposed concept, a small-scale physical model was constructed. Based on the analysis in the previous section, the model had three-ring nets and a rotation angle of 10°.

The triangular nets[2] were constructed on a paraboloidal mold of *Vivak*[3] with a diameter of 0.45 m and focal length of 0.134 m, Figure 7.10, on which the position of the net joints had been marked with a three-axis computer-controlled machine. The nets were made of 0.8 mm diameter Kevlar cords which were straightened and taped to the molds; the cords were joined with Nylon loops at all cross-over points and bonded with epoxy resin. This manufacturing technique was not very accurate. Systematic length errors were introduced when the cords followed the arc lengths between nodes instead of the straight lines and at the cross-over points where only one of the three cords lay on the surface of the mold. The latter error could have been minimised by using thin steel or CFRP tapes instead of the cords but since this was the first model, at a rather small scale, it was decided not to choose material not readily available. To summarise, the total length error was estimated at about 1 mm per net element, which is undesirably high, but with the available material it could not be made smaller. Corresponding nodes of the two nets were later connected by length-adjusted fishing line and steel springs.

[2]The configuration of each net was not exactly as given earlier; the additional 6 joints and 24 elements outside the edges were left out as the net configuration of the demonstration model was based on an earlier study, cf. [169].

[3]Vivak is a registered trademark of Sheffield Plastics Inc. for glycol modified polyethylene terephthalate (PETG), a thermoplastic copolyester.

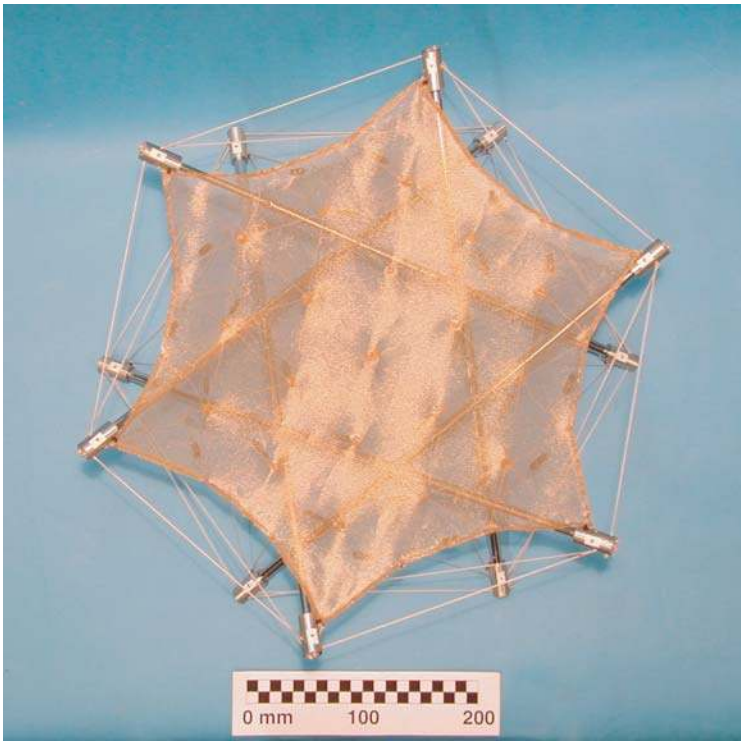

(a)

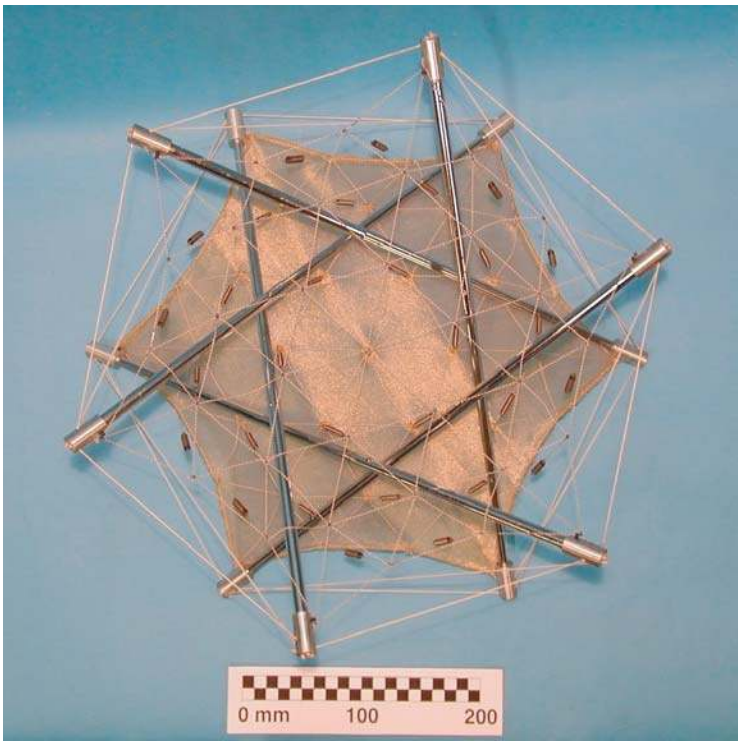

(b)

Figure 7.11: Demonstration model: (a) top view and (b) bottom view.

Based on the experience from the construction of the tensegrity masts, it was decided to manufacture special joints with precision-drilled holes for the ring structure. Twelve identical aluminium alloy, 30 mm long joint fittings of cylindrical shape with a diameter of 15 mm were manufactured. In each joint fitting, holes with 2.0 mm diameter in the direction of each ring cable and a radial net cable were drilled. A 1.0 mm Kevlar cord was used for the ring cables. The cords were connected to the joint fittings by epoxy resin. The struts were made of 6.4 mm diameter aluminium rods, which fitted in 20 mm long holes at the bottom of the joint fittings. These holes were co-axial with the joints. Grub screws held the joints on the struts. The joints were well made and functioned satisfactorily, despite them being too large compared to the rest of the model. A smaller, spherical joint would have been ideal, but also more costly to produce.

The model worked quite well, considering it was the first time that a structure of this kind had been constructed in DSL. However, some of the cables in the two nets remained slack after deployment and there was some interference between the nets and struts, Figure 7.12. This was mainly due to the length errors in the nets, which made them deeper. Since, in the vicinity of the ring connections, the nets are close to the joints, even in an ideal structures, a large length error is bound to result in strut-to-net contact. This interference could hardly have been avoided by further separating the nets; the length errors were simply too large. In addition, the relatively large diameter and cylindrical shape of the joint fittings prevented the nets from being attached close to ring structure, Figure 7.13. Correcting these problems should be possible in a second-generation model, e.g., by using thin bands for the nets, a more accurate mold and smaller joints in the ring structure.

7.5 Deployment Schemes

The success of any deployable structure lies in the actual deployment; it does not matter how accurate or stiff the structure is in its deployed state if it fails to deploy. The deployment of the present structure relies entirely on the way the struts are unfolded; the unfolding rate must be easy to control. Facing the identical problem, Knight [72] lists four possible solutions for strut deployment:

- Hinged struts,
- Sliding coupling struts,
- Telescopic struts, and
- Inflatable struts.

Hinges of various types have been used on deployable systems for several decades. A simple and reliable hinge is the TSR hinge described in section 4.5.1. Its automatic locking capability makes it especially interesting for this application.

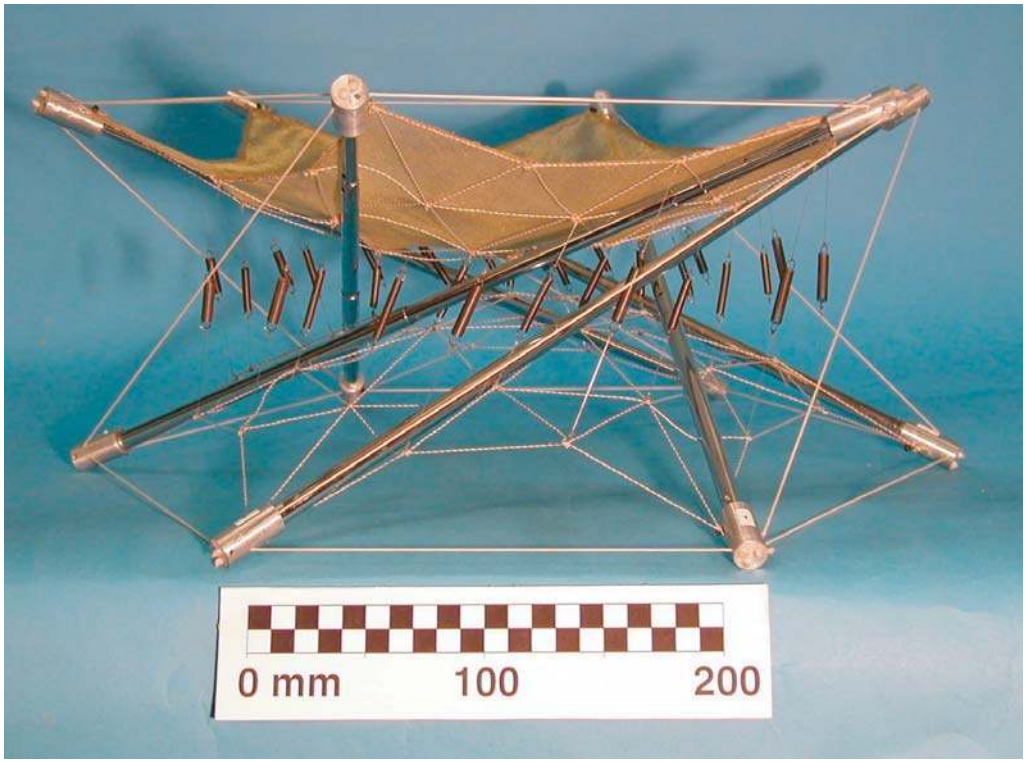

Figure 7.12: Side view of demonstration model.

Figure 7.13: Cylindrical joint fitting with grub screw.

A sliding coupling, with a locking mechanism, is an alternative to the hinge. With sliding couplings it takes minimal force to deploy the strut but significant force to stow it again. However, sliding couplings are fairly new and also introduce stiffness non-linearities [72].

Telescoping structures have not been used very often in space applications due to excessive weight and drive force required [72]. However, Becchi and Dell'Amico, [7], have developed an interesting 2.4 m telescopic mast consisting of seven tubes. For increased stiffness, the tubes slide on tight-fitting *Vespel*[4] pads, and a minimum overlap of one tube diameter is maintained.

The last option is to use inflatable struts. This approach can minimise the stowed volume, but the size and weight is comparable to the three previous schemes [72]. An inflatable strut would use manufacturing and inflation techniques similar to those of inflatable antennas. After inflation, the struts need to be rigidised to ensure their structural integrity throughout the mission lifetime. A rigidised strut would have a uniform cross-section and a minimum of stiffness non-linearities [72].

One design issue, which is critical for deployable structures with cables, is snag prevention. There is a potentially large risk that the long slack ring cables get caught or looped around a strut during deployment. To avoid snagging they must be stowed in a clever way. Knight [72] and Duffy *et al.* [35] study the possibility of using highly elastic cables, which efficiently prevent snagging. However, in such an approach the structure is subjected to very high stowage forces and stiffness creep. In addition, no deployable structure can be allowed to have a too quick deployment sequence as high shock and vibration may be introduced into the spacecraft [72]. A slow, controlled deployment is desired.

Following this brief review of deployment options, it was decided to investigate the folding of the small reflector model using, first, hinged struts and, then, telescopic struts.

7.5.1 Hinged Struts

The aluminium rods were replaced by wooden rods, each having two hinges along its length. The hinges were made by small pieces of metal plate which easily could be bent to a specific angle, Figure 7.14. More refined struts were not made as it seemed that the chances for this folding approach to work were very low given the almost certain entanglement of the struts in the tension springs; still it had to be tried. Figure 7.15 shows the reflector under two early stages of folding. The entanglement started immediately and became more severe as the folding continued. On top of that, the struts started to interfere with each other, and thereby prevented a compact package. These problems can be seen in Figure 7.15(b). This simple test showed that, for this structure, hinged struts were not an option. Even for the three-ring configuration, which had relatively few tension ties, the entanglement problems were too severe.

[4]Vespel is a registered trademark of E. I. du Pont de Nemours and Company.

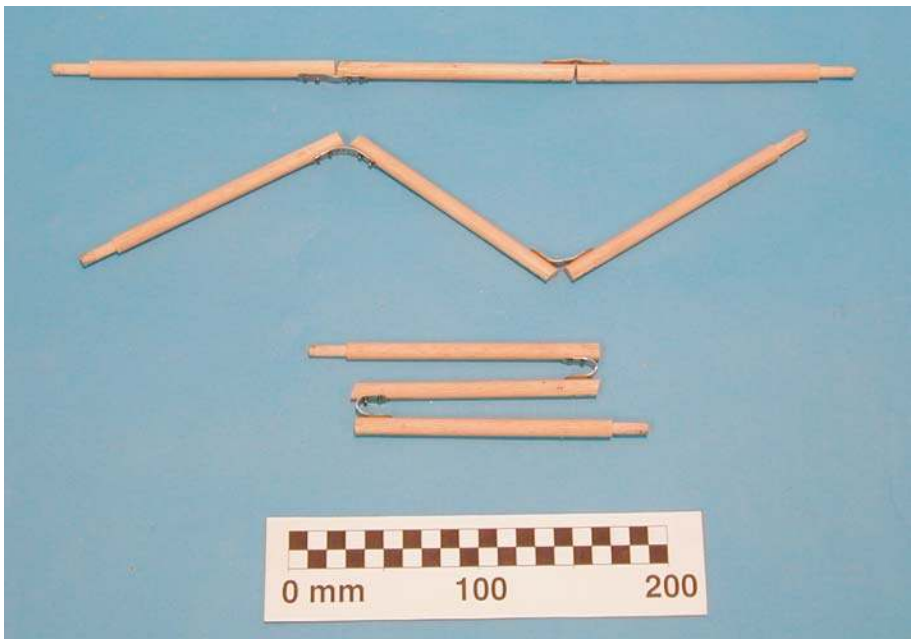

Figure 7.14: Wooden struts with two hinges at different stages of folding.

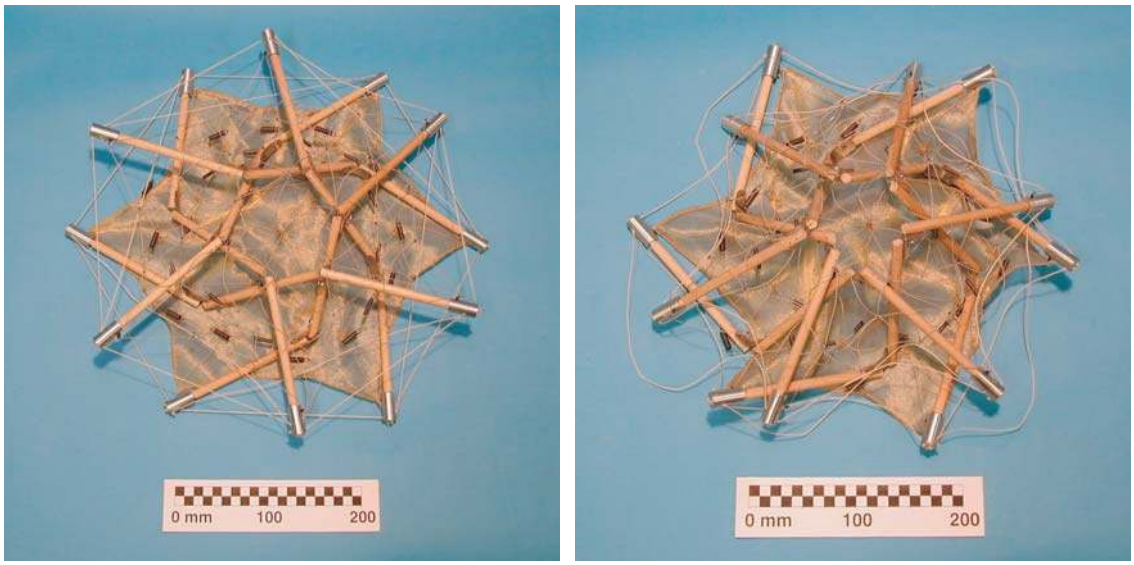

(a) (b)

Figure 7.15: Folding of the antenna using hinged struts ended in failure.

7.5.2 Telescopic Struts

Six telescopic struts, each 0.46 m long, were made by cutting off the sticks of six identical foldable umbrellas. Special connections were made at the ends of the sticks to make them fit in the cylindrical joint fittings. Each strut consisted of three tubes of different lengths as the umbrella sticks had to be shortened, Figure 7.16. The stowed length of the strut, including the joint fittings, was about 0.28 m. Of course,

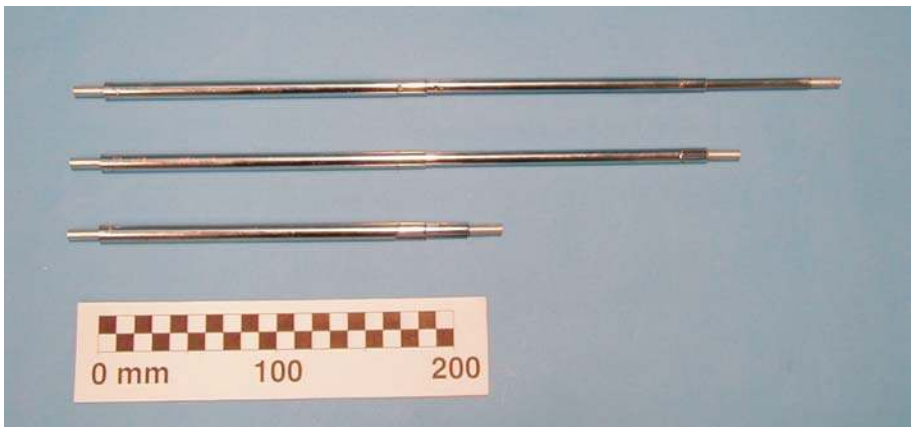

Figure 7.16: Three-piece telescopic strut at different stages of folding.

a more efficient packaging could be achieved using custom made struts. The folding improvement was immediate; no entanglement between struts and springs or interference between struts occurred. To crudely simulate an actual folding, the model was suspended by a fishing line and then folded by hand, followed by a length adjustment of the fishing line, Figure 7.17. This simple simulation looked very promising, but problems could arise if the struts deploy in an unsynchronised manner. A conclusion from this simple test was that synchronously deployable telescopic struts, with some kind of motor synchronisation, would be the best alternative for a successful deployment.

7.6 Preliminary Design of 3 m Reflectors

In this section, the full scale antenna for a future STRV mission will be designed. First, the design procedure will be described, including various simplifications and engineering judgements. This procedure will then be applied to axi-symmetric and offset reflector configurations. Finally, the dynamic characteristics of the best antenna configuration will be computed.

7.6.1 Design Scheme

Network Density

As shown in section 5.4 the required network density, i.e. the number of rings in the tension truss, depends on the wavelength λ and the focal length F. Due to mesh saddling the actual facet surface error is higher than the ideal one. Hedgepeth [56] sets the force t in the net elements equal to ten times the mesh tension p multiplied by the facet side length ℓ. Equation (5.27) yields the surface error

$$\delta_{\mathrm{rms},z} = 0.01667\frac{\ell^2}{F}, \tag{7.15}$$

(a) (b)

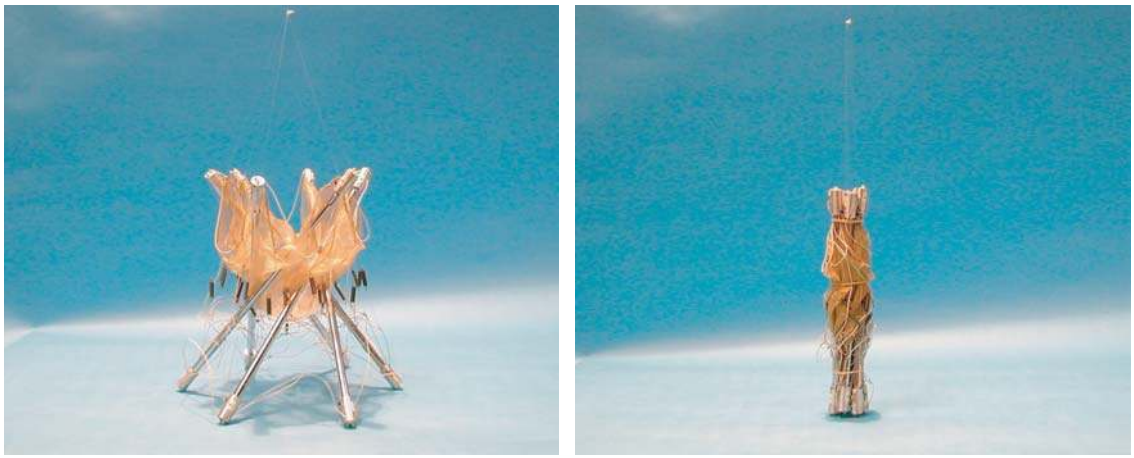

(c) (d)

Figure 7.17: Simple folding simulation with the antenna model suspended in a fishing line.

which is only 3.3% larger than the ideal one, (5.29). To preserve this surface error, the smallest internal force in the tension truss should be $t = 10p\ell$. The corresponding required triangle side length ℓ is

$$\ell = 7.745\sqrt{F\delta_{\mathrm{rms},z}}. \tag{7.16}$$

As decided in section 5.4.6, two accuracy goals apply, with facet error contributions of $\lambda/100$ and $\lambda/50$, respectively. At 9.65 GHz the wavelength is 31 mm, so the allowable facet errors were 0.3 mm and 0.6 mm. Note, however, that the number of rings was maximised to seven according to Chapter 6, so the lower error might not be achievable with a deep reflector.

The nets were assumed to be constructed from CFRP band with a cross-section of 5×0.2 mm^2. The density of the bands was 1740 kg/m^3. This value was doubled

in the mass estimation to take the weight of the joints into account. It was further assumed that the same CFRP bands were to be used throughout the net, although the elements along the edges might be too highly stressed and need strengthening. To take this strengthening into consideration, the total length of the net bands was increased by 10% in the mass calculation.

Mesh

The RF reflective mesh were tensioned to either 2 or 10 N/m, as discussed in section 5.5.2. Previous results on the present reflector, cf. [169], are based only on the lower mesh tension. A higher mesh tension will more efficiently smooth out the creases formed during folding and give a more robust antenna structure as the prestress level increases. A higher mesh tension will, however, result in a heavier structure. To facilitate comparison, both values were used in the design study.

When estimating the antenna mass, the surface density of the mesh, 0.025 kg/m^2, was doubled to account for seams and surface treatment. The mesh area could be approximated with that of a spherical cap of equal height and equivalent radius as the reflector. However, for a more accurate mass comparison between different antenna configurations, it was decided to compute the actual area of the stretched mesh.

Tension Tie Forces

At each node, each of the three bands running continuously through the node turns an angle $\ell/2F$, Figure 7.18. The required force in the tension tie to equilibrate these net forces is

$$t_{\text{tie}} = 1.5\frac{t\ell}{F}. \tag{7.17}$$

Using this value might result in net forces less than $10p\ell$, but as long as the majority of the net elements have this force the surface degradation should be negligible. For practical purposes t_{tie} was given in full Newtons only, with a minimum value of 1 N. Hence, the tension tie force by (7.17) was rounded to the nearest integer towards infinity.

Ring Structure

Once the required net tension and tension tie forces had been established, the forces in the ring structure could be computed.

First, a safety factor with respect to material failure had to be set. This factor depends on the acceptable risk of failure for the mission and may vary for different structural details, cf. [143]. For CFRP compression members, Hedgepeth *et al.* [62] use a maximum stress of 200 MPa, which corresponds to a safety factor against material failure between 5 and 10, depending on the strength of the CFRP. This

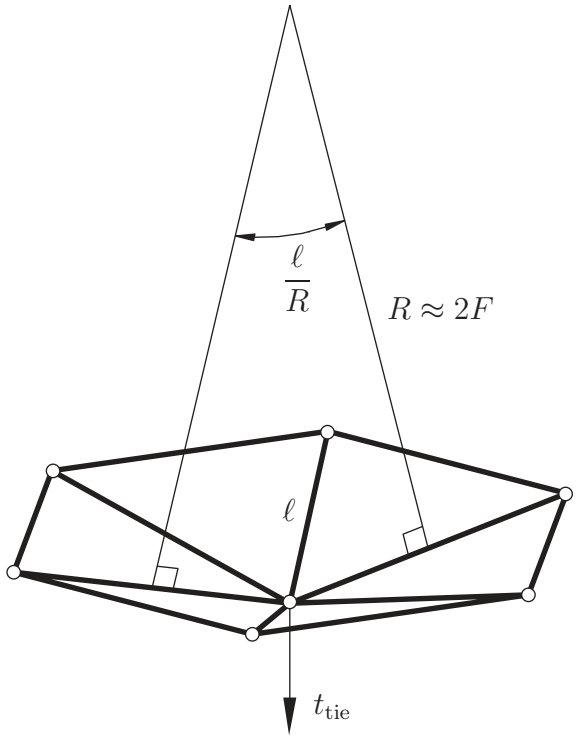

Figure 7.18: Equilibrium of a node in the tension truss.

allowable stress value was also used here for the net elements, ring cables and struts, for the case of material failure.

The struts were basically designed to resist Euler buckling, subject to constraints on the slenderness, l_e/r_g, where l_e is the effective length of the strut and r_g the radius of gyration. The minimum slenderness ratio was found by equating the critical buckling stress and the proportional limit stress σ_{pl}:

$$\left(\frac{l_e}{r_g}\right)_{\min} = \sqrt{\frac{\pi^2 E}{\sigma_{\text{pl}}}}. \tag{7.18}$$

This slenderness was used only for confirmation of the elastic buckling assumption. For the present application, $E = 227.5$ GPa and $\sigma_{\text{pl}} \approx 1500$ MPa, $(l_e/r_g)_{\min} = 39$. The maximum slenderness depends on the required axial stiffness and length precision of the strut. If the strut is not straight, the axial stiffness is severely degraded. For a strut with both ends pin-jointed, an initial sinusoidal imperfection, $w = \epsilon \sin(\pi x/l)$, reduces the axial stiffness to [57]

$$AE_{\text{eff}} = \frac{AE}{1 + \frac{1}{2}\left(\frac{\epsilon}{r_g}\right)^2}. \tag{7.19}$$

For a thin-walled tube of radius a and wall thickness τ

$$r_g = \sqrt{\frac{I}{A}} \approx \sqrt{\frac{\pi a^3 \tau}{2\pi a \tau}} = \frac{a}{\sqrt{2}}. \tag{7.20}$$

A 1% reduction of the axial stiffness corresponds to $\epsilon/r_g = 0.14$. A thin-walled tube should have $\epsilon/2a < 1/10$, [57]. However, it is believed that much less crookedness, say $\epsilon/2a < 1/50$, is needed for this application. During ground testing, the strut sags due to gravity. The midpoint deflection of a simply supported horizontal strut of length l_s is

$$\epsilon = \frac{5}{384}\frac{\rho g l_s^4}{E r_g^2}, \tag{7.21}$$

where ρ is the density and g the gravity. The change in length, Δl, of an incompressible beam due to bending is $\frac{1}{2}\int_0^l (\mathrm{d}w/\mathrm{d}x)^2 \mathrm{d}x$ where, in this case, $w(x) = \rho g x \left(l^3 - 2lx^2 + x^3\right)/24 E r_g^2$. The corresponding strain due to this change in length is

$$\frac{\Delta l_\epsilon}{l_s} = \frac{17}{40320}\left(\frac{\rho g l_s}{E}\right)^2 \left(\frac{l_s}{r_g}\right)^4. \tag{7.22}$$

The effective length of the struts is equal to their actual length, $l_e = l_s$, which changes with the rotation angle θ. The length of a deployed strut in an axi-symmetric reflector can be written as:

$$l_s = \left\{ \frac{D^2}{4}\left[\left(\frac{1}{2} + \cos\theta\right)^2 + \left(\frac{\sqrt{3}}{2} + \sin\theta\right)^2\right] + \left(\frac{D^2}{8F}\right)^2 \left[1 + \cos\left(60^\circ - \theta\right)\right]^2 \right\}^{1/2}. \tag{7.23}$$

With $D = 3$ m and $F/D = 0.4$, the strut length varies between 2.95 and 3.38 m, as θ varies between 0 and 30°. Setting $\epsilon/r_g = 2\sqrt{2}/50$ and substituting $l_s = 3.38$ m, $E = 227.5$ GPa, $\rho = 1740$ kg/m^3 and g = 9.80665 m/s^2 into (7.21) yielded $l_e/r_g = 257$. Inserting these values into (7.22) produced $\Delta l_\epsilon/l_s = 1.2 \cdot 10^{-7}$, which is about one order better than the required ring distortion $\sigma_\rho = 10^{-6}$. Hedgepeth *et al.* [62], use a maximum slenderness of 200 for 4.25 m long CFRP struts with identical material properties as above. In the following analysis, the maximum slenderness was, therefore, set to 200. Thus, an initial value for the minimal strut radius a was computed as:

$$a_{\mathrm{ini}} = \frac{l_e\sqrt{2}}{200}. \tag{7.24}$$

With the wall thickness fixed to 0.5 mm, the strut radius was adjusted until $l_e/r_g \leq 200$. A subsequent step checked that $P_{\mathrm{cr}} \geq 10P$, where 10 is the chosen safety factor against buckling and P the design compression force.

To fit in the launch envelope, $0.1 \times 0.2 \times 0.8$ m^3, the 3.38 m long struts had to be collapsed to less than a quarter of their length. In the telescopic mast by Becchi and Dell'Amico, [7], a minimum overlap of one tube diameter is maintained to achieve adequate stiffness. Thus, struts up to about 3.1 m in length can be constructed from four tubes. However, at this preliminary stage it is not possible to give a detailed mass calculation of the struts. Therefore, the mass of the tubular struts of constant cross-section was amplified by 50% to allow for tube overlap and the variation in the cross-section of the telescopic struts. The mass of the deployment motor, latches, cables and pulleys was estimated as 0.2 kg per strut [168].

The tendons of the ring structure are preferably CFRP bands, which easily can be folded. Bands are also less likely to get tangled up during folding because basically

only two folding directions are permitted. The maximum allowable stress in the cables was, as above, 200 MPa. The mass of the connections between the cables and the struts were estimated to 0.05 kg per connection.

7.6.2 Axi-Symmetric Reflectors

In Table 6.3, the required number of rings for a certain facet surface accuracy was given. The lower surface accuracy, 0.6 mm, was nearly obtained with seven rings for $F/D = 0.4$, six rings for $F/D = 0.6$, and five rings for $F/D = 0.8$. The higher surface accuracy, 0.3 mm, was nearly achievable with seven rings for $F/D = 0.8$. These four combinations, denoted I–IV, were analysed in terms of internal forces for different values of the rotation angle θ and mesh tension p. Figure 7.19 shows the results from the analysis of the internal forces when $p = 10$ N/m. In Figure 7.19(a), the forces in the ring structure are shown. Like the three-ring reflector antenna, they decreased rather rapidly in the beginning and are ended where a net force ceases to be in tension. The minimum net forces in Figure 7.19(b) have almost constant downward slopes; the steepness of the curves seems to depend on the number of net rings. It was significant that the minimum net force for the seven-ring configurations, I and IV, was much lower than for the other configurations. To preserve the surface accuracy it ought to be about $10p\ell = 21$ N for seven rings, which is about ten times the value at $\theta = 10°$. A closer study revealed that the elements with the minimum force were located outside the highly stressed edge elements and therefore not attached to the mesh. Slightly lower forces, say $2p\ell$, which increase the additional rms surface error from 3.3% to 16.5%, may in some cases be also accepted in elements connected to the mesh, if the affected elements are in the minority. Here, the forces were just too low and the two seven-ring configurations, I and IV, were discarded from further analysis. Thus, this eliminated the possibility of achieving the higher surface accuracy, $\lambda/50$. Good designs for the remaining two configurations, II and III, were obtained at $\theta = 10°$. At that angle the ring forces had come down from their very large values at 5° and the minimum net forces were acceptable at 6.2 and 18.7 N, respectively. Mass estimates, following the scheme in the previous section, for configurations II and III at $\theta = 10°$, are given in Table 7.1.

7.6.3 Offset Reflectors

For offset reflectors, the separation of the nets for the offset reflector is computed by (7.13), but with a corrected focal length $F_{\text{eq}} = \xi F$, where ξ is the ellipticity, (5.10). This takes into account that for identical focal lengths and aperture diameters the offset reflector is shallower than the axi-symmetric one. For example, $D = 3$ m, $F/D = 1.2$, $X_A = 0$ m, and $\theta = 10°$ give a total ring height of 1.54 m in the axi-symmetric case but only 1.31 m in the offset case ($H_a = 0.40$ m and $\Delta H = 0.51$ m). Similarly, when computing the tension tie force from (7.17), F should be substituted with F_{eq}.

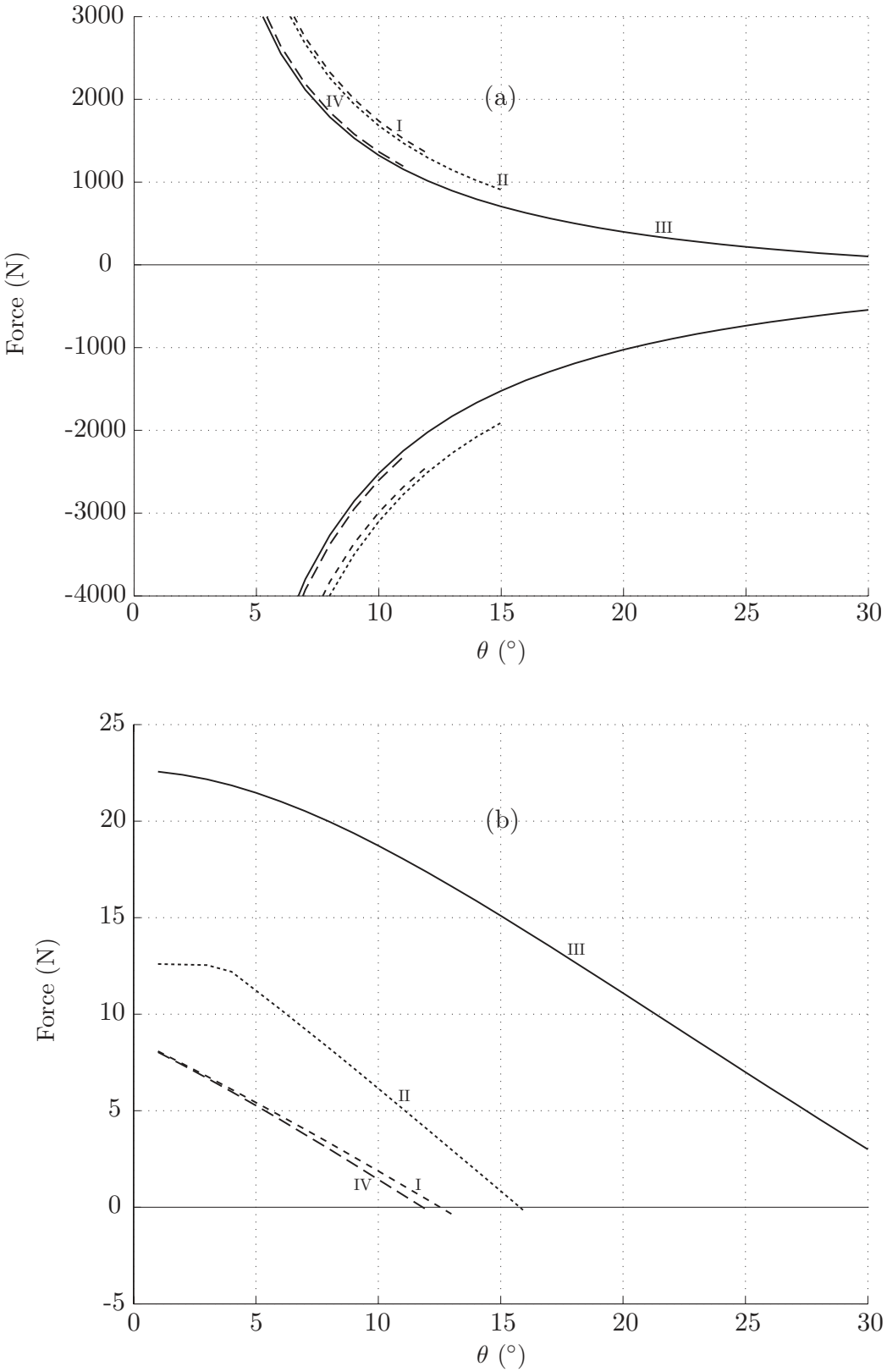

Figure 7.19: Forces in (a) strut and most stressed ring cable, and (b) least stressed net member for four different axi-symmetric configurations with $p = 10$ N/m: (I) $F/D = 0.4$, $n = 7$; (II) $F/D = 0.6$, $n = 6$; (III) $F/D = 0.8$, $n = 5$; (IV) $F/D = 0.8$, $n = 7$.

The number of net rings for the required surface accuracy was computed using (7.16). With focal lengths $F = 1.5,\ 1.8$, and 2.1 m the higher surface accuracy of 0.3 mm could not be achieved with less than eight rings. But, as stated before, the number of rings was limited to seven. To achieve the lower surface accuracy of 0.6 mm seven rings were required for $F = 1.5$ m, while six rings were sufficient for $F = 1.8$ and 2.1 m. In Table 6.2, the net forces for different offset configurations are shown. However, a preliminary analysis with a three-ring offset reflector showed that the tension tie forces determined in the previous chapter do not produce the same force distribution in the nets when the whole antenna structure was considered. In addition, the mirror symmetry of the internal forces in the net was lost. This was most likely a result of the loss of symmetry for the whole structure. The bottom net was a mirror image of the top one in the aperture plane so that corresponding nodes were connected by tension ties. Hence, neither mirror nor rotational symmetry existed. However, the internal forces in the two nets were identical as the structure still had the quasi-flip symmetry, i.e. the effect of turning the antenna upside down so that the top net becomes the bottom net will only change the direction of the struts and θ. Slight changes in the tension tie forces along the edges were, therefore, necessary to re-obtain a satisfactory internal force distribution.

For the present study, the reflectors had an offset value of 0 or 0.3 m, as their force relations were about the same for $n = 6$ and slightly worse for $n = 7$, as seen in Table 6.2. Considering the increased prestressing problems discussed above, the offset antenna analysis were limited to six rings. Thus, only reflectors with focal lengths of 1.8 and 2.1 m were studied. Figure 7.20 shows the modified tension tie distribution along the edges for the six-ring nets; the only change was an increase from 4.5 to 5.0 for six of the ties. The results for the three offset configurations are shown in Figure 7.21. The variations of the forces in the ring structure were similar for all three configurations. However, the variations of the minimum net forces were drastically different from those of the axi-symmetric case. For configuration V, $F = 1.8$ m and $X_A = 0$, the minimum net force was maximised at about 10°, while for VI, $F = 2.1$ m and $X_A = 0$ m, and VII, $F = 2.1$ m and $X_A = 0.3$ m, it was maximised at 8° and 12°, respectively. For $F = 1.8$ m and $X_A = 0.3$ m, it was not possible to prestress the nets with the present tension tie distribution. Hence, a feasible configuration VIII did not exist. Note also that the minimum net force was lower than the $10p\ell$ required for good surface accuracy. However, the majority of the net cables were stressed to the required value, so the overall surface accuracy should not be seriously affected by the lower tensions. Considering the magnitude of the strut force and the strut–tie interference issues discussed earlier, it, once again, seems that $\theta = 10°$ is a good choice for the offset configurations. Mass estimates for configurations V–VII at $\theta = 10°$ are given in Table 7.1. As the forces in the ring structure were similar for all of the five remaining configurations, the resulting masses were almost identical. Configuration VI seems slightly better than the others because of a larger minimum net force and a marginally lower weight.

Table 7.1: Mass estimates of reflector configurations II, III, and V–VII at $\theta = 10°$.

Description		Configuration									
		II		III		V		VI		VII	
Focal length	(m)	1.8		2.4		1.8		2.1		2.1	
Offset distance (X_A)	(m)	—		—		0		0		0.3	
Number of net rings		6		5		6		6		6	
Mesh tension	(N/m)	10	2	10	2	10	2	10	2	10	2
Internal tie force[a]	(N)	6	2	6	2	5	1	5	1	5	1
Minimum net force	(N)	6.2	2.1	18.7	6.2	5.4	1.1	8.2	1.6	6.0	1.2
Maximum net force	(N)	367	123	298	99	446	90	471	95	505	101
Ring cable force	(N)	1681	561	1323	441	1692	339	1846	370	1901	381
Strut force	(N)	−3100	−1034	−2520	−840	−3220	−644	−3545	−709	−3677	−736
Effective strut length	(m)	2.91		2.83		3.04		2.96		3.00	
Strut diameter[b]	(mm)	84	58	77	53	88	51	89	52	91	53
Euler buckling force	(kN)	30.31	9.90	24.65	7.97	31.96	6.14	34.88	6.87	36.31	7.09
Mesh area	(m^2)	5.06		5.07		5.48		5.37		5.50	
Net length	(m)	201.36		170.33		209.24		206.59		209.13	
Ring cables length	(m)	30.02		29.31		31.94		31.07		31.70	
Struts length	(m)	17.46		16.98		17.92		17.54		17.71	
Ring height	(m)	1.03		0.77		0.94		0.83		0.81	
Mass composition											
Mesh	(kg)	0.25		0.25		0.27		0.27		0.28	
Net	(kg)	0.77		0.65		0.80		0.79		0.80	
Connections	(kg)	0.60		0.60		0.60		0.60		0.60	
Motors and latches	(kg)	1.20		1.20		1.20		1.20		1.20	
Ring cables[c]	(kg)	0.47	0.16	0.36	0.15	0.50	0.11	0.54	0.11	0.55	0.11
Struts	(kg)	5.98	4.12	5.33	3.65	6.43	3.71	6.36	3.70	6.57	3.81
Total	(kg)	9.27	7.10	8.39	6.51	9.80	6.70	9.76	6.67	10.00	6.80

[a]Tension tie forces are rounded to nearest integer (N) towards infinity.
[b]Buckling failure has a higher safety factor than material failure to account for imperfections and cross-sectional variations. The buckling force may in some cases produce a stress a little higher than 200 MPa, but this is neglected to facilitate a fair mass comparison.
[c]Cross-sectional areas are rounded to nearest integer (mm^2) towards infinity.

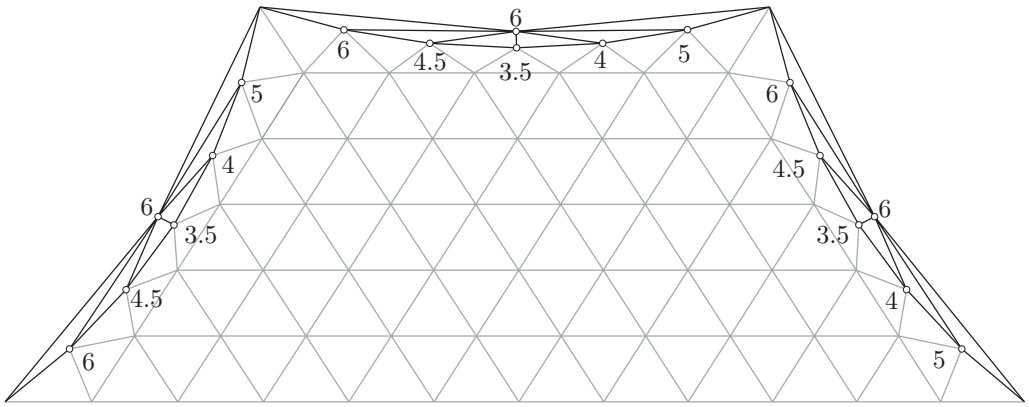

Figure 7.20: Tension tie forces along the edges for six-ring offset reflector antennas (mirror symmetry). Interior elements are drawn thinner for clarity.

7.6.4 Stowage Considerations

Configuration V has the longest struts, 3.04 m. If this strut is divided into four pieces and the minimum overlap is one diameter, 88 mm, the stowed height of the struts is 0.848 m. This is in excess of the limit 0.8 m. Only configuration III with the shortest struts, 2.83 m, came under the limit at 0.785 m. Using the smaller tube diameter decreased the stowed height a little but only configurations II, III, and VI stayed below the limit. The height limit can easily be met by dividing the strut into five pieces or by accepting longer stowed struts. However, according to Figure 5.4 there is a hard limit of 891 mm on the stowed height, so the recommended limit of 800 mm should not be exceeded and more tube segments only complicate the strut design. Besides the height constraint, the stowed package must conform to the width and depth requirements of 200 mm and 100 mm, respectively. Rectangular stowage dimensions for a mesh reflector antenna are rather odd. Most mesh antennas have a supporting structure composed of only stiff elements so the package with the stowed antenna tends to be cylindrical. The present structure, however, is not bound to any particular shape of the stowed configuration since the struts are not connected to each other. Two natural ways of arranging the struts are shown in Figure 7.22. The rectangular configuration, Figure 7.22(a), is preferable in the present case. With a maximum depth of 100 mm, the maximum strut diameter was $2 \cdot 100/(2+\sqrt{3}) \approx 53.5$ mm. Note that this is only a theoretical value, not achievable in practice, as space in between the struts must be provided for the folded mesh and nets. At present, this space requirement cannot be quantified.

A circular configuration, Figure 7.22(b), provides sufficient space in the middle for the nets and mesh. The maximum diameter of the struts was $100/3 \approx 33$ mm, which yields a slenderness of 257 for $l_e = 3$ m. Hence, the circular configuration was not feasible. Returning to the rectangular configuration it was immediately recognised that a mesh tension of 10 N/m yielded a package that was too large to fit into the launch envelope. The lower mesh tension, 2 N/m, gave diameters 51–58 mm, which better fit the requirements on stowed volume. Considering both the stowage volume and net forces, VI again seems to be the best configuration.

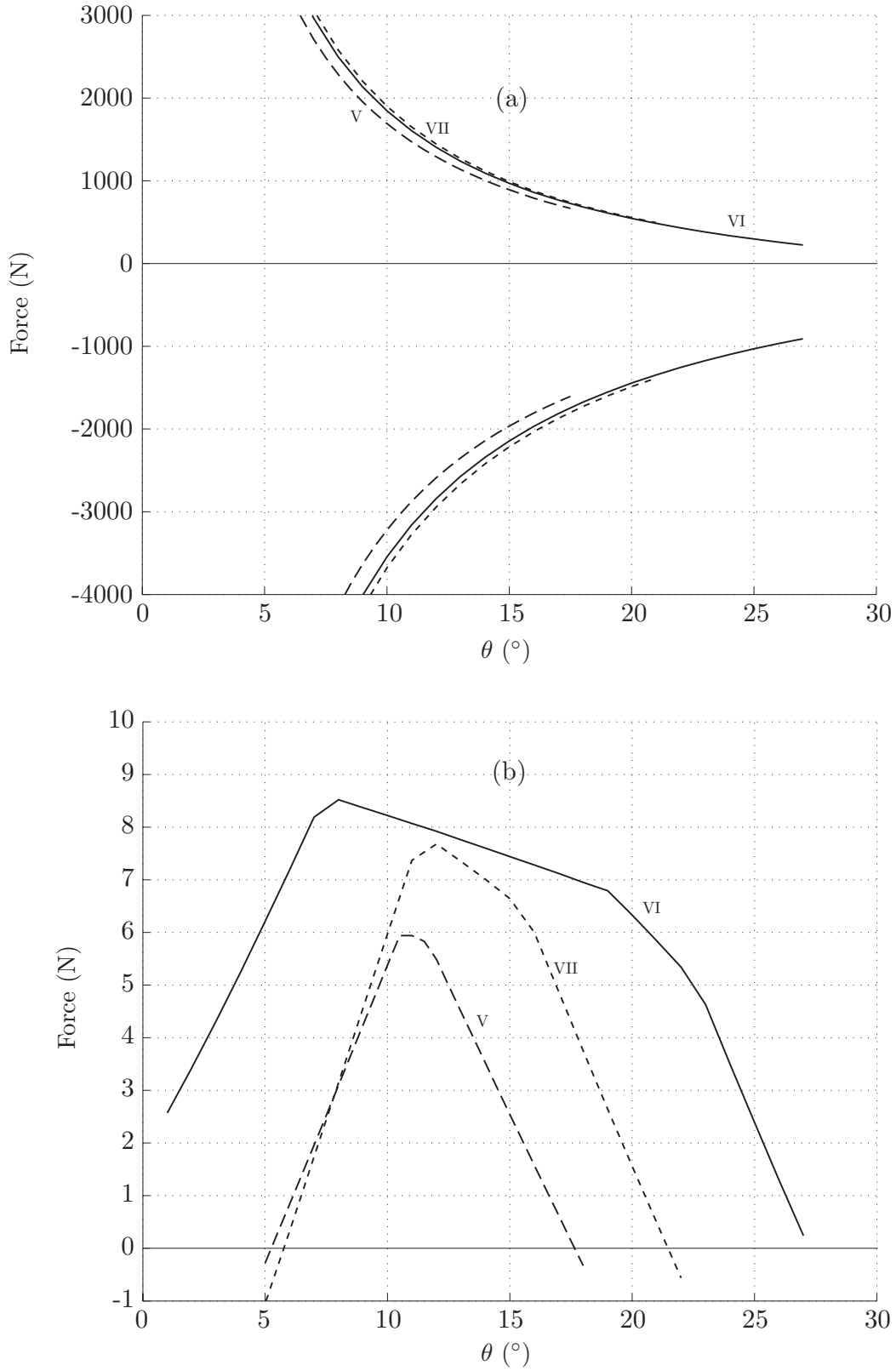

Figure 7.21: Forces in (a) strut and most stressed ring cable, and (b) least stressed net member for three different offset configurations with $n = 6$ and $p = 10$ N/m: (V) $F = 1.8$ m, $X_A = 0$ m; (VI) $F = 2.1$ m, $X_A = 0$ m; (VII) $F = 2.1$, $X_A = 0.3$ m.

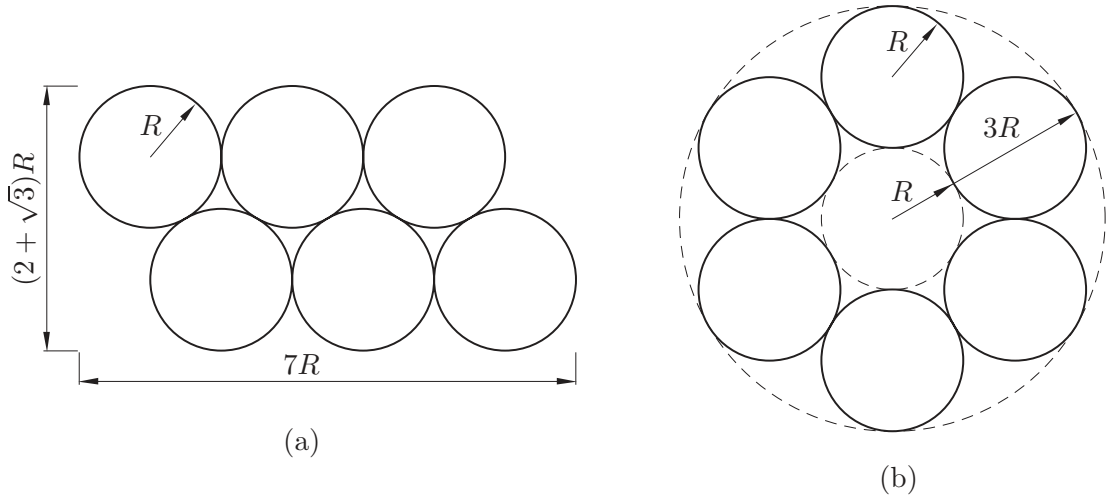

Figure 7.22: Stowing of the struts: (a) rectangular and (b) circular.

7.7 Vibration Analysis

An important characteristic is the natural frequency of the deployed antenna. Here, only configuration VI, which was found to be slightly better than the others, was analysed. For the vibration analysis, all data except the stiffness of the tension ties are available. In the Monte Carlo simulations of Chapter 6, a maximum force variation of $\sigma_\tau = 0.1$ was used. In general, the softer the springs of the tension ties, the easier it is to control the force. However, too soft springs might cause dimensional stability problems during ground testing, e.g. sagging of the bottom net due to self-weight. During ground testing it is common to test the antenna in two positions, cup-up and cup-down, to estimate the effects of gravity. Here, the weight of the lower net was about 0.40 kg at a cup-up position and 0.66 kg in the cup-down position. In the cup-down position, the mass per internal node of the lower net was $0.66/127 \approx 0.005$ kg or 0.05 N, in force units. By itself, this additional loading will not cause severe degradation of the surface as its magnitude is of the same order as the force variation $\sigma_\tau = 0.1$ N ($t_{\text{tie}} = 1$ N). However, for a tie stiffness of, say 10 N/m, the node was displaced 5 mm vertically by the 0.05 N load, which is unacceptable. Assuming that a vertical displacement, i.e. de-focus, of 0.2 mm could be accepted in the cup-down position during ground testing, the required tie stiffness was 250 N/m. Steel springs with this stiffness are readily available, but some applications may require springs of another material with a smaller CTE.

In the following vibration analysis, the tension ties were assumed to be weightless. The mass of the mesh was added to that of the top net, giving a length density of 0.0064 kg/m, while the mass of the bottom net was 0.0038 kg/m. The mass of the strut–cable connections were uniformly distributed over the total length of the ring cables and the struts, and the mass of the motors and latches were uniformly distributed over the total length of the struts. This gave a ring cable mass and a strut mass of 0.0158 and 0.2919 kg/m, respectively. The total antenna weight remained unchanged, 6.67 kg. As stated earlier, the attachment of the antenna

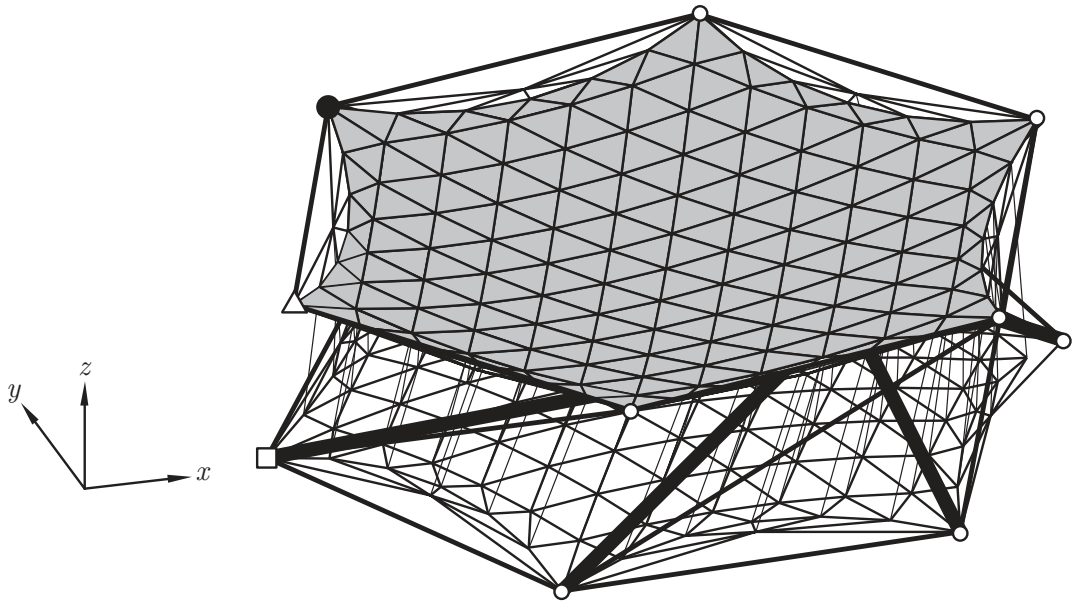

Figure 7.23: Supports for the reflector antenna in the vibration analysis. Symbols: □ restrained in x-, y- and z-direction, △ in x and y, • in x and ∘ unrestrained.

to the spacecraft was not investigated. Nevertheless, it is highly likely that the antenna will be connected at point A, cf. Figure 5.7, and therefore the support configuration in Figure 7.23 was used in the vibration analysis. All element were modelled using two-node bar elements with a consistent mass matrix, cf. [27]. The ten lowest natural frequencies were 9.19, 13.32, 19.88, 26.58, 35.98, 47.27, 57.74, 65.77, 75.37, and 76.12 Hz. The modes for the two lowest frequencies are shown in Figure 7.24. If the support with constraints in the x- and y-direction, i.e. △, was constrained in the z-direction, i.e., became □, the first two frequencies increased to 13.30 and 17.78 Hz, respectively.

The lowest vibration frequency of a pin-ended strut is

$$f_{s,1} = \frac{\pi}{2}\sqrt{\frac{EI}{ml^4}}. \tag{7.25}$$

Assuming a constant tubular cross-section of 52 mm in diameter and 0.5 mm thickness, the 2.96 m long strut has $f_{s,1} = 37.33$ Hz, which is well above the fundamental frequency of the complete structure. The actual telescopic strut has lower bending stiffness, which somewhat decreases the natural frequency. Figure 7.25 shows the ratio of the buckling loads of a telescopic and a constant cross-section beam. The beam was tubular with a maximum diameter of 52 mm and a tube thickness of 0.5 mm. The telescopic beam was divided into four segments and at each intersection the diameter decreases Δd; the minimum value of $\Delta d = 2t$. It was assumed that the tubes are free of any imperfections and have zero play at the intersections. The buckling load was computed by the finite difference method, cf. [173], with a subdivision of $l/100$. For sufficient stiffness, the gap between the tube segments should not be more than 3 mm ($\Delta d = 4$ mm). Hence, the safety factor of 10 for buckling

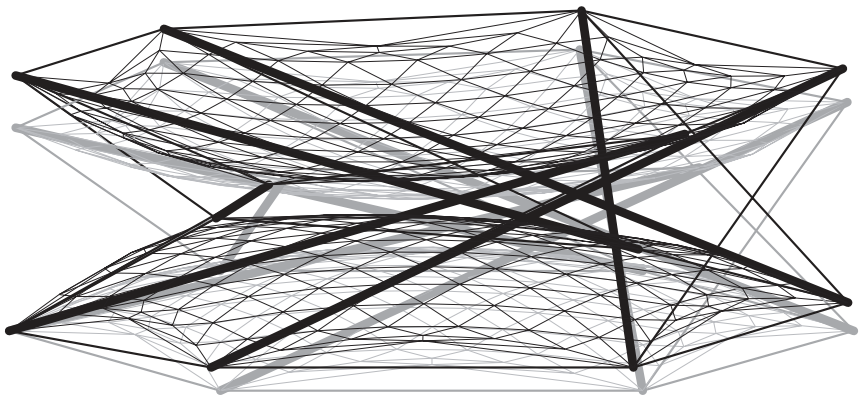

(a) $f_1 = 9.19$ Hz

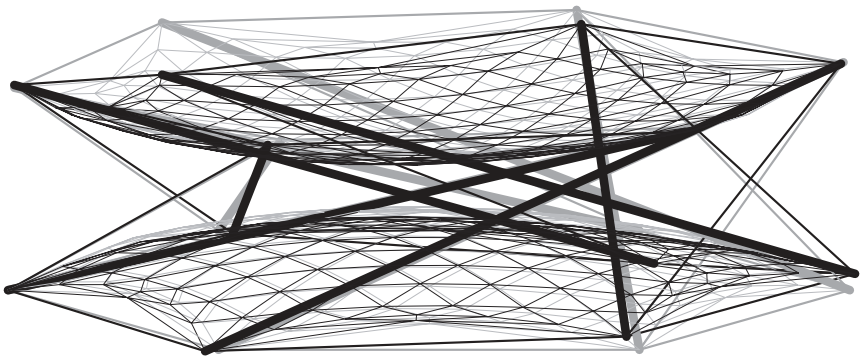

(b) $f_2 = 13.32$ Hz

Figure 7.24: The two lowest vibration modes of the offset antenna configuration VI with $p = 2$ N/m (the tension ties are removed for clarity).

has now decreased and will diminish further for the real strut due to manufacturing errors, e.g. play between tube segments.

7.8 Discussion

It can be concluded that the requirements on the stowed dimensions are approximately met; the package has to be slightly deeper, maybe 140 mm, to make room for the folded nets and mesh. This yields the following stowed dimensions: $d/D = \sqrt{4 \cdot 0.2 \cdot 0.14/\pi}/3 \approx 0.06$ and $h/D = 0.8/3 \approx 0.27$. Only the 15 m diameter HCA has so low stowed dimension values.

It is observed that the mass limit of 20 kg, set up by DERA, is easily achieved by the present antenna at 6.67 kg or 1.24 kg/m^2 ($A = 5.37$ m^2). Compared to the 2.4×1.6 m^2 SAR reflect array with a mass of around 15.5 kg or 4.04 kg/m^2,

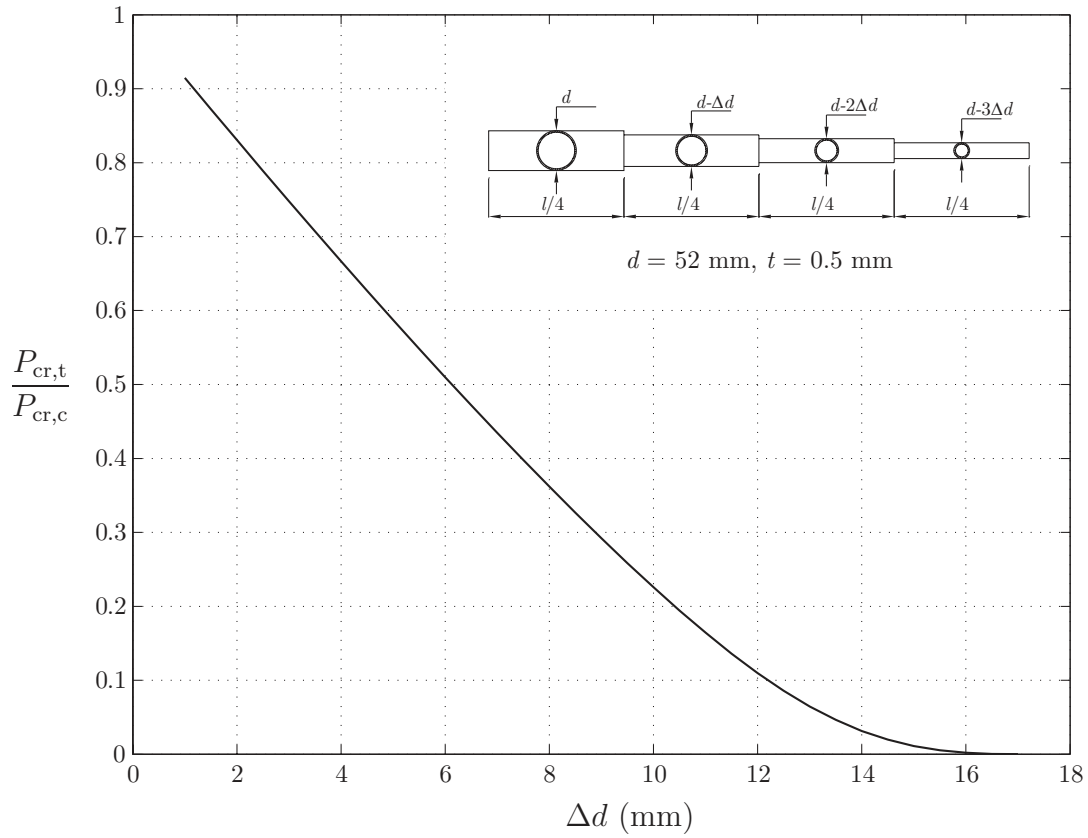

Figure 7.25: Buckling load of a four-piece perfectly straight telescopic strut, $P_{\mathrm{cr,t}}$, divided by the buckling load of a constant cross-section strut, $P_{\mathrm{cr,c}}$.

cf. [130], the reflector antenna is superior. Comparing the areal densities of the mesh antennas in Table 2.1, which vary between 0.36 and 4.58 kg/m^2, the present value is amongst the best. The mass composition of the present antenna is 84.1% for the ring structure (including connections, motors and latches), 11.8% for the nets, and the remaining 4.1% for the mesh. In comparison, the 23.56 m diameter AstroMesh ($\xi = 1.118,\ n = 27$) of reference [62] has a total weight of 144.9 kg, of which 67.0% is the mass of the ring structure, 15.7% the mass of the nets and the remaining 17.3% belonging to the mesh. Although these two antennas differ significantly in aperture size, it is apparent that the ring structure is the dominating factor when considering the total mass. The relationship between the mass of the nets and that of the mesh depends entirely on the number of net rings.

Earth observing systems typically require a fundamental natural frequency above 0.1 Hz [55]. With a lowest frequency of 9 Hz, the present antenna easily fulfils this requirement. A high stiffness is also an advantage in ground testing as the gravity compensation system can be simplified. In comparison, the SAR reflect array has a frequency of 0.9 Hz [130].

Although it seems that the present antenna is suitable for a future STRV mission, some issues remain that are either solved unsatisfactorily or not at all. Beside the attachment to the spacecraft, which was mentioned earlier, the position of the struts

will always be an obstacle in the concept. The current position, where the struts go right through the forest of tension ties, will seriously limit the number of net rings and thereby the achievable surface accuracy. If the struts in some way could be moved closer to the perimeter of the aperture, a great deal would be won, e.g. the ring structure height could diminish. A possible refinement of the ring structure is to use a two-stage tensegrity module instead of the one-stage. The main advantages are that the struts are closer to the boundary and that two parameters, the overlap η and the rotation angle θ, can be used to change the prestress in the structure. Consider a two-stage tensegrity module with six struts per stage which has $m = 7$ and $s = 1$ by (4.3). Then add two interconnected, central joints and 13 bars in the same fashion as in Figure 7.5. The resulting structure has $m - s = -1$. In the configuration given by (4.5), the stress in the added bars is zero. By changing η and θ, the added bars can be stressed. Figure 7.26 shows the variation of the force density in the bars. It is observed that the area of feasible configurations is very small. Still, there is a possibility that such a configuration will also work when the extra bars are replaced with triangular networks.

Another aspect that needs further investigation is the layout of the nets for static

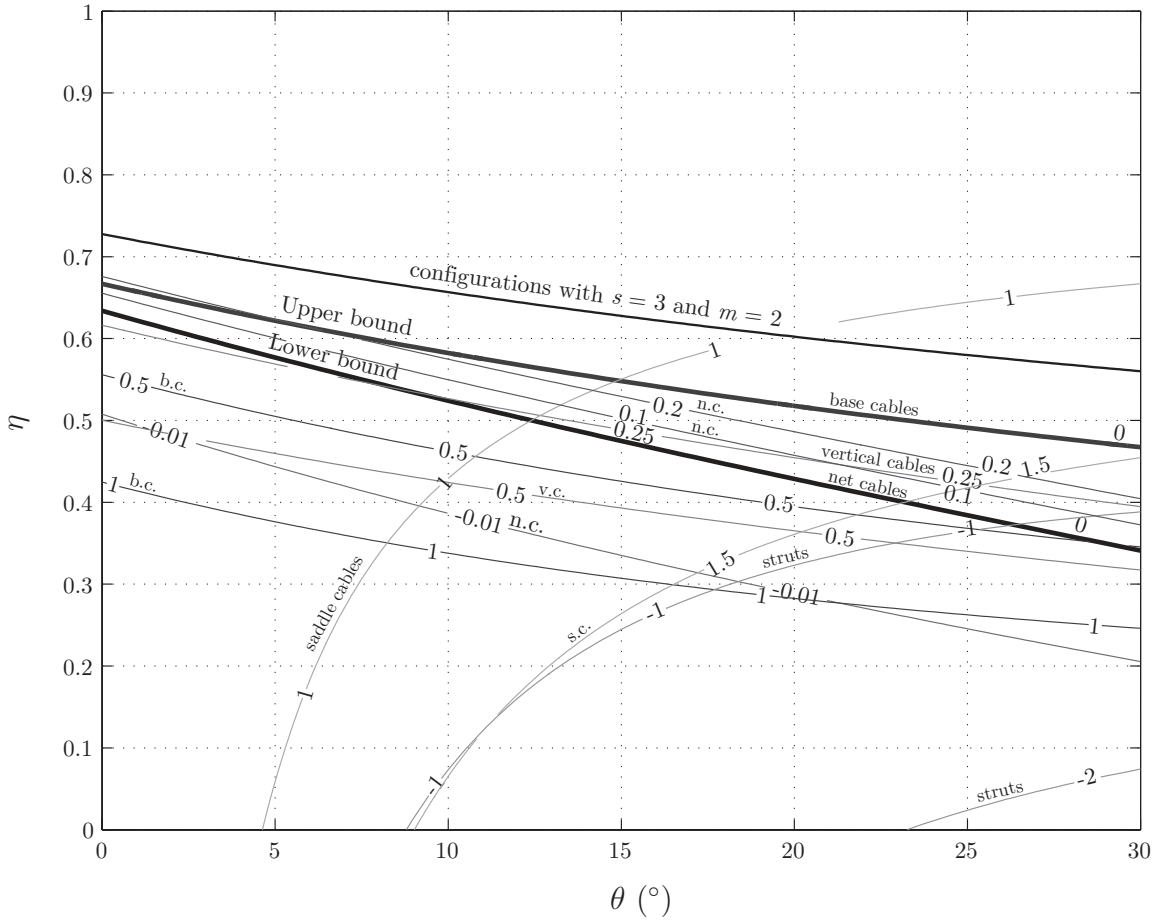

Figure 7.26: Force density values for the stiffened two-stage tensegrity module ($R = H = 1$, $\Delta H = H/100$). The two thickest lines represent the upper ($q_{\text{base}} = 0$) and lower ($q_{\text{net}} = 0$) bound for the overlap ($q_{\text{diagonal}} = 1$).

determinacy of the complete structure and easy prestressing. In was shown in Chapter 6 that it became more difficult to prestress the nets as the number of rings increases. Finally, there are several manufacturing issues that will need to be investigated before the antenna can be constructed. Those concerned with the achievable manufacturing accuracies are especially important.

Chapter 8

Conclusions

8.1 Analysis Methods

One of the aims of the present work was to scrutinise the various methods for form-finding of tensegrity structures. It was found that the methods could be classified into two groups—kinematic and static methods. Kinematic methods determine the configuration of either maximal length of the struts or minimal length of the cables, while the length of the other type of element is kept constant. Static methods search for equilibrium configurations that permit the existence of a state of prestress in the structure with certain required characteristics.

The force density method and the energy method are found to be equivalent. In the search for new configurations, the force density method is well suited since the lengths of the elements of the structure are not specified at the start. However, it is difficult to control the variation in the lengths of the elements as the set of force densities is varied. In general, the static methods seem to possess more usable features than the kinematic ones. The reduced coordinate method or the force method are suitable for problems where some parts of the geometry are known.

It is concluded that methods for analysing tensegrity structures are available, but no single method is suitable for general problems. This is unsatisfactory and is contrary to the form-finding of cable nets and membrane structures, where the most popular methods, i.e. the force density and the dynamic relaxation methods, can handle general structures. The present review of form-finding methods for tensegrity structures offers a base for anyone intending to further continue the subject.

The force method is very efficient and highly suitable for the structural analysis of large frameworks. It may be argued that the FEM is computationally more efficient, but these methods normally do not provide any information on the static and kinematic properties of the framework; this information is essential in the early stages of the structural design.

8.2 Deployable Masts

Using recent advances in form-finding techniques, the equilibrium configurations of tensegrity masts with adequate internal force distributions are easily found. This design step is thus no longer a major obstacle.

The proposed manufacturing scheme worked well when all the early mistakes had been eliminated. The use of joints with holes manufactured to the correct three-dimensional angles should produce a net with the required accuracy. A high length accuracy is generally required, in the construction of cable structures, to obtain the desired prestress and straightness of the mast.

The suggested strut deployment approach worked well. However, an important deficiency of the present approach is that the mast do not achieve full stiffness until the last stage has been deployed. Hence, the mast is very flexible throughout the entire deployment process and this seriously limits the applicability of the masts. In the physical model, stiffness during deployment was provided by a central rod which also controlled the rate of unfolding. For longer masts, some other means of stiffening is needed.

The structural behaviour of the masts was in agreement with the findings of previous studies. The masts were relatively stiff axially but very flexible in bending. Adding cables to remove the internal mechanism did not improve the stiffness substantially. While the additional cables improved the initial axial stiffness by about 50%, the bending stiffness remained almost entirely unchanged, the first cables becoming slack under a small imposed load. This structural inefficiency of tensegrity structures with non-contacting struts has also been observed in studies of double-layer tensegrity grids, cf. [53,179]. One way to stiffen tensegrities, which is suggested in these studies, is to accept contacting struts. This will, however, reduce the excellent deployment capabilities associated with discontinuous struts. The design will thus be a trade-off between ease of deployment and compact packaging on one side and stiffness and strength on the other.

8.3 Deployable Antennas

Miura and Pellegrino [105], inventors of several deployable structures concepts, claim that "it is impossible to approach the field of deployable structures with a single, general concept or theory." This statement is certainly true in the case of the antenna proposed here. Several unique methods and concepts, each with its own particular features, were combined to produce a robust structure which conforms well to the requirements of a future space mission involving a small satellite.

The most critical constraint was the size of the stowed structure, and this restriction more or less dictated the design of the ring structure. Due to its special characteristics and maturity, the tension truss was chosen to approximate the reflecting surface. However, some modifications had to be done to the tension truss to render the assem-

bly kinematically determinate, which is needed for the dimensional stability. One aspect that needs further investigation is the layout of the nets, in order to ensure static determinacy of the complete structure and easy prestressing. It was apparent that the prestressing became more difficult with the present layout, as the number of rings increased. An accurate tension truss requires very tight length tolerances for the elements. Typically, a maximum error of one part per million is required. The variations of the coefficient of thermal expansion and tension tie forces must also be very low.

The proposed antenna concept is considered feasible for a future small-satellite mission as it approximately meets the requirements on the stowed dimensions and easily meets the mass goal. The stiffness of the antenna, as indicated by the lowest natural frequencies, is high compared to other antenna concepts. High stiffness is beneficial for ground testing as the gravity compensation system can be simplified.

Nevertheless, there are some issues that remain unsolved or solved unsatisfactorily. One aspect is the attachment to the satellite bus and this has to be designed along with the primary spacecraft structure. Another is the position of the struts. In their current position the struts go right through the tension tie forest. This seriously limits the number of net rings and thereby the achievable surface accuracy. There are also several manufacturing issues that will need to be investigated before the full scale antenna can be constructed. Critical factors are those aspects concerned with the achievable manufacturing accuracies.

8.4 Further Research

To develop new tensegrity structures, suitable areas of application must be identified and detailed requirements need to be formulated. Concerning the morphology of tensegrities, the number of conceivable configurations exceeds the likely range of applications. The main focus for future research must be on the implementation of tensegrities. In this respect, some form-finding studies are certainly needed to find configurations that meet the requirements, but the primary objective must be to solve the technological problems that still remain. This work should be aimed at simplicity and reliability.

One specific issue that needs more research is the how a tensegrity structure can be stiffened during deployment. The load bearing capacity during deployment is generally non-existent until the last cable has been prestressed. This mobility or looseness is especially undesirable in the case of masts, which often support other structures, such as solar panels and therefore must deploy in a predicted manner. Stiffness during deployment is also required for the numerical simulation of the process.

As indicated by the mast analysis, the bending strength of tensegrity masts must be improved. Skelton *et al.* [150] analyse planar tensegrity structures that are efficient in bending. Three-dimensional tensegrity structures with greater efficiency in bending

need to be developed to make tensegrity structures useful for applications requiring long slender masts.

The kinematic indeterminacy of tensegrities is not always a disadvantage. Since the shape changes with the equilibrium of the structure only a small quantity of control energy is needed to change its configuration. The use of tensegrity structures as sensors and actuators is therefore another area of application. This has been explored by Skelton and Sultan [150, 159].

Bibliography

[1] AEC-Able Engineering Company, Inc. http://www.aec-able.com (15 November 2001).

[2] Agrawal, P. K., Anderson, M. S., and Card, M. F. Preliminary design of large reflectors with flat facets. *IEEE Transactions on Antennas and Propagation AP-29*, 4 (1981), 688–694.

[3] Arianespace. "Ariane 4 ASAP" and "Ariane 5 payloads: ASAP". http://www.arianespace.com (21 June 2001).

[4] Baier, H., Datashvili, L., Gogava, Z., Medzmariashvili, E., and Montuori, V. Building blocks of large deployable precision membrane reflectors. In *42nd AIAA/ASME/ASCE/AHS/ASC Structures, Structural Dynamics, and Materials Conference and Exhibit* (Seattle, WA, USA, 16–19 April 2001). AIAA 2001-1478.

[5] Barnes, M. R. Applications of dynamic relaxation to the design of cable, membrane and pneumatic structures. In *Proceedings of Second International Conference on Space Structures* (Guildford, 1975), W. J. Supple, Ed.

[6] Barnes, M. R. Form-finding and analysis of prestressed nets and membranes. *Computers & Structures 30*, 3 (1988), 685–695.

[7] Becchi, P., and Dell'Amico, S. Design and testing of a deployable, retrievable boom for space applications. In *Proceedings of the 23rd Aerospace Mechanisms Symposium* (Marshall Space Flight Center, Huntsville, AL, USA, 3–5 May 1989), pp. 101–112. NASA CP-3032.

[8] Belkacem, S. *Recherche de forme par relaxation dynamique des structures réticulées spatiales autoconstraintes*. PhD thesis, Université Paul Sabatier de Toulouse, Toulouse, France, 1987.

[9] Belvin, W. K. Quasistatic shape adjustment of a 15-meter-diameter space antenna. *Journal of Spacecraft and Rockets 26*, 3 (1989), 129–136.

[10] Boeing Satellite Systems. http://www.hughespace.com (28 November 2001).

[11] Bouderbala, M., and Motro, R. Folding tensegrity systems. In *IUTAM-IASS Symposium on Deployable Structures: Theory and Applications* (Cambridge, UK, 6–9 September 1998), S. Pellegrino and S. D. Guest, Eds., Kluwer Academic Publishers, Dordrecht, The Netherlands, 2000, pp. 27–36.

[12] Brown, K. W., and Prata, Jr., A. A design procedure for classical offset dual reflector antennas with circular apertures. *IEEE Transactions on Antennas and Propagation 42*, 8 (1994), 1145–1153.

[13] Calladine, C. R. Buckminster Fuller's "tensegrity" structures and Clerk Maxwell's rules for the construction of stiff frames. *International Journal of Solids and Structures 14*, 2 (1978), 161–172.

[14] Calladine, C. R., and Pellegrino, S. Authors' closure. *International Journal of Solids and Structures 27*, 4 (1991), 521–522.

[15] Calladine, C. R., and Pellegrino, S. First-order infinitesimal mechanisms. *International Journal of Solids and Structures 27*, 4 (1991), 505–515.

[16] Calladine, C. R., and Pellegrino, S. Further remarks on first-order infinitesimal mechanisms. *International Journal of Solids and Structures 29*, 17 (1992), 2119–2122.

[17] Campbell, G., Bailey, M. C., and Belvin, W. K. The development of the 15-meter hoop column deployable antenna system with final structural and electromagnetic performance results. *Acta Astronautica 17*, 1 (1988), 69–77.

[18] Chesley, B., Lutz, R., and Brodsky, R. F. Space payload design and sizing. In *Space Mission Analysis and Design*, J. R. Wertz and W. J. Larson, Eds., third ed., Space Technology Series. Microcosm Press and Kluwer Academic Publishers, El Segundo, CA, USA and Dordrecht, The Netherlands, 1999, ch. 9.3, pp. 255–265.

[19] Chironis, N. P. *Mechanisms & Mechanical Devices Sourcebook*. McGraw-Hill, New York, 1991, ch. 4, pp. 164–171.

[20] Chmielewski, A. B. *et al.* ARISE—mission and spacecraft description. Jet Propulsion Laboratory Document 16330, 1998. 83 pages.

[21] Connelly, R. Rigidity and energy. *Inventiones Mathematicae 66*, 1 (1982), 11–33.

[22] Connelly, R. Rigidity. In *Handbook of convex geometry, Vol. A*, P. M. Gruber and J. M. Wills, Eds. North-Holland, Amsterdam, 1993, pp. 223–271.

[23] Connelly, R. Tensegrity structures: why are they stable? In *Rigidity Theory and Applications* (New York, 1999), M. F. Thorpe and P. M. Duxbury, Eds., Plenum Press, pp. 47–54.

[24] Connelly, R., and Back, A. Mathematics and tensegrity. *American Scientist 86*, 2 (1998), 142–151.

[25] Connelly, R., and Servatius, H. Higher-order rigidity—what is the proper definition? *Discrete & Computational Geometry 11* (1994), 193–200.

[26] Connelly, R., and Terrell, M. Globally rigid symmetric tensegrities. *Structural Topology 21* (1995), 59–78.

[27] Cook, R. D., Malkus, D. S., and Plesha, M. E. *Concepts and applications of finite element analysis*, third ed. John Wiley & Sons, New York, 1989.

[28] Crone, G. Large deployable reflector antenna for advanced mobile communications. ESA/Industry Briefing Meeting. 9 May, 2000.

[29] Dahlquist, G., and Björk, Å. *Numerical methods*. Prentice-Hall, Englewood Cliffs, New Jersey, 1974.

[30] Daton-Lovett, A. J. An extendible member. Patent Cooperation Treaty Application PCT/GB97/00839, Publication Number WO 97/35706. Filed 25 March 1997, Published 2 October 1997.

[31] Day, A., and Bunce, J. The analysis of hanging roofs. *Arup Journal* (September 1969), 30–31.

[32] Defence Evaluation and Research Agency. Space Technology Research Vehicle (STRV). http://www.dera.gov.uk/html/space/strv/home.htm (21 June 2001).

[33] Deutschen Zentrum für Luft- und Raumfahrt. http://www.dlr.de (4 December 2001).

[34] Dietrich, R., and Pellegrino, S. Feasibility study of a deployable mesh reflector: phase II. Tech. Rep. CUED/D-STRUCT/TR199, Department of Engineering, University of Cambridge, Cambridge, UK, 20 June 2001.

[35] Duffy, J., Rooney, J., Knight, B., and Crane III, C. D. A review of a family of self-deploying tensegrity structures with elastic ties. *The Shock and Vibration Digest 32*, 2 (2000), 100–106.

[36] El Naschie, M. S. *Stress, stability and chaos in structural engineering: an energy approach*. McGraw-Hill, London, 1990.

[37] Emmerich, D. G. Self-tensioning spherical structures: single and double layer spheroids. *International Journal of Space Structures 5*, 3&4 (1990), 353–374.

[38] Fichter, W. B. Reduction of root-mean-square error in faceted space antennas. *AIAA Journal 22*, 11 (1984), 1679–1684.

[39] Fleeter, R. Design of low-cost spacecraft. In *Space Mission Analysis and Design*, J. R. Wertz and W. J. Larson, Eds., third ed., Space Technology Series. Microcosm Press and Kluwer Academic Publishers, El Segundo, CA, USA and Dordrecht, The Netherlands, 1999, ch. 22, pp. 853–882.

[40] Freeland, R. E. Survey of deployable antenna concepts. In *Large Space Antenna Systems Technology—1982* (Houston, TX, USA, 30 November–3 December 1982), vol. 1, NASA Langley Research Center, pp. 381–421. NASA CP-2269.

[41] Freeland, R. E., and Bilyeu, G. D. IN-STEP inflatable antenna experiment. In *43rd International Astronautical Federation Congress* (Washington, USA, 28 August–5 September 1992). IAF-92-0301.

[42] Freeland, R. E., Bilyeu, G. D., and Mikulas, M. M. Inflatable deployable space structures—technological summary. In *49th International Astronautical Congress* (Melbourne, Australia, 28 September–2 October 1998). IAF-98-I.5.01.

[43] Freeland, R. E., Bilyeu, G. D., and Veal, G. R. Development of flight hardware for a large, inflatable-deployable antenna experiment. In *46th International Astronautical Congress* (Oslo, Norway, 2–6 October 1995). IAF-95-I501.

[44] Fuller, R. B. Tensile-integrity structures. United States Patent 3,063,521, 1962. Filed 31 August 1959, Granted 13 November 1962.

[45] Furuya, H. Concept of deployable tensegrity structures in space application. *International Journal of Space Structures 7*, 2 (1992), 143–151.

[46] Geiger, D., Stefaniuk, A., and Chen, D. The design and construction of two cable domes for the Korean Olympics. In *Shells, Membranes and Space Frames, Proceedings IASS Symposium, Vol. 2* (Osaka, Japan, 1986), pp. 265–272.

[47] Géradin, M., and Rixen, D. *Mechanical vibrations*, second ed. John Wiley & Sons, New York, 1997.

[48] Grahn, S., and Rathsman, A. Astrid—An attempt to make the microsatellite a useful tool for space science. http://www.ssc.se/ssd/papers/ (12 September 2001).

[49] Greene, W. H. Effects of random member length errors on the accuracy and internal loads of truss antennas. *Journal of Spacecraft and Rockets 22*, 5 (1985), 554–559.

[50] Greschik, G., Palisoc, A., Cassapakis, C., Veal, G., and Mikulas, M. M. Sensitivity study of precision pressurized membrane reflector deformations. *AIAA Journal 39*, 2 (2001), 308–314.

[51] Guest, S. D., and Pellegrino, S. A new concept for solid surface deployable antennas. *Acta Astronautica 38*, 2 (1996), 103–113.

[52] Hachkowski, M. R., and Peterson, L. D. A comparative study of the precision of deployable spacecraft structures. Tech. Rep. CU-CAS-95-22,

Center for Aerospace Structures, University of Colorado, Boulder, CO, USA, December 1995.

[53] Hanaor, A. Engineering properties of double-layer tensegrity grids. In *Spatial Structures at the Turn of the Millennium. Proceedings of the International IASS Symposium* (Copenhagen, Denmark, 2–6 September 1991), T. Wester, S. J. Medwadowski, and I. Mogensen, Eds., vol. 2, pp. 195–200.

[54] Hanaor, A. Geometrically rigid double-layer tensegrity grids. *International Journal of Space Structures 9*, 4 (1994), 227–238.

[55] Hearth, D. P., and Boyer, W. J. Flexibility of space structures makes design shaky. *Aerospace America 23*, 5 (1985), 100–103.

[56] Hedgepeth, J. M. Accuracy potentials for large space antenna structures. In *39th Annual Conference of the Society of Allied Weight Engineers, Inc.* (St. Louis, MO, USA, 12–14 May 1980). SAWE Paper No. 1375, ii+33 pages.

[57] Hedgepeth, J. M. Critical requirements for the design of large space structures. NASA CR-3484, November 1981.

[58] Hedgepeth, J. M. Accuracy potentials for large space antenna reflectors with passive structure. *Journal of Spacecraft and Rockets 19*, 3 (1982), 211–217.

[59] Hedgepeth, J. M. Influence of fabrication tolerances on the surface accuracy of large antenna structures. *AIAA Journal 20*, 5 (1982), 680–686.

[60] Hedgepeth, J. M. Structures for remotely deployable precision antennas. Astro Aerospace Corporation Technical Document, AAC-TN-1154, 16 January 1989.

[61] Hedgepeth, J. M., and Adams, L. R. Design concepts for large reflector antenna structures. NASA CR-3663, 1983.

[62] Hedgepeth, J. M., Thomson, M. W., and Chae, D. Design of large lightweight precise mesh reflector structures. Astro Aerospace Corporation Technical Document, AAC-TN-1164, 8 November 1991.

[63] Hirosawa, H. *et al.* Space VLBI satellite HALCA and its engineering accomplishments. *Acta Astronautica* (2001). Paper IAF-98-Q1.01, In press.

[64] Ingber, D. E. The architecture of life. *Scientific American 278*, 1 (January 1998), 48–57.

[65] Iqbal, K., Pellegrino, S., and Daton-Lovett, A. Bi-stable composite slit tubes. In *IUTAM-IASS Symposium on Deployable Structures: Theory and Applications* (Cambridge, UK, 6–9 September 1998), S. Pellegrino and S. D. Guest, Eds., Kluwer Academic Publishers, Dordrecht, The Netherlands, 2000, pp. 153–162.

[66] Itanami, T., Minomo, M., and Ohtomo, I. Fan rib type deployable mesh antenna for satellite use. *Acta Astronautica 17*, 5 (1988), 561–566.

[67] Jenkins, C. H. M. *Gossamer spacecraft: membrane and inflatable structures technology for space applications*, vol. 191 of *Progress in Astronautics and Aeronautics*. AIAA, Reston, VA, USA, 2001.

[68] Jensen, F., and Pellegrino, S. Arm development—review of existing technologies. Tech. Rep. CUED/D-STRUCT/TR198, Department of Engineering, University of Cambridge, Cambridge, UK, 25 June 2001.

[69] Kangwai, R. D., Guest, S. D., and Pellegrino, S. An introduction to the analysis of symmetric structures. *Computers & Structures 71*, 6 (1999), 671–688.

[70] Kenner, H. *Geodesic math and how to use it*. University of California Press, Berkeley, CA, USA, 1976.

[71] Knight, B., Duffy, J., Crane, C., and Rooney, J. Innovative deployable antenna developments using tensegrity design. In *41st AIAA/ASME/ASCE/AHS/ASC Structures, Structural Dynamics, and Materials Conference and Exhibit* (Atlanta, GA, USA, 3–6 April 2000), pp. 984–994. AIAA 2000-1481.

[72] Knight, B. F. *Deployable antenna kinematics using tensegrity structure design*. PhD thesis, University of Florida, Gainesville, FL, USA, 2000.

[73] Kötter, E. Über die Möglichkeit, n Punkte in der Ebene oder im Raume durch weniger als $2n-3$ oder $3n-6$ Stäbe von ganz unveränderlicher Länge unverschieblich miteinander zu verbinden. In *Festschrift Heinrich Müller-Breslau*, A. Kröner, Ed. Leipzig, 1912, pp. 61–80.

[74] Kuznetsov, E. N. On immobile kinematic chains and a fallacious matrix analysis. *Journal of Applied Mechanics, Transactions of the ASME 56*, 1 (1989), 222–224.

[75] Kuznetsov, E. N. Discussion of "first-order infinitesimal mechanisms". *International Journal of Solids and Structures 27*, 4 (1991), 517–519.

[76] Kuznetsov, E. N. *Underconstrained structural systems*. Springer, New York, 1991.

[77] Kwan, A. S. K. *A pantographic deployable mast*. PhD thesis, University of Cambridge, Cambridge, UK, 1991.

[78] Lai, C.-Y. *Analysis and design of a deployable membrane reflector*. PhD thesis, University of Cambridge, 2001.

[79] Lai, C.-Y., and Pellegrino, S. Feasibility study of a deployable mesh reflector. Tech. Rep. CUED/D-STRUCT/TR186, Department of Engineering, University of Cambridge, Cambridge, UK, 17 September 2000.

[80] Lai, C.-Y., and Pellegrino, S. Umbrella-type furlable reflector based on tension truss concept. In *42nd AIAA/ASME/ASCE/AHS/ASC Structures, Structural Dynamics, and Materials Conference and Exhibit* (Seattle, WA, USA, 16-19 April 2001). AIAA 2001-1481.

[81] Lai, C.-Y., You, Z., and Pellegrino, S. Shape of deployable reflectors. *Journal of Aerospace Engineering 11*, 3 (July 1998), 73–80.

[82] Lake, M. S. Launching a 25-meter space telescope: are astronauts a key to the next technically logical step after NGST? In *2001 IEEE Aerospace Conference* (Big Sky, MT, USA, 10–17 March 2001). IEEE Paper No. 2001-460.

[83] Lalvani, H. (Editor). Origins of tensegrity: views of Emmerich, Fuller and Snelson. *International Journal of Space Structures 11*, 1&2 (1996), 27–55.

[84] Lee, S., and Rahmat-Samii, Y. Simple formulas for designing an offset multibeam parabolic reflector. *IEEE Transactions on Antennas and Propagation AP-29*, 3 (1981), 472–478.

[85] Linkwitz, K. Formfinding by the "direct approach" and pertinent strategies for the conceptual design of prestressed and hanging structures. *International Journal of Space Structures 14*, 2 (1999), 73–87.

[86] Linkwitz, K., and Schek, H.-J. Einige Bemerkungen zur Berechnung von vorgespannten Seilnetzkonstruktionen. *Ingenieur-Archiv 40* (1971), 145–158. In German.

[87] Love, A. W. Some highlights in reflector antenna development. *Radio Science 11*, 8-9 (1976), 671–684.

[88] Marks, R., and Fuller, R. B. *The dymaxion world of Buckminster Fuller*. Reinhold Publications, New York, 1960.

[89] Mathworks Inc., The. MATLAB function reference—version 5. http://www.mathworks.com, 1999.

[90] Maxwell, J. C. On the calculation of the equilibrium and stiffness of frames. *London, Edinburgh and Dublin Philosophical Magazine 27* (1864), 294–299.

[91] Medzmariashvili, E., Kinteraya, G., Datashvili, L., Bedukadze, G., Siradze, N., Efremov, I., Chernyavski, A., and Kravchenko, Y. Space experiment "reflector" on testing the large-scale deployable high precision offset antenna reflector of a new generation at the orbital station MIR. In *AP2000 Millennium Conference on Antennas & Propagation* (Davos, Switzerland, 9–14 April 2000). Abstract 1508, http://www.estec.esa.nl/ap2000/abstracts/a01508.html (7 November 2001).

[92] Meguro, A., Tsujihata, A., Hamamoto, N., and Homma, M. Technology status of the 13 m aperture deployment antenna reflectors for Engineering Test Satellite VIII. *Acta Astronautica 47*, 2–9 (2000), 147–152.

[93] Micheletti, A. On the kinematics of tensegrity towers. Oral presentation at "Colloquium Lagrangianum—Strutture Tensegrity: Analisi e Progetti", 6–8 May 2001, Rome, Italy.

[94] Micheletti, A. On the kinematics of tensegrity structures. Draft, 2 October 2001.

[95] Mikulas, M. M., and Thomson, M. *State of the art and technology needs for large space structures*, vol. 1: New and Projected Aeronautical and Space Systems, Design Concepts, and Loads of *Flight-Vehicle Materials, Structures, and Dynamics—Assessment and Future Directions*. ASME, New York, 1994, ch. 3, pp. 173–238.

[96] Mikulas Jr., M. M., Collins, T. J., and Hedgepeth, J. M. Preliminary design considerations for 10–40 meter-diameter precision truss reflectors. *Journal of Spacecraft and Rockets 28*, 4 (1991), 439–447.

[97] Miller, I., Freund, J. E., and Johnson, R. A. *Miller & Freund's probability and statistics for engineers*, sixth ed. Prentice Hall, Upper Saddle River, New Jersey, 1987.

[98] Mitsugi, J., Ando, K., Senbokuya, Y., and Meguro, A. Deployment analysis of large space antenna using flexible multibody dynamics simulation. *Acta Astronautica 47*, 1 (2000), 19–26.

[99] Mitsugi, J., and Yasaka, T. A modular approach to build a large space antenna. In *42nd International Astronautical Congress* (Montreal, Canada, 5–11 October 1991). IAF-91-315, 10 pages.

[100] Mitsugi, J., Yasaka, T., and Miura, K. Shape control of the tension truss antenna. *AIAA Journal 28*, 2 (1990), 316–322.

[101] Miura, K. Concepts of deployable space structures. *International Journal of Space Structures 8*, 1&2 (1993), 3–16.

[102] Miura, K., April 2001. Private communication.

[103] Miura, K., Furuya, H., and Suzuki, K. Variable geometry truss and its application to deployable truss and space crane arm. *Acta Astronautica 12*, 7/8 (1985), 599–607.

[104] Miura, K., and Miyazaki, Y. Concept of the tension truss antenna. *AIAA Journal 28*, 6 (1990), 1098–1104.

[105] Miura, K., and Pellegrino, S. *Structural concepts*. 1999. Draft.

[106] Miura, K., and Tanizawa, K. Tension truss antenna—concept, reality and future. In *IUTAM-IASS Symposium on Deployable Structures: Theory and Applications* (Cambridge, UK, 6–9 September 1998), S. Pellegrino and S. D. Guest, Eds., Kluwer Academic Publishers, Dordrecht, The Netherlands, 2000, pp. 291–300.

[107] Miyasaki, A., Homma, M., Tsujigata, A., Nakamura, K., Yamada, K., and Meguro, A. Design and ground verification of large deployable reflector. In *42nd AIAA/ASME/ASCE/AHS/ASC Structures, Structural Dynamics, and Materials Conference and Exhibit* (Seattle, WA, USA, 16-19 April 2001). AIAA 2001-1480.

[108] Möbius, A. F. *Lehrbuch der Statik*, vol. 2. Leipzig, 1837.

[109] Moholy-Nagy, L. *Von Material zu Architektur*. Albert Langen Verlag, München, 1929.

[110] Motro, R. Forms and forces in tensegrity systems. In *Third International Conference on Space Structures* (Guildford, 1984), H. Nooshin, Ed., Elsevier, pp. 180–185.

[111] Motro, R. Tensegrity systems and geodesic domes. *International Journal of Space Structures 5*, 3&4 (1990), 341–351.

[112] Motro, R. Tensegrity systems: the state of the art. *International Journal of Space Structures 7*, 2 (1992), 75–83.

[113] Motro, R. Structural morphology of tensegrity systems. *International Journal of Space Structures 11*, 1&2 (1996), 233–240.

[114] Motro, R., Belkacem, S., and Vassart, N. Form finding numerical methods for tensegrity systems. In *Spatial, Lattice and Tension structures, Proceedings of the IASS-ASCE International Symposium 1994* (Atlanta, USA, 1994), J. F. Abel, J. W. Leonard, and C. U. Penalba, Eds., ASCE, pp. 704–713.

[115] Murakami, H. Static and dynamic analyses of tensegrity structures. Part I. Nonlinear equations of motion. *International Journal of Solids and Structures 38* (2001), 3599–3613.

[116] Murakami, H., and Nishimura, Y. Initial shape finding and modal analyses of cyclic right-cylindrical tensegrity modules. *Computers & Structures 79*, 9 (2001), 891–917.

[117] Nishimura, Y. *Static and dynamic analyses of tensegrity structures*. PhD thesis, University of California at San Diego, La Jolla, CA, USA, 2000.

[118] Pak, H. Y. E. Deployable tensegrity structures. Fourth-year undergraduate project report, 24 May 2000. Department of Engineering, University of Cambridge, Cambridge, UK.

[119] Panetti, A. Thermal. In *Space Mission Analysis and Design*, J. R. Wertz and W. J. Larson, Eds., third ed., Space Technology Series. Microcosm Press and Kluwer Academic Publishers, El Segundo, CA, USA and Dordrecht, The Netherlands, 1999, ch. 11.5, pp. 428–458.

[120] Paz, M. *Structural dynamics: theory and computation*, fourth ed. Chapman & Hall, New York, 1997.

[121] Pellegrino, S. *Mechanics of kinematically indeterminate structures*. PhD thesis, University of Cambridge, Cambridge, UK, 1986.

[122] Pellegrino, S. Analysis of prestressed mechanisms. *International Journal of Solids and Structures 26*, 12 (1990), 1329–1350.

[123] Pellegrino, S. A class of tensegrity domes. *International Journal of Space Structures 7*, 2 (1992), 127–142.

[124] Pellegrino, S. Structural computations with the singular value decomposition of the equilibrium matrix. *International Journal of Solids and Structures 30*, 21 (1993), 3025–3035.

[125] Pellegrino, S. Large retractable appendages in spacecraft. *Journal of Spacecraft and Rockets 32*, 6 (1995), 1006–1014.

[126] Pellegrino, S., 2001. Private communication.

[127] Pellegrino, S., and Calladine, C. R. Matrix analysis of statically and kinematically indeterminate frameworks. *International Journal of Solids and Structures 22*, 4 (1986), 409–428.

[128] Pellegrino, S., Green, C., Guest, S. D., and Watt, A. SAR advanced deployable structure. Tech. Rep. CUED/D-STRUCT/TR191, Department of Engineering, University of Cambridge, Cambridge, UK, 18 November 2000.

[129] Pellegrino, S., and Guest, S. D., Eds. *IUTAM-IASS Symposium on Deployable Structures: Theory and Applications*, vol. 80 of *Solid Mechanics and Its Applications*. Kluwer Academic Publishers, Dordrecht, The Netherlands, 2000.

[130] Pellegrino, S., Kukathasan, S., Tibert, G., and Watt, A. Small satellite deployment mechanisms. Tech. Rep. CUED/D-STRUCT/TR190, Department of Engineering, University of Cambridge, Cambridge, UK, 9 November 2000.

[131] Pontoppidan, K. Electrical consequences of mechanical antenna characteristics. In *Workshop on Mechanical Technology for Antennas* (Noordwijk, The Netherlands, 26–28 June 1984), ESA/ESTEC, pp. 41–47. ESA SP-225.

[132] Pugh, A. *An introduction to tensegrity*. University of California Press, Berkeley, CA, USA, 1976.

[133] Rebouillat, S., Peng, J. C. M., Donnet, J.-B., and Ryu, S.-K. Carbon fiber applications. In *Carbon Fibers*, J. Donnet, T. K. Wang, J. C. M. Peng, and S. Rebouillat, Eds., third ed. Marcel Dekker, New York, 1998, ch. 7, pp. 463–542.

[134] Reibaldi, G. G. Antenna mechanical technologies within ESA. In *Second ESA Workshop on Mechanical Technology for Antennas* (Noordwijk, The Netherlands, 20–22 May 1986), ESA/ESTEC, pp. 5–13. ESA SP-261.

[135] Reibaldi, G. G., and Bernasconi, M. C. QUASAT program: the ESA reflector. *Acta Astronautica 15*, 3 (1987), 181–187.

[136] Reynolds, T. Small satellite deployment mechanisms requirement report. DERA Report, DERA/KIS/SPACE/CR000495/1.0, September 2000.

[137] Rimrott, F. P. J., and Fritsche, G. Fundamentals of STEM mechanics. In *IUTAM-IASS Symposium on Deployable Structures: Theory and Applications* (Cambridge, UK, 6–9 September 1998), S. Pellegrino and S. D. Guest, Eds., Kluwer Academic Publishers, Dordrecht, The Netherlands, 2000, pp. 321–333.

[138] Roederer, A. G., and Rahmat-Samii, Y. Unfurable satellite antennas: a review. *Annales des Télécommunications 44*, 9–10 (1989), 475–488.

[139] Rogers, C. A., Stutzman, W. L., Campbell, T. G., and Hedgepeth, J. M. Technology assessment and development of large deployable antennas. *Journal of Aerospace Engineering, ASCE 6*, 1 (1993), 34–54.

[140] Rusch, W. V. T. *Analysis of reflector antennas*. Academic Press, New York, 1970.

[141] Russell, A. G. Development of a large deployable space reflector structure. *Proceedings of the Institution of Mechanical Engineers, Part G—Journal of Aerospace Engineering 206*, G2 (1992), 111–123.

[142] Ruze, J. Antenna tolerance theory—a review. *Proceedings of the IEEE 54*, 4 (April 1966), 633–640.

[143] Sarafin, T. P., Doukas, P. G., McCandless, J. R., and Britton, W. R. Structures and mechanisms. In *Space Mission Analysis and Design*, J. R. Wertz and W. J. Larson, Eds., third ed., Space Technology Series. Microcosm Press and Kluwer Academic Publishers, El Segundo, CA, USA and Dordrecht, The Netherlands, 1999, ch. 11.6, pp. 459–497.

[144] Sarafin, T. P., and Larson, W. J., Eds. *Spacecraft Structures and Mechanisms—From Concept to Launch*. Space Technology Series. Microcosm Press and Kluwer Academic Publishers, El Segundo, CA, USA and Dordrecht, The Netherlands, 1995.

[145] Satellite News Digest. Satellite outages and failures. http://www.satindex.com/failures/ (24 August 2001).

[146] Schäfer, W. Stand der Technik auf dem Gebiet größerer entfaltbarer Parabolantennen-Strukturen für Raumfluggeräte. *Zeitschrift für Flugwissenschaften und Weltraumforschung 4*, 5 (1980), 255–267.

[147] Schek, H.-J. The force density method for form finding and computation of general networks. *Computational Methods in Applied Mechanics and Engineering 3* (1974), 115–134.

[148] Sjöberg, F. The design and manufacturing of a thermally stable submillimetre wave space-borne radio telescope. http://www.ssc.se/ssd/papers/ (24 August 2001).

[149] Skelton, R. E., and He, M. Smart tensegrity structure for NESTOR. In *Smart Structures and Materials 1997—Smart Structures and Integrated Systems* (San Diego, 3-6 March 1997), M. E. Regelbrugge, Ed., vol. 3041, SPIE—The International Society for Optical Engineering, pp. 780–787.

[150] Skelton, R. E., Helton, J. W., Adhikari, R., Pinaud, J.-P., and Chan, W. An introduction to the mechanics of tensegrity structures. Draft, 19 April 2001. http://www.mae.ucsd.edu/research/reskelton/ (11 November 2001).

[151] Snelson, K. D. Continuous tension, discontinuous compression structures. United States Patent 3,169,611, 1965. Filed 14 March 1960, Granted 16 February 1965.

[152] Southwell, R. V. *An introduction to the theory of elasticity*. Dover Publications, New York, 1969.

[153] Specht, N. Deployment simulation of a parabolic space antenna with rigid panels. *International Journal of Space Structures 8*, 1&2 (1993), 63–70.

[154] Stern, I., November 2001. Private communication.

[155] Strang, G. *Introduction to applied mathematics*. Wellesley-Cambridge Press, Wellesley, MA, USA, 1988.

[156] Strang, G. *Linear algebra and its applications*, third ed. Harcourt Brace Jovanovich College Publishers, San Diego, USA, 1988.

[157] Strock, J. D. Development of zero coefficient of thermal expansion composite tubes for stable structures. In *Design of Optical Instruments* (Orlando, FL, USA, 22–24 April 1992), vol. 1690, SPIE—The International Society for Optical Engineering, pp. 223–230.

[158] Stutzman, W. L., and Thiele, G. A. *Antenna theory and design*, second ed. John Wiley & Sons, New York, 1998, pp. 342–347.

[159] Sultan, C. *Modeling, design, and control of tensegrity structures with applications*. PhD thesis, Purdue University, West Lafayette, USA, 1999.

[160] Sultan, C., Corless, M., and Skelton, R. E. Reduced prestressability conditions for tensegrity structures. In *40st AIAA/ASME/ASCE/AHS/ASC Structures, Structural Dynamics, and Materials Conference* (St. Louis, MO, USA, 12–15 April 1999).

[161] Sultan, C., and Skelton, R. E. Force and torque smart tensegrity sensor. In *Smart Structures and Materials 1998—Mathematics and Control in Smart Structures* (San Diego, California, 2–5 March 1998), V. V. Varadan, Ed.,

vol. 3323, SPIE—The International Society for Optical Engineering, pp. 357–368.

[162] Sultan, C., and Skelton, R. E. Tendon control deployment of tensegrity structures. In *Smart Structures and Materials 1998—Mathematics and Control in Smart Structures* (San Diego, California, 2–5 March 1998), V. V. Varadan, Ed., vol. 3323, SPIE—The International Society for Optical Engineering, pp. 455–466.

[163] Swedish Space Corporation. Microsatellites. http://www.ssc.se/ssd/msat/ (12 September 2001).

[164] Swedish Space Corporation. Odin—a Swedish small satellite project for astronomical and atmospheric research. http://www.ssc.se/ssd/ssat/odin.html (12 September 2001).

[165] Thomson, M. W. The AstroMesh deployable reflector. In *Proceeding of the Fifth International Mobile Satellite Conference (IMSC '97)* (Pasadena, CA, USA, 16–18 June 1997), pp. 393–398.

[166] Thomson, M. W. The AstroMesh deployable reflector. In *IUTAM-IASS Symposium on Deployable Structures: Theory and Applications* (Cambridge, UK, 6–9 September 1998), S. Pellegrino and S. D. Guest, Eds., Kluwer Academic Publishers, Dordrecht, The Netherlands, 2000, pp. 435–446.

[167] Thomson, M. W., Marks, G. W., and Hedgepeth, J. M. Light-weight reflector for concentrating radiation. United States Patent 5,680,145. Filed 12 March 1996, Granted 21 October 1997.

[168] Tibert, A. G., and Pellegrino, S. Deployable tensegrity reflectors for small satellites, 2001. Submitted to *Journal of Spacecraft and Rockets*.

[169] Tibert, A. G., and Pellegrino, S. Furlable reflector concept for small satellites. In *42nd AIAA/ASME/ASCE/AHS/ASC Structures, Structural Dynamics, and Materials Conference and Exhibit* (Seattle, WA, USA, 16–19 April 2001). AIAA 2001-1261.

[170] Tibert, A. G., and Pellegrino, S. Review of form-finding methods for tensegrity structures, 2001. Accepted by *International Journal of Space Structures*.

[171] Tibert, G. *Numerical analyses of cable roof structures*. Licentiate thesis, Royal Institute of Technology, Stockholm, Sweden, 1999.

[172] TRW, Inc. TRW-built AstroMesh reflector deployed aboard Thuraya spacecraft. http://www.trw.com (5 December 2000).

[173] Ugural, A. C., and Fenster, S. K. *Advanced strength and applied elasticity*, third ed. Prentice-Hall, New Jersey, 1995.

[174] VAN 'T KLOOSTER, K., RITS, W., PAGANA, E., MANTICA, P. G., AND BERNASCONI, M. C. An inflatable parabolic reflector antenna: its realisation and electrical predictions. *ESA Journal 14*, 2 (1990), 211–216.

[175] VASSART, N. *Recherche de forme et stabilité des systèmes réticulés spatiaux autocontraints: Applications aux systèmes de tenségrité*. PhD thesis, Université des Sciences et Techniques du Languedoc, Montpellier, France, 1997.

[176] VASSART, N., LAPORTE, R., AND MOTRO, R. Determination of mechanism's order for kinematically and statically indetermined systems. *International Journal of Solids and Structures 37*, 28 (2000), 3807–3839.

[177] VASSART, N., AND MOTRO, R. Multiparametered formfinding method: Application to tensegrity systems. *International Journal of Space Structures 14*, 2 (1999), 147–154.

[178] VON HOERNER, S., AND WONG, W.-Y. Gravitational deformation and astigmatism of tiltable radio telescopes. *IEEE Transactions on Antennas and Propagation AP-23* (1975), 689–695.

[179] WANG, B.-B. A new type of self-stressed equilibrium cable-strut system made of reciprocal prisms. *International Journal of Space Structures 11*, 4 (1996), 357–362.

[180] WATT, A. M. *Lightweight deployable SAR structures*. MPhil thesis, University of Cambridge, Cambridge, UK. 2000.

[181] WATT, A. M., AND PELLEGRINO, S. Tape-spring rolling hinges. In *Proceedings of the 36th Aerospace Mechanisms Symposium* (Glenn Research Center, Cleveland, OH, USA, 15–17 May 2002), NASA.

[182] WEBB, J. E. Deployable lattice column. United States Patent 3,486,279. Filed 30 November 1967, Granted 30 December 1969.

[183] WERTZ, J. R., AND LARSON, W. J., Eds. *Space Mission Analysis and Design*, third ed. Space Technology Series. Microcosm Press and Kluwer Academic Publishers, El Segundo, CA, USA and Dordrecht, The Netherlands, 1999.

[184] WESTED, J. H. Effect of deviation from the ideal paraboloid shape of large antenna reflectors. In *Design & Construction of Large Steerable Aerials for Satellite Communication, Radio Astronomy, and Radar* (6–8 June 1966), pp. 115–119. IEE Conference Publication Number 21.

[185] WU, K. C., AND LAKE, M. S. Multicriterion preliminary design of tetrahedral truss platform. *Journal of Spacecraft and Rockets 33*, 3 (1996), 410–415.

[186] YOU, Z. *Deployable structures for masts and reflector antennas*. PhD thesis, University of Cambridge, Cambridge, UK, 1994.

[187] You, Z., and Pellegrino, S. Deployable mesh reflector. In *Spatial, Lattice and Tension Structures, Proceedings of the IASS-ASCE International Symposium* (Atlanta, USA, 1994), J. F. Abel, J. W. Leonard, and C. U. Penalba, Eds., ASCE, pp. 103–112.

[188] You, Z., and Pellegrino, S. Cable-stiffened pantographic deployable structures Part 2: mesh reflector. *AIAA Journal 35*, 8 (1997), 1348–1355.

[189] Zarghamee, M. S. On antenna tolerance theory. *IEEE Transactions on Antennas and Propagation AP-15* (1967), 777–781.

[190] Zwanenburg, R. Olympus solar array structure and mechanisms. In *Proceedings of the Fourth European Symposium: Photovoltaic Generators in Space* (Cannes, France, 18–20 September 1984), ESA-SP-210, ESA, pp. 411–419.

Appendix A

Overlap Values for Tensegrity Masts

To construct a tensegrity mast, the overlap between stages, which gives a feasible self-stress, must be found. This overlap η is both dependent on the total number of stages n of the tower and on the relative rotation θ. Definitions of η and θ are found in Chapter 4. The overlap for the mast with three struts per stage is given for up to 50 stages for θ from $-10°$ to $29°$ at $1°$ intervals. These overlap values might be useful for any one who wants to construct a tensegrity mast.

Table A.1: Non-dimensional overlap versus the total number of stages n for a tensegrity tower with $3n$ struts for different values of the rotation angle θ.

n	θ (°)									
	−10	−9	−8	−7	−6	−5	−4	−3	−2	−1
2	.60878	.59824	.58763	.57696	.56622	.55541	.54451	.53353	.52246	.51128
3	.51817	.50810	.49802	.48793	.47784	.46772	.45758	.44741	.43721	.42696
4	.48298	.47326	.46355	.45385	.44415	.43444	.42473	.41499	.40524	.39546
5	.46483	.45532	.44584	.43636	.42689	.41742	.40794	.39845	.38895	.37942
6	.45399	.44463	.43529	.42595	.41663	.40730	.39798	.38864	.37929	.36992
7	.44693	.43766	.42841	.41918	.40995	.40072	.39149	.38226	.37301	.36374
8	.44203	.43283	.42365	.41449	.40533	.39617	.38701	.37785	.36867	.35947
9	.43849	.42934	.42021	.41109	.40198	.39288	.38377	.37465	.36553	.35638
10	.43583	.42672	.41763	.40855	.39948	.39041	.38134	.37226	.36317	.35407
11	.43378	.42470	.41564	.40659	.39755	.38851	.37947	.37042	.36136	.35229
12	.43217	.42311	.41407	.40505	.39603	.38701	.37800	.36897	.35994	.35088
13	.43087	.42184	.41282	.40381	.39481	.38582	.37682	.36781	.35879	.34976
14	.42982	.42080	.41180	.40280	.39382	.38484	.37586	.36687	.35786	.34884
15	.42895	.41994	.41095	.40197	.39300	.38403	.37506	.36608	.35709	.34809
16	.42822	.41923	.41025	.40128	.39232	.38336	.37440	.36543	.35645	.34745
17	.42761	.41862	.40965	.40069	.39174	.38279	.37384	.36488	.35591	.34692
18	.42708	.41810	.40914	.40019	.39125	.38231	.37336	.36441	.35545	.34646
19	.42663	.41766	.40871	.39976	.39082	.38189	.37295	.36401	.35505	.34607
20	.42624	.41728	.40833	.39939	.39046	.38153	.37260	.36366	.35470	.34573
21	.42591	.41694	.40800	.39907	.39014	.38122	.37229	.36335	.35440	.34544
22	.42561	.41665	.40771	.39878	.38986	.38094	.37202	.36309	.35414	.34518
23	.42535	.41639	.40746	.39853	.38961	.38070	.37178	.36285	.35391	.34495
24	.42511	.41616	.40723	.39831	.38939	.38048	.37157	.36264	.35370	.34475
25	.42491	.41596	.40703	.39811	.38920	.38029	.37138	.36246	.35352	.34457
26	.42472	.41578	.40685	.39794	.38903	.38012	.37121	.36229	.35336	.34441
27	.42455	.41561	.40669	.39778	.38887	.37997	.37106	.36214	.35321	.34426
28	.42440	.41547	.40655	.39763	.38873	.37983	.37092	.36201	.35308	.34413
29	.42427	.41533	.40641	.39751	.38860	.37970	.37080	.36188	.35296	.34401
30	.42415	.41521	.40629	.39739	.38849	.37959	.37068	.36177	.35285	.34391
31	.42403	.41510	.40619	.39728	.38838	.37948	.37058	.36167	.35275	.34381
32	.42393	.41500	.40609	.39718	.38829	.37939	.37049	.36158	.35266	.34372
33	.42384	.41491	.40600	.39709	.38820	.37930	.37040	.36150	.35258	.34364
34	.42375	.41483	.40591	.39701	.38812	.37922	.37033	.36142	.35250	.34356
35	.42367	.41475	.40584	.39694	.38804	.37915	.37025	.36135	.35243	.34350
36	.42360	.41468	.40577	.39687	.38797	.37908	.37019	.36128	.35237	.34343
37	.42353	.41461	.40570	.39680	.38791	.37902	.37013	.36122	.35231	.34337
38	.42347	.41455	.40564	.39674	.38785	.37896	.37007	.36117	.35225	.34332
39	.42341	.41449	.40559	.39669	.38780	.37891	.37002	.36112	.35220	.34327
40	.42336	.41444	.40553	.39664	.38775	.37886	.36997	.36107	.35215	.34322
41	.42331	.41439	.40548	.39659	.38770	.37881	.36992	.36102	.35211	.34318
42	.42326	.41434	.40544	.39655	.38766	.37877	.36988	.36098	.35207	.34314
43	.42322	.41430	.40540	.39650	.38762	.37873	.36984	.36094	.35203	.34310
44	.42318	.41426	.40536	.39647	.38758	.37869	.36980	.36091	.35199	.34306
45	.42314	.41422	.40532	.39643	.38754	.37866	.36977	.36087	.35196	.34303
46	.42311	.41419	.40529	.39640	.38751	.37862	.36974	.36084	.35193	.34300
47	.42307	.41416	.40525	.39636	.38748	.37859	.36971	.36081	.35190	.34297
48	.42304	.41412	.40522	.39633	.38745	.37856	.36968	.36078	.35187	.34294
49	.42301	.41410	.40519	.39630	.38742	.37854	.36965	.36075	.35185	.34292
50	.42298	.41407	.40517	.39628	.38739	.37851	.36962	.36073	.35182	.34289

n	θ (°)									
	0	1	2	3	4	5	6	7	8	9
2	.50000	.48861	.47709	.46544	.45365	.44170	.42959	.41730	.40482	.39213
3	.41667	.40632	.39590	.38542	.37485	.36420	.35344	.34258	.33159	.32047
4	.38564	.37579	.36588	.35592	.34590	.33580	.32563	.31536	.30499	.29451
5	.36987	.36028	.35065	.34097	.33123	.32143	.31156	.30160	.29155	.28140
6	.36053	.35110	.34163	.33212	.32255	.31293	.30323	.29346	.28359	.27364
7	.35445	.34513	.33577	.32637	.31691	.30740	.29782	.28816	.27842	.26858
8	.35025	.34100	.33172	.32239	.31301	.30357	.29407	.28449	.27483	.26508
9	.34721	.33802	.32878	.31951	.31018	.30080	.29135	.28183	.27223	.26254
10	.34494	.33578	.32658	.31735	.30806	.29872	.28931	.27983	.27028	.26063
11	.34319	.33406	.32489	.31568	.30643	.29712	.28774	.27830	.26877	.25915
12	.34181	.33270	.32356	.31437	.30514	.29585	.28650	.27708	.26758	.25799
13	.34070	.33161	.32249	.31332	.30411	.29484	.28551	.27611	.26662	.25705
14	.33980	.33072	.32162	.31247	.30327	.29401	.28470	.27531	.26584	.25629
15	.33905	.32999	.32090	.31176	.30257	.29333	.28403	.27465	.26520	.25565
16	.33843	.32938	.32029	.31117	.30199	.29276	.28346	.27410	.26465	.25512
17	.33791	.32886	.31978	.31067	.30150	.29227	.28299	.27363	.26420	.25467
18	.33746	.32842	.31935	.31024	.30108	.29186	.28258	.27323	.26381	.25429
19	.33707	.32804	.31898	.30987	.30072	.29151	.28224	.27289	.26347	.25396
20	.33674	.32771	.31866	.30955	.30040	.29120	.28193	.27260	.26318	.25367
21	.33645	.32743	.31837	.30928	.30013	.29093	.28167	.27234	.26292	.25343
22	.33619	.32718	.31813	.30903	.29989	.29070	.28144	.27211	.26270	.25321
23	.33597	.32696	.31791	.30882	.29968	.29049	.28123	.27191	.26250	.25301
24	.33577	.32676	.31772	.30863	.29950	.29031	.28105	.27173	.26233	.25284
25	.33559	.32659	.31754	.30846	.29933	.29014	.28089	.27157	.26217	.25269
26	.33543	.32643	.31739	.30831	.29918	.28999	.28075	.27143	.26203	.25255
27	.33529	.32629	.31725	.30817	.29905	.28986	.28062	.27130	.26191	.25243
28	.33516	.32616	.31713	.30805	.29892	.28974	.28050	.27119	.26180	.25232
29	.33505	.32605	.31701	.30794	.29882	.28964	.28040	.27108	.26169	.25221
30	.33494	.32594	.31691	.30784	.29872	.28954	.28030	.27099	.26160	.25212
31	.33484	.32585	.31682	.30775	.29863	.28945	.28021	.27090	.26151	.25204
32	.33476	.32576	.31673	.30766	.29854	.28937	.28013	.27082	.26144	.25196
33	.33468	.32568	.31666	.30759	.29847	.28929	.28006	.27075	.26137	.25189
34	.33460	.32561	.31658	.30752	.29840	.28923	.27999	.27069	.26130	.25183
35	.33454	.32554	.31652	.30745	.29833	.28916	.27993	.27062	.26124	.25177
36	.33447	.32548	.31646	.30739	.29828	.28911	.27987	.27057	.26119	.25172
37	.33441	.32543	.31640	.30734	.29822	.28905	.27982	.27052	.26113	.25167
38	.33436	.32537	.31635	.30729	.29817	.28900	.27977	.27047	.26109	.25162
39	.33431	.32532	.31630	.30724	.29812	.28896	.27973	.27042	.26104	.25158
40	.33427	.32528	.31626	.30719	.29808	.28891	.27968	.27038	.26100	.25154
41	.33422	.32524	.31622	.30715	.29804	.28887	.27964	.27034	.26096	.25150
42	.33418	.32520	.31618	.30711	.29800	.28884	.27961	.27031	.26093	.25146
43	.33415	.32516	.31614	.30708	.29797	.28880	.27957	.27027	.26090	.25143
44	.33411	.32513	.31611	.30705	.29793	.28877	.27954	.27024	.26086	.25140
45	.33408	.32509	.31608	.30701	.29790	.28874	.27951	.27021	.26084	.25137
46	.33405	.32506	.31605	.30698	.29788	.28871	.27948	.27018	.26081	.25134
47	.33402	.32504	.31602	.30696	.29785	.28868	.27946	.27016	.26078	.25132
48	.33399	.32501	.31599	.30693	.29782	.28866	.27943	.27013	.26076	.25129
49	.33397	.32498	.31597	.30691	.29780	.28863	.27941	.27011	.26074	.25127
50	.33394	.32496	.31594	.30688	.29778	.28861	.27939	.27009	.26071	.25125

n	θ (°)									
	10	11	12	13	14	15	16	17	18	19
2	.37921	.36605	.35261	.33889	.32485	.31045	.29567	.28046	.26477	.24856
3	.30920	.29777	.28615	.27434	.26231	.25003	.23748	.22464	.21146	.19790
4	.28390	.27316	.26226	.25119	.23993	.22846	.21676	.20481	.19256	.17999
5	.27113	.26074	.25020	.23951	.22864	.21758	.20631	.19480	.18302	.17095
6	.26357	.25338	.24305	.23258	.22194	.21112	.20010	.18885	.17735	.16556
7	.25864	.24858	.23839	.22806	.21757	.20690	.19603	.18495	.17362	.16203
8	.25522	.24525	.23516	.22492	.21452	.20396	.19320	.18223	.17102	.15955
9	.25274	.24283	.23280	.22263	.21231	.20181	.19113	.18024	.16911	.15773
10	.25088	.24101	.23103	.22091	.21063	.20019	.18956	.17873	.16767	.15635
11	.24943	.23961	.22966	.21957	.20934	.19893	.18835	.17756	.16654	.15528
12	.24830	.23850	.22857	.21852	.20831	.19794	.18738	.17663	.16565	.15442
13	.24738	.23760	.22770	.21766	.20748	.19713	.18661	.17588	.16492	.15373
14	.24663	.23687	.22698	.21697	.20680	.19647	.18597	.17526	.16433	.15315
15	.24601	.23626	.22639	.21639	.20624	.19593	.18543	.17474	.16383	.15268
16	.24549	.23575	.22590	.21590	.20577	.19547	.18499	.17431	.16341	.15227
17	.24505	.23532	.22547	.21549	.20536	.19507	.18461	.17394	.16306	.15193
18	.24468	.23496	.22511	.21514	.20502	.19474	.18428	.17363	.16275	.15164
19	.24435	.23464	.22480	.21484	.20472	.19445	.18400	.17335	.16249	.15138
20	.24407	.23436	.22453	.21457	.20447	.19420	.18375	.17311	.16226	.15116
21	.24383	.23412	.22430	.21434	.20424	.19398	.18354	.17291	.16205	.15096
22	.24361	.23391	.22409	.21414	.20404	.19379	.18335	.17272	.16188	.15079
23	.24342	.23373	.22391	.21396	.20387	.19361	.18318	.17256	.16172	.15064
24	.24325	.23356	.22375	.21380	.20371	.19346	.18304	.17241	.16158	.15050
25	.24310	.23341	.22360	.21366	.20357	.19333	.18290	.17229	.16145	.15038
26	.24297	.23328	.22347	.21353	.20345	.19320	.18278	.17217	.16134	.15027
27	.24285	.23316	.22336	.21342	.20334	.19309	.18268	.17206	.16124	.15017
28	.24274	.23305	.22325	.21331	.20323	.19300	.18258	.17197	.16114	.15008
29	.24264	.23296	.22315	.21322	.20314	.19291	.18249	.17188	.16106	.15000
30	.24255	.23287	.22307	.21314	.20306	.19282	.18241	.17181	.16098	.14993
31	.24247	.23279	.22299	.21306	.20298	.19275	.18234	.17173	.16092	.14986
32	.24239	.23271	.22292	.21299	.20291	.19268	.18227	.17167	.16085	.14980
33	.24232	.23265	.22285	.21292	.20285	.19262	.18221	.17161	.16079	.14974
34	.24226	.23258	.22279	.21286	.20279	.19256	.18215	.17155	.16074	.14969
35	.24220	.23253	.22273	.21281	.20274	.19251	.18210	.17150	.16069	.14964
36	.24215	.23247	.22268	.21276	.20269	.19246	.18205	.17146	.16064	.14959
37	.24210	.23243	.22263	.21271	.20264	.19241	.18201	.17141	.16060	.14955
38	.24205	.23238	.22259	.21267	.20260	.19237	.18197	.17137	.16056	.14951
39	.24201	.23234	.22255	.21262	.20256	.19233	.18193	.17133	.16053	.14948
40	.24197	.23230	.22251	.21259	.20252	.19230	.18190	.17130	.16049	.14944
41	.24193	.23226	.22247	.21255	.20249	.19226	.18186	.17127	.16046	.14941
42	.24190	.23223	.22244	.21252	.20245	.19223	.18183	.17124	.16043	.14938
43	.24187	.23220	.22241	.21249	.20242	.19220	.18180	.17121	.16040	.14936
44	.24184	.23217	.22238	.21246	.20240	.19217	.18177	.17118	.16038	.14933
45	.24181	.23214	.22235	.21243	.20237	.19215	.18175	.17116	.16035	.14931
46	.24178	.23211	.22233	.21241	.20234	.19212	.18173	.17113	.16033	.14928
47	.24176	.23209	.22230	.21238	.20232	.19210	.18170	.17111	.16031	.14926
48	.24173	.23207	.22228	.21236	.20230	.19208	.18168	.17109	.16029	.14924
49	.24171	.23204	.22226	.21234	.20228	.19206	.18166	.17107	.16027	.14922
50	.24169	.23202	.22224	.21232	.20226	.19204	.18164	.17105	.16025	.14921

n	θ (°)									
	20	21	22	23	24	25	26	27	28	29
2	.23175	.21428	.19604	.17694	.15682	.13552	.11282	.08842	.06191	.03273
3	.18393	.16948	.15449	.13889	.12258	.10543	.08731	.06802	.04730	.02480
4	.16706	.15372	.13992	.12559	.11064	.09499	.07850	.06102	.04232	.02212
5	.15855	.14577	.13256	.11887	.10462	.08972	.07405	.05748	.03981	.02078
6	.15347	.14101	.12816	.11484	.10100	.08655	.07138	.05536	.03830	.01997
7	.15013	.13788	.12525	.11218	.09861	.08445	.06961	.05394	.03730	.01943
8	.14778	.13568	.12321	.11031	.09692	.08296	.06834	.05294	.03658	.01904
9	.14606	.13406	.12170	.10892	.09566	.08186	.06740	.05219	.03604	.01876
10	.14475	.13283	.12055	.10786	.09470	.08101	.06668	.05160	.03563	.01853
11	.14373	.13187	.11965	.10703	.09395	.08033	.06610	.05114	.03529	.01835
12	.14291	.13110	.11893	.10636	.09334	.07979	.06564	.05077	.03502	.01820
13	.14225	.13047	.11834	.10581	.09284	.07935	.06526	.05046	.03480	.01808
14	.14170	.12995	.11785	.10536	.09242	.07898	.06494	.05020	.03461	.01798
15	.14125	.12952	.11744	.10498	.09207	.07866	.06467	.04997	.03445	.01789
16	.14086	.12915	.11709	.10465	.09178	.07840	.06443	.04978	.03431	.01782
17	.14053	.12883	.11680	.10438	.09152	.07817	.06423	.04962	.03419	.01775
18	.14025	.12856	.11654	.10414	.09130	.07797	.06406	.04948	.03408	.01769
19	.14001	.12833	.11632	.10393	.09111	.07779	.06391	.04935	.03399	.01764
20	.13979	.12813	.11612	.10375	.09094	.07764	.06377	.04924	.03391	.01759
21	.13960	.12795	.11595	.10358	.09079	.07750	.06365	.04914	.03383	.01755
22	.13944	.12779	.11580	.10344	.09065	.07738	.06354	.04905	.03376	.01751
23	.13929	.12764	.11567	.10331	.09054	.07727	.06345	.04897	.03370	.01748
24	.13916	.12752	.11555	.10320	.09043	.07717	.06336	.04889	.03365	.01745
25	.13904	.12741	.11544	.10310	.09033	.07709	.06328	.04883	.03360	.01742
26	.13893	.12730	.11534	.10300	.09025	.07701	.06321	.04877	.03355	.01739
27	.13884	.12721	.11525	.10292	.09017	.07693	.06315	.04871	.03351	.01737
28	.13875	.12713	.11517	.10285	.09010	.07687	.06309	.04866	.03347	.01735
29	.13867	.12705	.11510	.10278	.09003	.07681	.06303	.04862	.03344	.01733
30	.13860	.12698	.11503	.10271	.08997	.07675	.06298	.04858	.03341	.01731
31	.13854	.12692	.11497	.10265	.08992	.07670	.06294	.04854	.03338	.01729
32	.13848	.12686	.11492	.10260	.08987	.07666	.06290	.04850	.03335	.01727
33	.13842	.12681	.11486	.10255	.08982	.07661	.06286	.04847	.03332	.01726
34	.13837	.12676	.11482	.10251	.08978	.07657	.06282	.04844	.03330	.01724
35	.13832	.12671	.11477	.10246	.08974	.07654	.06279	.04841	.03327	.01723
36	.13828	.12667	.11473	.10243	.08970	.07650	.06276	.04838	.03325	.01722
37	.13824	.12663	.11470	.10239	.08967	.07647	.06273	.04835	.03323	.01720
38	.13820	.12659	.11466	.10236	.08964	.07644	.06270	.04833	.03321	.01719
39	.13817	.12656	.11463	.10232	.08961	.07641	.06268	.04831	.03320	.01718
40	.13813	.12653	.11460	.10230	.08958	.07639	.06265	.04829	.03318	.01717
41	.13810	.12650	.11457	.10227	.08955	.07636	.06263	.04827	.03316	.01716
42	.13808	.12647	.11454	.10224	.08953	.07634	.06261	.04825	.03315	.01715
43	.13805	.12645	.11452	.10222	.08951	.07632	.06259	.04823	.03314	.01714
44	.13802	.12642	.11449	.10220	.08948	.07630	.06257	.04822	.03312	.01714
45	.13800	.12640	.11447	.10218	.08946	.07628	.06255	.04820	.03311	.01713
46	.13798	.12638	.11445	.10216	.08944	.07626	.06254	.04819	.03310	.01712
47	.13796	.12636	.11443	.10214	.08943	.07624	.06252	.04817	.03309	.01711
48	.13794	.12634	.11441	.10212	.08941	.07623	.06251	.04816	.03308	.01711
49	.13792	.12632	.11440	.10210	.08939	.07621	.06249	.04815	.03307	.01710
50	.13790	.12630	.11438	.10209	.08938	.07620	.06248	.04813	.03306	.01710

Appendix B

Flat Cable Net for Constructing Tensegrity Masts

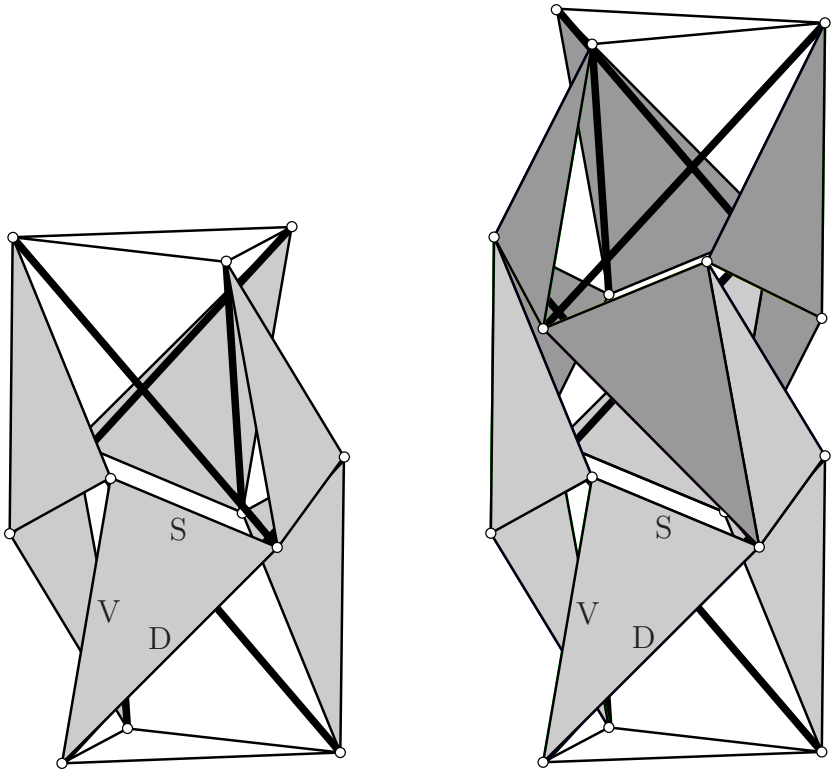

(a) Two-stage tensegrity mast (b) Three-stage tensegrity mast

Figure B.1: Three-dimensional configurations of tensegrity masts. Saddle cable is denoted S, diagonal cable D and vertical cable V.

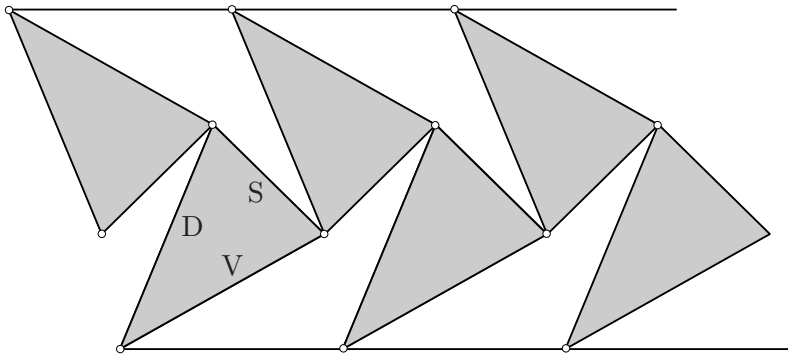

(a) Net 1

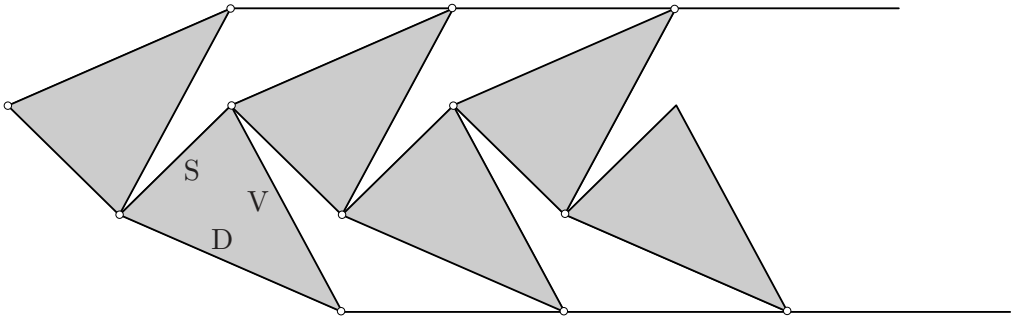

(b) Net 2

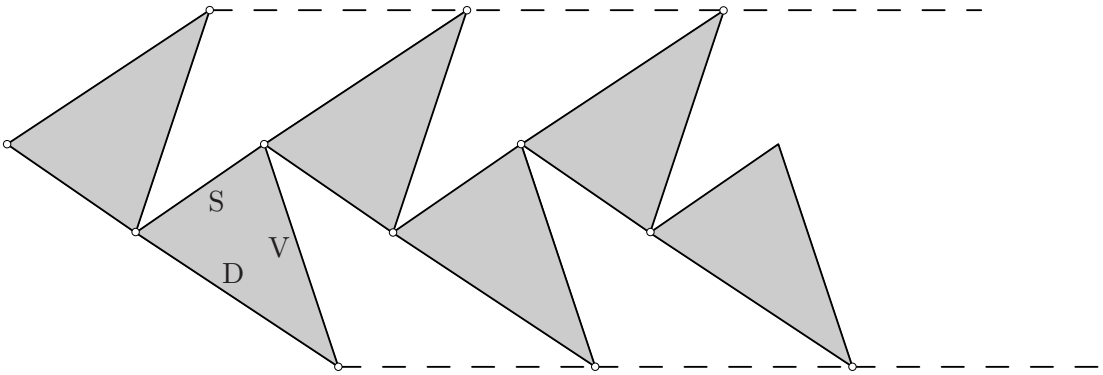

(c) Net 3

Figure B.2: Different two-dimensional configurations of two-stage tensegrity masts.

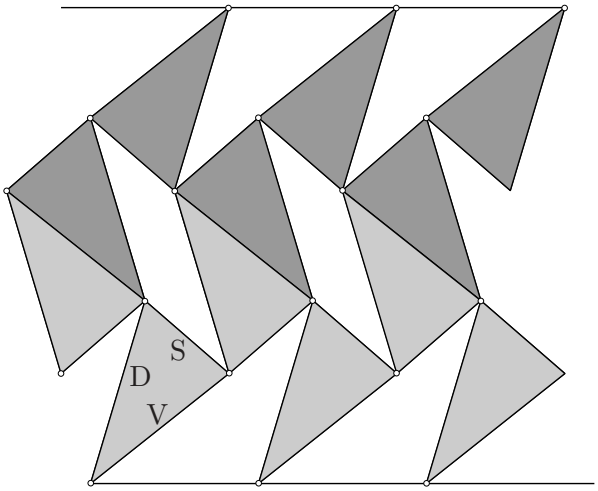

(a) Net 1

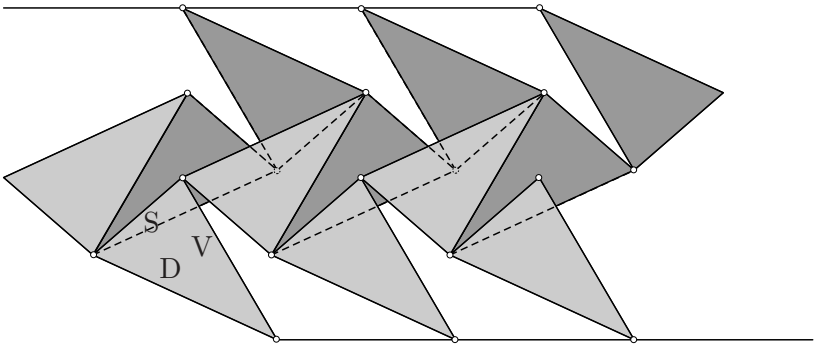

(b) Net 2

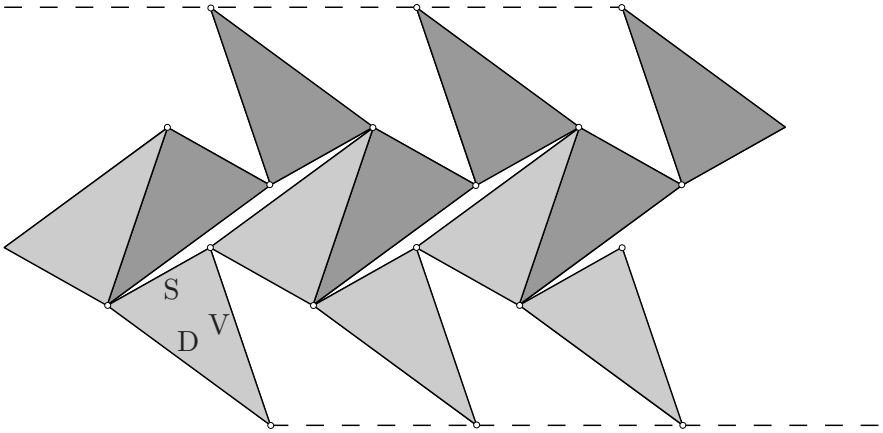

(c) Net 3

Figure B.3: Different two-dimensional configurations of three-stage tensegrity masts.

Appendix C

Mesh Generation Procedure for the Tension Truss

In this appendix, the procedure used for generating the triangular mesh of the paraboloidal cable nets is described in detail. The procedure is applicable to nets with bases that form a regular polygon and is illustrated in Figure C.1. First, the v-sided polygon sides are divided into v triangular bays, Figure C.1(a). Each triangular section is then subdivided into n triangles along each side, Figure C.1(b). Finally, the horizontal triangular mesh with a predefined sag-to-span ratio ρ is projected onto the paraboloidal surface giving the shape of the cable net, Figure C.1(c). In the final net, the number of triangles t, elements b and joints j are

$$t = vn^2, \tag{C.1}$$

$$b = v\frac{n(1+3n)}{2}, \tag{C.2}$$

$$j = 1 + v\frac{n(1+n)}{2}, \tag{C.3}$$

respectively.

In the following, a description of the n subdivision of the triangular bays is given. Given parameters are: the number of polygon sides v, the subdivision n, the radius R, and the two-dimensional sag-to-span ratio ρ. Here, ρ is defined as, Figure C.2:

$$\rho = \frac{\delta_{\text{sag}}}{2R_0 \tan(\theta/2)} \tag{C.4}$$

where δ_{sag} is the sag of the edge cable, $\theta = 2\pi/v$, and R_0 the effective radius of the net. Note that the span used in the definition, $2R_0 \tan(\theta/2)$, is different from the distance between the outer vertices which is $2R \tan(\theta/2)$, usually used to define the sag-to-span ratio. This is, however, of minor importance since the three-dimensional sag of the edge cable is dependent on the curvature, i.e. the relation between focal length and diameter of the reflector surface.

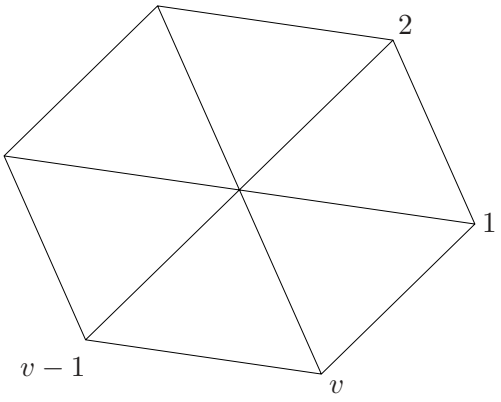

(a) v sided polygon.

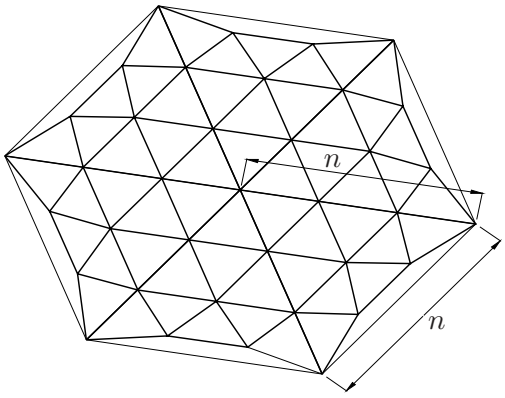

(b) Triangular n subdivision.

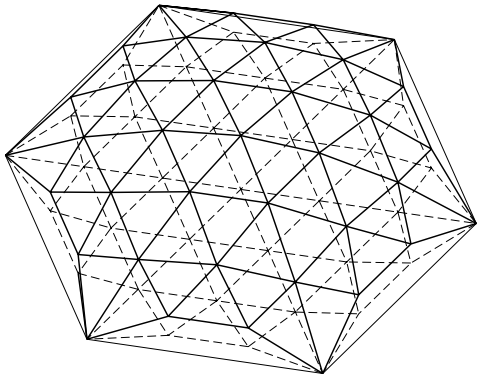

(c) Vertical mapping to paraboloidal surface.

Figure C.1: Mesh generation of net.

With the sag-to-span ratio known, R_0 is calculated by subtracting from R the following lengths, Figure C.2:

$$\Delta_1 = R\frac{1-\cos(\theta/2)}{\cos(\theta/2)} \tag{C.5}$$

$$\Delta_2 = \frac{\delta_{\text{sag}}}{\cos(\theta/2)} \tag{C.6}$$

With Equations (C.4)–(C.6), the relation between R and R_0 is written as

$$\frac{R}{R_0} = \frac{1+2\rho\tan(\theta/2)}{\cos(\theta/2)} \tag{C.7}$$

The radius R is divided into n equal parts giving identical triangles in the first $n-1$ rings. In the outer ring, the triangles are distorted by the sag of the edge cables.

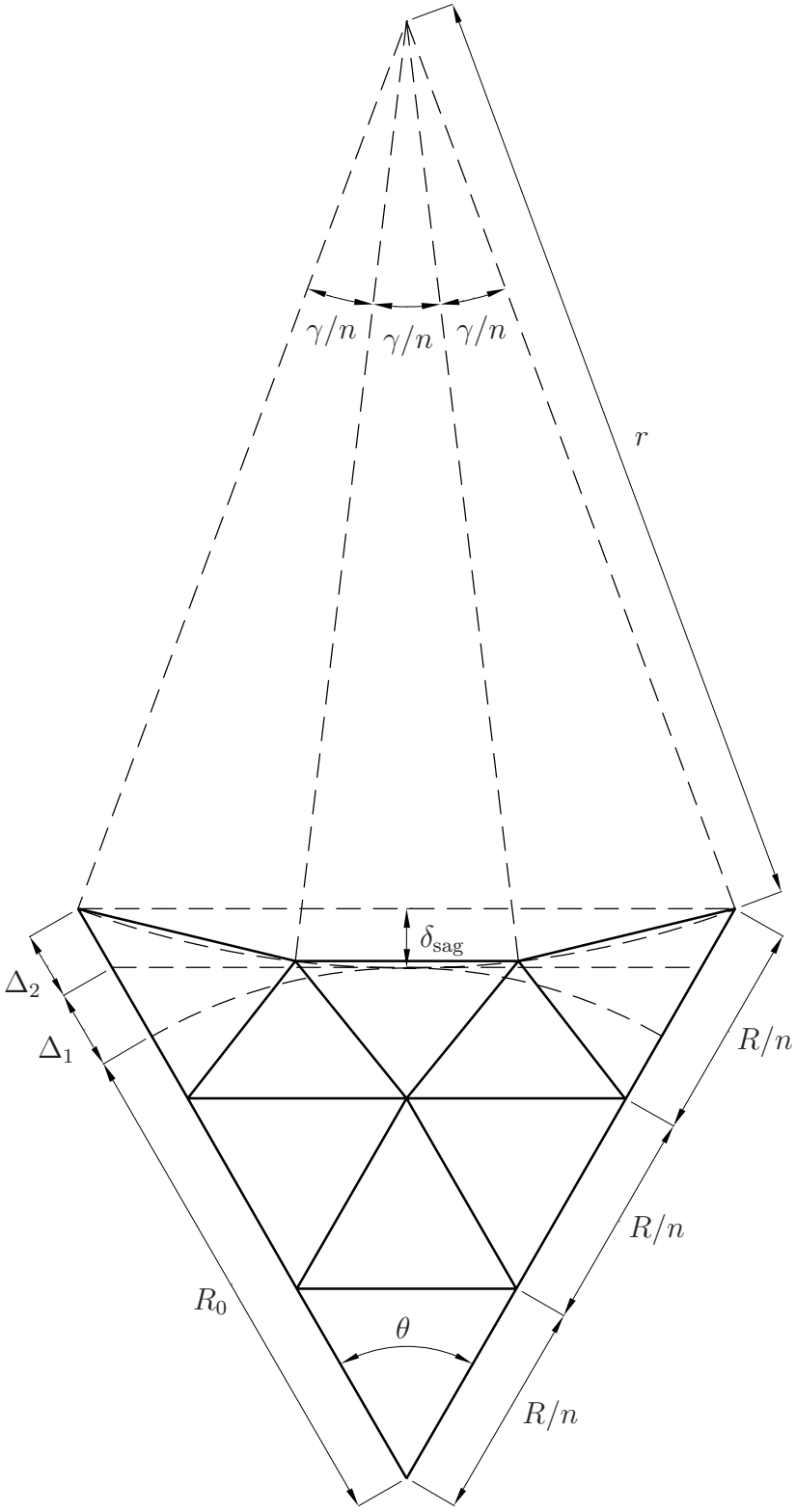

Figure C.2: Triangular subdivision of a bay ($n = 3$).

The edge joints are equidistantly positioned on an arc with radius r and opening angle γ, Figure C.2, which are given by

$$r = \frac{\delta_{\text{sag}}^2 + R^2 \sin^2(\theta/2)}{2\delta_{\text{sag}}} \tag{C.8}$$

$$\gamma = 2 \arccos \frac{r - \delta_{\text{sag}}}{r} \tag{C.9}$$

The horizontal projection of the length of the edge elements is $2r \sin(\gamma/2n)$. It should also be noted that for an odd n the actual two-dimensional sag of the edge elements will be slightly less than δ_{sag} as shown in Figure C.2 where $n = 3$.

Note that in the present mesh generation routine the sagging edge cable only affects the outermost ring of triangles. Therefore, there is a limit on the maximum number of rings n for a certain value of the sag-to-span ratio ρ. From Figure C.2, the maximum value for δ_{sag} is

$$\delta_{\text{sag}}^{\max} = \frac{R \cos(\theta/2)}{n} \tag{C.10}$$

Equations (C.4), (C.7) and (C.10) yield the maximum sag-to-span ratio as

$$\rho_{\max} = \frac{1}{2(n-1)\tan(\theta/2)} \tag{C.11}$$

Royal Institute of Technology
Department of Mechanics
SE-100 44 Stockholm, Sweden
http://www.mech.kth.se